NASA/TM-2006-214306

Shuttle Return To Flight Experimental Results: Protuberance Effects on Boundary Layer Transition

Derek S. Liechty, Scott A. Berry, and Thomas J. Horvath
Langley Research Center, Hampton, Virginia

June 2006

The NASA STI Program Office . . . in Profile

Since its founding, NASA has been dedicated to the advancement of aeronautics and space science. The NASA Scientific and Technical Information (STI) Program Office plays a key part in helping NASA maintain this important role.

The NASA STI Program Office is operated by Langley Research Center, the lead center for NASA's scientific and technical information. The NASA STI Program Office provides access to the NASA STI Database, the largest collection of aeronautical and space science STI in the world. The Program Office is also NASA's institutional mechanism for disseminating the results of its research and development activities. These results are published by NASA in the NASA STI Report Series, which includes the following report types:

- TECHNICAL PUBLICATION. Reports of completed research or a major significant phase of research that present the results of NASA programs and include extensive data or theoretical analysis. Includes compilations of significant scientific and technical data and information deemed to be of continuing reference value. NASA counterpart of peer-reviewed formal professional papers, but having less stringent limitations on manuscript length and extent of graphic presentations.

- TECHNICAL MEMORANDUM. Scientific and technical findings that are preliminary or of specialized interest, e.g., quick release reports, working papers, and bibliographies that contain minimal annotation. Does not contain extensive analysis.

- CONTRACTOR REPORT. Scientific and technical findings by NASA-sponsored contractors and grantees.

- CONFERENCE PUBLICATION. Collected papers from scientific and technical conferences, symposia, seminars, or other meetings sponsored or co-sponsored by NASA.

- SPECIAL PUBLICATION. Scientific, technical, or historical information from NASA programs, projects, and missions, often concerned with subjects having substantial public interest.

- TECHNICAL TRANSLATION. English-language translations of foreign scientific and technical material pertinent to NASA's mission.

Specialized services that complement the STI Program Office's diverse offerings include creating custom thesauri, building customized databases, organizing and publishing research results ... even providing videos.

For more information about the NASA STI Program Office, see the following:

- Access the NASA STI Program Home Page at ***http://www.sti.nasa.gov***

- E-mail your question via the Internet to help@sti.nasa.gov

- Fax your question to the NASA STI Help Desk at (301) 621-0134

- Phone the NASA STI Help Desk at (301) 621-0390

- Write to:
  NASA STI Help Desk
  NASA Center for AeroSpace Information
  7121 Standard Drive
  Hanover, MD 21076-1320

NASA/TM-2006-214306

Shuttle Return To Flight Experimental Results: Protuberance Effects on Boundary Layer Transition

Derek S. Liechty, Scott A. Berry, and Thomas J. Horvath
Langley Research Center, Hampton, Virginia

National Aeronautics and
Space Administration

Langley Research Center
Hampton, Virginia 23681-2199

June 2006

Available from:

NASA Center for AeroSpace Information (CASI)
7121 Standard Drive
Hanover, MD 21076-1320
(301) 621-0390

National Technical Information Service (NTIS)
5285 Port Royal Road
Springfield, VA 22161-2171
(703) 605-6000

Table of Contents

List of Figures

List of Tables

Abstract

The effect of isolated roughness elements on the windward boundary layer of the Shuttle Orbiter has been experimentally examined in the Langley Aerothermodynamic Laboratory in support of an agency-wide effort to prepare the Shuttle Orbiter for return to flight. This experimental effort was initiated to provide a roughness effects database for developing transition criteria to support on-orbit decisions to repair damage to the thermal protection system. Boundary layer transition results were obtained using trips of varying heights and locations along the centerline and attachment lines of 0.0075-scale models. Global heat transfer images using phosphor thermography of the Orbiter windward surface and the corresponding heating distributions were used to infer the state of the boundary layer (laminar, transitional, or turbulent). Test parametrics included angles-of-attack of 30- and 40-deg, side-slip angle of 0-deg, free stream unit Reynolds numbers from $0.02x10^6$ to $7.3x10^6$ per foot, edge-to-wall temperature ratios from 0.4 to 0.8, and normal shock density ratios of approximately 5 (Mach 6 Air and Mach 10 Air Tunnels) and 12 (CF_4 Tunnel). The database contained within this report will be used to formulate protuberance-induced transition correlations using predicted boundary layer edge parameters.

Introduction

In August of 2003, the Columbia Accident Investigation Board (CAIB) released the final report[1] of the investigation into the February 1, 2003 loss of the Space Shuttle *Columbia* and its seven-member crew. The report concluded that:

> *"The physical cause of the loss of Columbia and its crew was a breach in the Thermal Protection System on the leading edge of the left wing, caused by a piece of insulating foam which separated from the left bipod ramp section of the External Tank at 81.7 seconds after launch, and struck the wing in the vicinity of the lower half of Reinforced Carbon-Carbon panel number 8. During reentry this breach in the Thermal Protection System allowed superheated air to penetrate through the leading edge insulation and progressively melt the aluminum structure of the left wing, resulting in a weakening of the structure until increasing aerodynamic forces caused loss of control, failure of the wing, and breakup of the Orbiter."*

From the report came many recommendations, some specifically identified and prefaced as "before return to flight." These return-to-flight (RTF) recommendations were largely related to the physical cause of the accident, such as preventing the loss of foam, and on-orbit inspection and repair of the Thermal Protection System (TPS). For instance, recommendation R6.4-1 was listed for the TPS:

> *"For missions to the International Space Station, develop a practicable capability to inspect and effect emergency repairs to the widest possible range of damage to the Thermal Protection System, including both tile and Reinforced Carbon-Carbon, taking advantage of the additional capabilities available when near to or docked at the International Space Station.*
>
> *For non-Station missions, develop a comprehensive autonomous (independent of Station) inspection and repair capability to cover the widest possible range of damage scenarios.*
>
> *Accomplish an on-orbit Thermal Protection System inspection, using appropriate assets and capabilities, early in all missions.*
>
> *The ultimate objective should be a fully autonomous capability for all missions to address the possibility that an International Space Station mission fails to achieve the correct orbit, fails to dock suc-*

cessfully, or is damaged during or after undocking."

Resolving and implementing these recommendations in a timely manner has facilitated return to flight.

In response to recommendation R6.4-1, strategies for a TPS repair capability have been developed. Figure 1 illustrates the potential steps associated with TPS damage disposition and repair at the time of this publication. For the first reflight missions, an on-orbit inspection, using a newly developed Orbiter Boom Sensor System (OBSS), will be used to characterize any impact damage to the Orbiter TPS prior to entry. Damage to the Reinforced Carbon-Carbon (RCC) will be assessed and repaired if possible. For the Orbiter wing leading edge, the RCC repair project team has selected a plug concept (shown conceptually in Fig. 1). Damage to the ceramic tiles that cover a majority of the windward surface is typically in the form of cavities resulting from debris impacts (from either foam or ice shed from the External Tank). Depending on the size and location of the resulting cavity, the disposition of the damage site will be either "use-as-is" or "repair" (as shown in Fig. 1) using a cure in place ablator (CIPA) using silicone. Of particular concern with ablative materials is the fact that under entry aeroheating environments, the repair material will not be shape stable and the local repair will likely swell and outgas into (and perhaps destabilize) the boundary layer. All three of these repair scenarios, use-as-is (cavity), repair with an ablator (protuberance and/or ablation products), or repair with the plug concept (protuberance), represent significant perturbations to the existing Shuttle outer mold lines (OML).

The present protuberance boundary layer transition tests are part of a series of wind tunnel tests performed[2,3] to characterize the effect of these localized OML changes on the Shuttle windward surface boundary layer. Hypersonic facilities at the NASA Langley Research Center (LaRC) that had a profound impact on the direction and utilization of agency resources[4] in the Columbia Accident Investigation (CAI) were subsequently requested to support RTF based upon prior experience with developing an Orbiter roughness-dominated boundary layer transition database[5,6]. The intent of experimental wind tunnel cavity, protuberance, and ablation investigations are to develop a technical basis to assess tile damage and to determine thresholds for deciding when to repair Shuttle TPS damage, whether a candidate repair material is feasible from a boundary layer transition perspective, and finally how large can a repair site be without adversely affecting the aerothermodynamic performance of the TPS. This report documents five wind tunnel tests conducted in the NASA Langley Aerothermodynamics Laboratory (LAL) to assess the effect of protuberances on the windward surface boundary layer of a 0.0075-scale Shuttle Orbiter. The corresponding analysis and development of the boundary layer transition correlation can be found in Ref. 7. A literature review was performed on the effects of protuberances on boundary layer transition and additional reports not referenced are included at the end of this document.

Nomenclature

h	heat transfer coefficient, $h=q/(H_{aw}-H_w)$, (lbm/ft^2/s)
H	enthalpy (btu/lbm)
k	protuberance height (in.)
L	model reference length (in)
p	pressure (psi)
q	surface heat transfer rate (btu/ft^2/s)
R_n	model reference nose radius (in)
Re	unit Reynolds number (1/ft)
T	temperature (˚R)
U	velocity magnitude (ft/s)
w	protuberance width (in.)
x	axial distance from nose of model (in)
y	spanwise distance from centerline of model (in)
α	angle-of-attack (deg)
γ	ratio of specific heats
ρ	density (slugs/ft^3)

Subscripts

∞	freestream static conditions

aw	adiabatic wall conditions
FR	conditions from Fay-Riddell calculation for a hemisphere
t1	reservoir conditions
t2	stagnation conditions behind a normal shock
w	wall conditions

Experimental Methods

Test Facilities

20-Inch Mach 6 Air Tunnel

The 20-Inch Mach 6 Air Tunnel (Fig. 2) is a blow-down facility in which heated, dried and filtered air is used as the test gas. The tunnel has a two-dimensional, contoured nozzle which opens into a 20.5-in. by 20-in. test section. The tunnel is equipped with a bottom-mounted injection system that can transfer a model from the sheltered model box to the tunnel centerline in less than 0.5 seconds. Run times of up to 15 minutes are possible in this facility, although for the current aeroheating study run times of only a few seconds were required. The nominal reservoir conditions of this facility are stagnation pressures of 30 psi to 500 psi with stagnation temperatures of 760 ˚R to 1000 ˚R, which very nearly produce perfect gas (γ = 1.4) free stream flows with Mach numbers between 5.8 and 6.1 and Reynolds numbers of 0.5×10^6/ft to 7.3×10^6/ft. The nominal flow conditions for this facility are listed in Table 1. A more detailed description of this facility is presented in Ref. 9.

Recent studies[10] have measured quantitative RMS free stream noise levels in the LaRC 20-Inch Mach 6 Air Tunnel obtained with a constant voltage anemometer (CVA) and a hybrid constant current anemometer (CCA). At reservoir conditions of p_{t1} = 130 psi and T_{t1} = 350˚ F, the CCA measurements yielded mass flux and total temperature fluctuations of 0.83% and 0.17%, respectively. The corresponding fluctuations from the CVA measurements were determined to be somewhat lower at 0.74% and 0.12%. In addition, the relative disturbance environment of the 20-Inch Mach 6 Air Tunnel has been deduced[11] via differences in smooth wall transition onset locations measured on a conical model previously tested in the LaRC Mach 6 Nozzle Test Chamber (NTC) Quiet Tunnel.

31-Inch Mach 10 Air Tunnel

The 31-Inch Mach 10 Air Tunnel (Fig. 2) is a blow-down facility in which heated, filtered air is used as the test gas. The tunnel has a square, contoured nozzle which opens into a 31 in. square test section. Models are supported on a hydraulically-operated, sidewall-mounted injection system that can transfer a model from the pneumatically sealed model box to the tunnel centerline in less than 0.6 seconds. Run times of approximately 60 seconds can be achieved, but the current study requires only a few seconds. The nominal reservoir conditions of this facility are stagnation pressures of 350 psi to 1450 psi with stagnation temperatures of 1740 ˚R to 1810 ˚R, which very nearly produce perfect gas (γ = 1.4) free stream flows with a Mach number of approximately 10 and Reynolds numbers of 0.2×10^6/ft to 2.2×10^6/ft. The nominal flow conditions for this facility can be seen in Table 2. A more detailed description of this test facility is presented in Ref. 9.

20-Inch CF_4 Tunnel

The 20-Inch CF_4 Tunnel (Fig. 2) is a blow-down facility in which heated, filtered CF_4 is used as the test gas. The flow is expanded through a contoured, axisymmetric nozzle having a throat diameter of 0.446 in. and an exit diameter of 20 in., providing Mach 6 flow at the exit, which, due to the use of the heavy gas (γ = 1.2), simulates Mach 15-25 flow over the models. The flow exhausts from the nozzle into an open-jet test section. Models are supported at the nozzle exit by a hydraulically-driven injection/support mechanism that can transfer the model to the tunnel centerline in about 0.5 seconds. Nominal run times are on the order of 10 seconds, but run times for the current study were only a few seconds. The low enthalpy (as opposed to impulse-type) CF_4 tunnel avoids complex chemistry typically associated with high enthalpy facilities by the use of a heavier than air test gas with a low ratio of specific heats and a correspondingly high normal shock density ratio characteristic of hypervelocity flight. In conjunction with the Mach 6 Air Tunnel, this tunnel provides the capability to test at the same free-stream Mach

and Reynolds numbers, but at two values of density ratio (approximately 5 in air and 12 in CF_4). This density ratio of 12 for CF_4 is relatively close to the values of 15-18 encountered near peak heating during entry of the Orbiter. The nominal reservoir conditions of this facility are stagnation pressures of 100 psi to 2000 psi with stagnation temperatures of 1100 ˚R to 1480 ˚R, which produce Reynolds numbers of $0.05x10^6$/ft to $0.75x10^6$/ft. The nominal flow conditions for this facility can be seen in Table 3. A more detailed description of this facility is presented in Ref. 9.

Phosphor Thermography Technique

Global surface heating distributions were calculated using the digital optical measurement method of two-color, relative-intensity, phosphor thermography[12-15]. Ceramic wind tunnel models are coated with a phosphor compound that fluoresces in two separate regions (green and red) of the visible light spectrum. During a wind tunnel run, the phosphor-coated model is illuminated by ultraviolet (UV) light sources, and the resulting fluorescent intensity of the model is recorded and digitized through a color CCD (charge coupled device) camera (Fig. 3). The fluorescent intensity is dependent on both the intensity of the incident UV light and the local model surface temperature. The UV intensity dependence is removed by taking the ratio of the green to red intensity images, from which surface temperature distributions can be determined through prior calibrations. Images are acquired before the wind tunnel run and after injection of the model to the tunnel centerline during a run. Global heat transfer distributions are then computed from these temperature data using one-dimensional, constant heat-transfer coefficient conduction theory[15].

The global phosphor thermography technique is now the standard method for aeroheating studies in the LAL. The global data obtained using this method can be used to identify the surface heating effects of complex three-dimensional flow phenomena such as transition fronts, vortex structures, and shock interactions which are difficult to examine using conventional discrete-sensor methods such as thin-film resistance gages or coaxial surface thermocouples.

Test Model Description

In order to manufacture ceramic test models, wax molds of metal, aerodynamic models were made, and then a patented[16] silica ceramic slip casting technique was used to form ceramic shells of the models. The shells were then back-filled with a hydraulically setting magnesia ceramic for strength and support. Finally, the models were coated with a mixture of phosphors suspended in a silica-based colloidal binder. The phosphor coatings typically do not require refurbishment between runs in the wind tunnel and have been measured to be approximately 0.001-in. thick. Global surface roughness measurements associated with a phosphor coated model were obtained with a non-intrusive laser-based system. Nominal surface roughness was determined to be approximately 400 micro-inches. For a detailed description of the fabrication process used for this test series and surface integrity measurements, see Ref. 8. The cast ceramic aeroheating models (the large set of models constructed for both the present protuberance study as well as the cavity testing is shown in Fig. 4) were 9.6-inch long (from nose to body-flap hinge), 0.0075-scale representations of the Space Shuttle Orbiter.

Small, ink-based identification marks were placed on all models (as shown in Fig. 5) to aid in data reduction, model orientation, and protuberance placement. These marks, referred to as fiducial marks, do not influence the flow over the model surface. The fiducial marks can be seen in run images as small discolorations. The locations of these marks can be seen in Fig. 6 and are listed in Table 4. Fiducial marks were placed along the model centerline (CL) and the attachment lines (port and starboard) based on viscous CFD solutions for 40-deg angle-of-attack (40-VIS), inviscid solutions for 40-deg angle-of-attack (40-INV), and inviscid solutions for 30-deg angle-of-attack (30-INV). The attachment lines, as seen in Fig. 6, generally ran from the model stagnation point to the wing crank (port and starboard) and then along the wing leading edge, and were dependent on angle-of-attack. The proximity to the wing leading edge allows the protuberance database to envelope the widest possible range on the Orbiter windward surface. As shown in Fig. 6 and listed in Table 4, the

trip stations along the centerline and attachment lines were spaced every x/L = 0.10. The locations of the attachment lines were then verified by a separate oil-flow surface visualization study (see Ref. 8 for a complete discussion). A laser alignment system was then used to properly align the model in the tunnel (an example is shown in Fig. 7).

The roughness elements as fabricated, simulate a raised TPS tile, as discussed in Refs. 5 and 6. The trips used for the present study, as discussed in detail in Ref. 8, were cut from various thicknesses of high-temperature polymer tapes and the roughness heights (k) available were 0.0035, 0.0045, 0.0065, and 0.0115-in. Roughness elements fabricated from the tape were easily applied to the trip locations and removed without adversely affecting the phosphor coating.

Data Reduction

One-dimensional, semi-infinite solid heat conduction theory[15] was used to compute surface heating distributions from the global surface temperature data acquired through the technique of two-color, relative-intensity, phosphor thermography. A constant heat-transfer coefficient is assumed in this theory, and empirical corrections[15] are made to account for changes in model substrate thermal properties with temperature. Phosphor images were acquired shortly after injection of the model to the tunnel centerline, which requires less than one second.

Data were extracted in the IHEAT[15] software package axially along the centerline and longitudinally at an axial location of x/L = 0.85. Results are presented herein in terms of a non-dimensional heat transfer coefficient ratio, h/h_{FR}, where h_{FR} is the theoretical stagnation point heating computed with the Fay-Riddell[17] method for a 0.09 in. radius sphere (the nose radius of the test models) for a wall temperature of 540 ˚R.

Error Analysis

The estimated experimental uncertainty of the thermographic phosphor system is a function of fluorescent intensity, which is dependent on model surface temperature. For higher surface temperatures (greater than 720˚R), such as those on most of the windward surface, the uncertainty[15] is approximately ±8% to ±10%, while for lower temperatures (less than 585 ˚R), the uncertainty is approximately ±15% to ±20%. Additional measurement uncertainty can be introduced due to internal, three-dimensional heat conduction in high-gradient regions such as the leading edge of the Shuttle Orbiter. This uncertainty is estimated to vary from less than ±5% at the lowest test Reynolds number to greater than ±10% at the highest Reynolds numbers.

Uncertainties can be introduced when extracting line cut data from an image due to perspective distortion of the image, lack of pixel resolution in high-gradient regions, and lack of precision in locating fiducial marks. These errors are estimated to be less than ±5% on relatively flat surfaces and up to ±10% on highly curved surfaces.

A square root of the sum-of-the-squares estimate for the total uncertainty based on the above factors gives a worst-case experimental uncertainty range of ±13% on flat areas of the windward surface to ±25% on areas such as the leeward surface (not shown in this study) at high Reynolds numbers. In addition to the sources of experimental uncertainty listed above, additional uncertainty may also be introduced model surface irregularities or variations in roughness element dimensions. The onset of transition can be influenced by the distributed roughness of the model surface and phosphor coating, which tends to degrade slightly over the length of a test due to handling of the model and pitting of the surface from particle impacts. Some variation in the roughness of the phosphor coating from model to model may also be expected. Because this uncertainty increases over time and varies from model to model, no fixed value for the uncertainty is assigned. Instead, if anomalous results are noted when viewing trends in the heating data, such as in the Reynolds number effects, the model and trip condition should be closely examined for signs of irregularities. Anomalies can be easily observed in the centerline results due to any flow asymmetries, but may be harder to identify along the attachment line as the flow is already locally asymmetric. For this reason, identical trips were placed on the corresponding

port and starboard attachment lines to help identify anomalous results.

Test Matrix and Tunnel Conditions

The data were collected on the Space Shuttle Orbiter models at angles-of-attack of 30-deg and 40-deg and free stream Reynolds numbers between 0.02×10^6 and 7.3×10^6 per foot. The run matrices for five different entries into the LAL facilities are listed in chronological order in Tables 5-9. Table 5 shows the chronological run matrix for Test 6883 in the 20-Inch Mach 6 Air Tunnel. This was an early study to compare the use of the viscous and inviscid attachment lines. Test 6886 in the 20-Inch Mach 6 Air Tunnel (run matrix presented in Table 6) was the primary Mach 6 entry. Test 6892 in the 20-Inch Mach 6 Air Tunnel (run matrix presented in Table 7) was the final Mach 6 entry to capture or correct any missing or anomalous results identified during analysis. Test 390 in the 31-Inch Mach 10 Air Tunnel (run matrix presented in Table 8) was the primary Mach 10 entry. Test 162 in the 20-Inch CF_4 Tunnel (run matrix presented in Table 9) was the primary entry into the CF_4 Tunnel.

For each run, test section flow conditions were computed using the GASPROPS[18] code with the measured reservoir stagnation pressures and temperatures and pitot pressure calibrations of the facility as inputs.

For some of the runs, an attachment line location of 40-INV+ is listed in the corresponding table. This means that the protuberance was placed half-way between the 40-VIS and 40-INV attachment line fiducial marks.

Experimental Results

Surface Heating Data

Global surface heating data are organized and presented in three appendices according to facility. Run images and plots are organized in each Appendix such that in each figure, the effect of varying Reynolds number may be seen for a specific model, angle-of-attack, and protuberance combination. Wherever applicable, the plot associated with a series of images is included immediately after the figure which contains the images. Under each global phosphor thermography image, the Reynolds number displayed is the average of all of the runs with the same pressure/temperature combination. The Reynolds number displayed in the corresponding plot is the actual Reynolds number achieved for the specific run. These two Reynolds numbers may not be exactly the same, but should be close (see Tables 1-2 for average tunnel conditions and associated uncertainties). During a run, the surface temperature of the model may exceed the calibrated range of the phosphor thermography technique. If this occurs, the heat transfer run image will show an “off-scale” condition as a purple region.

In general, the Appendices are organized first by angle-of-attack, then by protuberance location, then by protuberance height, then by model. When viewing the images, note that fiducial marks which were placed on the model surface (Fig. 6 and also included with each case in the appendices) are visible in the heat transfer images, and protuberances are located only where indicated on the image included with the figure. These fiducial marks do not cause the flow to transition or affect it in any way.

Although the primary intent of the present experimental program was to provide discrete protuberance data on the Orbiter windward surface, a few runs were obtained without trips to provide baseline results. Comparison of the baseline results from the various models tested can provide an indication of the background effect of the distributed roughness of the phosphor coating. For instance, the baseline results for α = 40-deg in the 20-Inch Mach 6 Air Tunnel (compare Figs. A.22 through A.30) provide a qualitative assessment of the scatter associated with “natural” transition onset (as influenced by the surface distributed roughness). Models P2 and P3 provided relatively consistent transition onset results (as indicated by the centerline plots; transition onset was at about $x/L = 0.70$) at $Re_\infty = 4.1 \times 10^6$/ft, while model P5 remained laminar along the entire windward centerline for this same Reynolds number. For this test series, the phosphor coating roughness levels have not been systematically measured for each model, but

instead representative models have been examined and the results are detailed in Ref. 8.

Discrete roughness transition effects were obtained in all three LAL facilities based on the existing Reynolds number capability of the tunnel and the range of trip heights available. Procedurally, trips were systematically placed first at the aft stations on the model, a Reynolds number sweep was then performed until the flow was fully turbulent behind the trip, before either changing to a taller trip or moving forward on the model. The 40-deg data were considered a higher priority, due to the fact that the Orbiter stays mostly near 40-deg above Mach 10, and thus were obtained first. As stated earlier, trips of consistent heights were placed on the port and starboard attachment lines, which were typically consistent with the centerline height, to be a final verification of results. If asymmetric results were observed, care was taken to check the status and veracity of the model surface and trips. Occasionally a trip corner was observed to be sticking up off the surface, which was then replaced and the run repeated. A total of 8 models were used over these five test entries and each one was typically replaced when the phosphor coating in and around the vicinity of the fiducial marks were adversely affected by the repeated application/removal of the trips.

As mentioned previously, trips of consistent height were typically placed at the same trip station on both the port and starboard attachment lines, as well as the centerline. One notable exception occurred towards the end of the test series in the CF_4 Tunnel, where a 0.0115-in. trip was placed on centerline at an $x/L = 0.5$ and 0.0065-in. trips were placed on the port and starboard attachment lines at $x/L = 0.66$ (on the wing leading edge) for $\alpha = 30$-deg (noted in Table 9 by listing the attachment line location with a station identification; also see Fig. C.7). This one exception to the testing procedure was allowed on the last day of testing to fill in holes in the centerline and attachment line databases.

The protuberance trip data provided in the following appendices represent only the “best” set of experimental results. Anomalous results were occasionally observed during the many test entries and when these discrepancies could be traced back to a known or observable root cause, these results were filtered out. One example, as mentioned earlier, was asymmetric transition patterns that resulted from trips that, for one reason or another, had inadequate adhesion to the model surface and pulled up during the run. When the trip corners were observed with a magnifying glass to be sticking up after a run, these trips were replaced an the run repeated. These anomalous results are not included in the data set presented herein. Therefore, the presented repeat results can be used to indicate the remaining experimental uncertainty associated with the accuracy of either the location and/or thickness of the trips as applied to the model surface. For instance, repeat trips results are provided in Figures A.7 through A.12. and indicate roughly a 40% increase in the transition onset Reynolds number on centerline from model PB to P5. These results were obtained on two separate entries into the 20-Inch Mach 6 Air Tunnel and represent the “worst-case” repeatability observed. Typically, the tripping results were very repeatable.

General trends observed from the images and line cuts, within the limitations of the current database, are:

1) as the Mach number increased, the trip height required to effect boundary layer transition also increased;

2) for any given trip cast that generated a noticeable wake disturbance, small increases in Reynolds number would typically dramatically increase the trip effectiveness;

3) for any given trip height and location, an increase in the model angle-of-attack would increase the trip effectiveness; and

4) for a consistent trip height and model station, the comparative effectiveness between the centerline and attachment line locations were relatively similar when on the forward half of the model. When on the aft portion of the model (the attachment line near the wing leading edge), the centerline location

required taller trip heights than the attachment line for similar effectiveness.

Summary and Conclusions

A discrete roughness transition database on the windward boundary layer of an 0.0075-scale Shuttle Orbiter model has been obtained from the hypersonic facilities of the Langley Aerothermodynamic Laboratory. This work was in support of an agency-wide effort to return the Orbiter program back to flight status. The database contained herein will be used to investigate methodologies for predicting boundary layer transition in flight, which ultimately would allow for timely disposition of surface damage and/or repair of the Orbiter TPS prior to entry.

Acknowledgements

The authors would like to acknowledge the contributions of the following individuals to this research: Harry Stotler, Grace Gleason, Roland Hatten, and Teck-Seng Kwa for operation of the 20-Inch Mach 6 Air Tunnel and data acquisition support; Melanie Lawhorne, Christal Kellam, and Glenn Bittner for operation of the 20-Inch CF_4 Tunnel and data acquisition support; Johnny Ellis Rhonda Mills, Henry Fitzgerald, and Kevin Hollingsworth for operation of the 31-Inch Mach 10 Air Tunnel and data acquisition support; Mike Powers and Mark Griffith for fabrication of the ceramic test models; and Ed Covington and Pete Veneris for model fidelity measurements and fiducial mark placement.

References

1. http://www.caib.us/news/report/default.html

2. Liechty, D. S., Horvath, T. J., and Berry, S. A., "Shuttle Return To Flight Experimental Results: Cavity Effects on Boundary Layer Transition," NASA TM 2006-214305

3. Merski, N. R., "A Preliminary Investigation of the Effect of Mass Addition on Boundary Layer Transition for Shuttle Return To Flight," OEAN-0305-010, 2005.

4. Horvath, T. J., "Experimental Aerothermodynamics In Support of the Columbia Accident Investigation," AIAA Paper 2004-1387, January 2004.

5. Berry, S. A. and Hamilton, H. H. II, "Discrete Roughness Effects on Shuttle Orbiter at Mach 6," AIAA Paper 2002-2744, June 2002.

6. Berry, S. A., Bouslog, S. A., Brauckmann, G. J. and Caram, J. M., "Shuttle Orbiter Experimental Boundary-Layer Transition Results with Isolated Roughness," *Journal of Spacecraft and Rockets*, Vol. 35, No. 3, pp 241-248, May-June 1998.

7. Berry, S. A., "Orbiter Protuberance Boundary Layer Transition Analysis and Results," OEAN-0305-007, 2005.

8. Buck, G. M., "Fabrication of 0.0075-Scale Orbiter Phosphor Thermography Test Models for Shuttle RTF Aeroheating Studies," NASA TM 2006-214303, 2006.

9. Micol, J.R., "Hypersonic Aerodynamic/Aerothermodynamic Testing Capabilities at Langley Research Center: Aerothermodynamic Facilities Complex," AIAA Paper 95-2107, June 1995.

10. Chokani, N., Shipluk, A. N., Sidorenko, A. A., and McGinley, C. B., "Comparison Between a Hybrid Constant-Current Anemometer and Constant-Voltage Anemometer in Hypersonic Flow," AIAA Paper 2004-2248, June 2004.

11. Horvath, T. J., Berry, S. A., Hollis, B. R., Chang, C. and Singer, B. A., "Boundary Layer Transition On Slender Cones in Conventional and Low Disturbance Mach 6 Wind Tunnels," AIAA Paper 2002-2743, June 2002.

12. Buck, G.M., "Automated Thermal Mapping Techniques Using Chromatic Image Analysis," NASA TM 101554, April 1989.

13. Buck, G.M., "Surface Temperature/Heat Transfer Measurement Using a Quantitative Phosphor Thermography System," AIAA Paper 91-0064, January 1991.

14. Merski, N.R., "A Relative-Intensity, Two-Color Phosphor Thermography System," NASA TM 104123, September 1991.

15. Merski, N.R., "An Improved Two-Color Relative-Intensity Phosphor Thermography Method For Hypersonic Wind Tunnel Aeroheating Measurements," NASA CDTP-1017, February 2001.

16. Buck, G.M., and Vasques, P., “An Investment Ceramic Slip-Casting Technique for Net-Form, Precision, Detailed Casting of Ceramic Models,” U.S. Patent 5,266,252, November 1993.

17. Fay, J.A., and Riddell, F.R., “Theory of Stagnation Point Heat Transfer in Dissociated Air,” *Journal of Aeronautical Sciences*, Vol. 25, No. 2, 1958, pp. 73-85.

18. Hollis, B.R., “Real-Gas Flow Properties for NASA Langley Research Center Aerothermodynamic Facilities Complex Wind Tunnels,” NASA CR 4755, September 1996.

Literature Search

Carver, D. B., “Heat-Transfer Tests on the Rockwell International Space Shuttle Orbiter with Boundary-Layer Trips,” AEDC-TR-76-28, May 1976.

Crosby, W. A., Carver, D. B. and Nutt, K. W., “Boundary-Layer Trip Investigations on a 5.5-Degree Blunt Cone at Mach Number 10,” AEDC-TSR-83-V31, September 1983.Luther, M., “Fixing Boundary-Layer Transition on Supersonic Wind-Tunnel Models,” *Journal of the Aeronautical Sciences*, August 1957.

Martellucci, A., Maguire, B. L. and Neff, R. S., “Analysis of Flight Test Transition and Turbulent Heating Data: Part I - Boundary Layer Transition Results,” NASA CR 129045, November 1972.

Nestler, D. E., “An Experimental Study of the Performance of Two-Dimensional Boundary Layer Trips for Decoys: Part I: Wind Tunnel Tests,” BMO TR-83-37, October 1983.

Noble, J. A., “Wind Tunnel Tests of the Performance Technology Program, Phase II, GE Vehicle at Mach 8 (Phase 3, Heat Transfer Tests)”, AEDC-TSR-79-V57, October 1979.

Stetson, K. F., “Hypersonic Laminar Boundary Layer Transition,” AFWAL-TR-86-3089, December 1986.

Tevertin, N., “An Emperical Equation for Prediction of Transition Location on Cones in Super- or Hypersonic Flight,” NOLTR 73-127, June 1973.

Tables

Table 1: 20-Inch Mach 6 Air Tunnel Average Flow Conditions.

Re_∞ (1/ft.)	M_∞	p_{t1} (psi)	T_{t1} ($^\circ$R)
0.56x10^6	5.93	30.63	856.33
0.84x10^6	5.91	46.20	863.70
1.07x10^6	5.93	61.02	875.05
1.39x10^6	5.95	81.19	887.51
1.71x10^6	5.96	101.52	896.23
2.08x10^6	5.97	126.25	904.11
2.48x10^6	5.98	151.16	905.37
2.97x10^6	5.99	181.86	905.38
3.46x10^6	6.00	212.52	906.28
4.12x10^6	6.00	252.54	906.36
4.65x10^6	6.01	292.75	920.01
5.41x10^6	6.02	343.57	924.47
6.13x10^6	6.02	393.28	929.03
6.98x10^6	6.03	450.89	933.62
7.38x10^6	6.03	476.62	933.80

Table 2: 31-Inch Mach 10 Air Tunnel Average Flow Conditions.

Re_∞ (1/ft.)	M_∞	p_{t1} (psi)	T_{t1} ($^\circ$R)
0.57x10^6	9.33	351.86	1792.29
0.83x10^6	9.52	539.82	1804.22
1.08x10^6	9.63	722.73	1803.13
1.16x10^6	9.66	783.66	1800.33
1.26x10^6	9.69	855.92	1797.45
1.31x10^6	9.70	894.09	1801.57
1.45x10^6	9.74	1004.46	1808.34
1.55x10^6	9.76	1076.36	1803.24
1.62x10^6	9.78	1125.83	1799.00
1.81x10^6	9.81	1253.88	1792.10
2.07x10^6	9.86	1453.24	1792.49

Table 3: 20-Inch Mach 6 CF_4 Tunnel Average Flow Conditions.

Re_∞ (1/ft.)	M_∞	p_{t1} (psi)	T_{t1} ($^\circ$R)
0.02x10^6	5.86	63.02	1254.10
0.05x10^6	5.82	165.81	1256.95
0.09x10^6	5.89	255.12	1181.28
0.17x10^6	5.85	507.55	1225.04
0.25x10^6	5.85	766.93	1237.49
0.32x10^6	5.93	863.55	1180.20
0.35x10^6	5.86	1050.07	1230.49
0.46x10^6	5.92	1270.56	1191.76
0.50x10^6	5.87	1510.81	1236.31
0.60x10^6	5.82	2066.55	1293.28

Table 4: Shuttle Orbiter Model Fiducial Mark Locations.

x/L	y/L		
	30-deg. INV	40-deg. INV	40-deg. VIS
0.10	0.2020	0.0134	0.0017
0.20	0.0370	0.0269	0.0084
0.30	0.0571	0.0454	0.0236
0.40	0.0824	0.0706	0.0504
0.50	0.1092	0.1008	0.0874
0.60	0.1462	0.1429	0.1311
0.62		0.1590	0.1489
0.64		0.1754	0.1701
0.66		0.1937	0.1908
0.68		0.2130	0.2111
0.70		0.2320	0.2298
0.80		0.3070	0.2937
1.00			

Table 5: Chronological Run Matrix for Test 6883 in the 20-Inch Mach 6 Air Tunnel.

Model ID	Run	α	Mach	Re_∞/ft.	p_{t1}	T_{t1}	Trip Setup			
			No.	x 10^6	psi	$^\circ$R	x/L	AL	k_{CL}	k_{AL}
RTF-BLT-P2	10	40	5.98	2.08	126.3	903.2				
RTF-BLT-P2	17	40	5.98	3.00	181.8	902.8				
RTF-BLT-P2	18	40	5.99	4.13	251.4	903.3				
RTF-BLT-P2	19	40	6.01	5.37	343.1	927.9				
RTF-BLT-P2	20	40	5.95	1.07	61.3	874.7				
RTF-BLT-P3	28	40	6.00	2.07	126.1	901.9				
RTF-BLT-P3	29	40	6.01	2.97	182.3	903.8				
RTF-BLT-P3	30	40	6.01	4.14	253.2	902.8				
RTF-BLT-P3	31	40	5.95	1.07	61.0	872.3				
RTF-BLT-P3	32	40	6.00	4.13	252.7	904.3				
RTF-BLT-P3	33	40	6.01	4.12	252.7	904.5	0.7	40-INV	0.0045	0.0045
RTF-BLT-P3	34	40	6.00	2.96	181.3	904.7	0.7	40-INV	0.0045	0.0045
RTF-BLT-P3	35	40	5.98	2.11	128.2	903.2	0.7	40-INV	0.0045	0.0045
RTF-BLT-P3	36	40	5.94	1.07	60.7	874.3	0.7	40-INV	0.0045	0.0045
RTF-BLT-P3	37	40	5.93	0.54	29.5	855.0	0.7	40-INV	0.0045	0.0045
RTF-BLT-P3	38	40	6.00	4.17	253.6	902.3	0.6	40-VIS	0.0045	0.0045
RTF-BLT-P3	39	40	6.00	3.45	212.8	910.4	0.6	40-VIS	0.0045	0.0045
RTF-BLT-P3	40	40	6.00	2.98	182.4	904.2	0.6	40-VIS	0.0045	0.0045
RTF-BLT-P3	41	40	5.99	2.48	150.9	903.0	0.6	40-VIS	0.0045	0.0045
RTF-BLT-P3	42	40	5.97	2.10	127.4	904.6	0.6	40-VIS	0.0045	0.0045
RTF-BLT-P3	44	40	5.93	0.56	30.7	855.3	0.6	40-VIS	0.0045	0.0045
RTF-BLT-P3	45	40	5.93	1.09	61.3	871.7	0.6	40-VIS	0.0045	0.0045
RTF-BLT-P3	46	40	5.94	1.40	81.2	883.3	0.6	40-VIS	0.0045	0.0045
RTF-BLT-P3	47	40	5.93	1.12	63.5	872.8	0.5	40-VIS	0.0045	0.0045
RTF-BLT-P3	49	40	5.97	2.12	127.8	900.2	0.5	40-VIS	0.0045	0.0045
RTF-BLT-P3	50	40	5.94	1.38	80.5	886.2	0.5	40-VIS	0.0045	0.0045
RTF-BLT-P3	51	40	5.98	2.49	150.6	900.1	0.5	40-VIS	0.0045	0.0045

Table 5: (Continued)Chronological Run Matrix for Test 6883 in the 20-Inch Mach 6 Air Tunnel.

Model ID	Run	α	Mach	Re_∞/ft.	p_{t1}	T_{t1}	Trip Setup			
			No.	x 10^6	psi	˚R	x/L	AL	k_{CL}	k_{AL}
RTF-BLT-P3	52	40	5.99	2.99	181.7	900.8	0.5	40-VIS	0.0045	0.0045
RTF-BLT-P3	53	40	6.00	3.50	213.0	904.4	0.5	40-VIS	0.0045	0.0045
RTF-BLT-P3	55	40	6.01	4.12	253.0	905.6	0.5	40-VIS	0.0045	0.0045
RTF-BLT-P3	58	40	6.00	4.14	252.5	902.4	0.4	40-VIS	0.0045	0.0045
RTF-BLT-P3	60	40	5.99	2.96	180.8	905.2	0.4	40-VIS	0.0045	0.0045
RTF-BLT-P3	61	40	5.99	2.96	180.8	905.2	0.4	40-VIS	0.0045	0.0045
RTF-BLT-P3	62	40	5.97	2.10	126.4	901.3	0.4	40-VIS	0.0045	0.0045
RTF-BLT-P3	63	40	5.99	3.00	182.1	901.6	0.4	40-VIS	0.0045	0.0045
RTF-BLT-P3	64	40	5.93	1.08	61.2	872.8	0.4	40-VIS	0.0045	0.0045
RTF-BLT-P3	65	40	5.95	1.40	81.3	885.2	0.4	40-VIS	0.0045	0.0045
RTF-BLT-P3	66	40	6.00	4.15	253.7	904.2	0.4	40-VIS	0.0045	0.0045
RTF-BLT-P3	67	40	5.94	1.06	60.1	874.5	0.3	40-VIS	0.0045	0.0045
RTF-BLT-P3	70	40	5.98	2.51	151.8	902.5	0.3	40-VIS	0.0045	0.0045
RTF-BLT-P3	71	40	5.94	1.39	80.8	885.7	0.3	40-VIS	0.0045	0.0045
RTF-BLT-P3	72	40	5.97	2.10	126.8	903.0	0.3	40-VIS	0.0045	0.0045
RTF-BLT-P3	73	40	5.99	2.98	182.4	906.8	0.3	40-VIS	0.0045	0.0045
RTF-BLT-P3	74	40	6.00	3.43	210.9	906.4	0.3	40-VIS	0.0045	0.0045
RTF-BLT-P3	75	40	5.95	1.71	101.6	895.1	0.3	40-VIS	0.0045	0.0045
RTF-BLT-P3	76	40	5.96	1.72	101.2	890.0	0.3	40-VIS	0.0045	0.0045
RTF-BLT-P3	77	40	5.95	1.72	101.3	890.3	0.3	40-VIS	0.0045	0.0045
RTF-BLT-P3	78	40	5.96	1.73	101.5	890.2	0.3	40-VIS	0.0045	0.0045
RTF-BLT-P3	79	40	5.96	1.72	101.3	891.6	0.3	40-VIS	0.0045	0.0045
RTF-BLT-P3	80	40	5.95	1.74	102.1	890.1	0.3	40-VIS	0.0045	0.0045

Table 6: Chronological Run Matrix for Test 6886 in the 20-Inch Mach 6 Air Tunnel.

Model ID	Run	α	Mach	Re_∞/ft.	p_{t1}	T_{t1}	Trip Setup			
			No.	x 10^6	psi	˚R	x/L	AL	k_{CL}	k_{AL}
RTF-BLT-P5	10	40	5.94	1.08	61.2	872.4				
RTF-BLT-P5	11	40	5.98	2.10	127.7	902.5				
RTF-BLT-P5	12	40	6.00	2.97	181.0	901.7				
RTF-BLT-P5	13	40	6.00	4.14	253.6	905.4				
RTF-BLT-P5	14	40	5.91	0.86	47.3	861.8	0.68	40-INV	0.0045	0.0045
RTF-BLT-P5	15	40	5.93	1.06	60.1	872.8	0.68	40-INV	0.0045	0.0045
RTF-BLT-P5	16	40	5.97	2.13	128.6	901.4	0.68	40-INV	0.0045	0.0045
RTF-BLT-P5	17	40	5.97	2.09	125.6	899.4	0.68	40-INV	0.0045	0.0045
RTF-BLT-P5	18	40	6.00	3.01	183.8	901.5	0.68	40-INV	0.0045	0.0045
RTF-BLT-P5	19	40	6.01	3.45	212.2	903.8	0.68	40-INV	0.0045	0.0045
RTF-BLT-P5	20	40	5.92	0.83	46.1	863.8	0.64	40-INV	0.0065	0.0045
RTF-BLT-P5	21	40	5.94	1.11	63.1	875.3	0.64	40-INV	0.0065	0.0045
RTF-BLT-P5	22	40	5.97	2.11	127.6	902.7	0.64	40-INV	0.0065	0.0045
RTF-BLT-P5	23	40	5.99	2.97	182.0	907.4	0.64	40-INV	0.0065	0.0045
RTF-BLT-P5	24	40	5.98	2.49	151.3	903.5	0.64	40-INV	0.0065	0.0045
RTF-BLT-P5	25	40	5.97	1.77	104.7	889.5	0.64	40-INV	0.0065	0.0045
RTF-BLT-P5	26	40	5.99	2.07	127.0	905.5	0.60	40-INV	0.0045	0.0045
RTF-BLT-P5	27	40	5.98	1.69	101.5	895.9	0.60	40-INV	0.0045	0.0045
RTF-BLT-P5	28	40	5.95	1.05	60.4	880.2	0.60	40-INV	0.0045	0.0045

Table 6: (Continued)Chronological Run Matrix for Test 6886 in the 20-Inch Mach 6 Air Tunnel.

Model ID	Run	α	Mach	Re_∞/ft.	p_{t1}	T_{t1}	Trip Setup			
			No.	x 10^6	psi	°R	*x/L*	AL	k_{CL}	k_{AL}
RTF-BLT-P5	29	40	5.97	1.38	81.6	891.3	0.60	40-INV	0.0045	0.0045
RTF-BLT-P5	30	40	6.01	2.93	181.0	906.9	0.60	40-INV	0.0045	0.0045
RTF-BLT-P5	31	40	5.99	2.46	151.5	909.2	0.60	40-INV	0.0045	0.0045
RTF-BLT-P5	32	40	6.01	3.43	212.3	909.0	0.60	40-INV	0.0045	0.0045
RTF-BLT-P5	43	40	6.00	2.97	182.2	905.8	0.50	40-INV	0.0045	0.0045
RTF-BLT-P5	44	40	5.99	2.48	151.8	906.8	0.50	40-INV	0.0045	0.0045
RTF-BLT-P5	45	40	5.97	2.08	126.4	906.4	0.50	40-INV	0.0045	0.0045
RTF-BLT-P5	46	40	5.93	1.05	59.8	878.4	0.50	40-INV	0.0045	0.0045
RTF-BLT-P5	47	40	5.95	1.39	81.3	890.0	0.50	40-INV	0.0045	0.0045
RTF-BLT-P5	48	40	5.97	1.71	102.1	895.9	0.50	40-INV	0.0045	0.0045
RTF-BLT-P5	49	40	6.01	4.16	256.1	907.4	0.50	40-INV	0.0045	0.0045
RTF-BLT-P5	78	40	5.97	2.05	125.2	907.5	0.40	40-INV	0.0065	0.0065
RTF-BLT-P5	79	40	5.96	1.70	101.3	894.7	0.40	40-INV	0.0065	0.0065
RTF-BLT-P5	80	40	5.95	1.40	82.2	888.3	0.40	40-INV	0.0065	0.0065
RTF-BLT-P5	81	40	5.93	1.09	61.6	875.3	0.40	40-INV	0.0065	0.0065
RTF-BLT-P5	82	40	5.97	2.49	151.8	907.3	0.40	40-INV	0.0065	0.0065
RTF-BLT-P5	83	40	5.98	2.97	182.5	911.6	0.40	40-INV	0.0065	0.0065
RTF-BLT-P5	86	40	6.00	2.47	152.0	905.9	0.30	40-INV	0.0065	0.0065
RTF-BLT-P5	87	40	5.97	1.37	81.6	892.0	0.30	40-INV	0.0065	0.0065
RTF-BLT-P5	88	40	5.95	1.08	61.3	874.2	0.30	40-INV	0.0065	0.0065
RTF-BLT-P5	89	40	5.97	1.71	102.4	895.5	0.30	40-INV	0.0065	0.0065
RTF-BLT-P5	90	40	5.99	2.06	126.4	906.4	0.30	40-INV	0.0065	0.0065
RTF-BLT-P5	91	40	6.00	2.95	183.1	911.6	0.30	40-INV	0.0065	0.0065
RTF-BLT-P5	92	40	5.98	2.08	127.0	906.4	0.20	40-INV	0.0115	0.0115
RTF-BLT-P5	93	40	5.94	1.09	62.3	875.3	0.20	40-INV	0.0115	0.0115
RTF-BLT-P5	94	40	5.92	0.83	45.7	863.9	0.20	40-INV	0.0115	0.0115
RTF-BLT-P5	98	40	5.99	2.48	152.0	906.7	0.50	40-INV	0.0065	0.0065
RTF-BLT-P5	99	40	6.00	2.96	182.1	906.4	0.50	40-INV	0.0065	0.0065
RTF-BLT-P5	100	40	5.98	2.09	127.7	906.6	0.50	40-INV	0.0065	0.0065
RTF-BLT-P5	101	40	5.94	1.10	62.4	875.4	0.50	40-INV	0.0065	0.0065
RTF-BLT-P5	102	40	5.96	1.73	102.9	895.5	0.50	40-INV	0.0065	0.0065
RTF-BLT-P5	103	40	5.97	2.08	126.4	905.7	0.60	40-INV	0.0115	0.0065
RTF-BLT-P5	104	40	5.94	1.07	60.9	874.6	0.60	40-INV	0.0115	0.0065
RTF-BLT-P5	105	40	5.92	0.83	46.0	864.7	0.60	40-INV	0.0115	0.0065
RTF-BLT-P5	106	40	5.95	1.41	82.0	886.2	0.60	40-INV	0.0115	0.0065
RTF-BLT-P5	107	40	5.93	0.57	31.4	858.3	0.64	40-INV	0.0115	0.0115
RTF-BLT-P5	108	40	5.91	0.84	46.3	864.4	0.64	40-INV	0.0115	0.0115
RTF-BLT-P5	109	40	5.93	1.09	61.9	874.6	0.64	40-INV	0.0115	0.0115
RTF-BLT-P5	110	40	5.95	1.39	80.7	885.7	0.64	40-INV	0.0115	0.0115
RTF-BLT-P5	111	40	5.96	1.72	102.1	895.2	0.64	40-INV	0.0115	0.0115
RTF-BLT-P5	119	30	5.99	3.47	214.3	910.2	0.40	30-INV	0.0065	0.0065
RTF-BLT-P5	120	30	6.00	4.13	253.7	907.4	0.40	30-INV	0.0065	0.0065
RTF-BLT-P5	121	30	6.02	4.53	294.1	935.8	0.40	30-INV	0.0065	0.0065
RTF-BLT-P5	122	30	5.99	2.44	149.8	907.4	0.40	30-INV	0.0065	0.0065
RTF-BLT-P5	123	30	5.98	2.06	125.4	904.0	0.40	30-INV	0.0065	0.0065
RTF-BLT-P5	124	30	5.99	3.00	183.6	906.5	0.40	30-INV	0.0065	0.0065

Table 6: (Continued)Chronological Run Matrix for Test 6886 in the 20-Inch Mach 6 Air Tunnel.

Model ID	Run	α	Mach	Re_∞/ft.	p_{t1}	T_{t1}	Trip Setup			
			No.	x 10^6	psi	˚R	*x/L*	AL	k_{CL}	k_{AL}
RTF-BLT-P5	127	30	6.01	3.45	212.8	907.5	0.60	30-INV	0.0065	0.0065
RTF-BLT-P5	128	30	6.01	4.08	251.8	908.8	0.60	30-INV	0.0065	0.0065
RTF-BLT-P5	129	30	5.99	2.98	182.7	906.2	0.60	30-INV	0.0065	0.0065
RTF-BLT-P5	130	30	5.97	2.10	128.1	907.4	0.60	30-INV	0.0065	0.0065
RTF-BLT-P5	131	30	5.97	1.69	100.9	895.1	0.60	30-INV	0.0065	0.0065
RTF-BLT-P5	132	30	5.96	1.40	81.7	885.6	0.60	30-INV	0.0065	0.0065
RTF-BLT-P5	133	30	5.93	1.09	62.1	875.9	0.60	30-INV	0.0065	0.0065
RTF-BLT-P5	134	30	5.91	0.84	46.7	865.0	0.60	30-INV	0.0065	0.0065
RTF-BLT-P5	135	30	5.99	3.47	213.2	908.9	0.64	40-INV	0.0065	0.0065
RTF-BLT-P5	136	30	5.99	4.14	253.9	908.7	0.64	40-INV	0.0065	0.0065
RTF-BLT-P5	137	30	6.01	4.55	294.0	935.6	0.64	40-INV	0.0065	0.0065
RTF-BLT-P5	138	30	5.98	2.98	182.4	907.7	0.64	40-INV	0.0065	0.0065
RTF-BLT-P5	139	30	5.97	2.09	127.1	906.7	0.64	40-INV	0.0065	0.0065
RTF-BLT-P5	140	30	5.98	2.50	152.5	907.2	0.64	40-INV	0.0065	0.0065
RTF-BLT-P5	141	30	5.93	1.05	59.6	875.9	0.64	40-INV	0.0065	0.0065
RTF-BLT-P5	142	30	5.93	1.04	59.4	881.2	0.64	40-INV	0.0065	0.0065
RTF-BLT-P5	143	30	5.93	0.56	30.9	856.7	0.64	40-INV	0.0065	0.0065
RTF-BLT-P5	149	30	5.98	2.10	127.5	904.0	0.20	30-INV	0.0065	0.0065
RTF-BLT-P5	150	30	5.97	1.73	102.9	893.4	0.20	30-INV	0.0065	0.0065
RTF-BLT-P5	151	30	5.99	2.96	181.2	905.3	0.20	30-INV	0.0065	0.0065
RTF-BLT-P5	152	30	6.02	3.41	211.3	905.9	0.20	30-INV	0.0065	0.0065
RTF-BLT-P5	153	30	6.02	4.08	252.7	907.4	0.20	30-INV	0.0065	0.0065

Table 7: Chronological Run Matrix for Test 6892 in the 20-Inch Mach 6 Air Tunnel.

Model ID	Run	α	Mach	Re_∞/ft.	p_{t1}	T_{t1}	Trip Setup			
			No.	x 10^6	psi	˚R	*x/L*	AL	k_{CL}	k_{AL}
RTF-BLT-PA	1	40	5.98	4.11	252.2	910.3				
RTF-BLT-PA	2	40	5.93	2.05	123.8	911.2				
RTF-BLT-PA	3	40	5.98	4.12	252.4	909.6				
RTF-BLT-PC	4	40	5.98	4.09	250.9	911.0				
RTF-BLT-PC	5	40	5.94	2.07	123.9	906.1				
RTF-BLT-PA	6	40	5.98	4.08	251.6	912.8				
RTF-BLT-PB	10	40	5.91	1.05	59.4	880.6	0.50	40INV	0.0065	0.0065
RTF-BLT-PB	15	40	5.96	2.06	125.5	910.5	0.50	40INV	0.0065	0.0065
RTF-BLT-PB	16	40	5.97	2.44	149.6	911.4	0.50	40INV	0.0065	0.0065
RTF-BLT-PB	17	40	5.95	1.70	100.6	895.9	0.50	40INV	0.0065	0.0065
RTF-BLT-PB	18	40	5.99	2.93	180.7	909.0	0.50	40INV	0.0065	0.0065
RTF-BLT-PB	19	40	5.93	1.36	79.3	890.8	0.50	40INV	0.0065	0.0065
RTF-BLT-PB	20	40	5.97	2.04	124.6	910.2	0.66	40INV	0.0045	0.0035
RTF-BLT-PB	21	40	5.94	1.67	99.6	900.3	0.66	40INV	0.0045	0.0035
RTF-BLT-PB	22	40	5.92	1.39	80.9	892.5	0.66	40INV	0.0045	0.0035
RTF-BLT-PB	23	40	5.96	2.44	149.7	913.3	0.66	40INV	0.0045	0.0035
RTF-BLT-PB	24	40	6.00	2.91	180.1	909.9	0.66	40INV	0.0045	0.0035
RTF-BLT-PB	30	40	5.96	2.05	124.8	909.9	0.10	40INV	0.0045	0.0045
RTF-BLT-PB	31	40	5.97	2.45	150.3	910.0	0.10	40INV	0.0045	0.0045
RTF-BLT-PB	32	40	5.99	2.96	181.8	909.6	0.10	40INV	0.0045	0.0045

Table 7: (Continued)Chronological Run Matrix for Test 6892 in the 20-Inch Mach 6 Air Tunnel.

Model ID	Run	α	Mach	Re_∞/ft.	p_{t1}	T_{t1}	Trip Setup			
			No.	x 10^6	psi	°R	*x/L*	AL	k_{CL}	k_{AL}
RTF-BLT-PB	33	40	5.95	1.68	99.9	898.9	0.68	40INV	0.0045	0.0045
RTF-BLT-PB	34	40	5.93	1.37	80.3	891.9	0.68	40INV	0.0045	0.0045
RTF-BLT-PB	35	40	5.90	1.06	60.1	881.5	0.68	40INV	0.0045	0.0045
RTF-BLT-PB	36	40	5.95	2.07	125.3	907.6	0.68	40INV	0.0045	0.0045
RTF-BLT-PB	37	40	5.97	2.47	150.4	909.1	0.68	40INV	0.0045	0.0045
RTF-BLT-PB	38	30	5.95	2.06	125.1	908.7	0.60	30INV	0.0065	0.0065
RTF-BLT-PB	39	30	5.96	2.45	150.3	911.8	0.60	30INV	0.0065	0.0065
RTF-BLT-PB	40	30	5.98	2.94	180.4	911.4	0.60	30INV	0.0065	0.0065
RTF-BLT-PB	41	30	5.99	3.42	211.0	911.3	0.60	30INV	0.0065	0.0065
RTF-BLT-PB	42	30	5.96	2.07	125.7	907.8	0.20	30INV	0.0065	0.0065
RTF-BLT-PB	43	30	5.96	2.48	150.6	908.6	0.20	30INV	0.0065	0.0065
RTF-BLT-PB	44	30	5.98	2.95	181.2	910.3	0.20	30INV	0.0065	0.0065
RTF-BLT-PB	45	30	5.99	2.01	124.4	912.1	0.40	30INV	0.0065	0.0065
RTF-BLT-PB	46	30	5.96	1.67	100.1	899.7	0.40	30INV	0.0065	0.0065
RTF-BLT-PB	47	30	5.98	2.45	151.3	912.2	0.40	30INV	0.0065	0.0065
RTF-BLT-PB	48	30	6.00	2.96	182.5	909.7	0.40	30INV	0.0065	0.0065
RTF-BLT-PB	49	30	6.01	3.42	212.1	909.6	0.40	30INV	0.0065	0.0065

Table 8: Chronological Run Matrix for Test 390 in the 31-Inch Mach 10 Air Tunnel.

Model ID	Run	α	Mach	Re_∞/ft.	p_{t1}	T_{t1}	Trip Setup			
			No.	x 10^6	psi	°R	*x/L*	AL	k_{CL}	k_{AL}
RTF-BLT-P7	18	40	9.33	0.57	352.0	1793.6				
RTF-BLT-P7	19	40	9.63	1.08	723.2	1799.5				
RTF-BLT-P7	20	40	9.69	1.25	852.7	1803.1				
RTF-BLT-P7	21	40	9.74	1.44	1008.5	1816.9				
RTF-BLT-P7	22	40	9.81	1.78	1250.8	1808.1				
RTF-BLT-P7	23	40	9.33	0.57	352.7	1794.7	0.40	40-INV	0.0115	0.0115
RTF-BLT-P7	24	40	9.63	1.08	724.1	1799.7	0.40	40-INV	0.0115	0.0115
RTF-BLT-P7	25	40	9.66	1.17	782.4	1789.1	0.40	40-INV	0.0115	0.0115
RTF-BLT-P7	26	40	9.69	1.26	852.4	1795.7	0.40	40-INV	0.0115	0.0115
RTF-BLT-P7	27	40	9.74	1.46	1005.8	1803.9	0.40	40-INV	0.0115	0.0115
RTF-BLT-P7	28	40	9.81	1.79	1254.9	1803.9	0.40	40-INV	0.0115	0.0115
RTF-BLT-P7	29	40	9.33	0.58	352.1	1790.4	0.30	40-INV	0.0115	0.0115
RTF-BLT-P7	30	40	9.63	1.07	722.7	1806.9	0.30	40-INV	0.0115	0.0115
RTF-BLT-P7	31	40	9.51	0.81	533.6	1810.7	0.30	40-INV	0.0115	0.0115
RTF-BLT-P7	32	40	9.66	1.17	784.1	1789.7	0.30	40-INV	0.0115	0.0115
RTF-BLT-P7	34	40	9.69	1.27	852.3	1789.3	0.30	40-INV	0.0115	0.0115
RTF-BLT-P7	35	40	9.74	1.45	1002.7	1804.9	0.30	40-INV	0.0115	0.0115
RTF-BLT-P7	36	40	9.81	1.80	1254.5	1795.7	0.30	40-INV	0.0115	0.0115
RTF-BLT-P7	37	40	9.63	1.08	721.3	1797.3	0.20	40-INV	0.0115	0.0115
RTF-BLT-P7	38	40	9.33	0.58	352.9	1790.6	0.20	40-INV	0.0115	0.0115
RTF-BLT-P7	39	40	9.51	0.81	533.3	1812.9	0.20	40-INV	0.0115	0.0115
RTF-BLT-P7	40	40	9.66	1.15	783.6	1810.3	0.20	40-INV	0.0115	0.0115
RTF-BLT-P7	41	40	9.69	1.26	852.1	1799.1	0.20	40-INV	0.0115	0.0115
RTF-BLT-P7	42	40	9.74	1.45	1004.2	1805.2	0.20	40-INV	0.0115	0.0115
RTF-BLT-P7	50	40	9.78	1.62	1124.8	1801.8	0.20	40-INV	0.0115	0.0115

Table 8: (Continued)Chronological Run Matrix for Test 390 in the 31-Inch Mach 10 Air Tunnel.

Model ID	Run	α	Mach	Re_∞/ft.	p_{t1}	T_{t1}	Trip Setup			
			No.	x 10^6	psi	°R	x/L	AL	k_{CL}	k_{AL}
RTF-BLT-P7	51	40	9.81	1.79	1252.9	1800.7	0.20	40-INV	0.0115	0.0115
RTF-BLT-P7	52	40	9.63	1.07	725.2	1811.1	0.50	40-INV	0.0115	0.0115
RTF-BLT-P7	53	40	9.33	0.58	352.4	1789.4	0.50	40-INV	0.0115	0.0115
RTF-BLT-P7	54	40	9.51	0.81	532.0	1811.3	0.50	40-INV	0.0115	0.0115
RTF-BLT-P7	55	40	9.66	1.16	784.6	1808.1	0.50	40-INV	0.0115	0.0115
RTF-BLT-P7	56	40	9.69	1.26	853.9	1796.7	0.50	40-INV	0.0115	0.0115
RTF-BLT-P7	57	40	9.74	1.43	1005.2	1823.1	0.50	40-INV	0.0115	0.0115
RTF-BLT-P7	58	40	9.77	1.61	1124.6	1810.0	0.50	40-INV	0.0115	0.0115
RTF-BLT-P7	59	40	9.81	1.79	1255.2	1802.8	0.50	40-INV	0.0115	0.0115
RTF-BLT-P7	60	40	9.63	1.09	723.1	1794.6	0.60	40-INV	0.0115	0.0115
RTF-BLT-P7	61	40	9.33	0.57	350.7	1794.5	0.60	40-INV	0.0115	0.0115
RTF-BLT-P7	62	40	9.52	0.82	533.2	1802.8	0.60	40-INV	0.0115	0.0115
RTF-BLT-P7	64	40	9.66	1.17	784.6	1793.0	0.60	40-INV	0.0115	0.0115
RTF-BLT-P7	65	40	9.69	1.28	852.8	1780.7	0.60	40-INV	0.0115	0.0115
RTF-BLT-P7	66	40	9.74	1.45	1003.9	1809.1	0.60	40-INV	0.0115	0.0115
RTF-BLT-P7	67	40	9.78	1.62	1126.1	1801.0	0.60	40-INV	0.0115	0.0115
RTF-BLT-P7	68	40	9.81	1.78	1251.4	1804.3	0.60	40-INV	0.0115	0.0115
RTF-BLT-P7	69	40	9.63	1.08	724.7	1800.9	0.70	40-INV	0.0115	0.0115
RTF-BLT-P7	70	40	9.66	1.18	783.2	1787.6	0.70	40-INV	0.0115	0.0115
RTF-BLT-P7	71	40	9.33	0.58	352.4	1785.2	0.70	40-INV	0.0115	0.0115
RTF-BLT-P7	72	40	9.70	1.31	853.6	1755.0	0.70	40-INV	0.0115	0.0115
RTF-BLT-P7	73	40	9.52	0.82	533.3	1795.8	0.70	40-INV	0.0115	0.0115
RTF-BLT-P7	74	40	9.75	1.49	1004.1	1779.5	0.70	40-INV	0.0115	0.0115
RTF-BLT-P7	75	40	9.78	1.63	1126.9	1794.6	0.70	40-INV	0.0115	0.0115
RTF-BLT-P7	76	40	9.82	1.89	1254.2	1745.0	0.70	40-INV	0.0115	0.0115
RTF-BLT-P7	78	30	9.64	1.13	722.0	1752.2				
RTF-BLT-P7	79	30	9.69	1.26	854.3	1794.9				
RTF-BLT-P7	80	30	9.74	1.45	1005.0	1810.2				
RTF-BLT-P7	81	30	9.81	1.80	1253.0	1794.3				
RTF-BLT-P7	82	30	9.33	0.58	351.2	1787.3				
RTF-BLT-P7	86	30	9.87	2.08	1461.7	1790.3	0.30	30-INV	0.0115	0.0115
RTF-BLT-P7	87	30	9.81	1.80	1251.9	1794.1	0.30	30-INV	0.0115	0.0115
RTF-BLT-P7	88	30	9.74	1.45	1002.5	1807.0	0.30	30-INV	0.0115	0.0115
RTF-BLT-P7	89	30	9.69	1.26	854.5	1795.8	0.30	30-INV	0.0115	0.0115
RTF-BLT-P7	90	30	9.63	1.07	722.5	1809.3	0.30	30-INV	0.0115	0.0115
RTF-BLT-P7	91	30	9.33	0.57	351.9	1801.6	0.30	30-INV	0.0115	0.0115
RTF-BLT-P7	92	30	9.86	2.05	1455.7	1804.4	0.40	30-INV	0.0115	0.0115
RTF-BLT-P7	93	30	9.81	1.80	1253.1	1794.1	0.40	30-INV	0.0115	0.0115
RTF-BLT-P7	94	30	9.74	1.44	1002.5	1810.4	0.40	30-INV	0.0115	0.0115
RTF-BLT-P7	95	30	9.69	1.27	854.1	1786.5	0.40	30-INV	0.0115	0.0115
RTF-BLT-P7	96	30	9.63	1.07	723.6	1806.2	0.40	30-INV	0.0115	0.0115
RTF-BLT-P7	97	30	9.33	0.06	351.6	1793.7	0.40	30-INV	0.0115	0.0115
RTF-BLT-P7	98	30	9.86	2.03	1458.7	1814.6	0.50	30-INV	0.0115	0.0115
RTF-BLT-P7	99	30	9.81	1.79	1251.1	1800.0	0.50	30-INV	0.0115	0.0115
RTF-BLT-P7	100	30	9.74	1.45	1005.7	1808.1	0.50	30-INV	0.0115	0.0115
RTF-BLT-P7	101	30	9.69	1.27	854.4	1793.6	0.50	30-INV	0.0115	0.0115

Table 8: (Continued)Chronological Run Matrix for Test 390 in the 31-Inch Mach 10 Air Tunnel.

Model ID	Run	α	Mach	Re_∞/ft.	p_{t1}	T_{t1}	Trip Setup			
			No.	x 10^6	psi	°R	*x/L*	AL	k_{CL}	k_{AL}
RTF-BLT-P7	102	30	9.63	1.08	722.0	1796.2	0.50	30-INV	0.0115	0.0115
RTF-BLT-P7	103	30	9.33	0.57	351.5	1792.9	0.50	30-INV	0.0115	0.0115
RTF-BLT-P7	104	30	9.85	2.01	1424.9	1803.8	0.20	30-INV	0.0115	0.0115
RTF-BLT-P7	105	30	9.81	1.78	1249.4	1802.9	0.20	30-INV	0.0115	0.0115
RTF-BLT-P7	106	30	9.74	1.45	1006.3	1808.5	0.20	30-INV	0.0115	0.0115
RTF-BLT-P7	107	30	9.69	1.26	854.7	1802.5	0.20	30-INV	0.0115	0.0115
RTF-BLT-P7	108	30	9.63	1.07	723.9	1807.4	0.20	30-INV	0.0115	0.0115
RTF-BLT-P7	109	30	9.33	0.58	351.4	1785.6	0.20	30-INV	0.0115	0.0115
RTF-BLT-P8	116	30	9.52	0.82	533.5	1800.9	0.20	40-INV	0.0115	0.0115
RTF-BLT-P8	117	30	9.63	1.08	724.2	1804.4	0.20	40-INV	0.0115	0.0115
RTF-BLT-P8	121	30	9.74	1.44	1005.8	1817.5	0.20	40-INV	0.0115	0.0115
RTF-BLT-P8	122	30	9.81	1.81	1253.6	1792.0	0.20	40-INV	0.0115	0.0115
RTF-BLT-P8	123	30	9.87	2.11	1459.5	1773.5	0.20	40-INV	0.0115	0.0115
RTF-BLT-P8	124	30	9.52	0.82	534.0	1801.3	0.60	40-INV	0.0065	0.0065
RTF-BLT-P8	125	30	9.63	1.07	723.0	1808.5	0.60	40-INV	0.0065	0.0065
RTF-BLT-P8	126	30	9.74	1.45	1003.8	1806.5	0.60	40-INV	0.0065	0.0065
RTF-BLT-P8	127	30	9.81	1.80	1251.0	1793.6	0.60	40-INV	0.0065	0.0065
RTF-BLT-P8	128	30	9.86	2.03	1456.3	1814.6	0.60	40-INV	0.0065	0.0065
RTF-BLT-P8	129	30	9.52	0.82	532.9	1801.8	0.40	40-INV	0.0065	0.0065
RTF-BLT-P8	130	30	9.63	1.08	724.0	1801.3	0.40	40-INV	0.0065	0.0065
RTF-BLT-P8	131	30	9.74	1.45	1002.5	1804.7	0.40	40-INV	0.0065	0.0065
RTF-BLT-P8	132	30	9.81	1.81	1254.2	1792.0	0.40	40-INV	0.0065	0.0065
RTF-BLT-P8	133	30	9.87	2.11	1462.2	1778.7	0.40	40-INV	0.0065	0.0065

Table 9: Chronological Run Matrix for Test 162 in the 20-Inch CF_4 Tunnel.

Model ID	Run	α	Mach	Re_∞/ft.	p_{t1}	T_{t1}	Trip Setup			
			No.	x 10^6	psi	°R	*x/L*	AL	k_{CL}	k_{AL}
RTF-BLT-P5	16	40	5.75	0.28	1042.6	1328.8	0.50	40INV	0.0115	0.0115
RTF-BLT-P5	17	40	5.73	0.14	512.9	1323.2	0.50	40INV	0.0115	0.0115
RTF-BLT-P5	19	40	5.75	0.40	1522.2	1341.4	0.50	40INV	0.0115	0.0115
RTF-BLT-P5	20	40	5.86	0.27	804.8	1222.7	0.50	40INV	0.0115	0.0115
RTF-BLT-PB	21	40	5.85	0.48	1523.2	1248.3	0.40	30INV	0.0065	0.0065
RTF-BLT-PB	22	40	5.82	0.33	1073.3	1267.2	0.40	30INV	0.0065	0.0065
RTF-BLT-PB	23	40	5.86	0.24	733.5	1229.1	0.40	30INV	0.0065	0.0065
RTF-BLT-PB	24	40	5.89	0.27	781.4	1206.2	0.40	40INV	0.0065	0.0065
RTF-BLT-PB	25	40	5.94	0.38	1024.1	1174.1	0.40	40INV	0.0065	0.0065
RTF-BLT-PB	26	40	5.93	0.45	1240.6	1184.2	0.40	40INV	0.0065	0.0065
RTF-BLT-PB	27	40	5.93	0.56	1527.7	1188.8	0.40	40INV	0.0065	0.0065
RTF-BLT-PB	28	40	5.93	0.19	496.5	1168.1	0.62	40INV	0.0115	0.0115
RTF-BLT-PB	29	40	5.93	0.39	1056.6	1182.7	0.62	40INV	0.0115	0.0115
RTF-BLT-PB	30	40	5.93	0.55	1527.0	1190.3	0.62	40INV	0.0115	0.0115
RTF-BLT-PB	31	40	5.89	0.01	256.0	1174.0	0.62	40INV	0.0115	0.0115
RTF-BLT-PC	32	40	5.88	0.09	245.7	1185.1				
RTF-BLT-PC	33	40	5.90	0.19	518.1	1191.7				
RTF-BLT-PC	34	40	5.90	0.38	1070.2	1201.6				
RTF-BLT-PC	35	40	5.93	0.55	1512.3	1192.3				

Table 9: (Continued)Chronological Run Matrix for Test 162 in the 20-Inch CF_4 Tunnel.

Model ID	Run	α	Mach	Re_∞/ft.	p_{t1}	T_{t1}	Trip Setup			
			No.	x 10^6	psi	°R	x/L	AL	k_{CL}	k_{AL}
RTF-BLT-PC	36	40	5.89	0.09	235.2	1175.5	0.68	40INV	0.0065	0.0065
RTF-BLT-PC	37	40	5.91	0.18	503.9	1183.2	0.68	40INV	0.0065	0.0065
RTF-BLT-PC	38	40	5.91	0.38	1058.3	1197.1	0.68	40INV	0.0065	0.0065
RTF-BLT-PC	39	40	5.95	0.57	1521.9	1179.4	0.68	40INV	0.0065	0.0065
RTF-BLT-PC	40	40	5.85	0.09	257.0	1211.0	0.64	40INV	0.0115	0.0115
RTF-BLT-PC	41	40	5.93	0.20	522.5	1168.1	0.64	40INV	0.0115	0.0115
RTF-BLT-PC	42	40	5.92	0.38	1042.9	1184.9	0.64	40INV	0.0115	0.0115
RTF-BLT-PC	43	40	5.94	0.55	1516.1	1188.9	0.64	40INV	0.0115	0.0115
RTF-BLT-PC	44	40	5.90	0.01	257.3	1173.2	0.64	40INV	0.0065	0.0065
RTF-BLT-PC	45	40	5.92	0.19	519.1	1175.5	0.64	40INV	0.0065	0.0065
RTF-BLT-PC	46	40	5.91	0.29	789.0	1188.3	0.64	40INV	0.0065	0.0065
RTF-BLT-PC	47	40	5.93	0.39	1041.5	1179.5	0.64	40INV	0.0065	0.0065
RTF-BLT-PC	48	40	5.93	0.53	1472.8	1190.8	0.64	40INV	0.0065	0.0065
RTF-BLT-PC	49	40	5.90	0.01	255.0	1172.2	0.60	40INV	0.0115	0.0115
RTF-BLT-PC	50	40	5.92	0.19	519.2	1176.4	0.60	40INV	0.0115	0.0115
RTF-BLT-PC	51	40	5.92	0.39	1067.9	1190.3	0.60	40INV	0.0115	0.0115
RTF-BLT-PC	52	40	5.96	0.57	1504.3	1172.9	0.60	40INV	0.0115	0.0115
RTF-BLT-PC	53	40	5.86	0.09	260.4	1200.9	0.60	40INV	0.0065	0.0065
RTF-BLT-PC	54	40	5.90	0.19	513.2	1189.2	0.60	40INV	0.0065	0.0065
RTF-BLT-PC	55	40	5.91	0.38	1070.0	1196.3	0.60	40INV	0.0065	0.0065
RTF-BLT-PC	56	40	5.93	0.55	1527.6	1194.9	0.60	40INV	0.0065	0.0065
RTF-BLT-PC	57	40	5.90	0.01	260.0	1171.6	0.60	40INV	0.0045	0.0045
RTF-BLT-PC	58	40	5.91	0.19	510.4	1179.6	0.60	40INV	0.0045	0.0045
RTF-BLT-PC	59	40	5.93	0.39	1053.6	1184.5	0.60	40INV	0.0045	0.0045
RTF-BLT-PC	60	40	5.93	0.55	1531.0	1190.4	0.60	40INV	0.0045	0.0045
RTF-BLT-PC	61	40	5.93	0.30	797.5	1172.4	0.60	40INV+	0.0065	0.0065
RTF-BLT-PC	62	40	5.93	0.40	1086.1	1181.2	0.60	40INV+	0.0065	0.0065
RTF-BLT-PC	63	40	5.95	0.48	1277.9	1173.0	0.60	40INV+	0.0065	0.0065
RTF-BLT-PC	64	40	5.93	0.55	1528.7	1192.9	0.60	40INV+	0.0065	0.0065
RTF-BLT-PC	65	40	5.90	0.01	255.0	1171.6	0.40	40INV+	0.0115	0.0115
RTF-BLT-PC	66	40	5.91	0.19	511.5	1178.2	0.40	40INV+	0.0115	0.0115
RTF-BLT-PC	67	40	5.93	0.40	1075.7	1181.7	0.40	40INV+	0.0115	0.0115
RTF-BLT-PC	68	40	5.94	0.55	1515.6	1189.3	0.40	40INV+	0.0115	0.0115
RTF-BLT-PC	69	40	5.90	0.01	254.6	1169.8	0.40	40INV+	0.0065	0.0065
RTF-BLT-PC	70	40	5.92	0.19	515.2	1177.5	0.40	40INV+	0.0065	0.0065
RTF-BLT-PC	71	40	5.92	0.39	1078.8	1188.6	0.40	40INV+	0.0065	0.0065
RTF-BLT-PC	73	40	5.98	0.59	1522.9	1163.0	0.40	40INV+	0.0065	0.0065
RTF-BLT-PC	74	40	5.89	0.24	687.7	1201.2	0.40	40INV+	0.0065	0.0065
RTF-BLT-PC	75	40	5.93	0.32	863.6	1180.2	0.40	40INV+	0.0065	0.0065
RTF-BLT-PC	76	40	5.90	0.10	257.8	1168.7	0.20	40INV+	0.0065	0.0065
RTF-BLT-PC	77	40	5.91	0.20	520.9	1175.9	0.20	40INV+	0.0065	0.0065
RTF-BLT-PC	78	40	5.93	0.30	790.4	1175.8	0.20	40INV+	0.0065	0.0065
RTF-BLT-PC	79	40	5.92	0.38	1051.2	1186.8	0.20	40INV+	0.0065	0.0065
RTF-BLT-PC	80	40	5.93	0.55	1524.8	1193.6	0.20	40INV+	0.0065	0.0065
RTF-BLT-PC	81	40	5.95	0.49	1289.9	1171.4	0.20	40INV+	0.0065	0.0065
RTF-BLT-PC	82	30	5.88	0.09	251.3	1188.4	0.20	30INV	0.0065	0.0065

Table 9: (Continued)Chronological Run Matrix for Test 162 in the 20-Inch CF_4 Tunnel.

Model ID	Run	α	Mach	Re_∞/ft.	p_{t1}	T_{t1}	Trip Setup			
			No.	x 10^6	psi	°R	*x/L*	AL	k_{CL}	k_{AL}
RTF-BLT-PC	83	30	5.89	0.18	505.4	1190.7	0.20	30INV	0.0065	0.0065
RTF-BLT-PC	84	30	5.90	0.28	791.5	1197.2	0.20	30INV	0.0065	0.0065
RTF-BLT-PC	85	30	5.90	0.38	1068.5	1197.5	0.20	30INV	0.0065	0.0065
RTF-BLT-PC	86	30	5.92	0.54	1516.7	1196.0	0.20	30INV	0.0065	0.0065
RTF-BLT-PC	87	30	5.94	0.30	785.7	1167.0	0.20	30INV	0.0115	0.0115
RTF-BLT-PC	88	30	5.88	0.18	511.3	1193.5	0.20	30INV	0.0115	0.0115
RTF-BLT-PC	89	30	5.95	0.41	1066.1	1168.1	0.20	30INV	0.0115	0.0115
RTF-BLT-PC	90	30	5.97	0.59	1514.2	1164.1	0.20	30INV	0.0115	0.0115
RTF-BLT-PC	91	30	5.87	0.18	514.3	1210.1	0.66	30INV	0.0115	0.0115
RTF-BLT-PC	92	30	5.90	0.10	268.4	1169.1	0.66	30INV	0.0115	0.0115
RTF-BLT-PC	93	30	5.92	0.29	788.3	1177.6	0.66	30INV	0.0115	0.0115
RTF-BLT-PC	94	30	5.92	0.39	1074.4	1189.6	0.66	30INV	0.0115	0.0115
RTF-BLT-PC	95	30	5.94	0.48	1294.6	1179.7	0.66	30INV	0.0115	0.0115
RTF-BLT-PC	96	30	5.93	0.55	1533.9	1193.5	0.66	30INV	0.0115	0.0115
RTF-BLT-PC	97	30	5.86	0.09	258.0	1206.8	0.50	66-30INV	0.0115	0.0065
RTF-BLT-PC	98	30	5.87	0.18	519.1	1211.2	0.50	66-30INV	0.0115	0.0065
RTF-BLT-PC	99	30	5.89	0.28	809.6	1207.8	0.50	66-30INV	0.0115	0.0065
RTF-BLT-PC	100	30	5.90	0.38	1076.8	1201.5	0.50	66-30INV	0.0115	0.0065
RTF-BLT-PC	101	30	5.84	0.39	1249.8	1250.5	0.50	66-30INV	0.0115	0.0065
RTF-BLT-PC	102	30	5.91	0.53	1527.9	1208.2	0.50	66-30INV	0.0115	0.0065

Figures

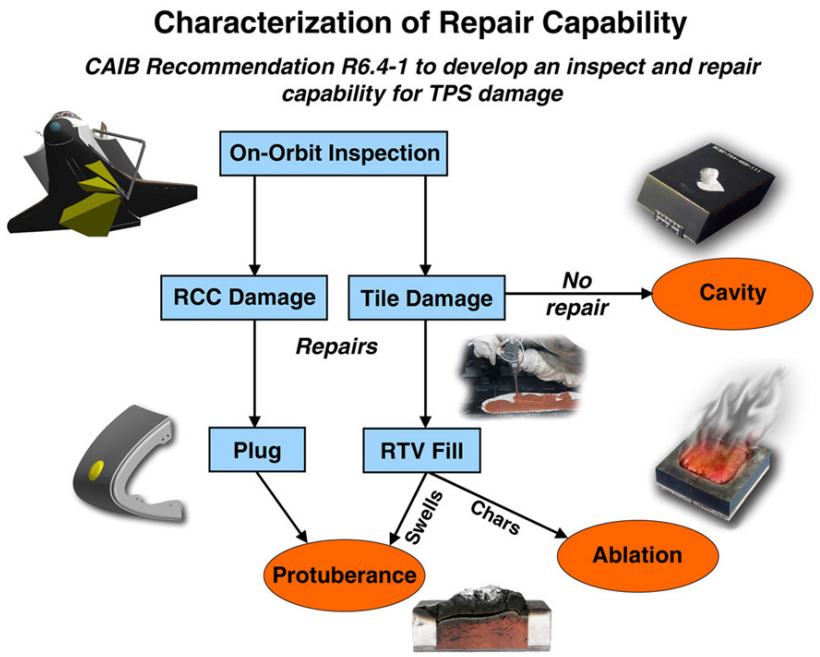

Figure 1: Development of a repair capability for Shuttle return to flight.

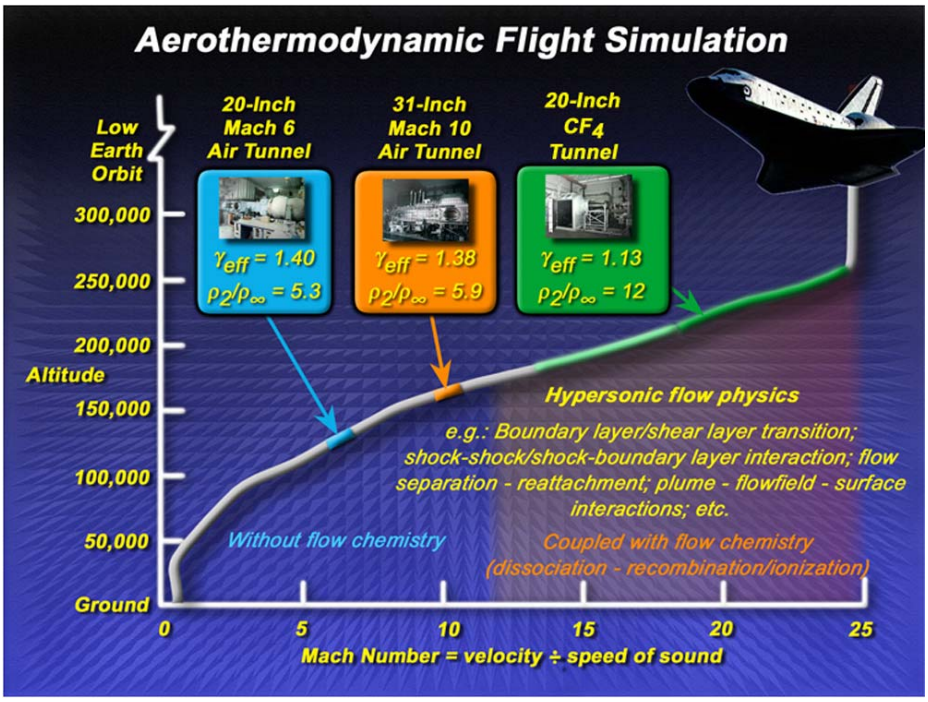

Figure 2: Facilities used in the current study.

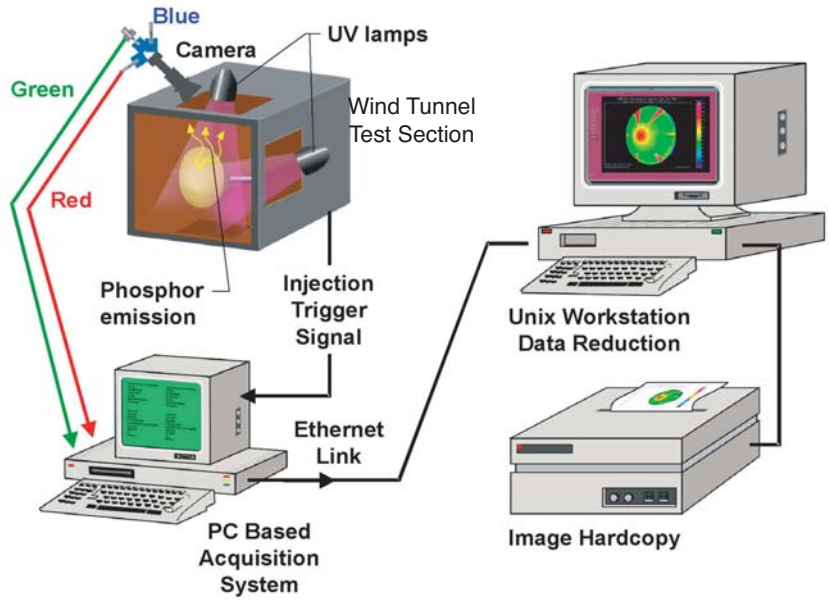

Figure 3: Schematic of thermographic phosphor system.

Figure 4: Ceramic Shuttle Orbiter models.

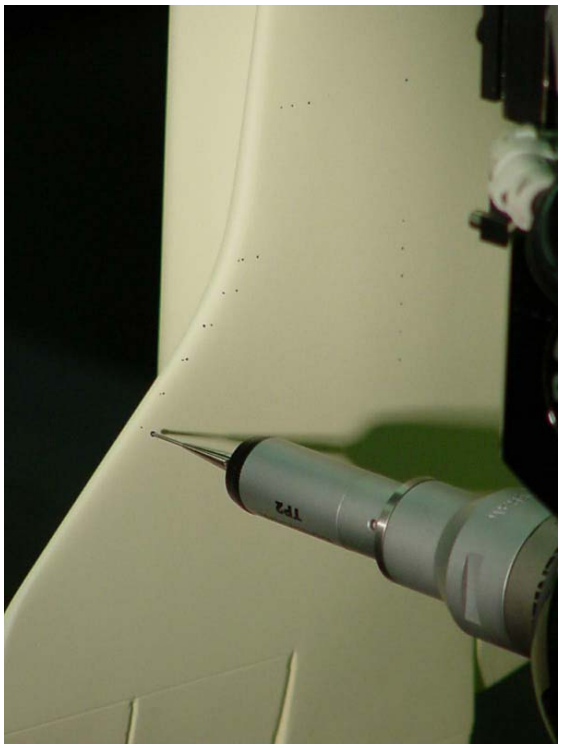

Figure 5: Placement of fiducial marks.

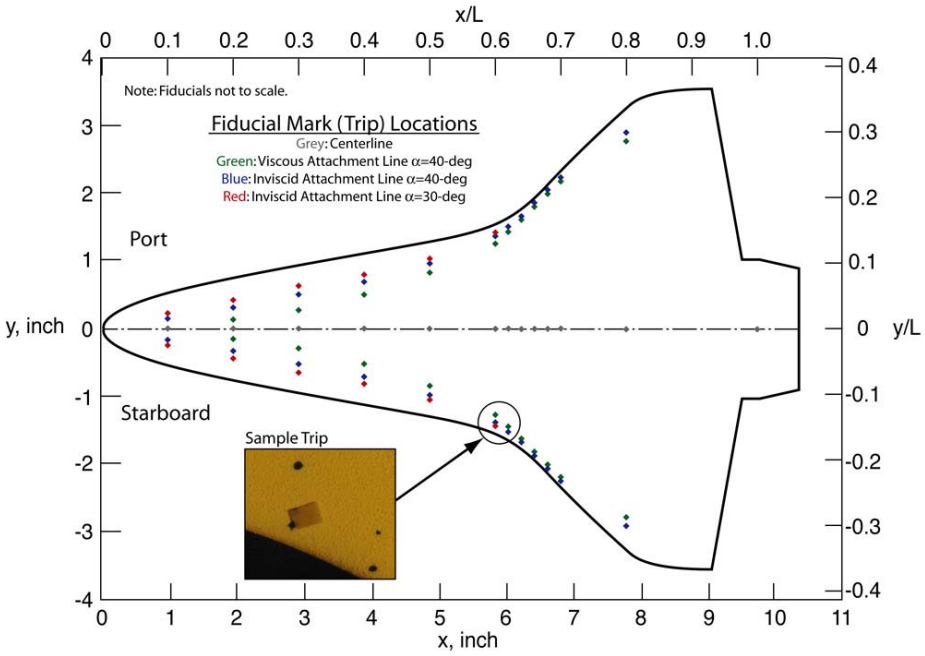

Figure 6: Shuttle Orbiter model fiducial mark locations.

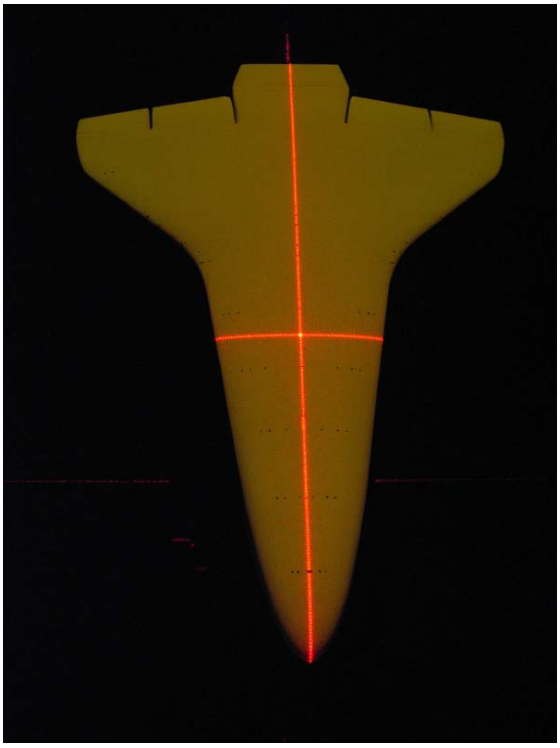

Figure 7: Model setup using laser alignment system.

Appendix A: 20-Inch Mach 6 Air Tunnel Aeroheating

Table A.1: Cross Reference of Figure Numbers Versus Parametrics for Phosphor Images from the 20-Inch Mach 6 Air Tunnel.

α (deg.)	Model	$(x/L)_{CL}$	k_{CL} (in.)	AL	$(x/L)_{AL}$ (in.)	k_{AL}	Figure
30	RTF-BLT-P5	0.20	0.0065	30-INV	0.20	0.0065	A.1
30	RTF-BLT-PB	0.20	0.0065	30-INV	0.20	0.0065	A.4
30	RTF-BLT-P5	0.40	0.0065	30-INV	0.40	0.0065	A.7
30	RTF-BLT-PB	0.40	0.0065	30-INV	0.40	0.0065	A.10
30	RTF-BLT-P5	0.60	0.0065	30-INV	0.60	0.0065	A.13
30	RTF-BLT-PB	0.60	0.0065	30-INV	0.60	0.0065	A.16
30	RTF-BLT-P5	0.64	0.0065	40-INV	0.64	0.0045	A.19
40	RTF-BLT-P2	-	-	-	-	-	A.22
40	RTF-BLT-P3	-	-	-	-	-	A.25
40	RTF-BLT-P5	-	-	-	-	-	A.28
40	RTF-BLT-PB	0.10	0.0045	40-INV	0.10	0.0045	A.31
40	RTF-BLT-P3	0.30	0.0045	40-VIS	0.30	0.0045	A.34
40	RTF-BLT-P5	0.30	0.0065	40-INV	0.30	0.0065	A.37
40	RTF-BLT-P3	0.40	0.0045	40-VIS	0.40	0.0045	A.40
40	RTF-BLT-P5	0.40	0.0065	40-INV	0.40	0.0065	A.43
40	RTF-BLT-P3	0.50	0.0045	40-VIS	0.50	0.0045	A.46
40	RTF-BLT-P5	0.50	0.0045	40-INV	0.50	0.0045	A.49
40	RTF-BLT-P5	0.50	0.0065	40-INV	0.50	0.0065	A.52
40	RTF-BLT-PB	0.50	0.0065	40-INV	0.50	0.0065	A.55
40	RTF-BLT-P3	0.60	0.0045	40-VIS	0.60	0.0045	A.58
40	RTF-BLT-P5	0.60	0.0045	40-INV	0.60	0.0045	A.61
40	RTF-BLT-P5	0.60	0.0115	40-INV	0.60	0.0065	A.64
40	RTF-BLT-P5	0.64	0.0065	40-INV	0.64	0.0045	A.67
40	RTF-BLT-P5	0.64	0.0115	40-INV	0.64	0.0115	A.70
40	RTF-BLT-PB	0.66	0.0045	40-INV	0.66	0.0035	A.73
40	RTF-BLT-P5	0.68	0.0045	40-INV	0.68	0.0045	A.76
40	RTF-BLT-PB	0.68	0.0045	40-INV	0.68	0.0045	A.79
40	RTF-BLT-P3	0.70	0.0045	40-INV	0.70	0.0045	A.82

Note: Corresponding data cuts are located immediately after figures.

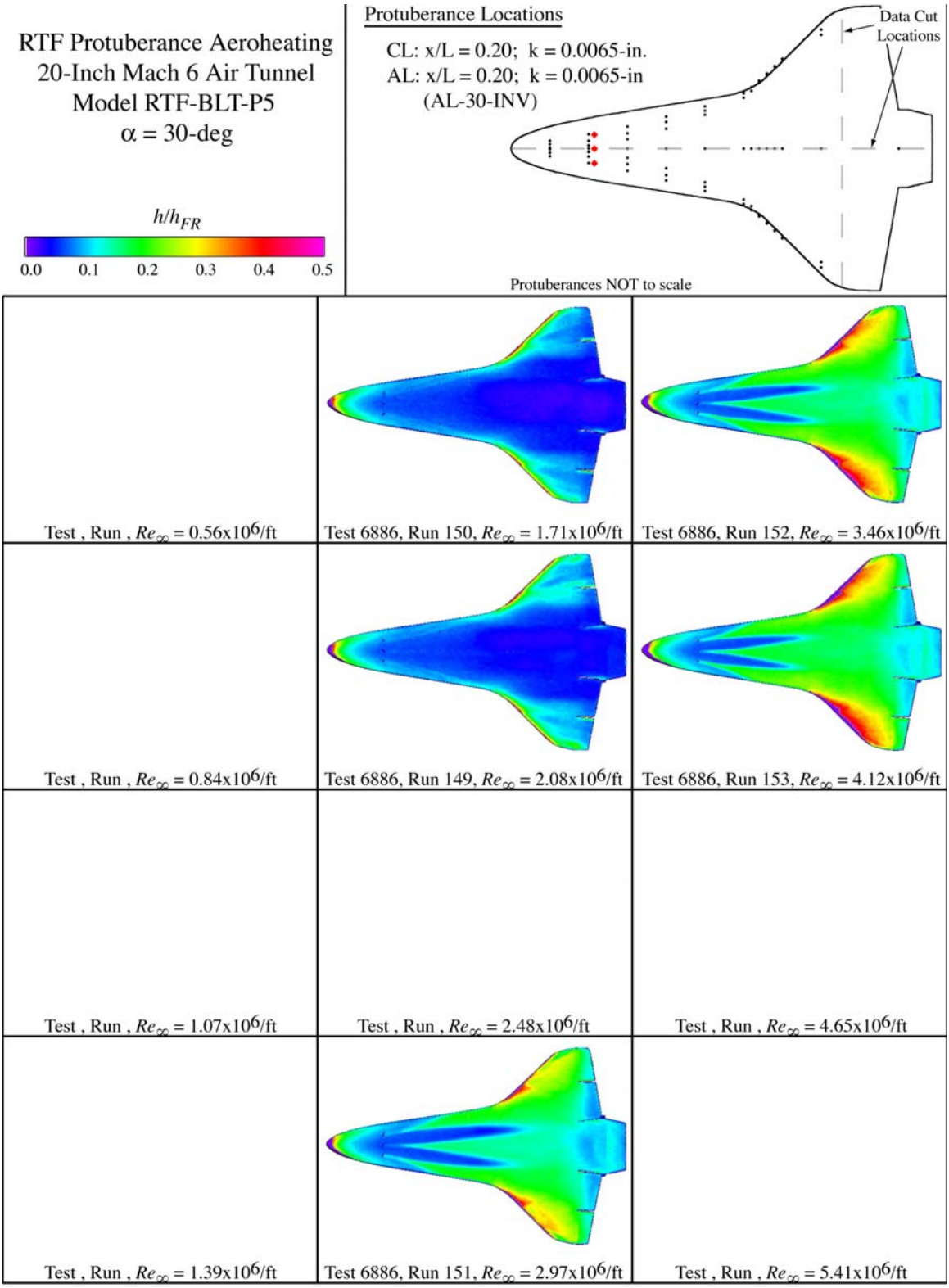

Figure A.1: RTF-BLT-P5 global aeroheating in the 20-Inch Mach 6 Air Tunnel at α = 30-deg, x/L = 0.20, k_{CL} = 0.0065-in., $k_{AL\text{-}30\text{-}INV}$ = 0.0065-in.

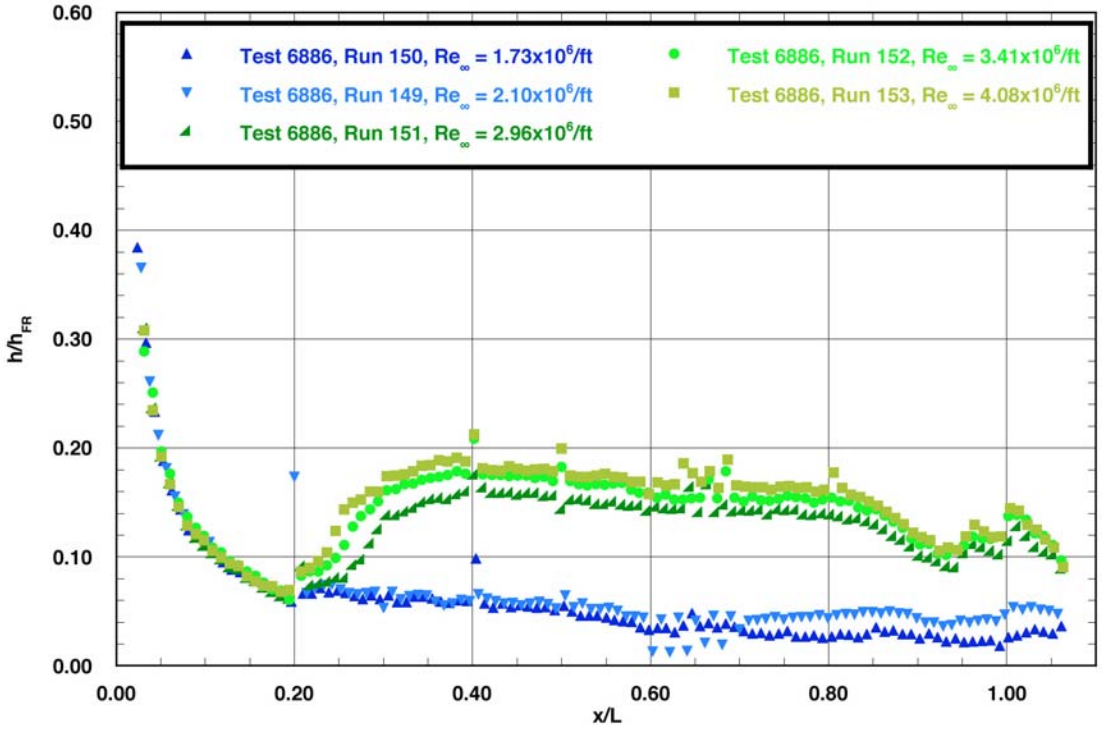

Figure A.2: RTF-BLT-P5 centerline data in the 20-Inch Mach 6 Air Tunnel at α = 30-deg, x/L = 0.20, k_{CL} = 0.0065-in., $k_{AL\text{-}30\text{-}INV}$ = 0.0065-in.

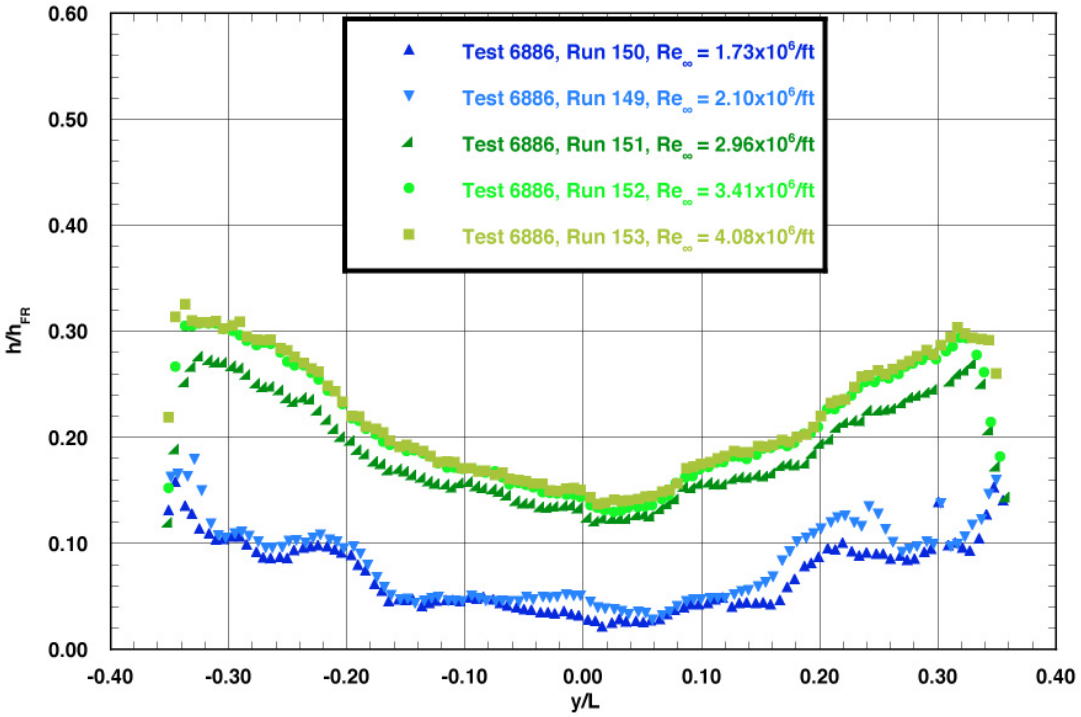

Figure A.3: RTF-BLT-P5 spanwise data (x/L = 0.85) in the 20-Inch Mach 6 Air Tunnel at α = 30-deg, x/L = 0.20, k_{CL} = 0.0065-in., $k_{AL\text{-}30\text{-}INV}$ = 0.0065-in.

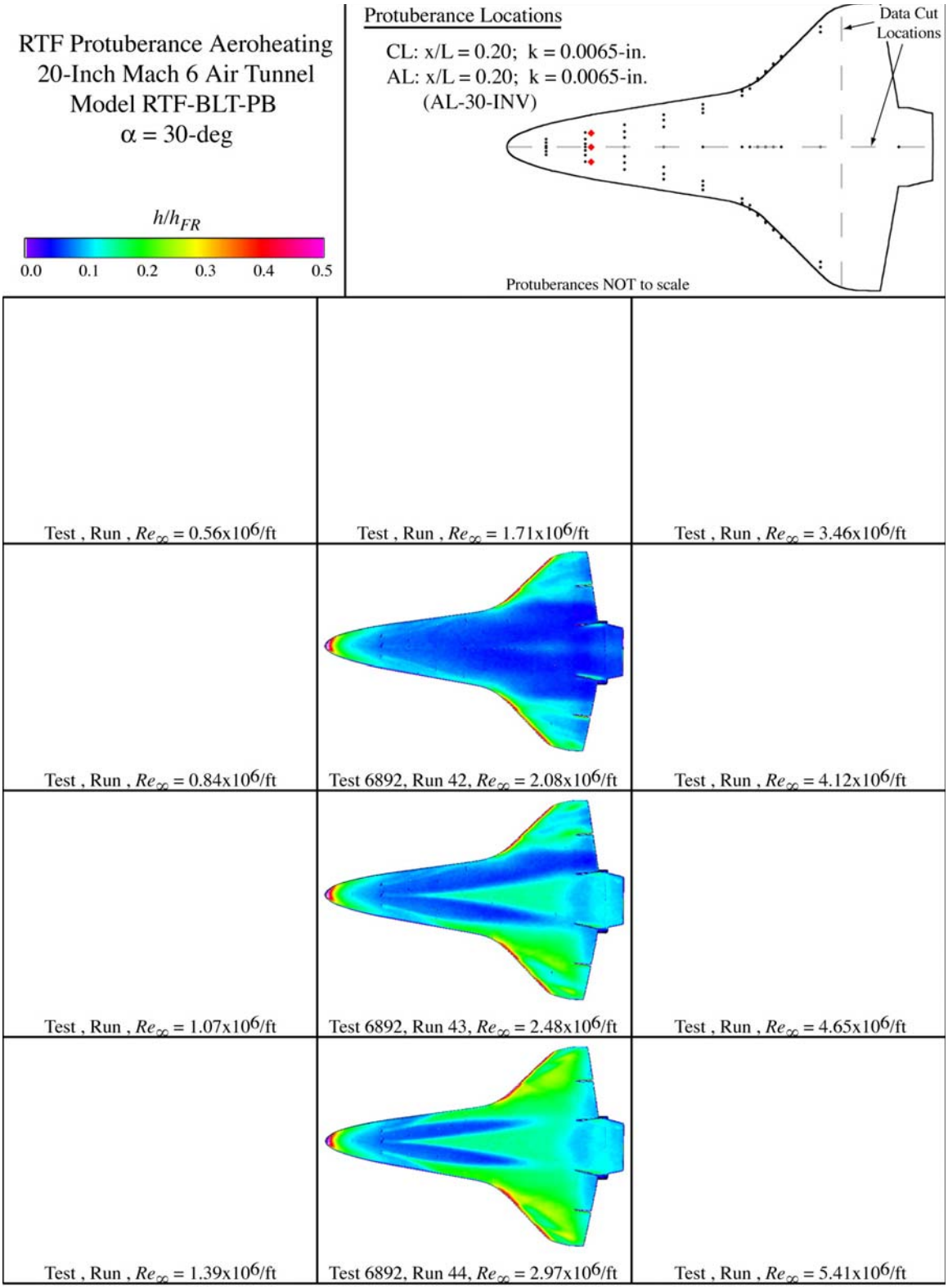

Figure A.4: RTF-BLT-PB global aeroheating in the 20-Inch Mach 6 Air Tunnel at α = 30-deg, x/L = 0.20, k_{CL} = 0.0065-in., $k_{AL\text{-}30\text{-}INV}$ = 0.0065-in.

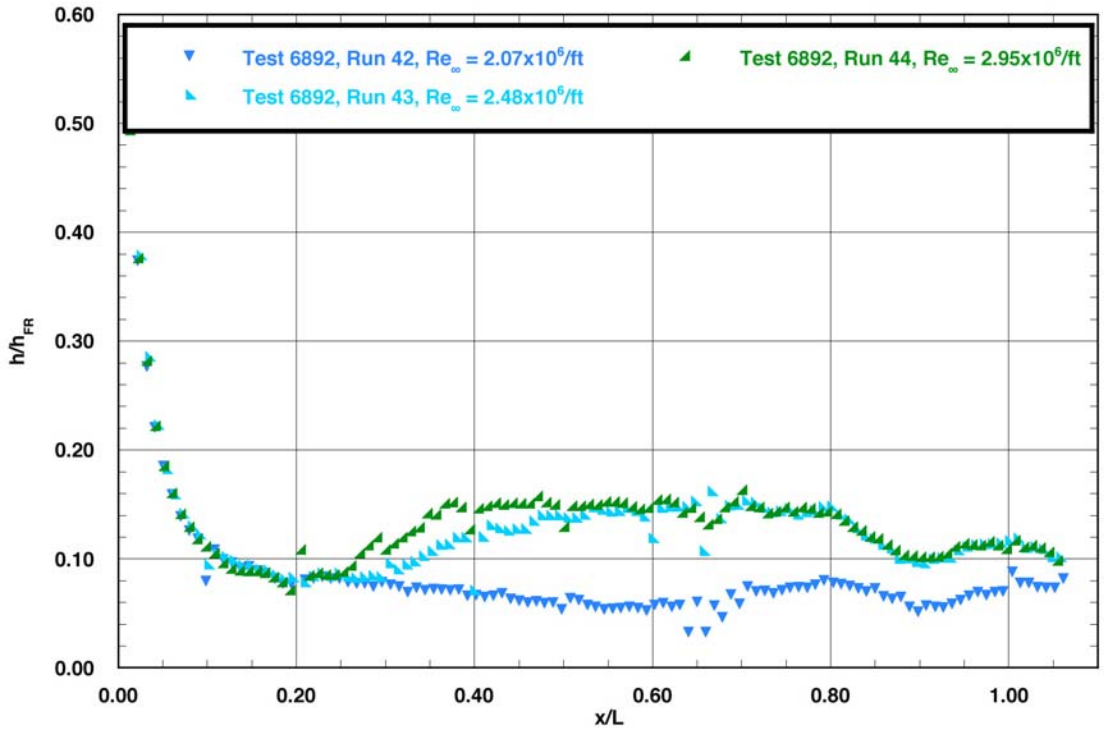

Figure A.5: RTF-BLT-PB centerline data in the 20-Inch Mach 6 Air Tunnel at α = 30-deg, x/L = 0.20, k_{CL} = 0.0065-in., $k_{AL\text{-}30\text{-}INV}$ = 0.0065-in.

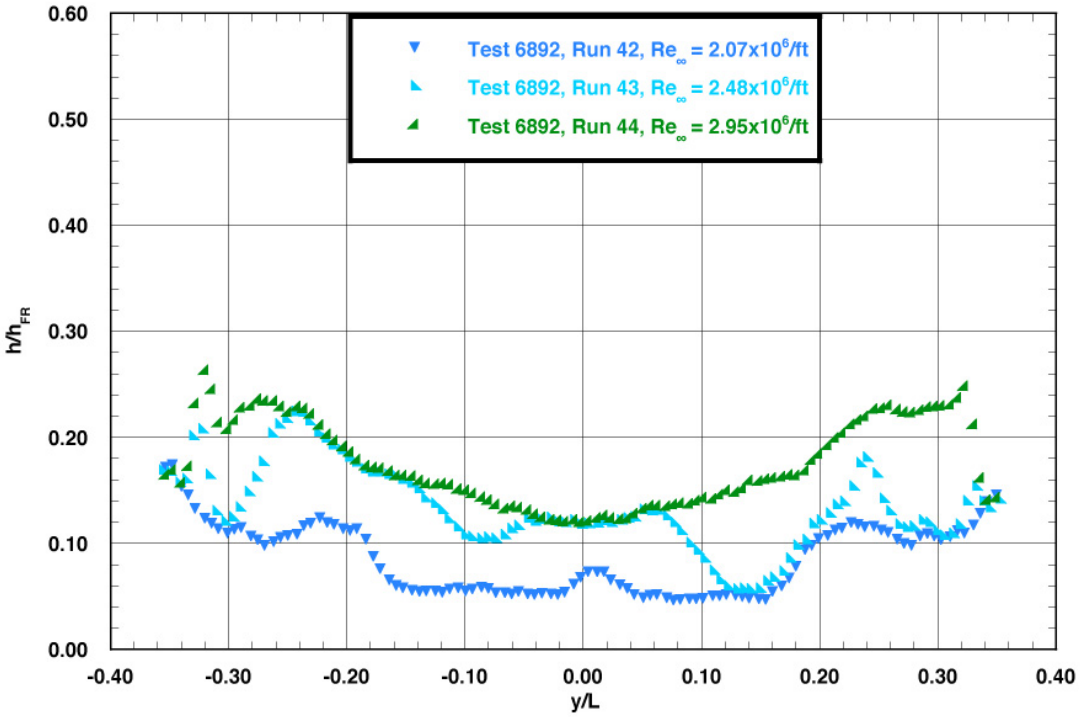

Figure A.6: RTF-BLT-PB spanwise data (x/L = 0.85) in the 20-Inch Mach 6 Air Tunnel at α = 30-deg, x/L = 0.20, k_{CL} = 0.0065-in., $k_{AL\text{-}30\text{-}INV}$ = 0.0065-in.

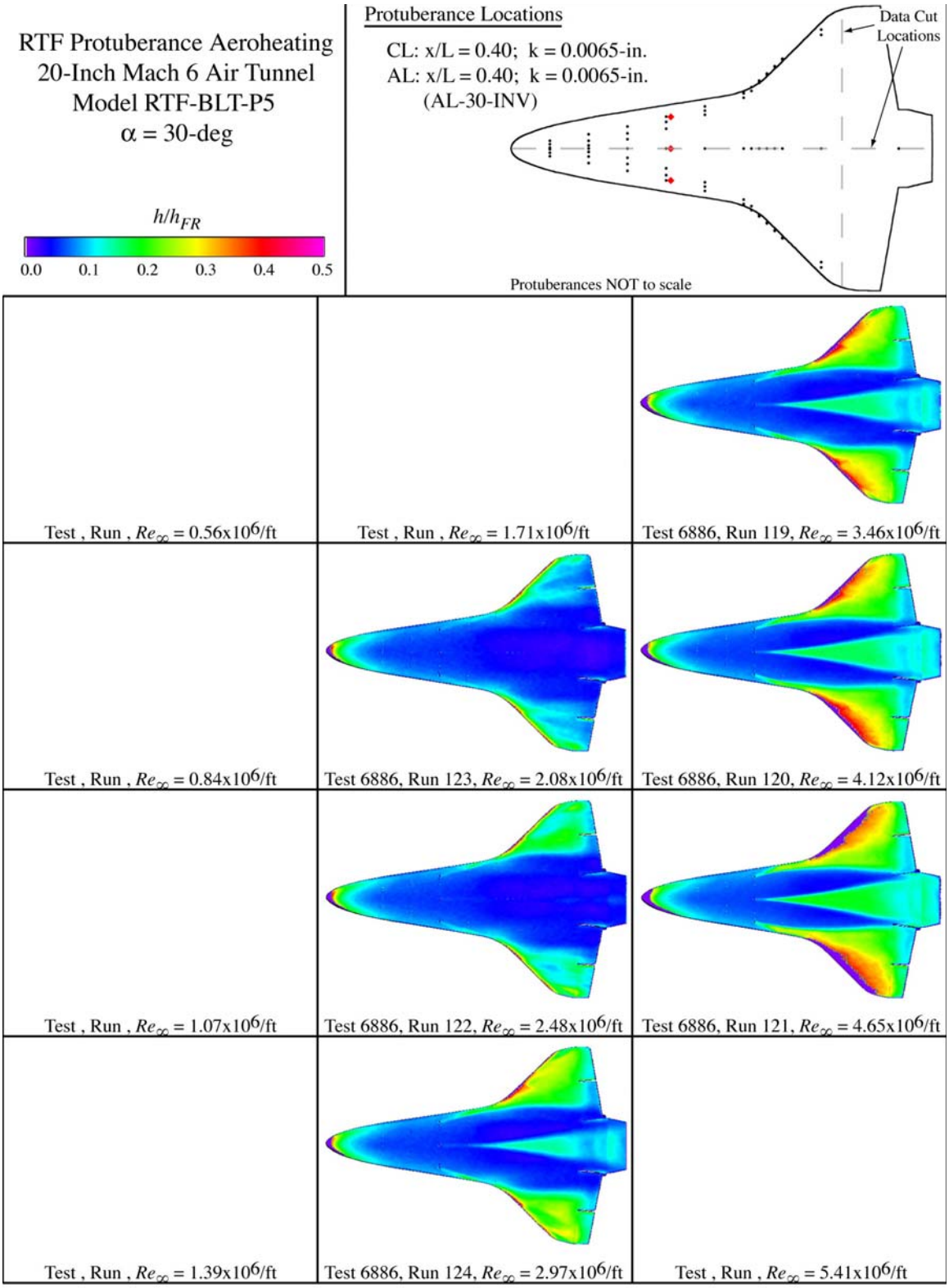

Figure A.7: RTF-BLT-P5 global aeroheating in the 20-Inch Mach 6 Air Tunnel at α = 30-deg, x/L = 0.40, k_{CL} = 0.0065-in., $k_{AL\text{-}30\text{-}INV}$ = 0.0065-in.

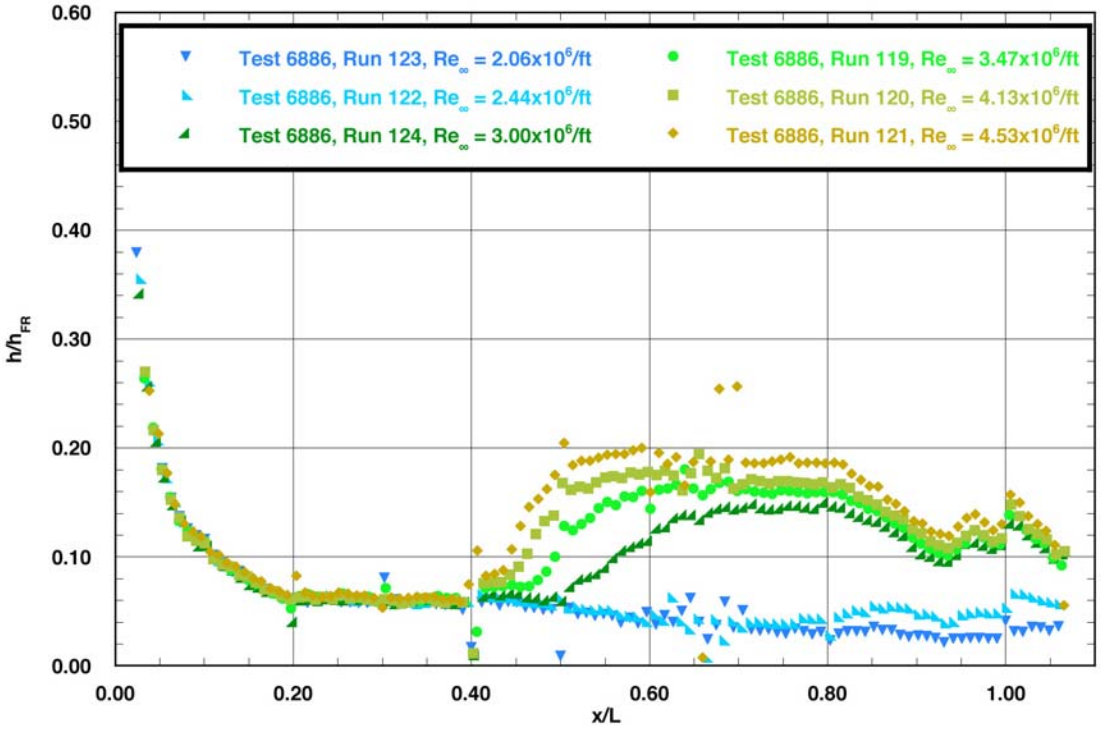

Figure A.8: RTF-BLT-P5 centerline data in the 20-Inch Mach 6 Air Tunnel at α = 30-deg, x/L = 0.40, k_{CL} = 0.0065-in., $k_{AL\text{-}30\text{-}INV}$ = 0.0065-in.

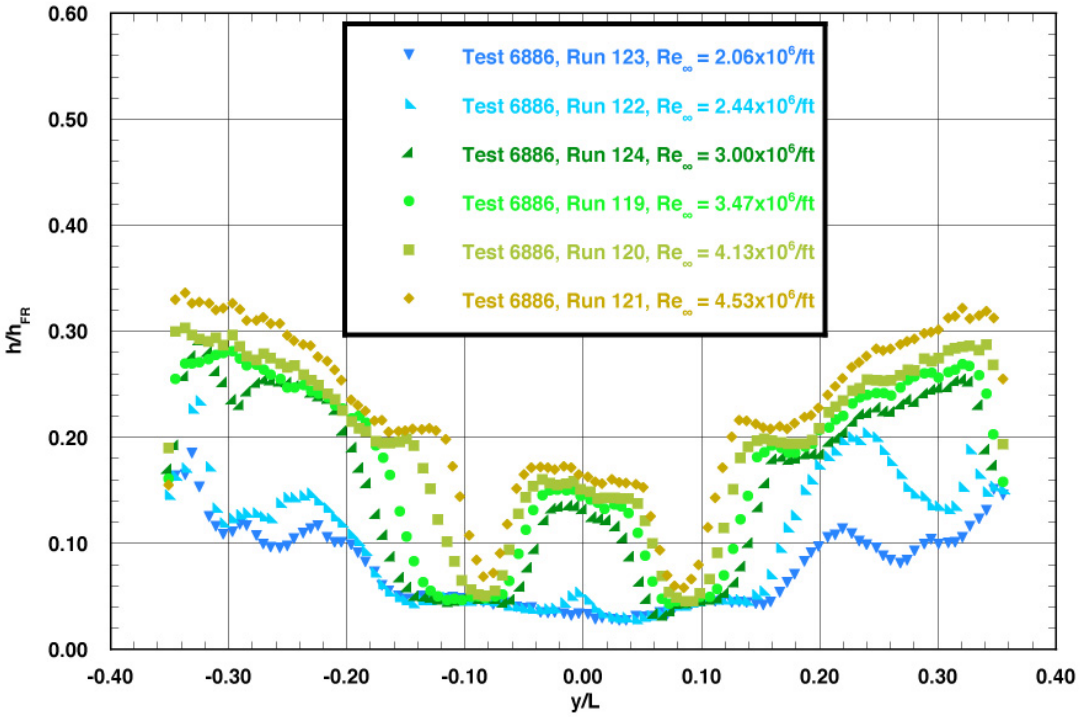

Figure A.9: RTF-BLT-P5 spanwise data (x/L = 0.85) in the 20-Inch Mach 6 Air Tunnel at α = 30-deg, x/L = 0.40, k_{CL} = 0.0065-in., $k_{AL\text{-}30\text{-}INV}$ = 0.0065-in.

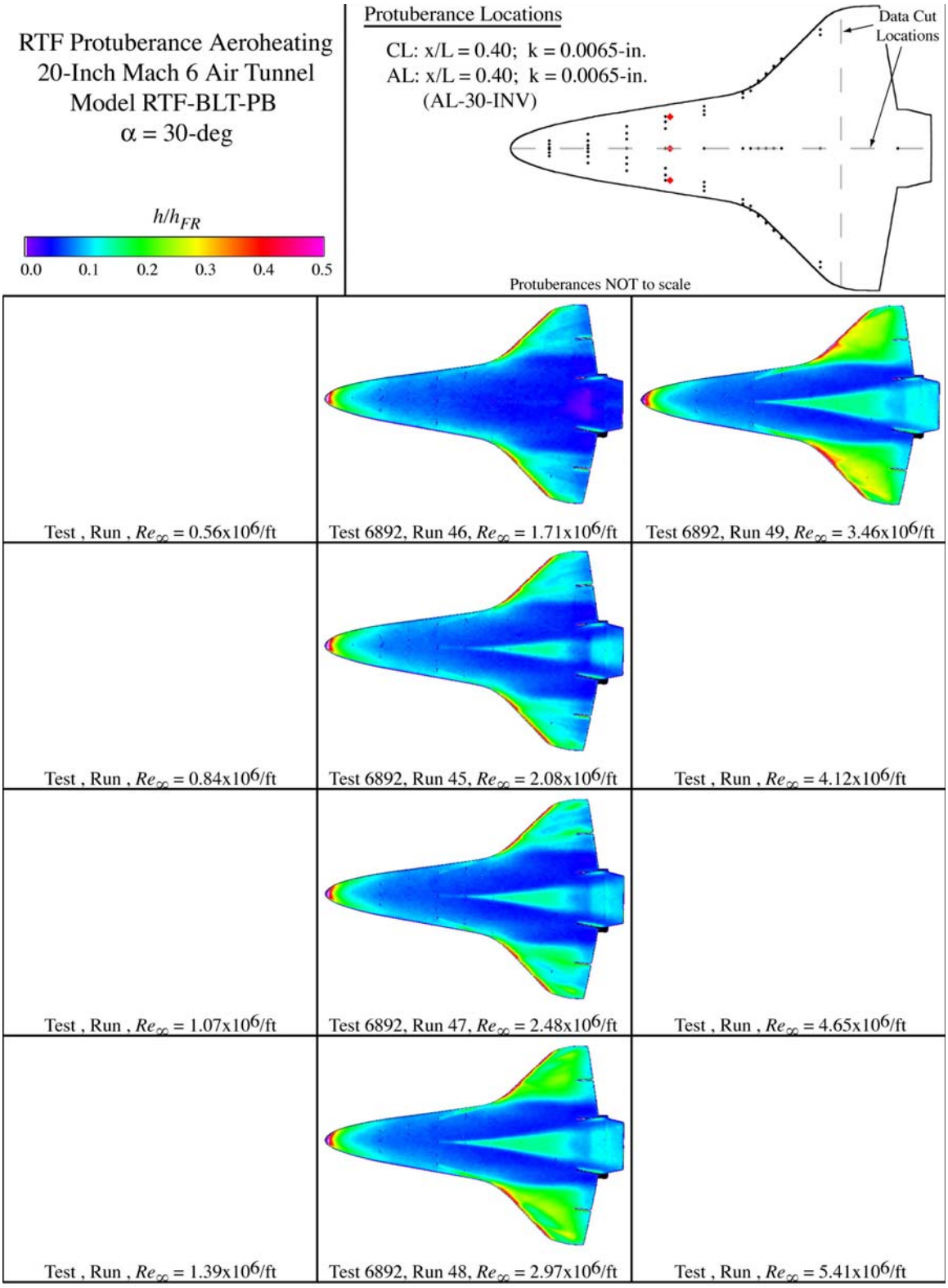

Figure A.10: RTF-BLT-PB global aeroheating in the 20-Inch Mach 6 Air Tunnel at α = 30-deg, x/L = 0.40, k_{CL} = 0.0065-in., $k_{AL\text{-}30\text{-}INV}$ = 0.0065-in.

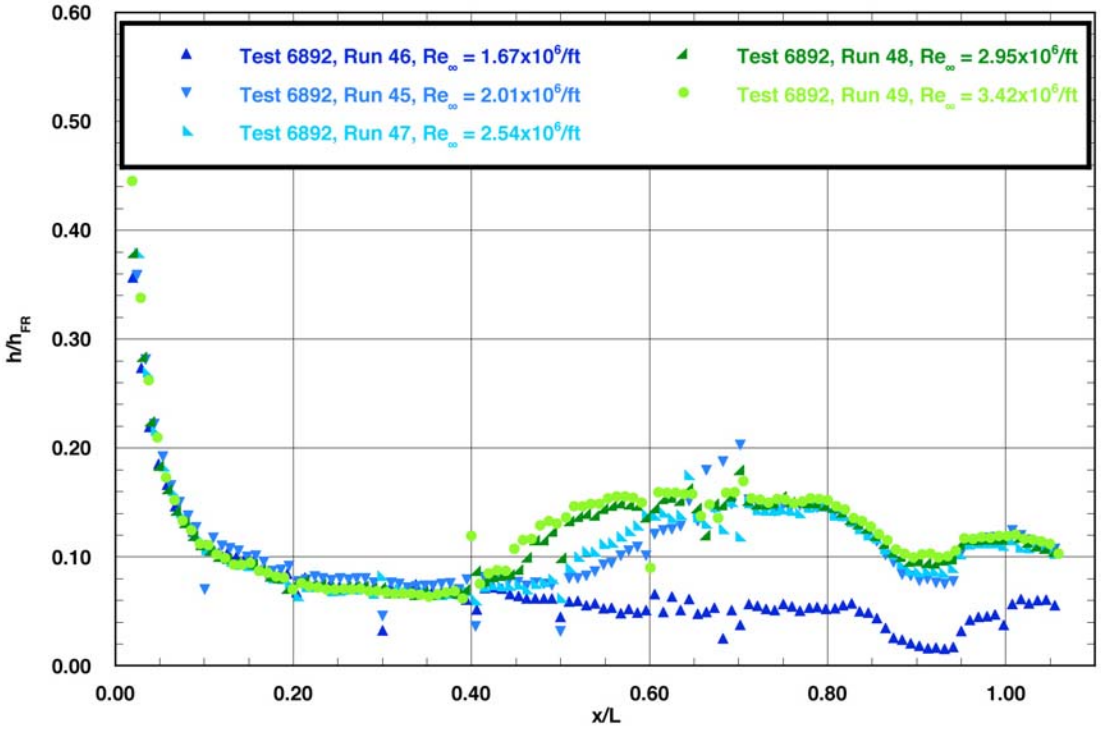

Figure A.11: RTF-BLT-PB centerline data in the 20-Inch Mach 6 Air Tunnel at α = 30-deg, x/L = 0.40, k_{CL} = 0.0065-in., $k_{AL\text{-}30\text{-}INV}$ = 0.0065-in.

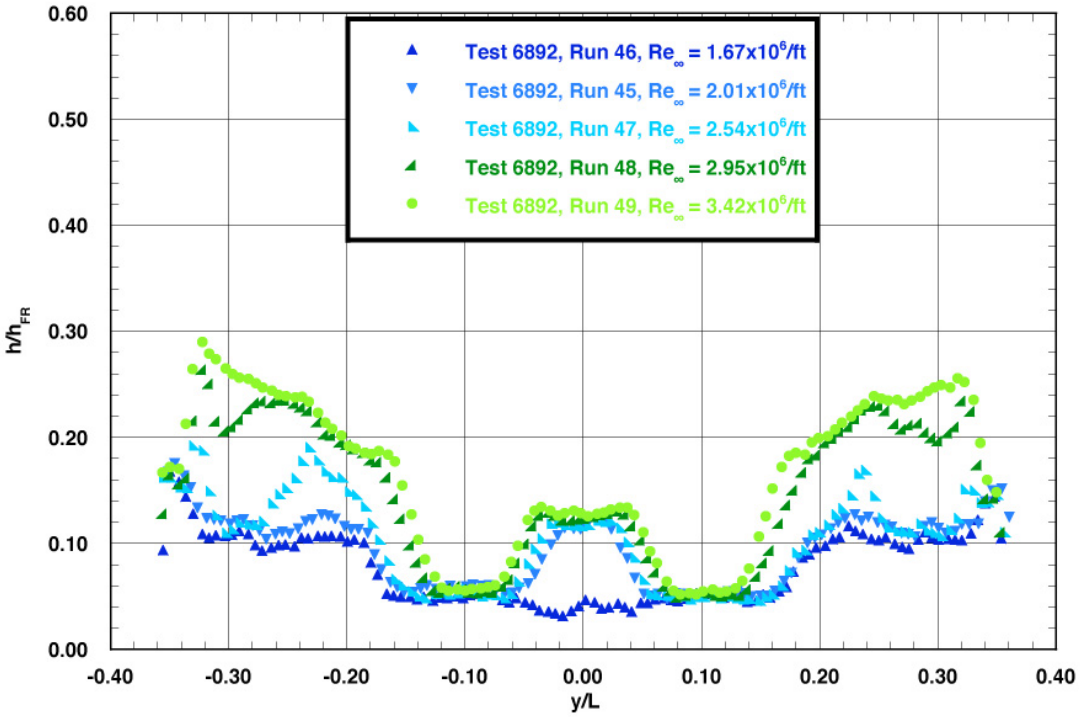

Figure A.12: RTF-BLT-PB spanwise data (x/L = 0.85) in the 20-Inch Mach 6 Air Tunnel at α = 30-deg, x/L = 0.40, k_{CL} = 0.0065-in., $k_{AL\text{-}30\text{-}INV}$ = 0.0065-in.

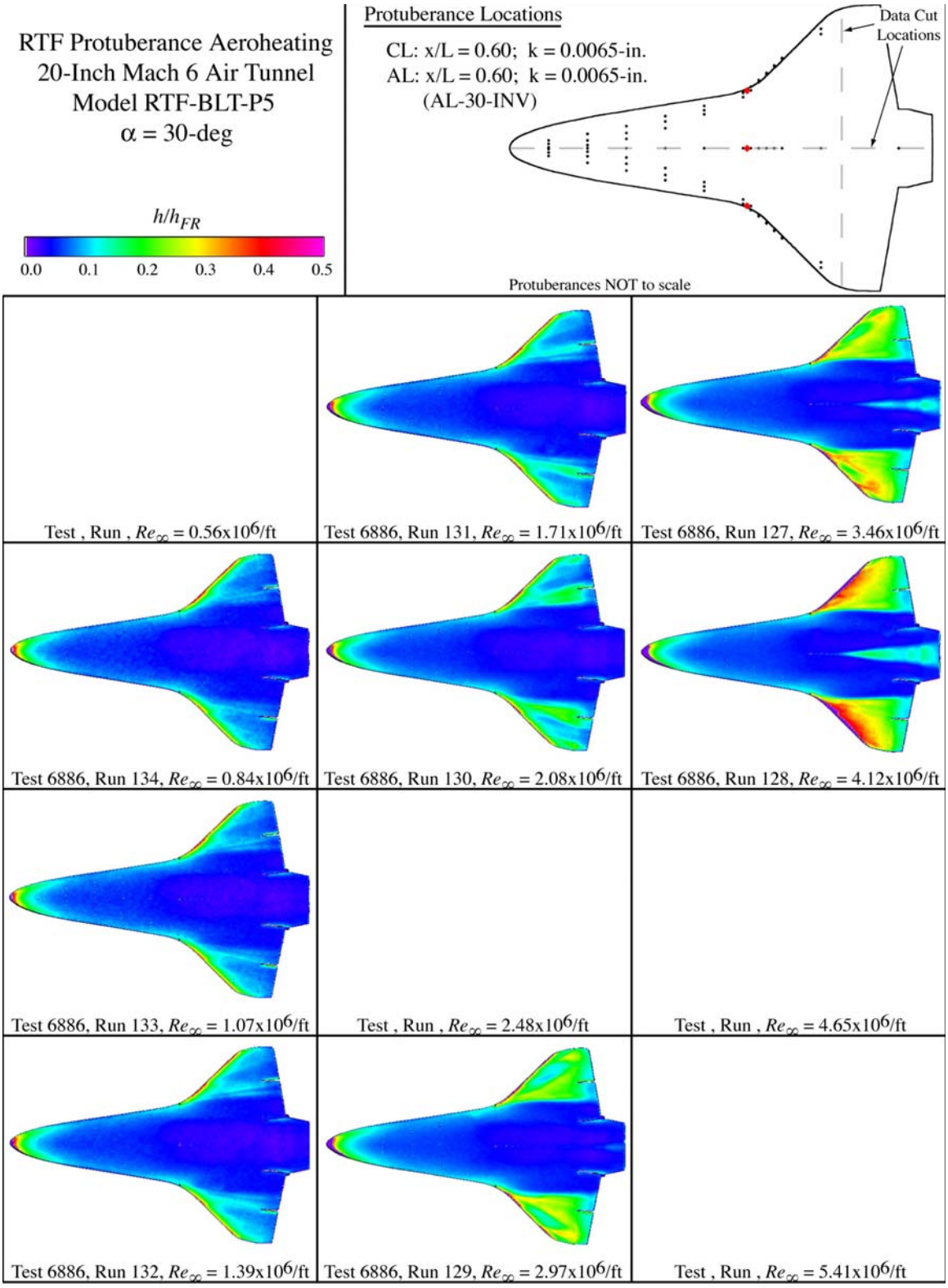

Figure A.13: RTF-BLT-P5 global aeroheating in the 20-Inch Mach 6 Air Tunnel at α = 30-deg, x/L = 0.60, k_{CL} = 0.0065-in., $k_{AL\text{-}30\text{-}INV}$ = 0.0065-in.

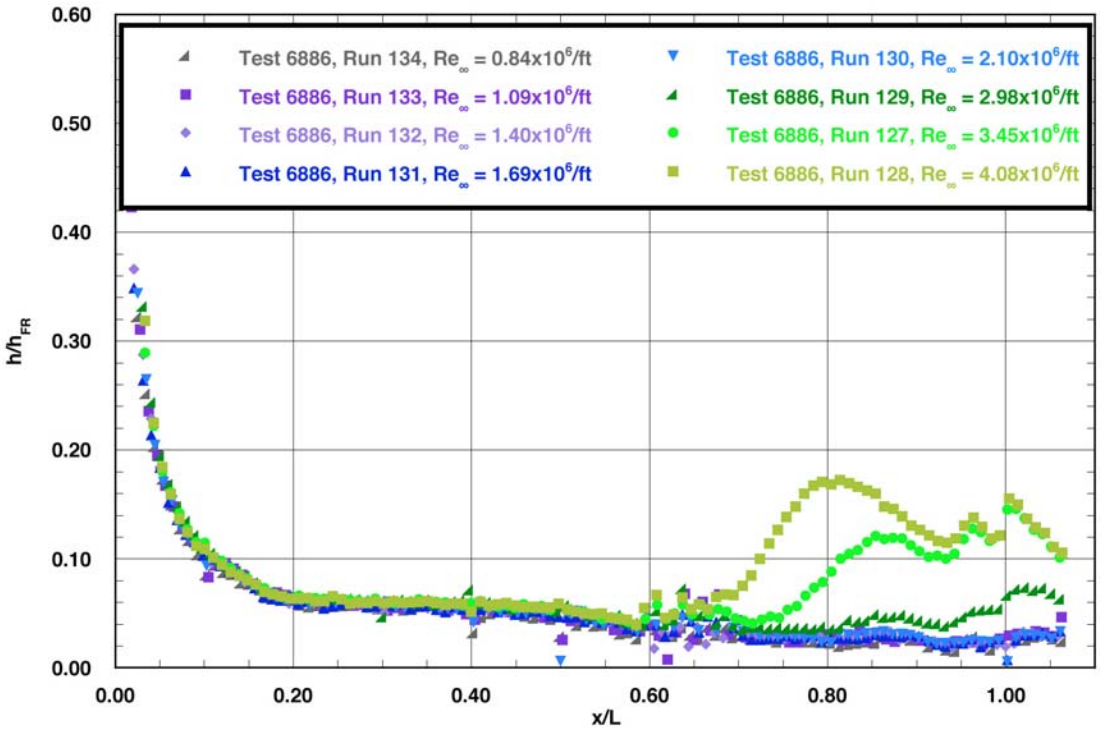

Figure A.14: RTF-BLT-P5 centerline data in the 20-Inch Mach 6 Air Tunnel at α = 30-deg, x/L = 0.60, k_{CL} = 0.0065-in., $k_{AL\text{-}30\text{-}INV}$ = 0.0065-in.

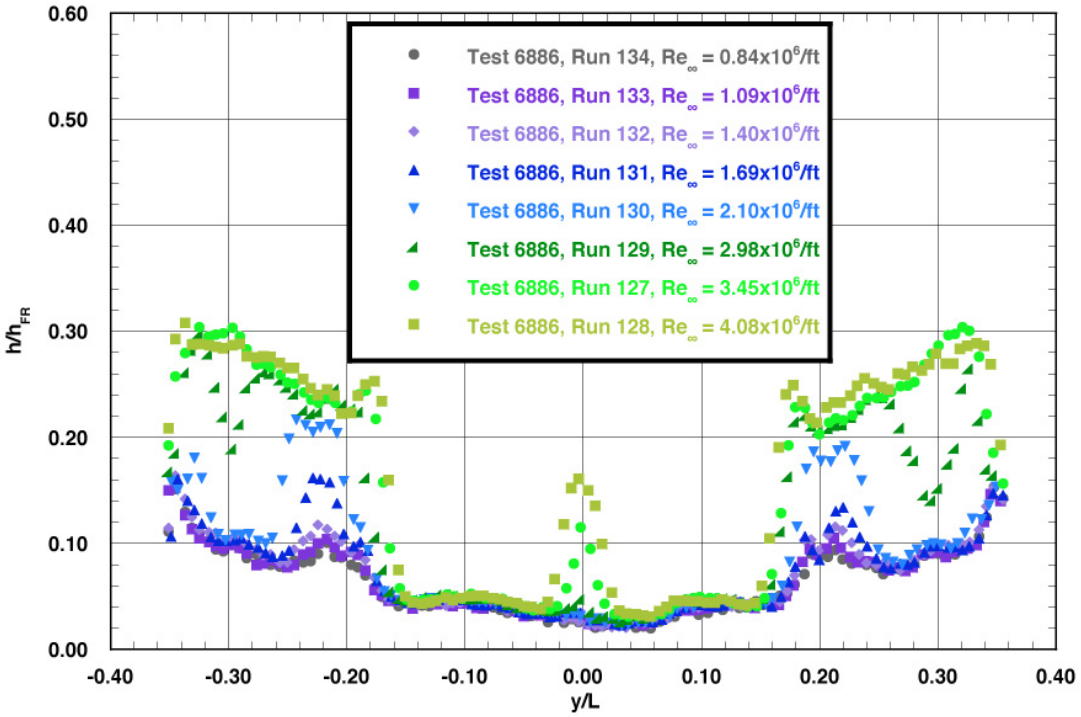

Figure A.15: RTF-BLT-P5 spanwise data (x/L = 0.85) in the 20-Inch Mach 6 Air Tunnel at α = 30-deg, x/L = 0.60, k_{CL} = 0.0065-in., $k_{AL\text{-}30\text{-}INV}$ = 0.0065-in.

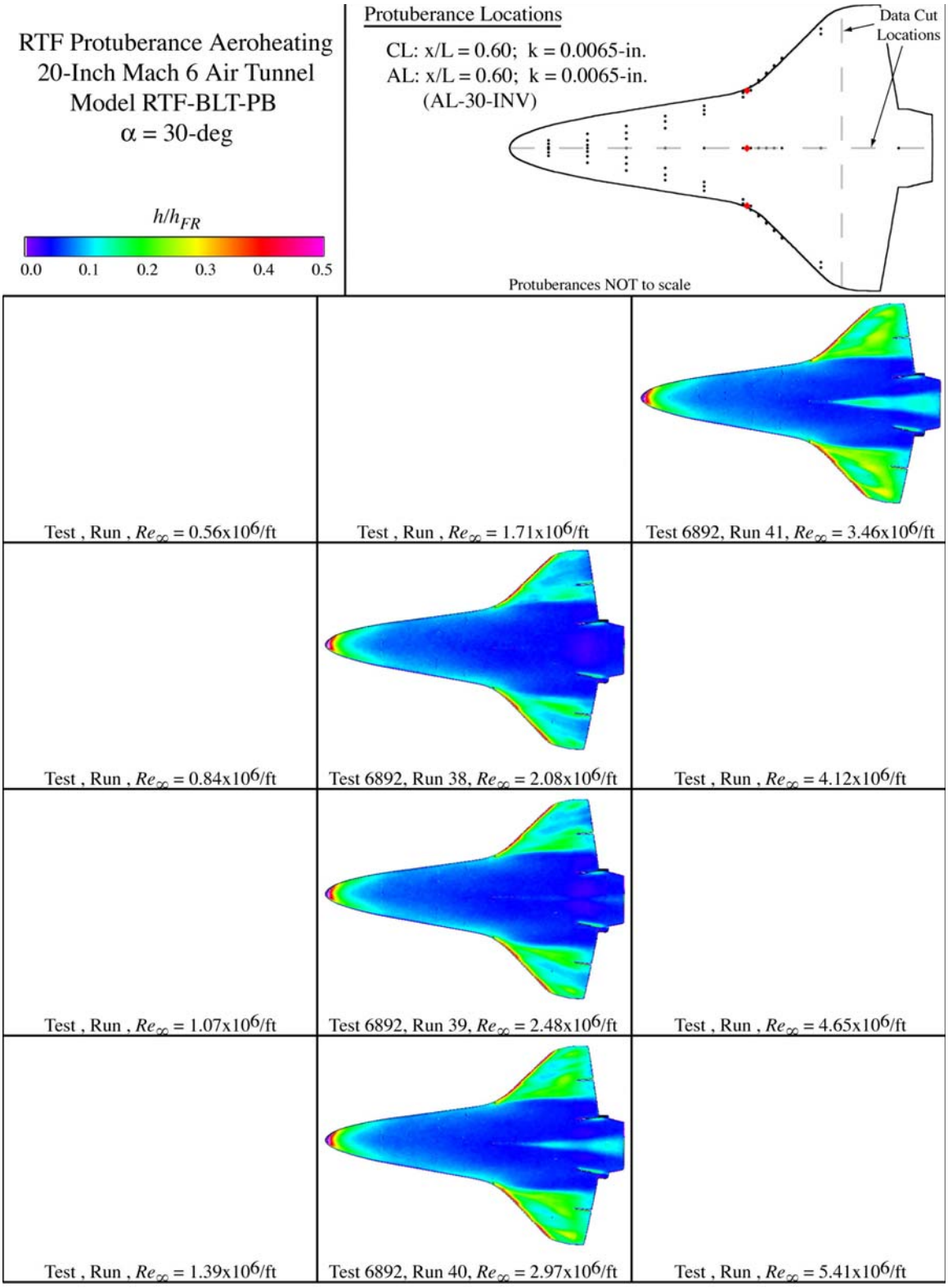

Figure A.16: RTF-BLT-PB global aeroheating in the 20-Inch Mach 6 Air Tunnel at α = 30-deg, x/L = 0.60, k_{CL} = 0.0065-in., $k_{AL\text{-}30\text{-}INV}$ = 0.0065-in.

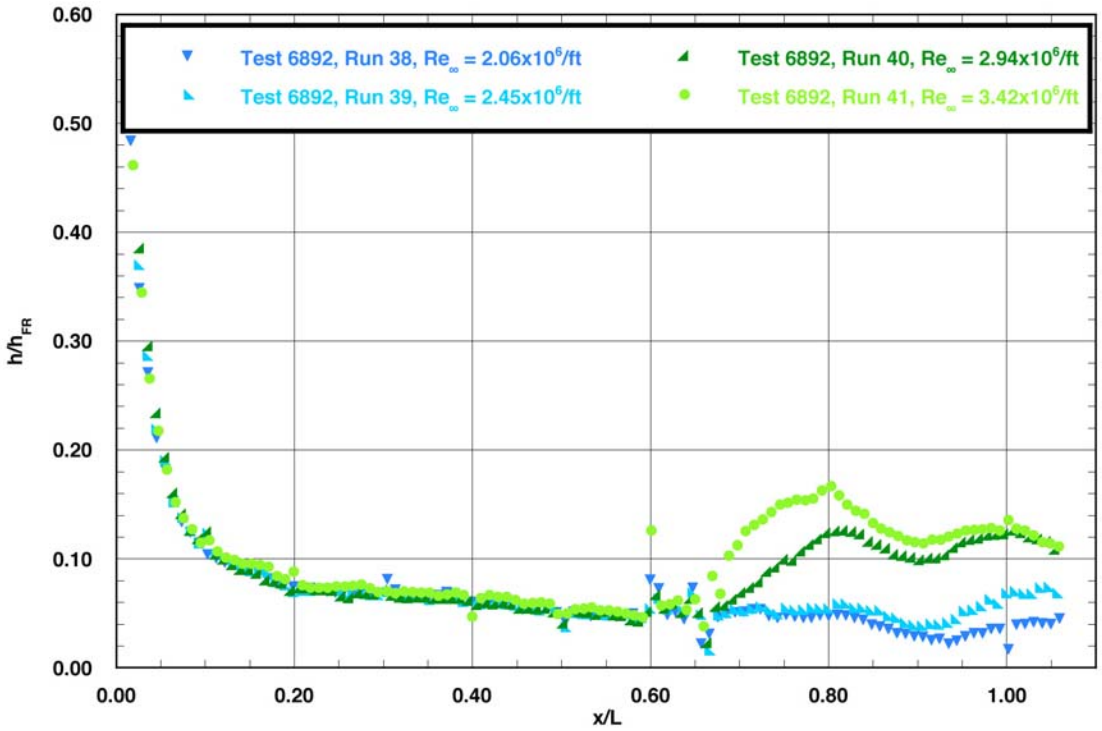

Figure A.17: RTF-BLT-PB centerline data in the 20-Inch Mach 6 Air Tunnel at α = 30-deg, x/L = 0.60, k_{CL} = 0.0065-in., $k_{AL\text{-}30\text{-}INV}$ = 0.0065-in.

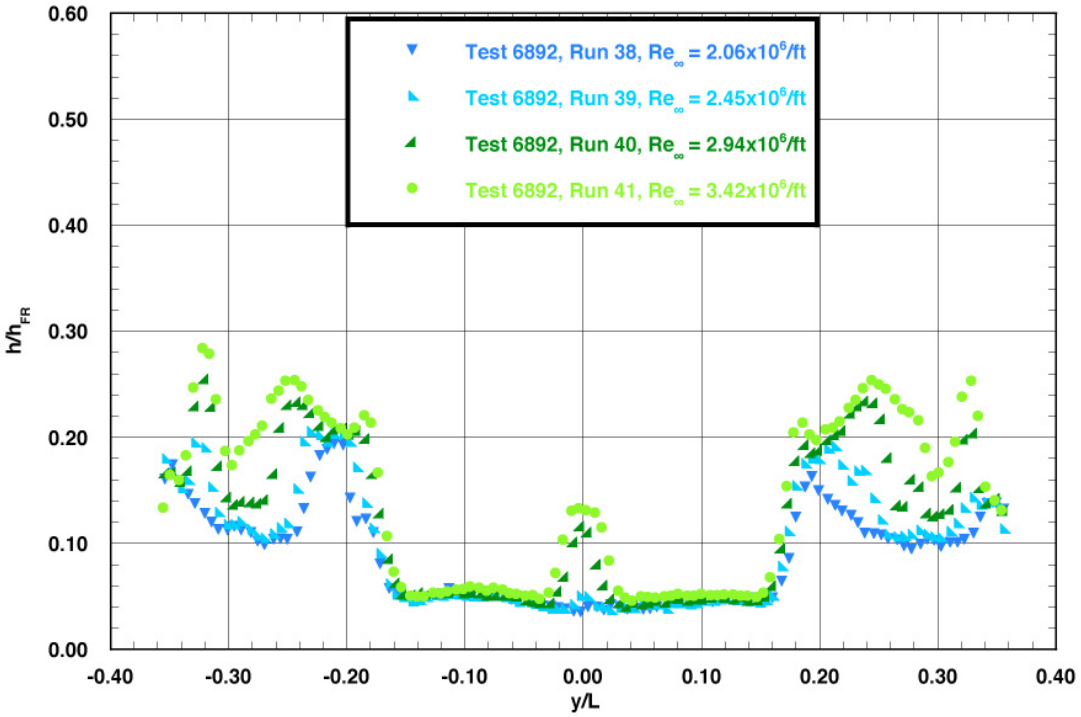

Figure A.18: RTF-BLT-PB spanwise data (x/L = 0.85) in the 20-Inch Mach 6 Air Tunnel at α = 30-deg, x/L = 0.60, k_{CL} = 0.0065-in., $k_{AL\text{-}30\text{-}INV}$ = 0.0065-in.

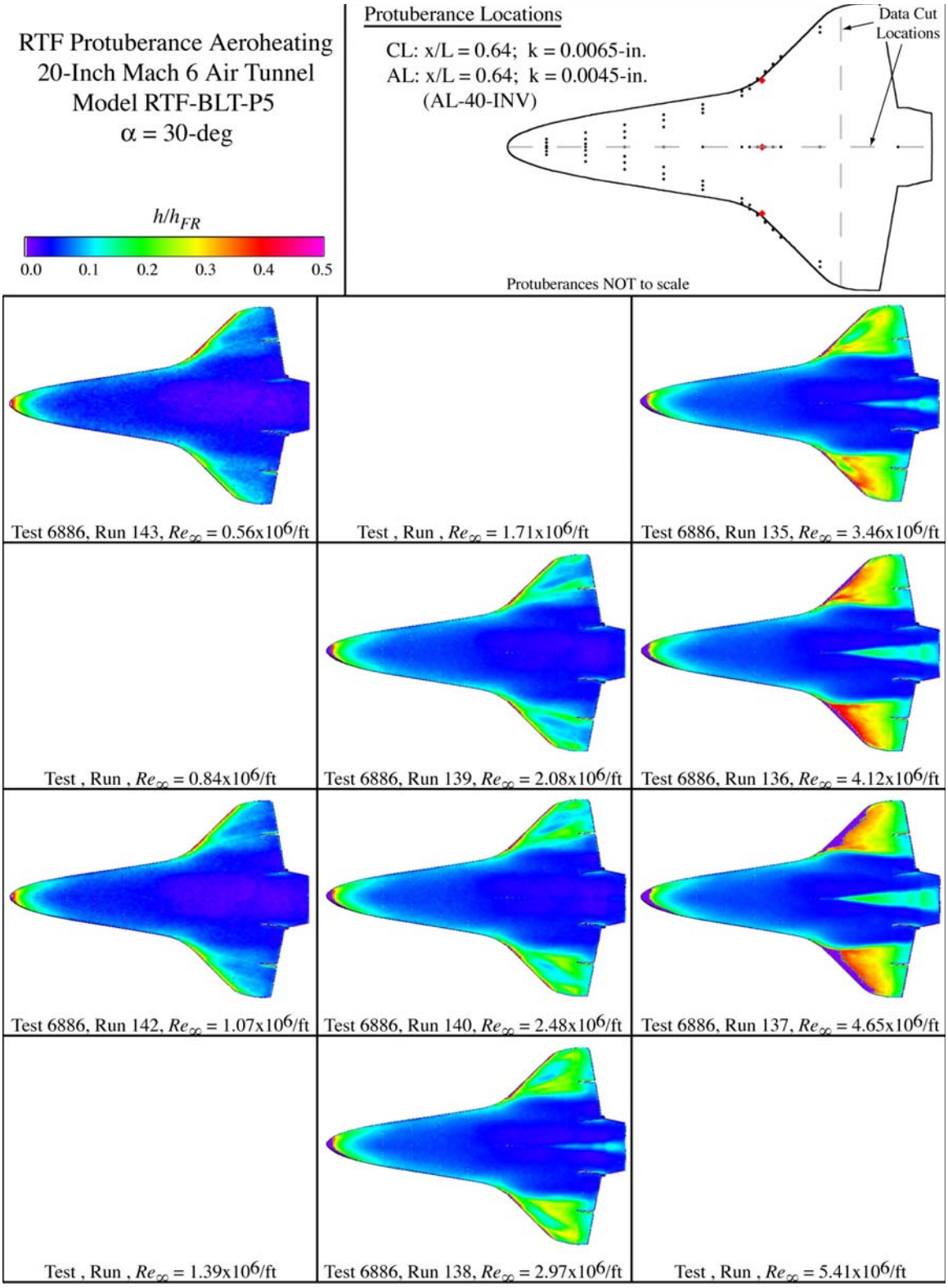

Figure A.19: RTF-BLT-P5 global aeroheating in the 20-Inch Mach 6 Air Tunnel at α = 30-deg, x/L = 0.64, k_{CL} = 0.0065-in., $k_{AL\text{-}40\text{-}INV}$ = 0.0045-in.

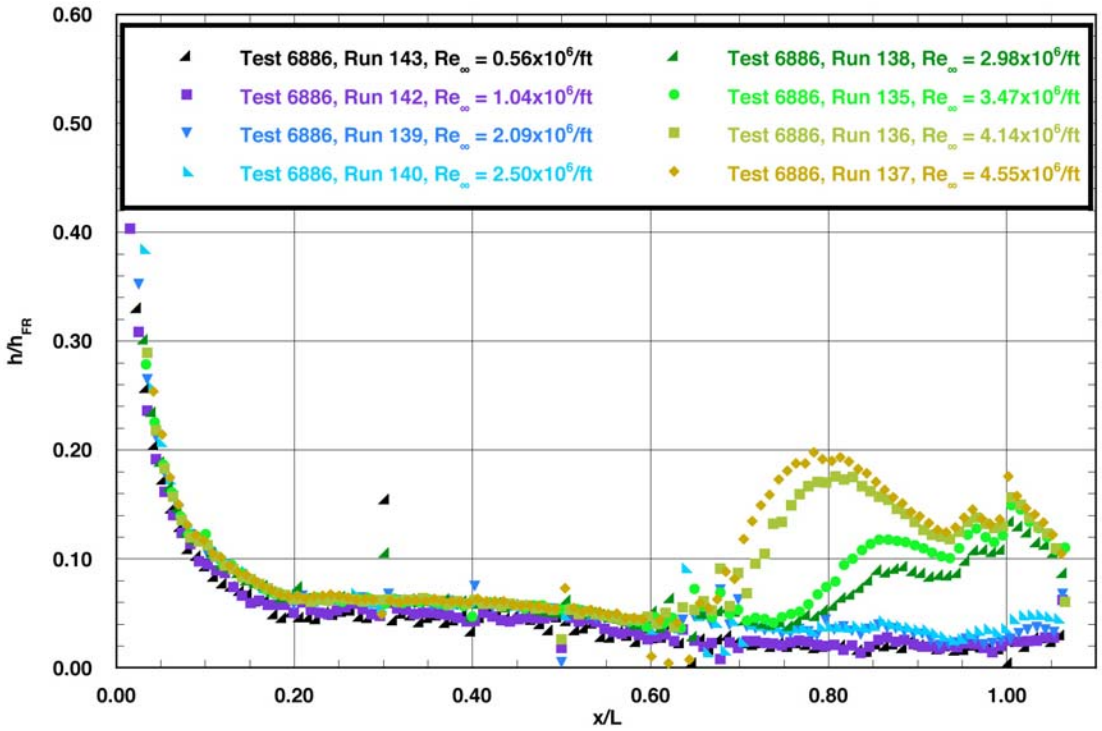

Figure A.20: RTF-BLT-P5 centerline data in the 20-Inch Mach 6 Air Tunnel at α = 30-deg, x/L = 0.64, k_{CL} = 0.0065-in., $k_{AL\text{-}40\text{-}INV}$ = 0.0045-in.

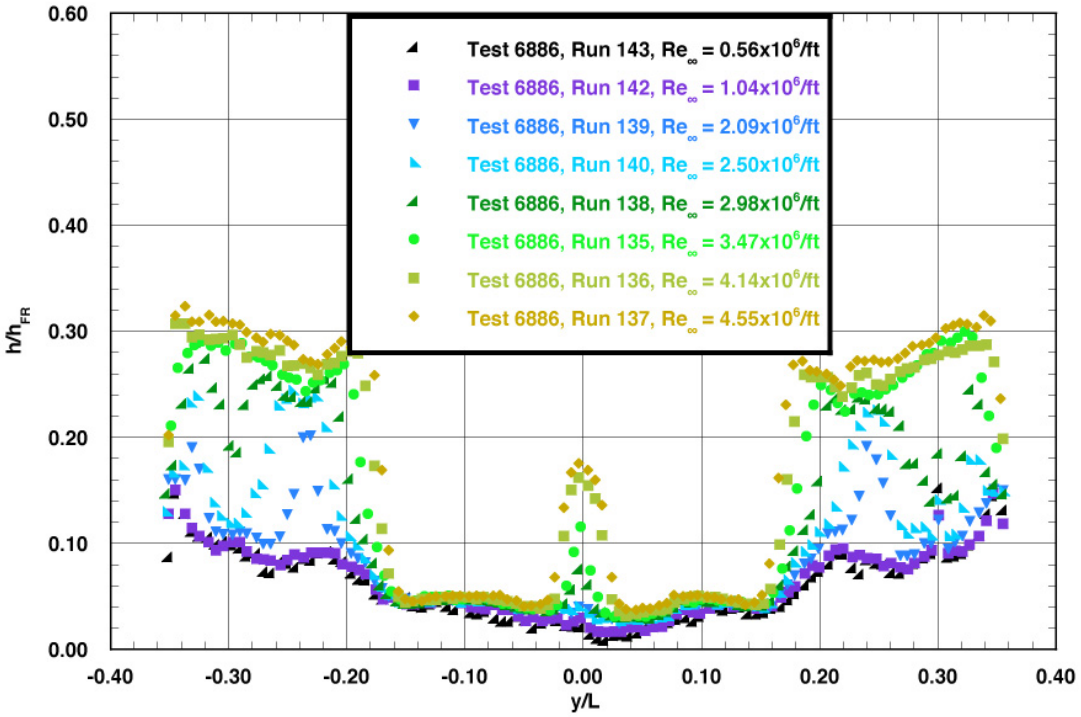

Figure A.21: RTF-BLT-P5 spanwise data (x/L = 0.85) in the 20-Inch Mach 6 Air Tunnel at α = 30-deg, x/L = 0.64, k_{CL} = 0.0065-in., $k_{AL\text{-}40\text{-}INV}$ = 0.0045-in.

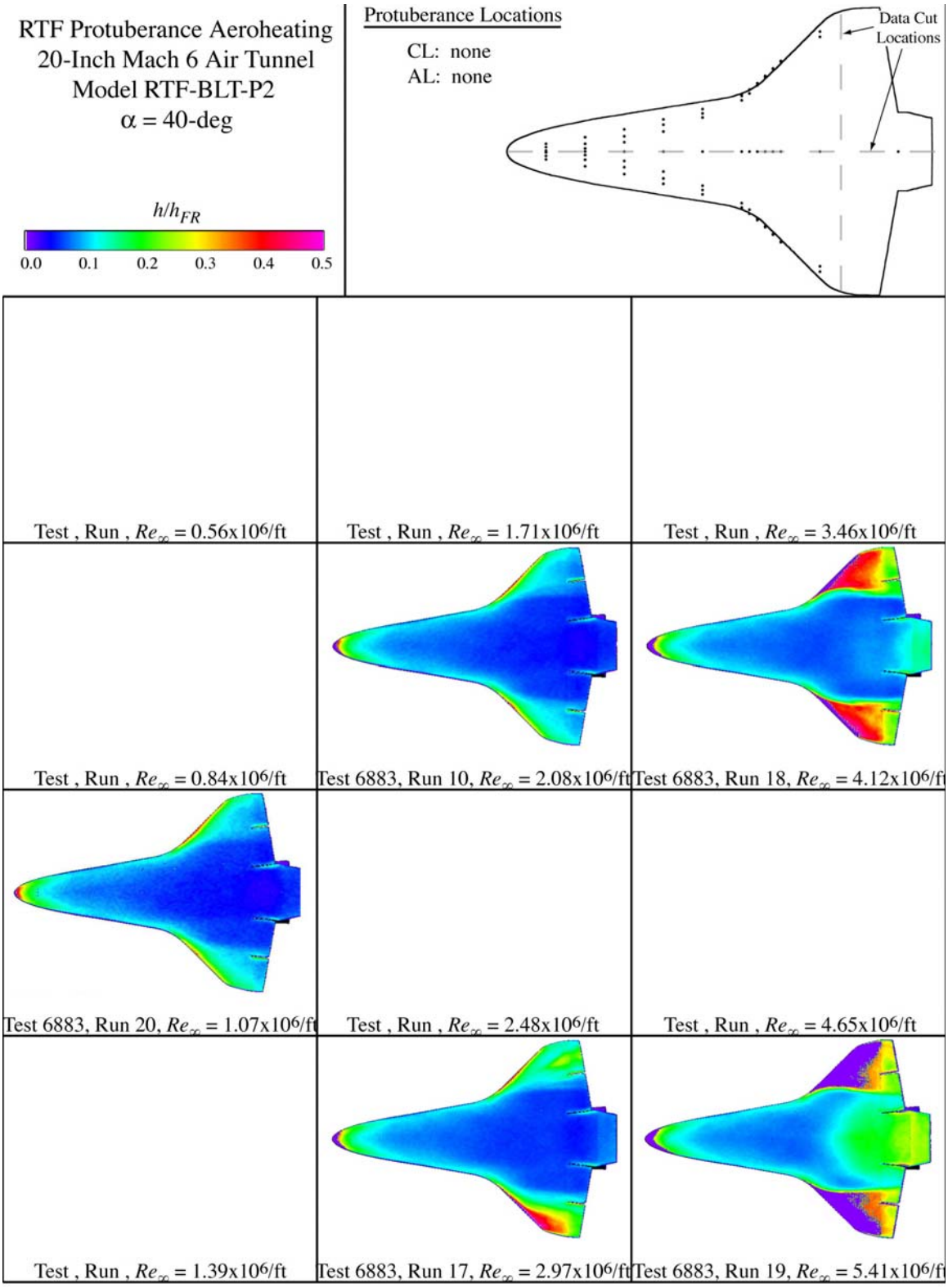

Figure A.22: RTF-BLT-P2 global aeroheating in the 20-Inch Mach 6 Air Tunnel at α = 40-deg, baseline.

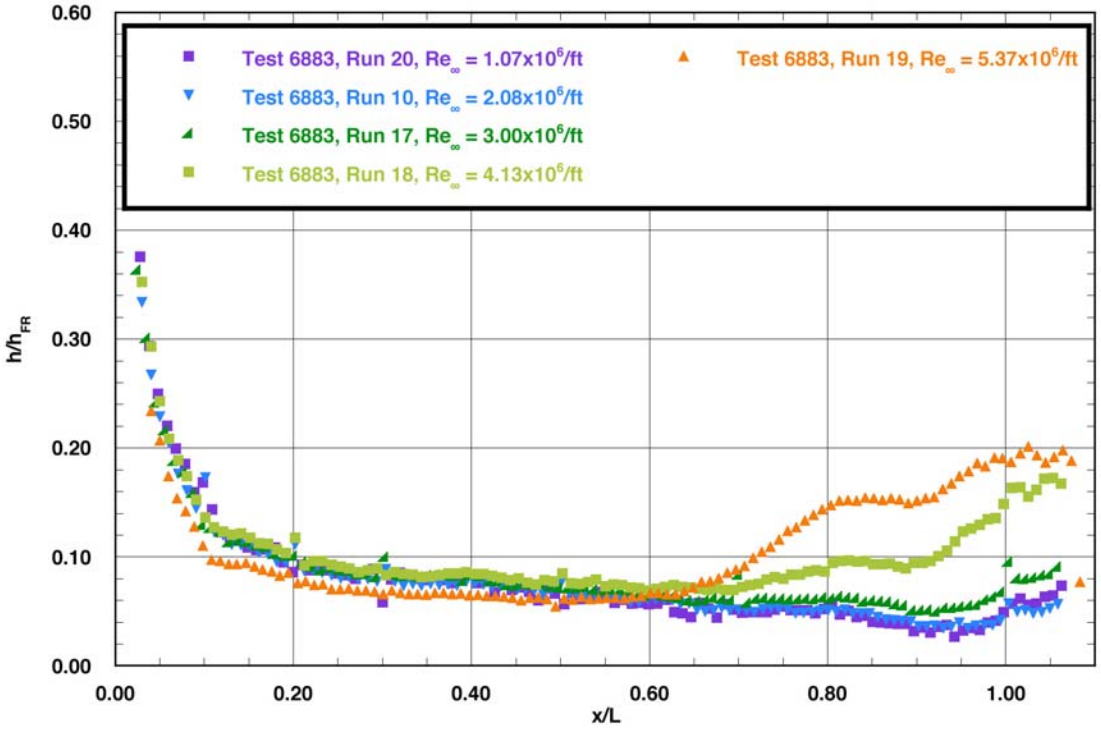

Figure A.23: RTF-BLT-P2 centerline data in the 20-Inch Mach 6 Air Tunnel at α = 40-deg, baseline.

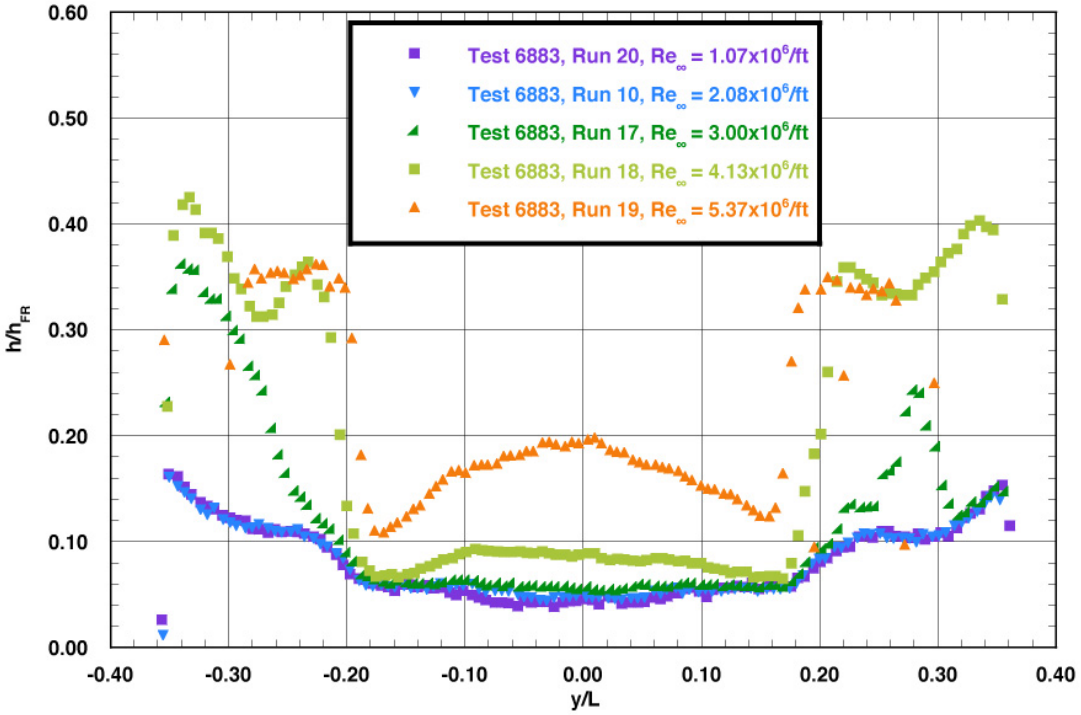

Figure A.24: RTF-BLT-P2 spanwise data (*x/L* = 0.85) in the 20-Inch Mach 6 Air Tunnel at α = 40-deg, baseline.

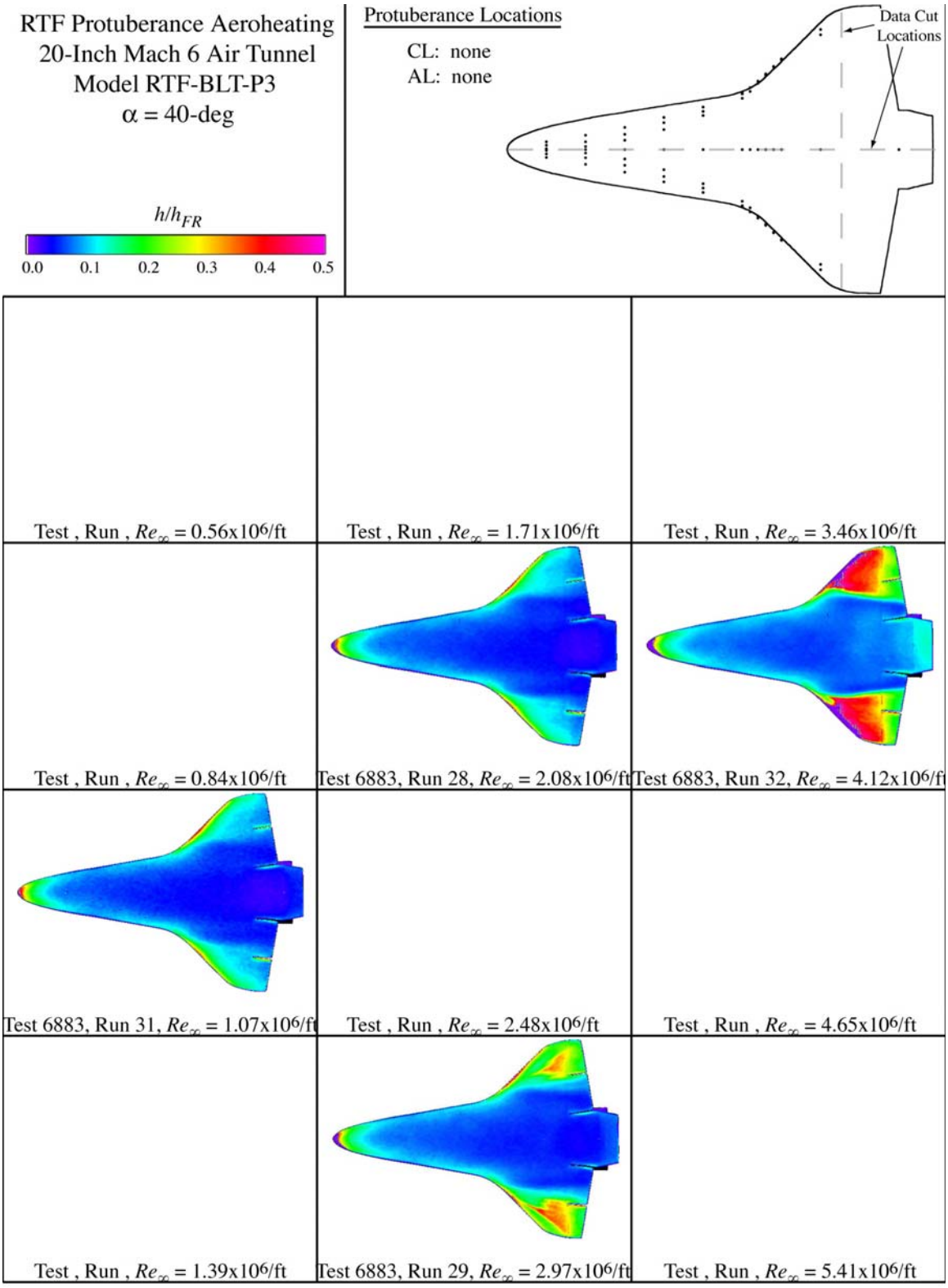

Figure A.25: RTF-BLT-P3 global aeroheating in the 20-Inch Mach 6 Air Tunnel at α = 40-deg, baseline.

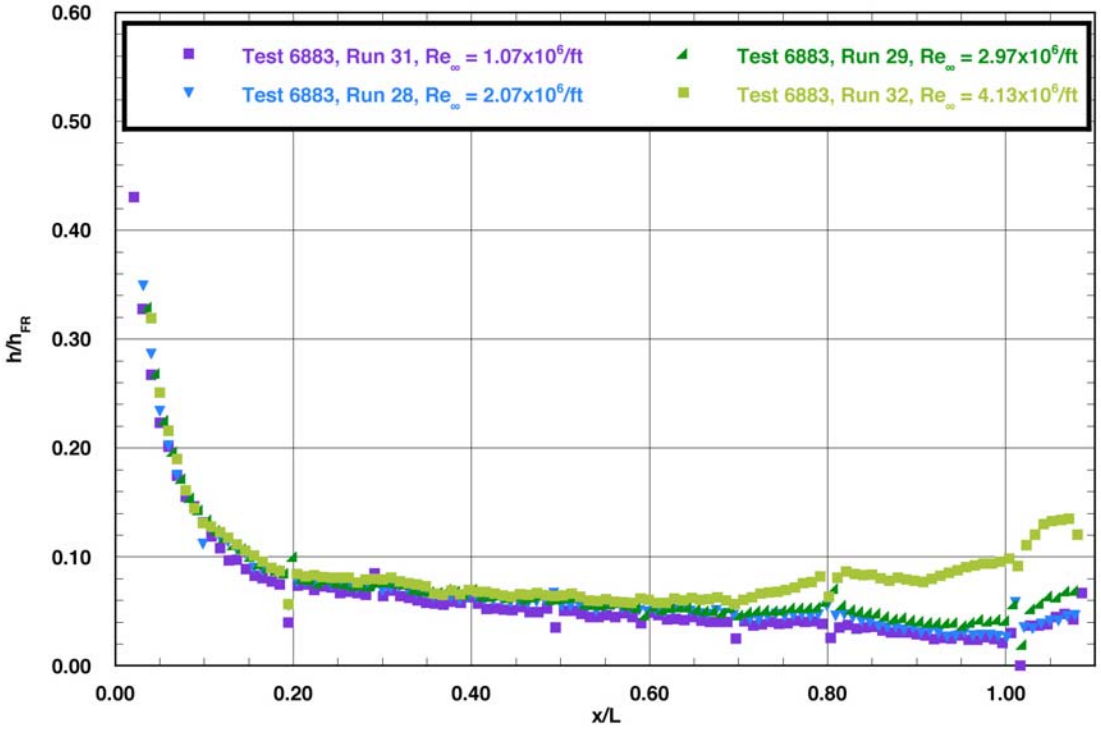

Figure A.26: RTF-BLT-P3 centerline data in the 20-Inch Mach 6 Air Tunnel at α = 40-deg, baseline.

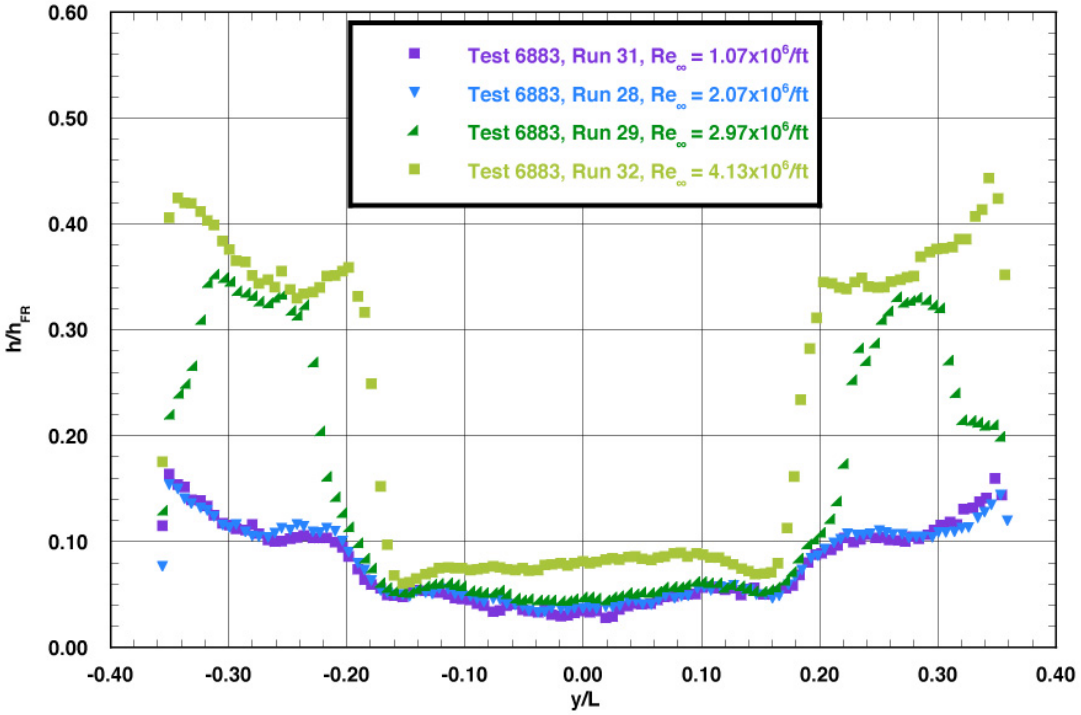

Figure A.27: RTF-BLT-P3 spanwise data (*x/L* = 0.85) in the 20-Inch Mach 6 Air Tunnel at α = 40-deg, baseline.

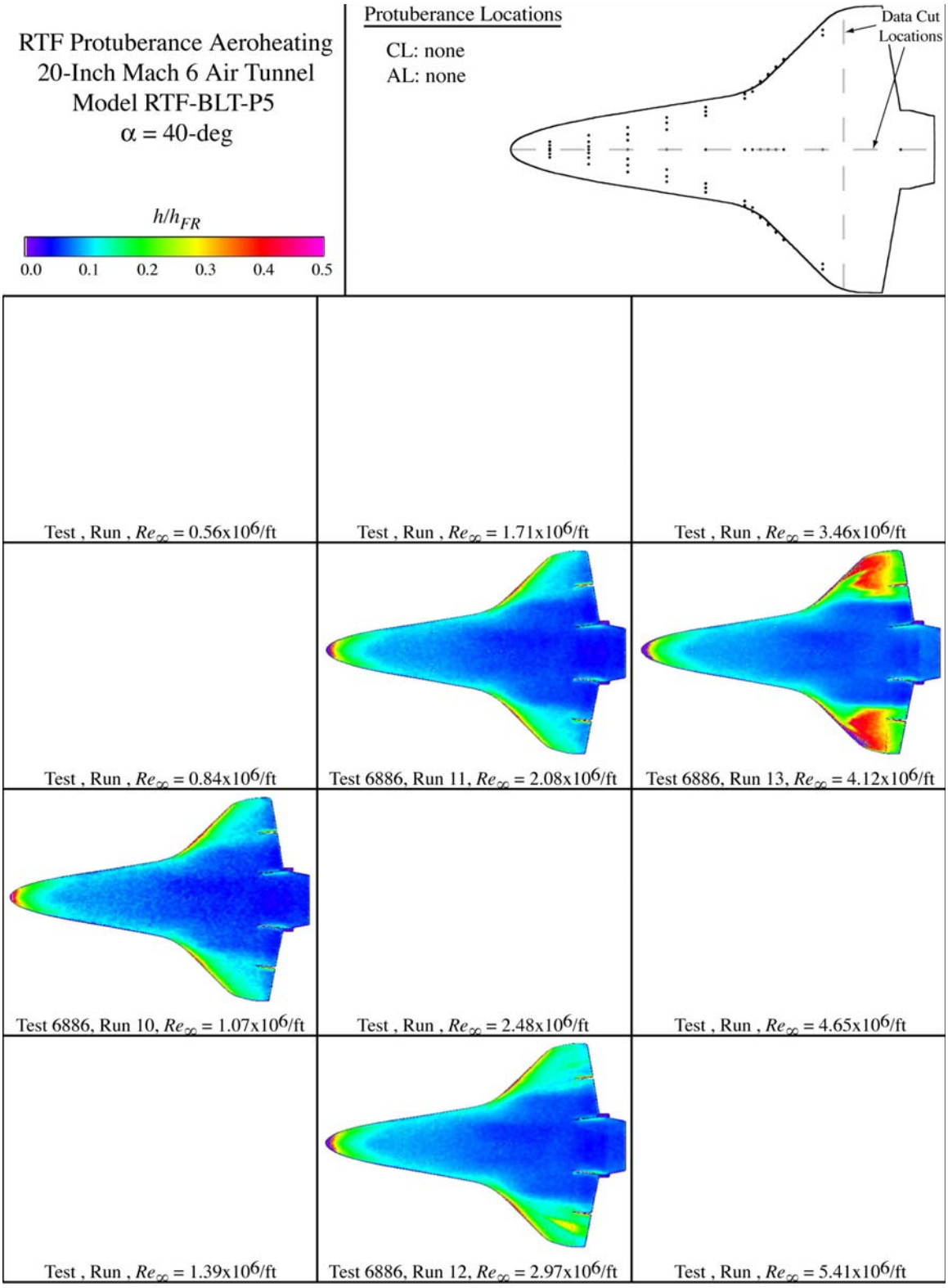

Figure A.28: RTF-BLT-P5 global aeroheating in the 20-Inch Mach 6 Air Tunnel at α = 40-deg, baseline.

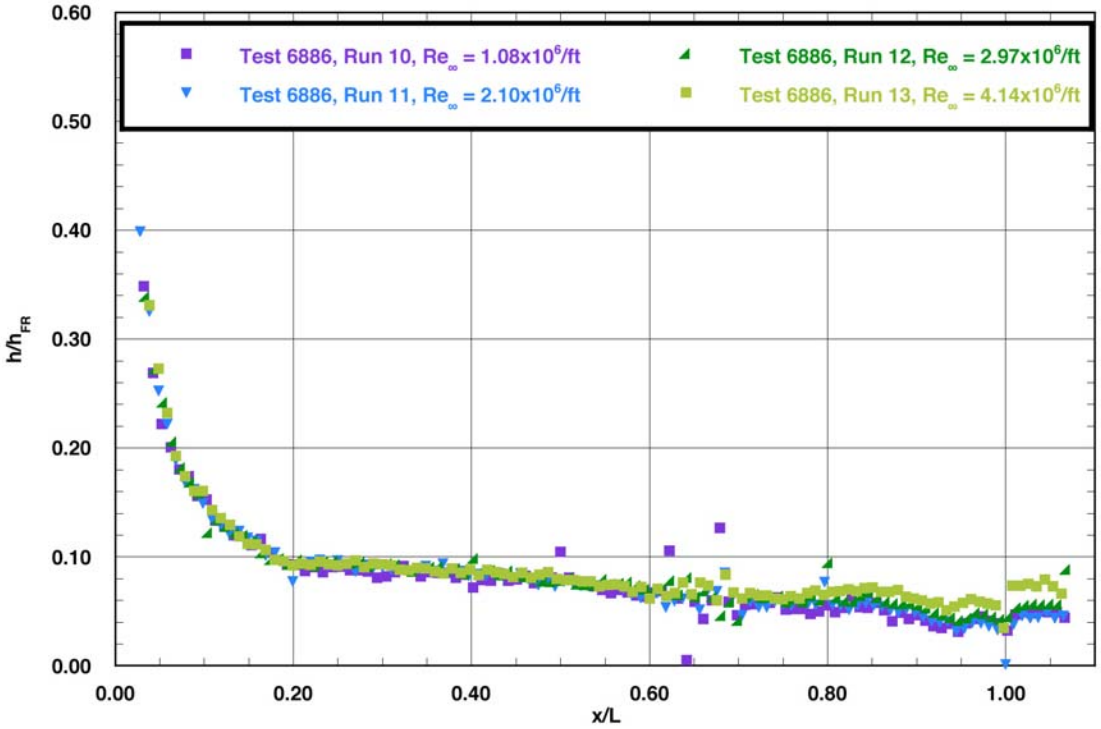

Figure A.29: RTF-BLT-P5 centerline data in the 20-Inch Mach 6 Air Tunnel at α = 40-deg, baseline.

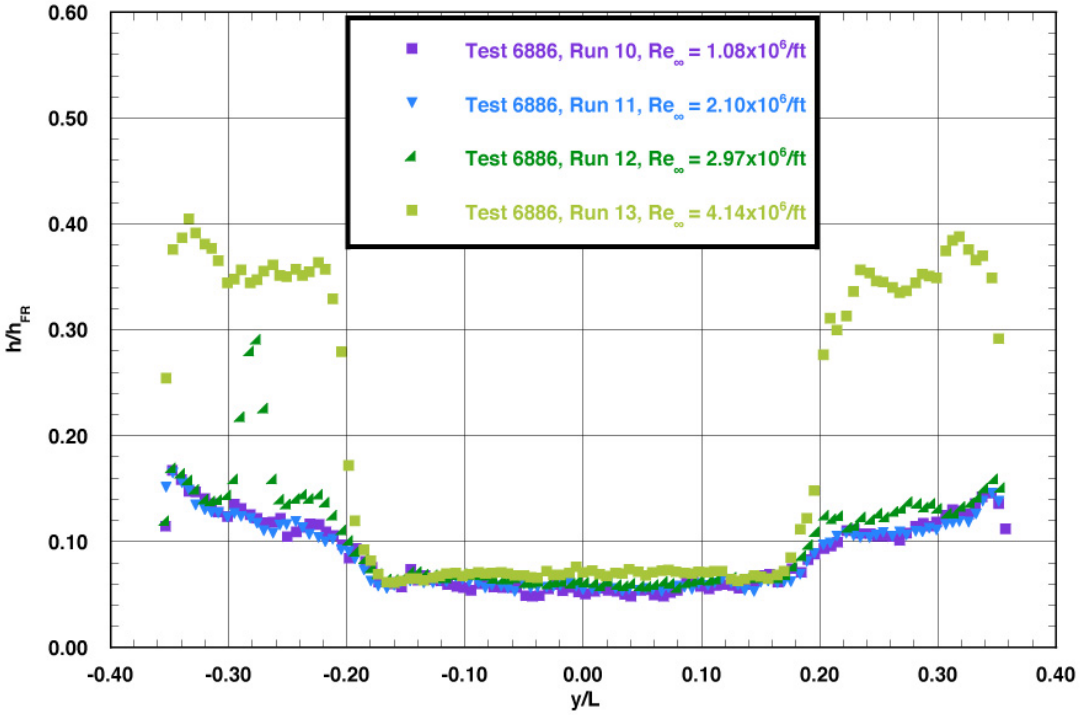

Figure A.30: RTF-BLT-P5 spanwise data (*x/L* = 0.85) in the 20-Inch Mach 6 Air Tunnel at α = 40-deg, baseline.

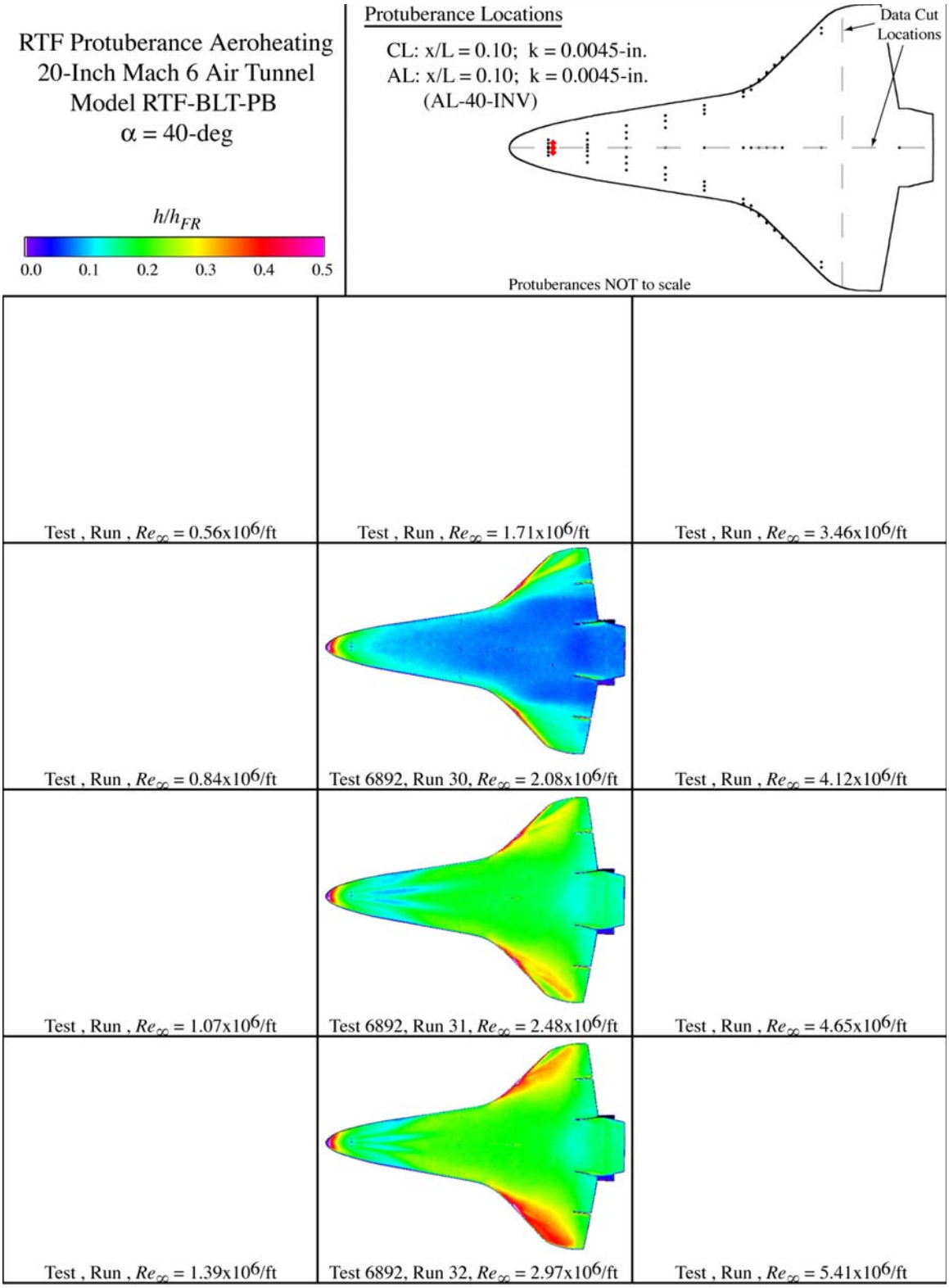

Figure A.31: RTF-BLT-PB global aeroheating in the 20-Inch Mach 6 Air Tunnel at α = 40-deg, x/L = 0.10, k_{CL} = 0.0045-in., $k_{AL\text{-}40\text{-}VIS}$ = 0.0045-in.

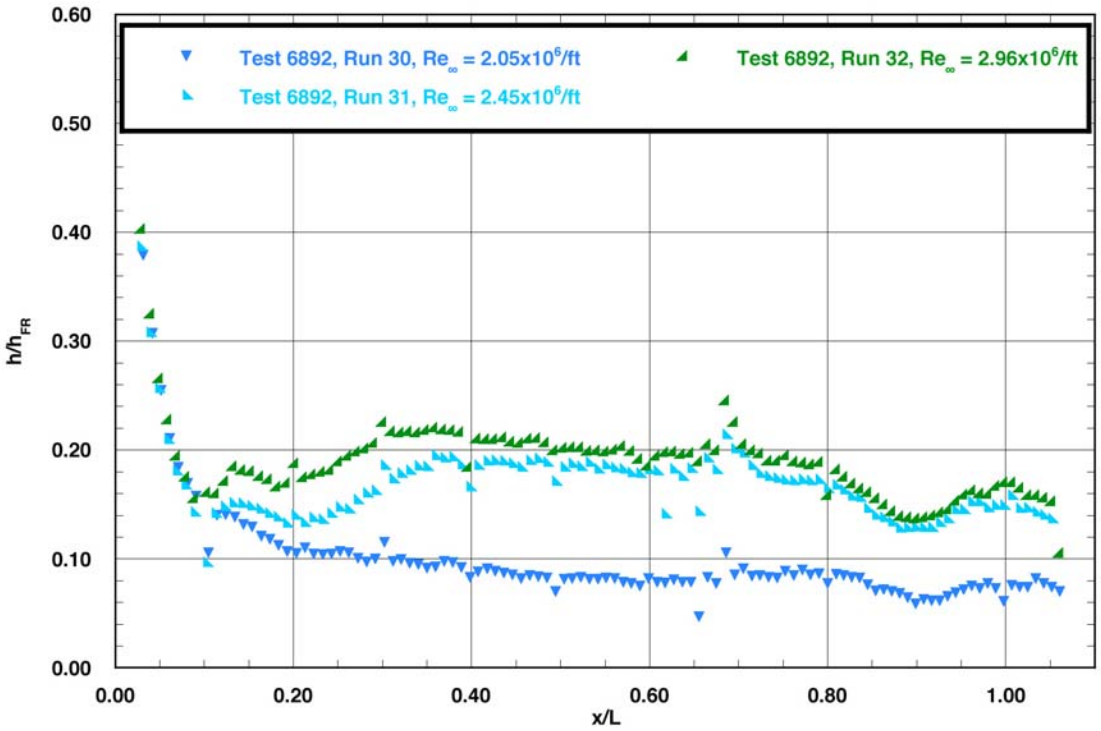

Figure A.32: RTF-BLT-PB centerline data in the 20-Inch Mach 6 Air Tunnel at α = 40-deg, x/L = 0.10, k_{CL} = 0.0045-in., $k_{AL\text{-}40\text{-}VIS}$ = 0.0045-in.

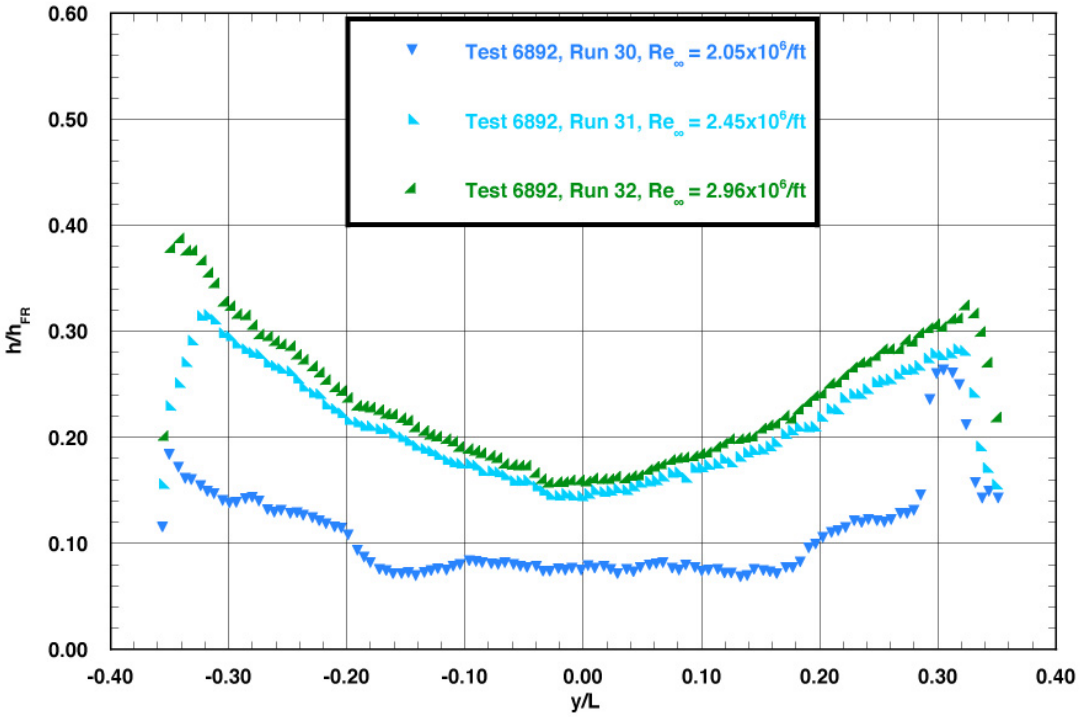

Figure A.33: RTF-BLT-PB spanwise data (x/L = 0.85) in the 20-Inch Mach 6 Air Tunnel at α = 40-deg, x/L = 0.10, k_{CL} = 0.0045-in., $k_{AL\text{-}40\text{-}INV}$ = 0.0045-in.

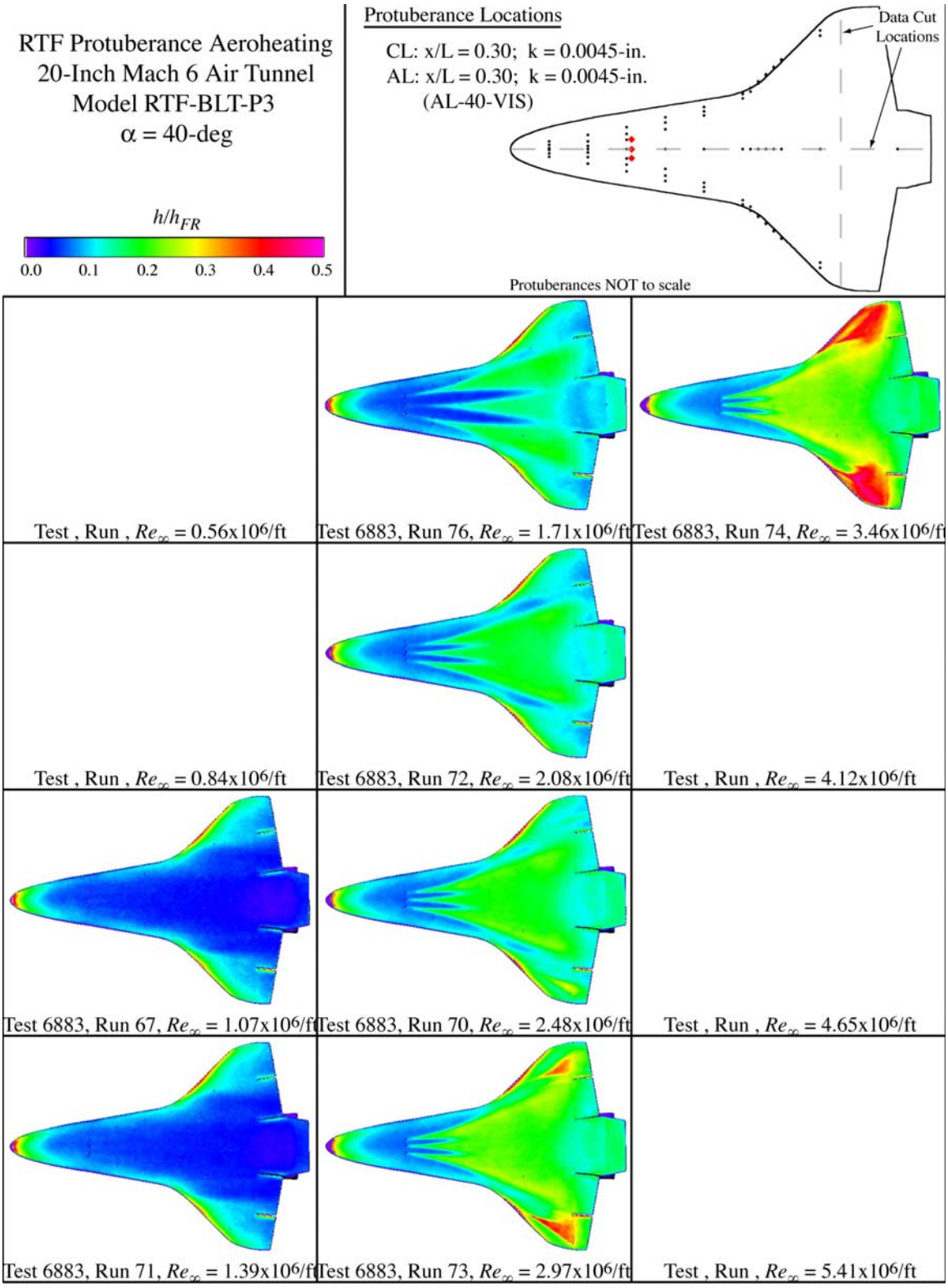

Figure A.34: RTF-BLT-P3 global aeroheating in the 20-Inch Mach 6 Air Tunnel at α = 40-deg, x/L = 0.30, k_{CL} = 0.0045-in., $k_{AL\text{-}40\text{-}VIS}$ = 0.0045-in.

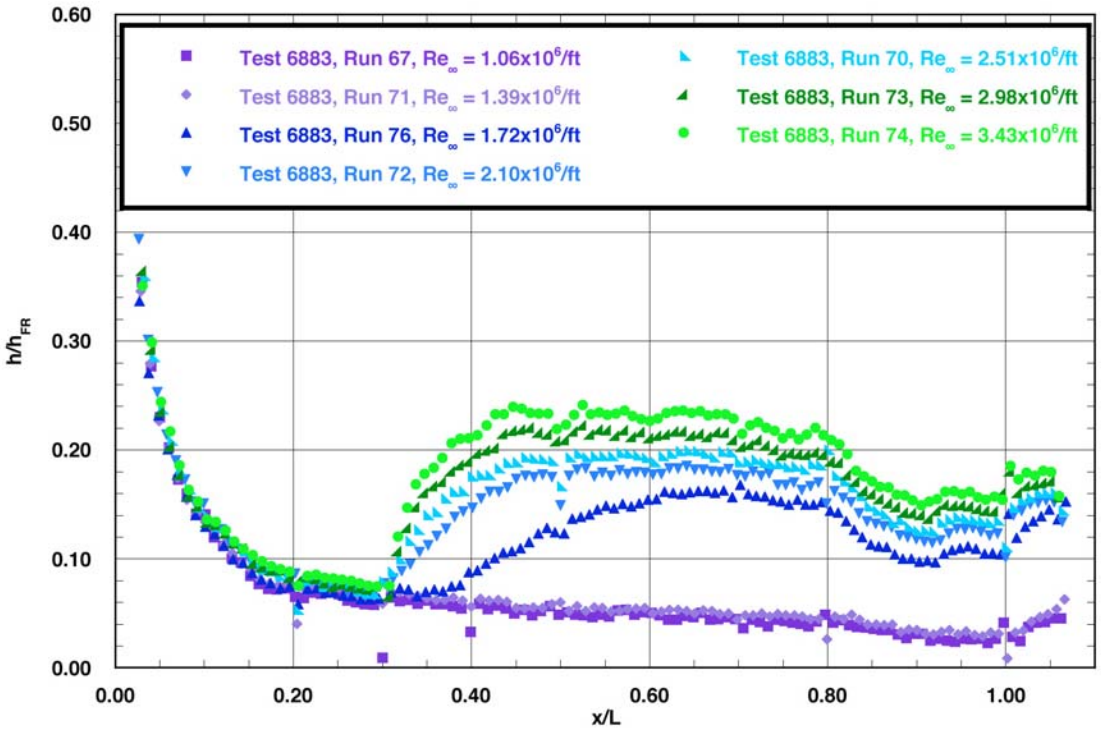

Figure A.35: RTF-BLT-P3 centerline data in the 20-Inch Mach 6 Air Tunnel at α = 40-deg, x/L = 0.30, k_{CL} = 0.0045-in., $k_{AL\text{-}40\text{-}VIS}$ = 0.0045-in.

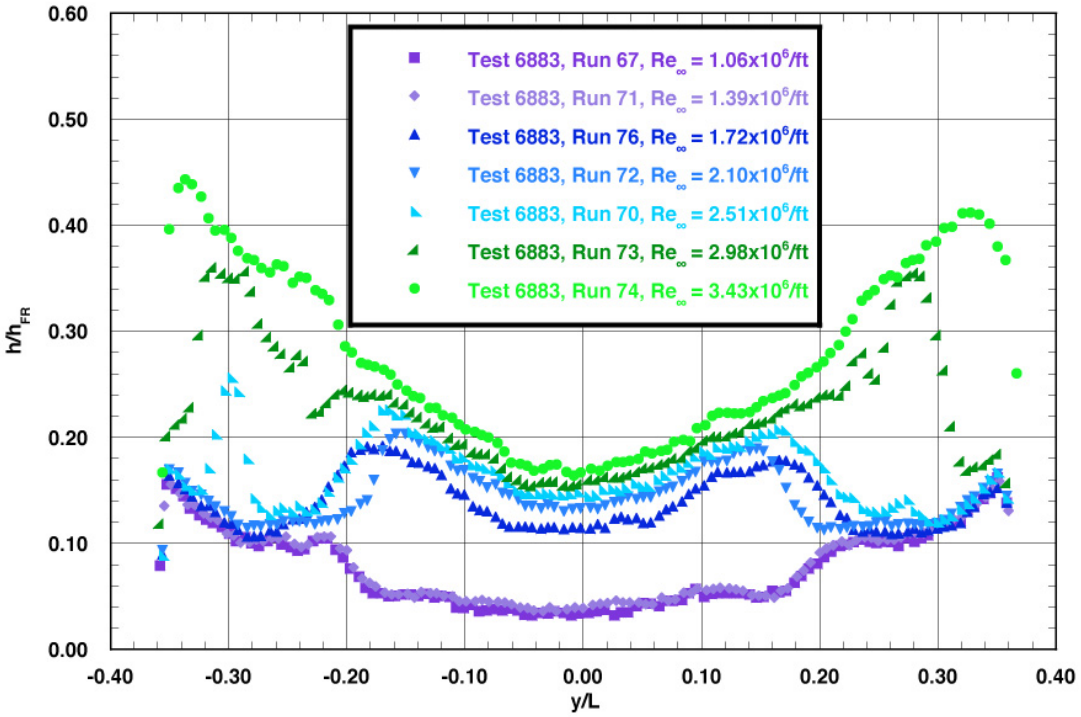

Figure A.36: RTF-BLT-P3 spanwise data (x/L = 0.85) in the 20-Inch Mach 6 Air Tunnel at α = 40-deg, x/L = 0.30, k_{CL} = 0.0045-in., $k_{AL\text{-}40\text{-}VIS}$ = 0.0045-in.

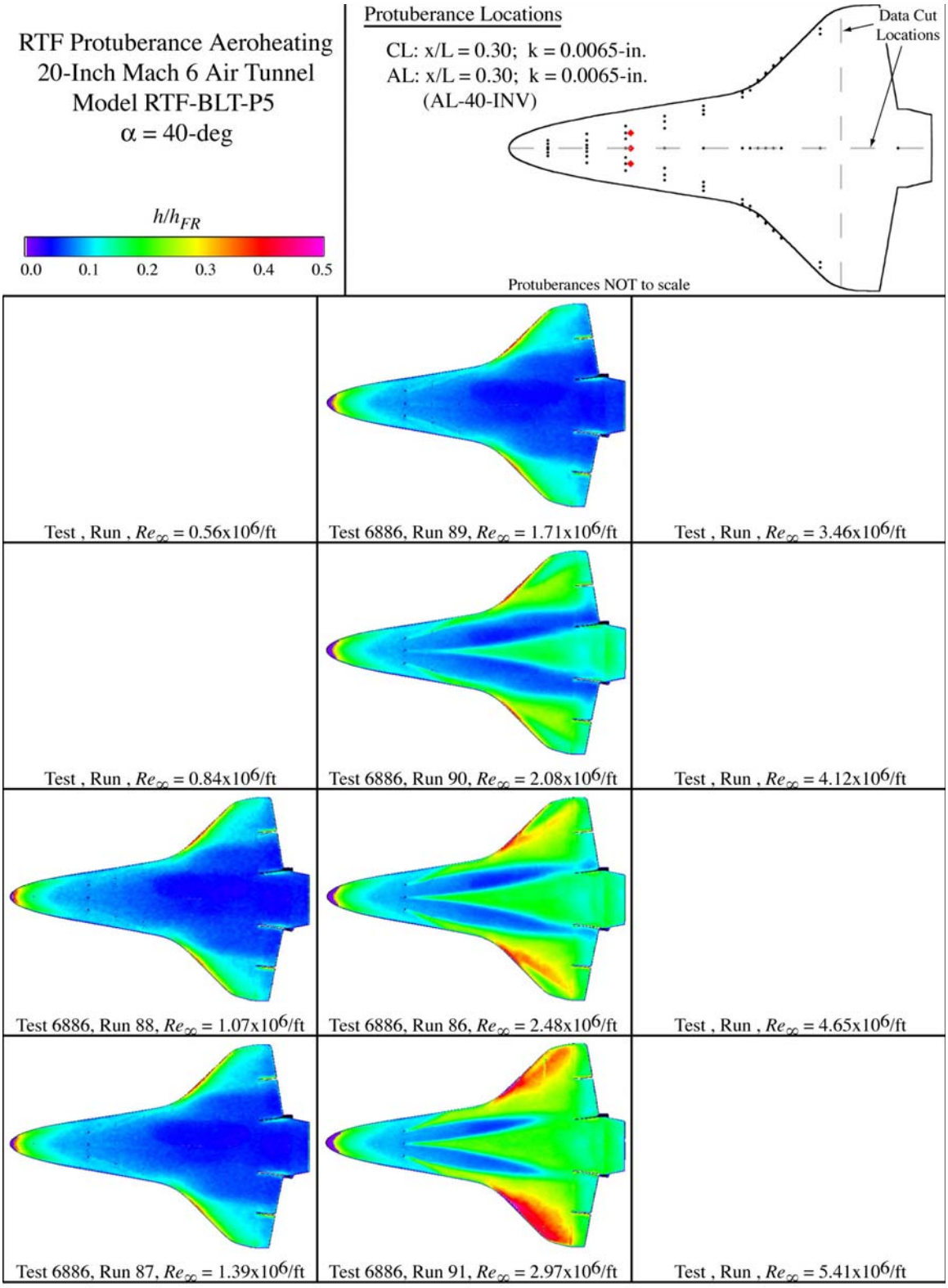

Figure A.37: RTF-BLT-P5 global aeroheating in the 20-Inch Mach 6 Air Tunnel at α = 40-deg, x/L = 0.30, k_{CL} = 0.0065-in., $k_{AL\text{-}40\text{-}INV}$ = 0.0065-in.

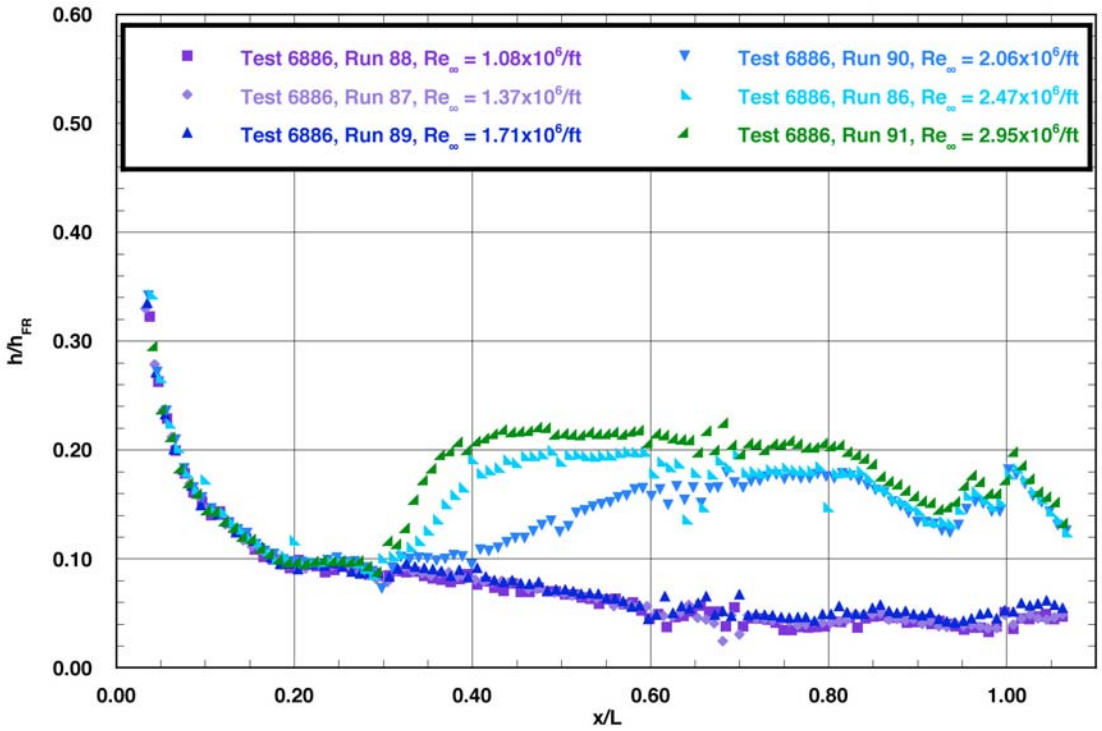

Figure A.38: RTF-BLT-P5 centerline data in the 20-Inch Mach 6 Air Tunnel at α = 40-deg, x/L = 0.30, k_{CL} = 0.0065-in., $k_{AL\text{-}40\text{-}INV}$ = 0.0065-in.

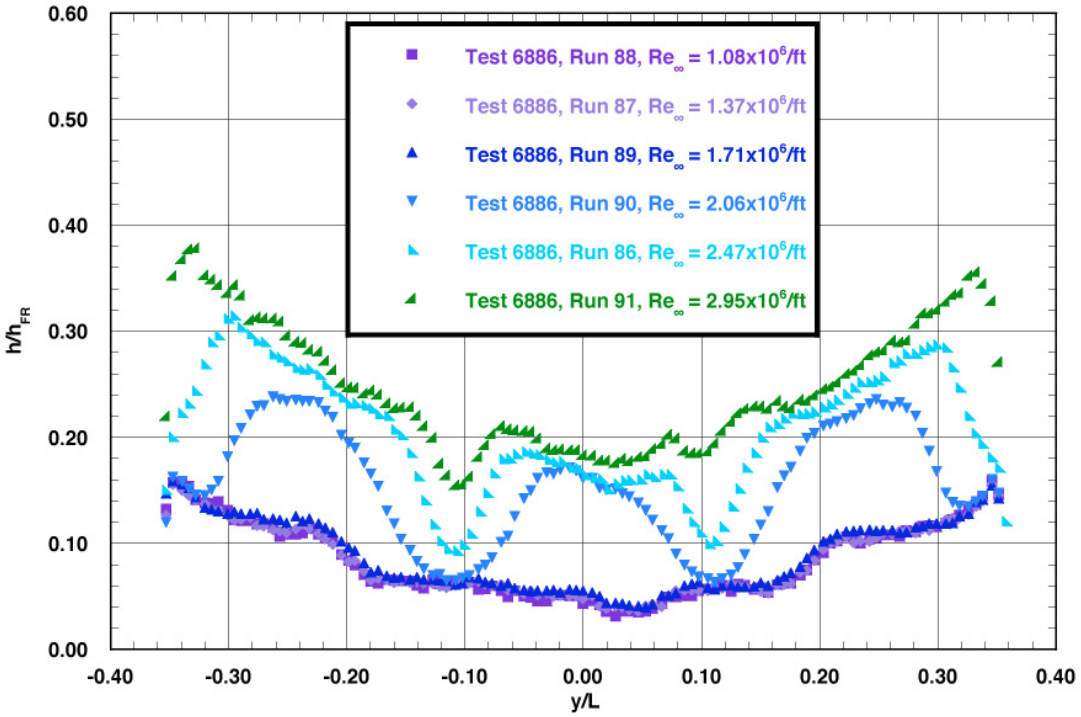

Figure A.39: RTF-BLT-P5 spanwise data (x/L = 0.85) in the 20-Inch Mach 6 Air Tunnel at α = 40-deg, x/L = 0.30, k_{CL} = 0.0065-in., $k_{AL\text{-}40\text{-}INV}$ = 0.0065-in.

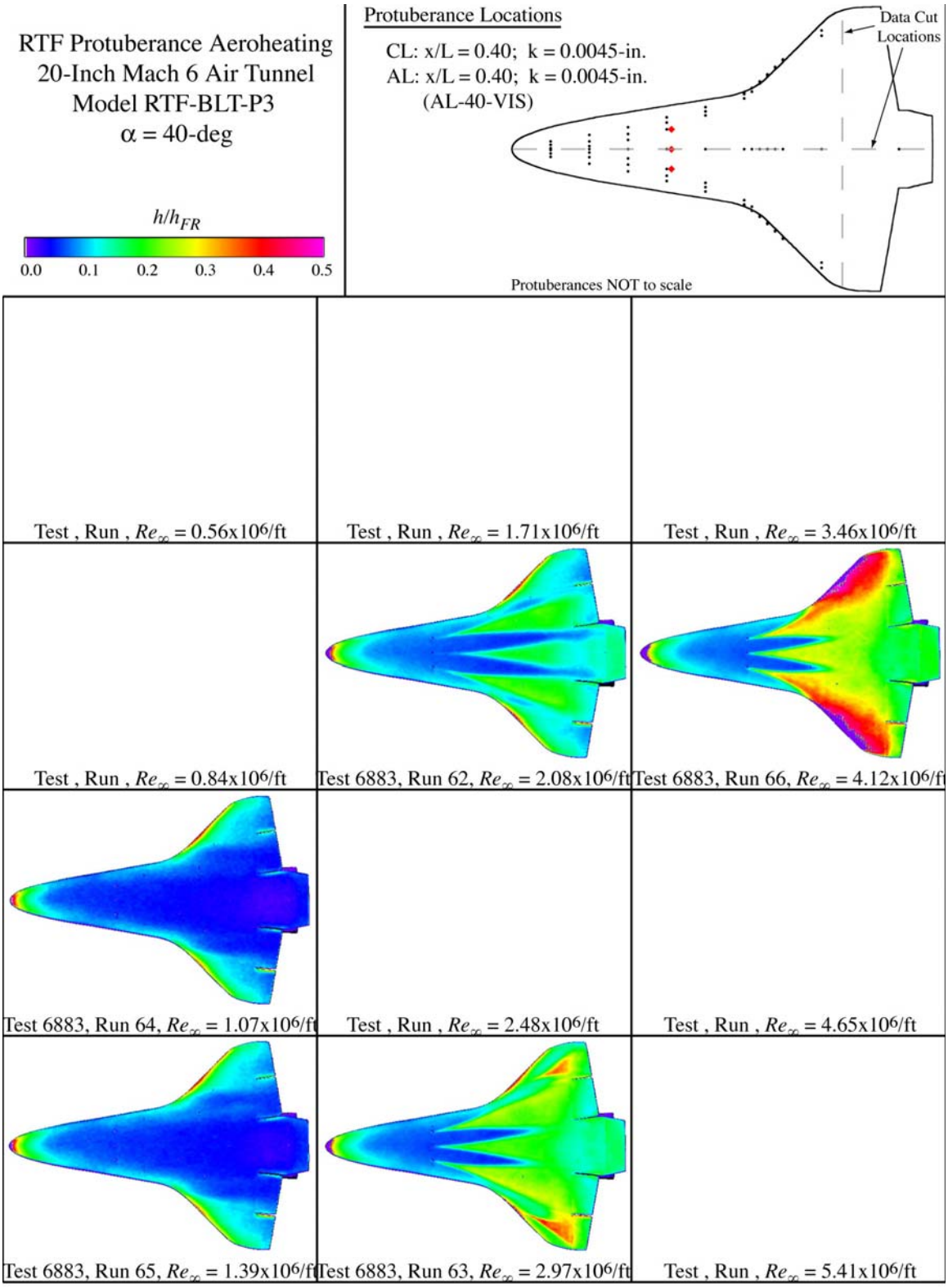

Figure A.40: RTF-BLT-P3 global aeroheating in the 20-Inch Mach 6 Air Tunnel at α = 40-deg, x/L = 0.40, k_{CL} = 0.0045-in., $k_{AL\text{-}40\text{-}VIS}$ = 0.0045-in.

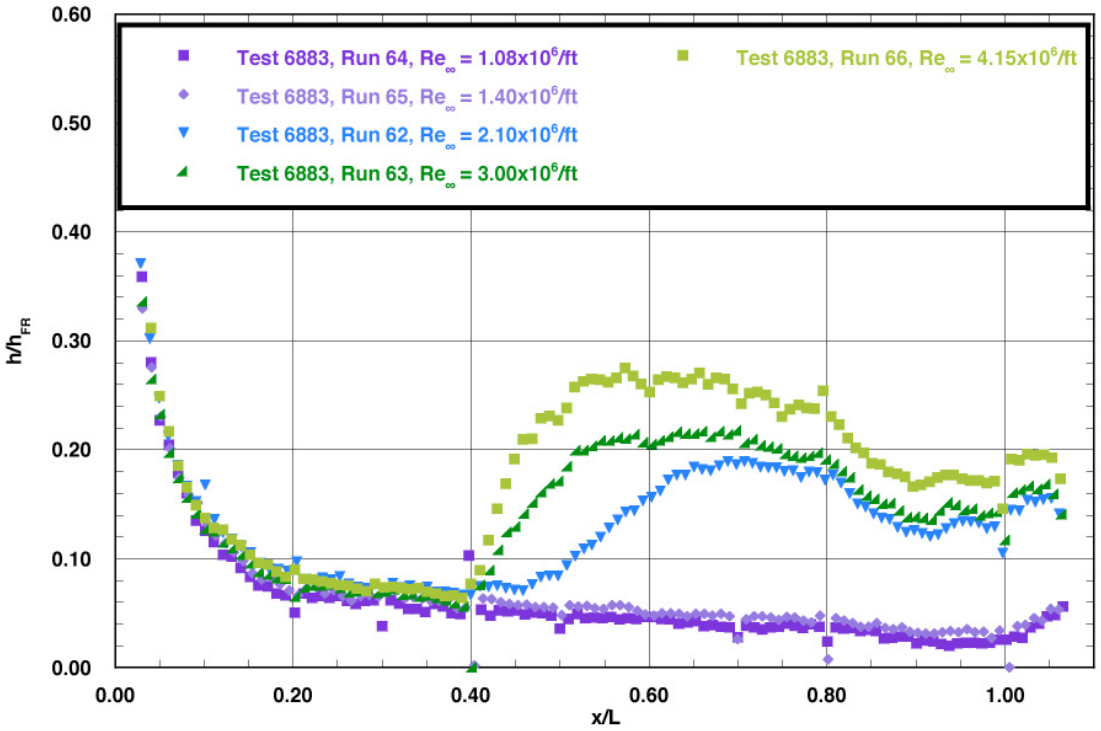

Figure A.41: RTF-BLT-P3 centerline data in the 20-Inch Mach 6 Air Tunnel at α = 40-deg, x/L = 0.40, k_{CL} = 0.0045-in., $k_{AL\text{-}40\text{-}VIS}$ = 0.0045-in.

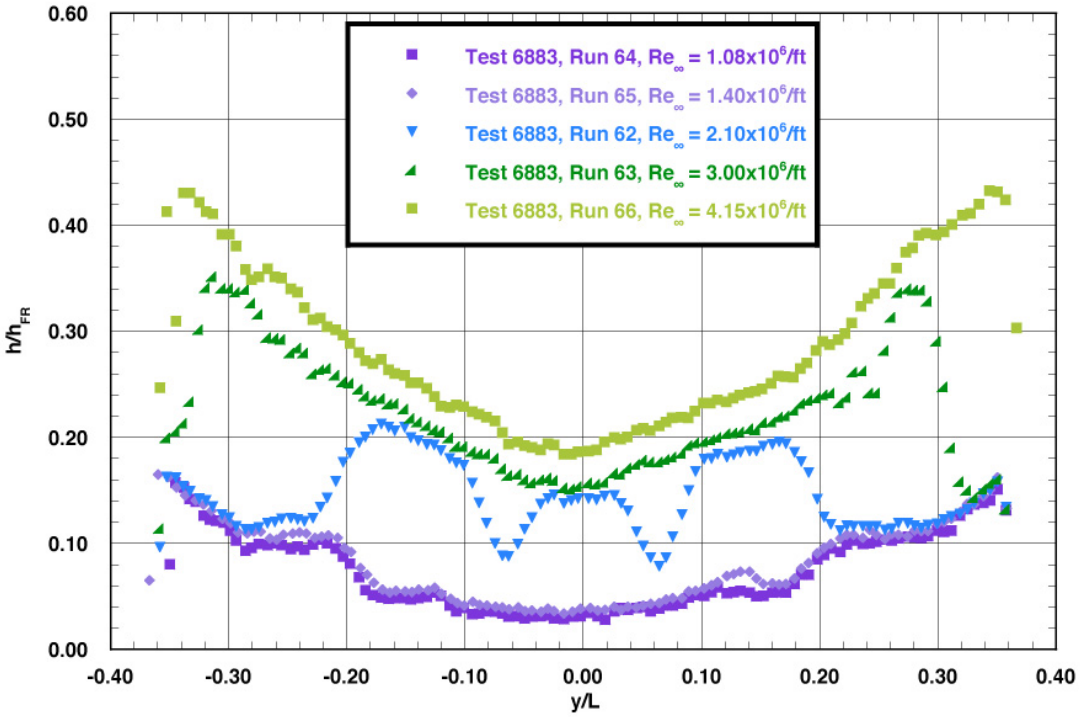

Figure A.42: RTF-BLT-P3 spanwise data (x/L = 0.85) in the 20-Inch Mach 6 Air Tunnel at α = 40-deg, x/L = 0.40, k_{CL} = 0.0045-in., $k_{AL\text{-}40\text{-}VIS}$ = 0.0045-in.

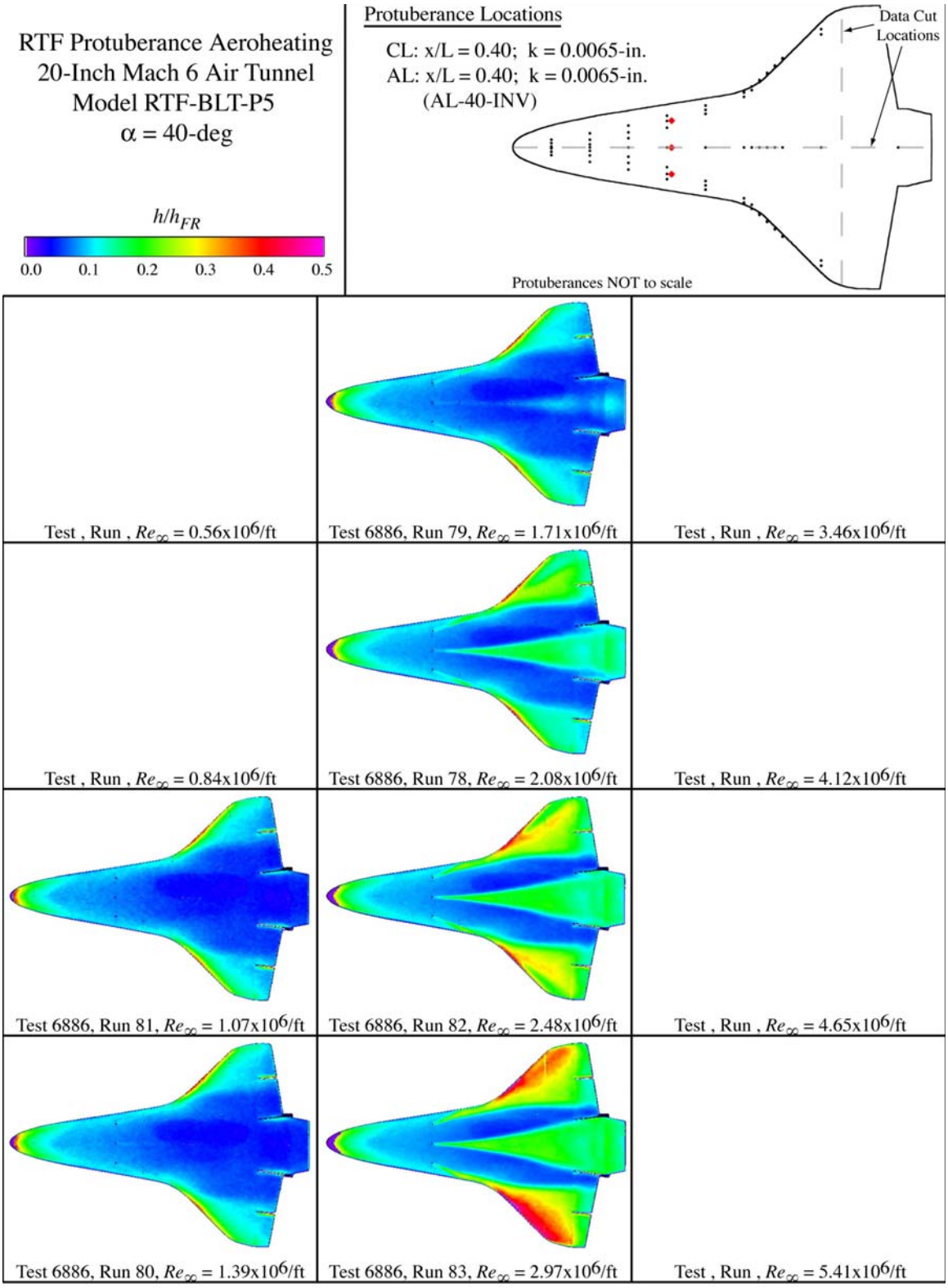

Figure A.43: RTF-BLT-P5 global aeroheating in the 20-Inch Mach 6 Air Tunnel at α = 40-deg, x/L = 0.40, k_{CL} = 0.0065-in., $k_{AL\text{-}40\text{-}INV}$ = 0.0065-in.

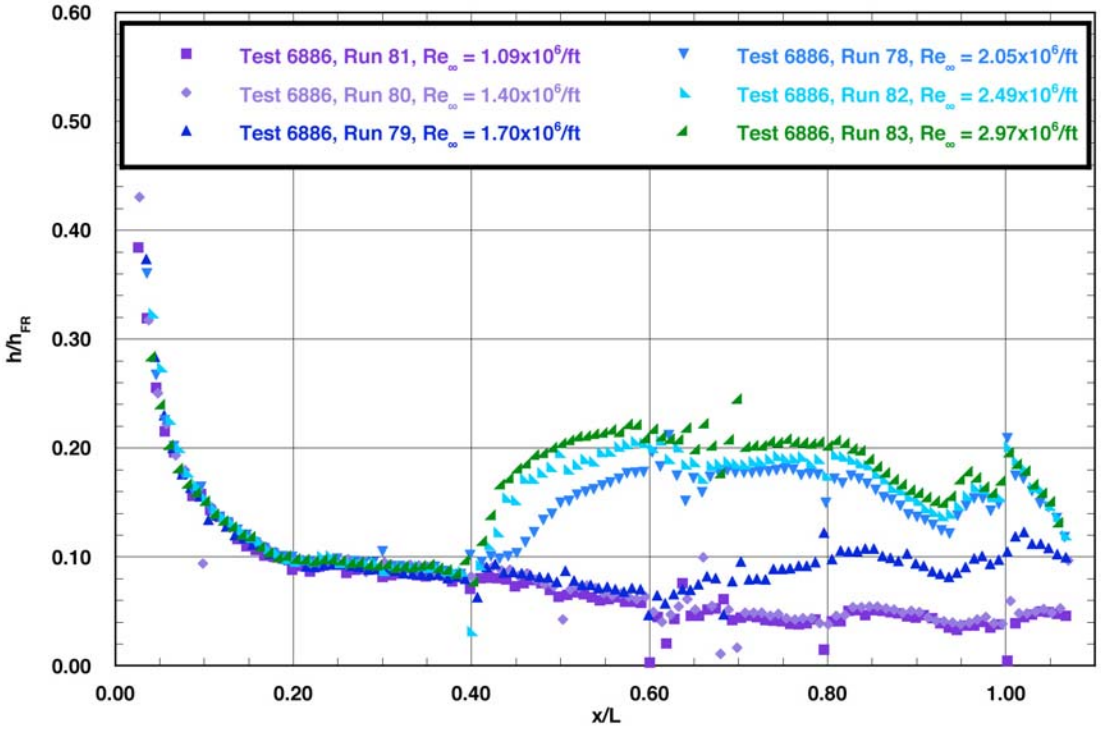

Figure A.44: RTF-BLT-P5 centerline data in the 20-Inch Mach 6 Air Tunnel at α = 40-deg, x/L = 0.40, k_{CL} = 0.0065-in., $k_{AL\text{-}40\text{-}INV}$ = 0.0065-in.

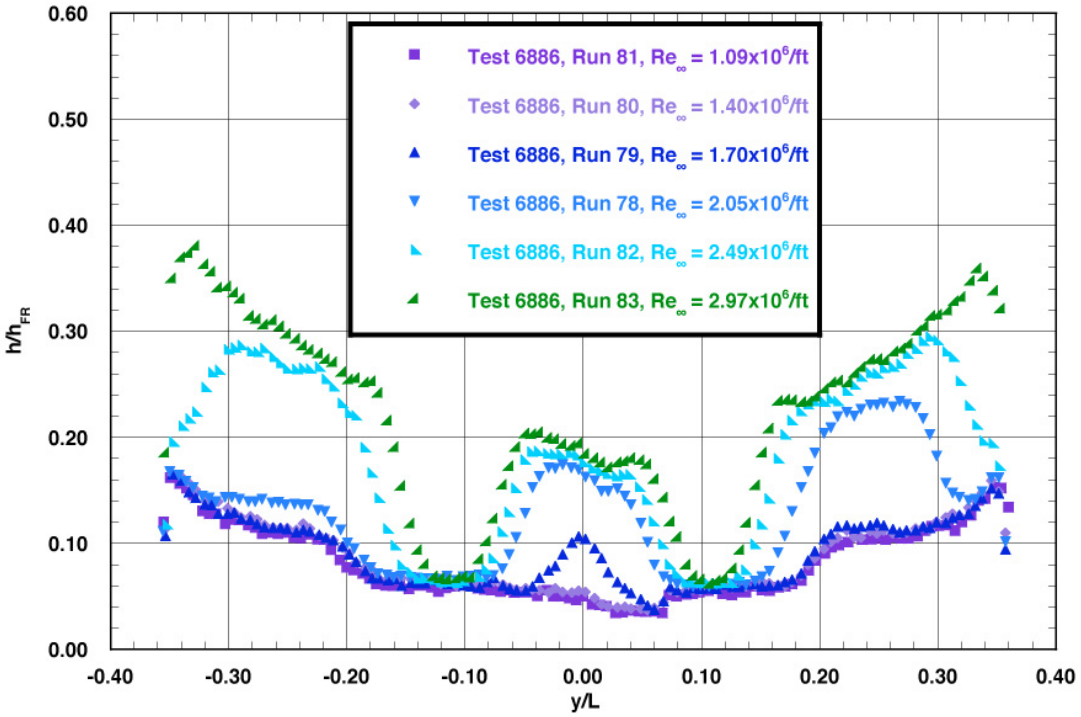

Figure A.45: RTF-BLT-P5 spanwise data (x/L = 0.85) in the 20-Inch Mach 6 Air Tunnel at α = 40-deg, x/L = 0.40, k_{CL} = 0.0065-in., $k_{AL\text{-}40\text{-}INV}$ = 0.0065-in.

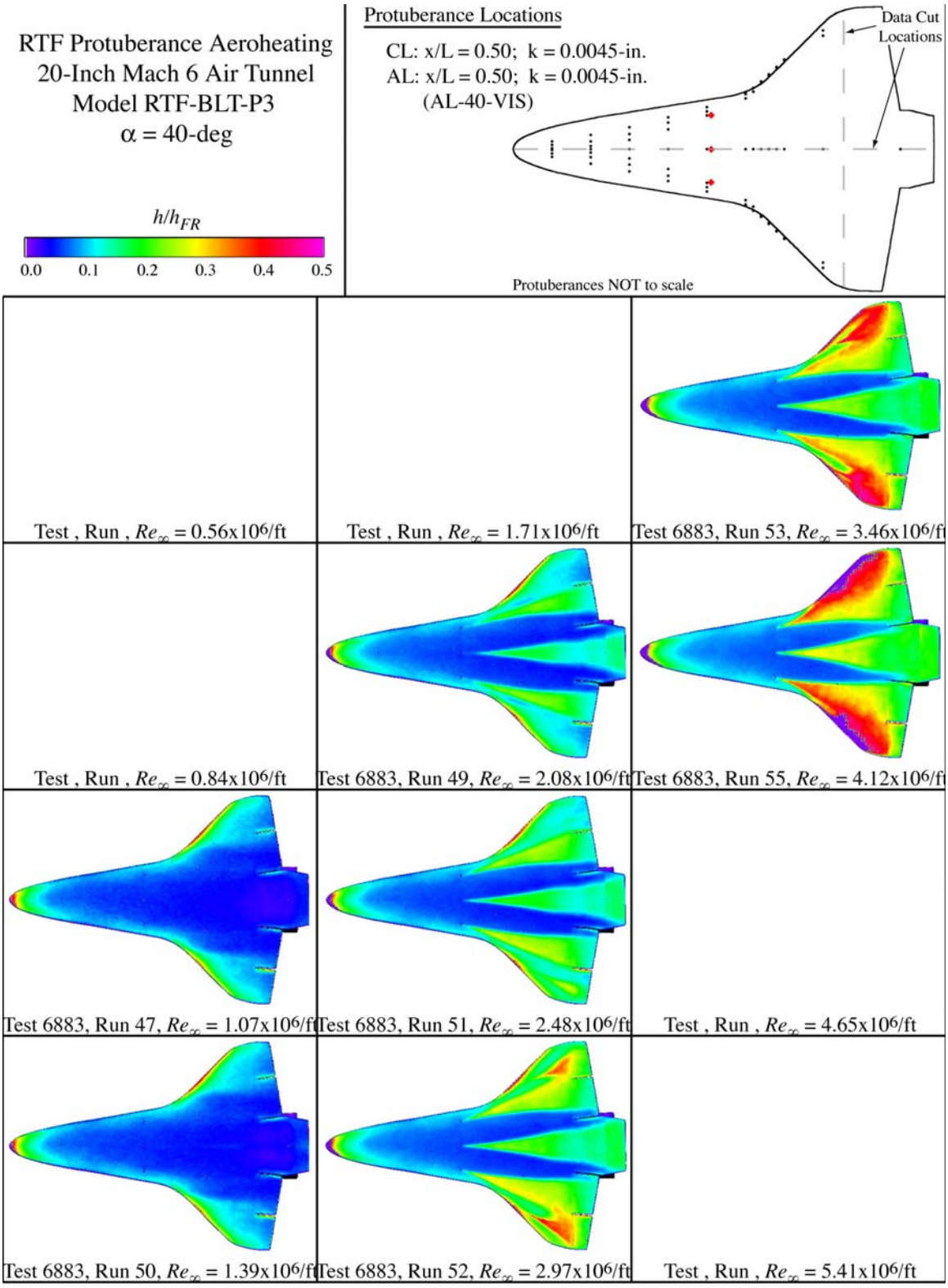

Figure A.46: RTF-BLT-P3 global aeroheating in the 20-Inch Mach 6 Air Tunnel at α = 40-deg, x/L = 0.50, k_{CL} = 0.0045-in., $k_{AL\text{-}40\text{-}VIS}$ = 0.0045-in.

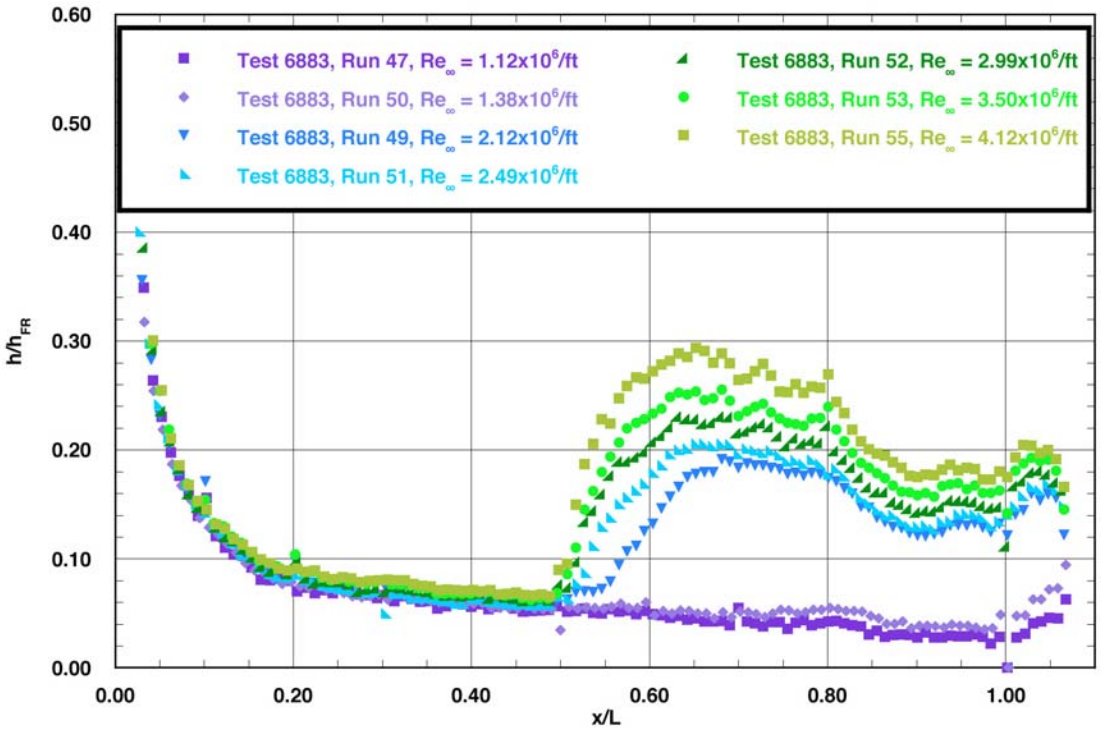

Figure A.47: RTF-BLT-P3 centerline data in the 20-Inch Mach 6 Air Tunnel at α = 40-deg, x/L = 0.50, k_{CL} = 0.0045-in., $k_{AL\text{-}40\text{-}VIS}$ = 0.0045-in.

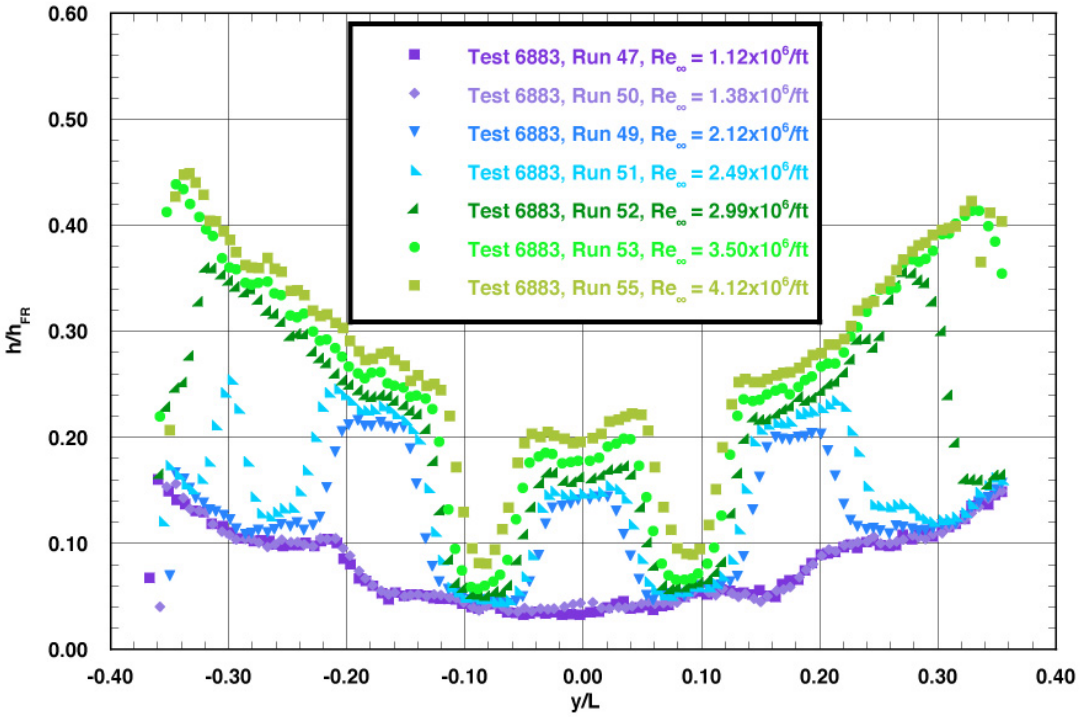

Figure A.48: RTF-BLT-P3 spanwise data (x/L = 0.85) in the 20-Inch Mach 6 Air Tunnel at α = 40-deg, x/L = 0.50, k_{CL} = 0.0045-in., $k_{AL\text{-}40\text{-}VIS}$ = 0.0045-in.

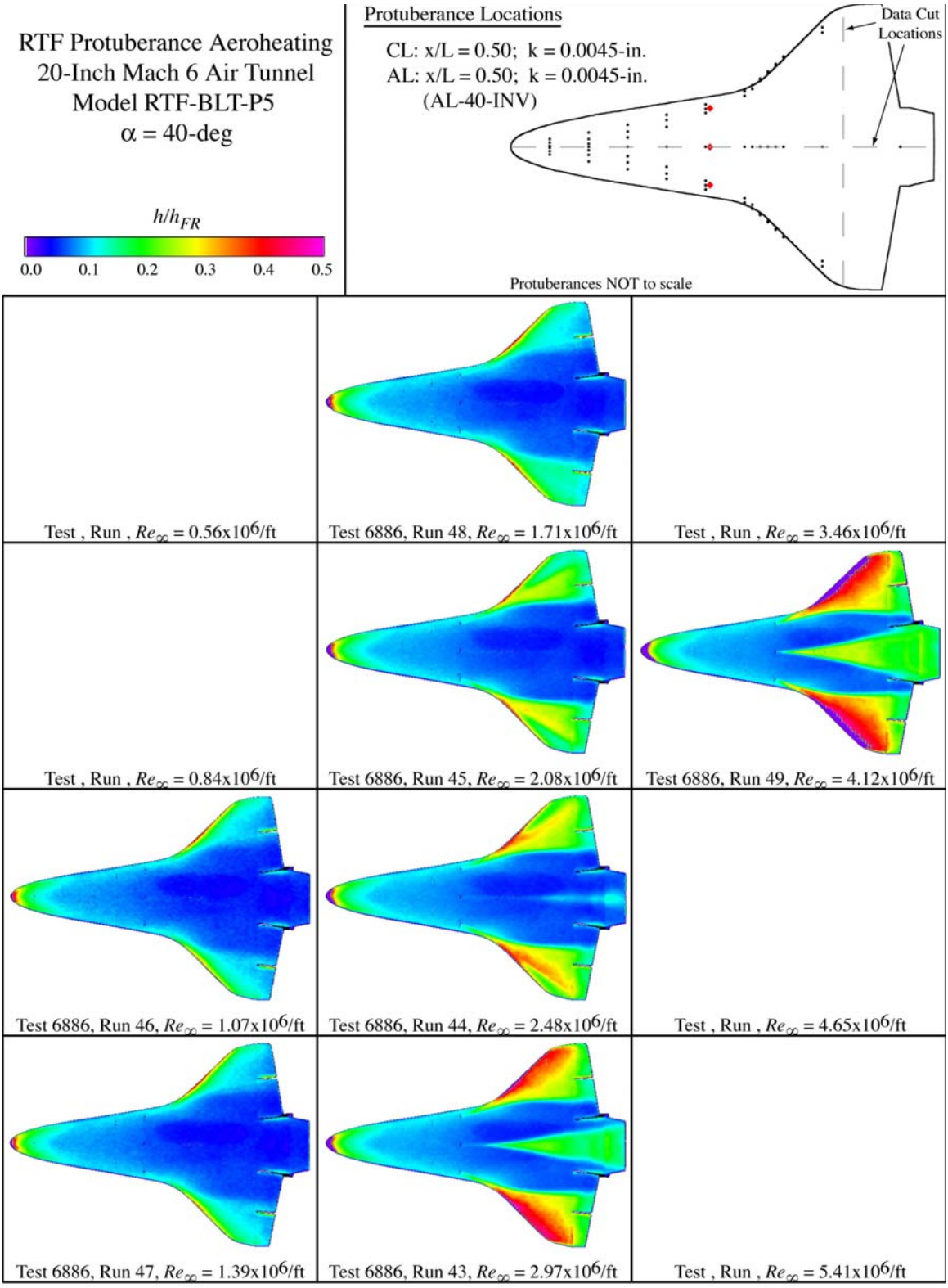

Figure A.49: RTF-BLT-P5 global aeroheating in the 20-Inch Mach 6 Air Tunnel at α = 40-deg, x/L = 0.50, k_{CL} = 0.0045-in., $k_{AL\text{-}40\text{-}INV}$ = 0.0045-in.

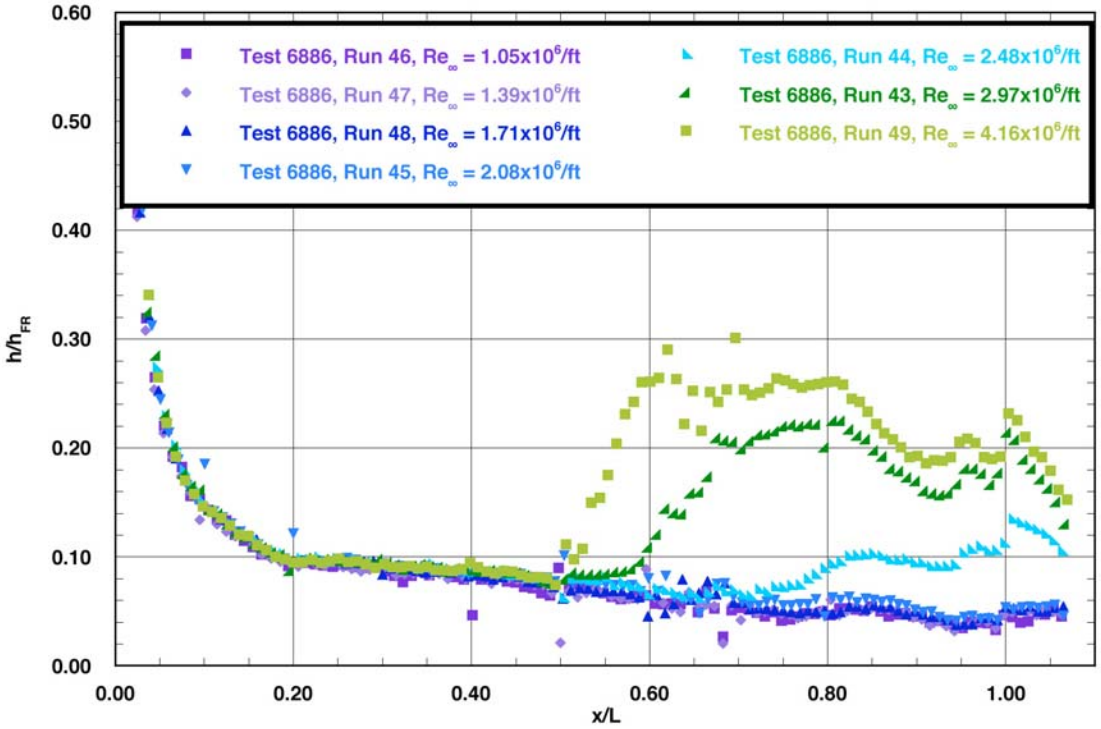

Figure A.50: RTF-BLT-P5 centerline data in the 20-Inch Mach 6 Air Tunnel at α = 40-deg, x/L = 0.50, k_{CL} = 0.0045-in., $k_{AL\text{-}40\text{-}INV}$ = 0.0045-in.

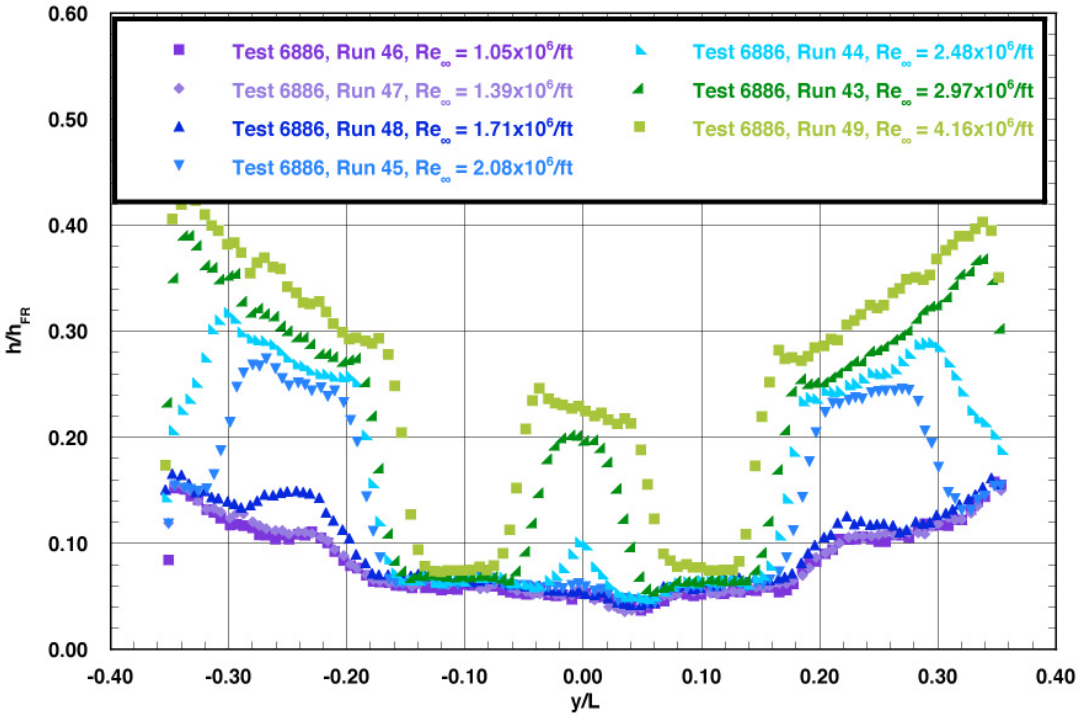

Figure A.51: RTF-BLT-P5 spanwise data (x/L = 0.85) in the 20-Inch Mach 6 Air Tunnel at α = 40-deg, x/L = 0.50, k_{CL} = 0.0045-in., $k_{AL\text{-}40\text{-}INV}$ = 0.0045-in.

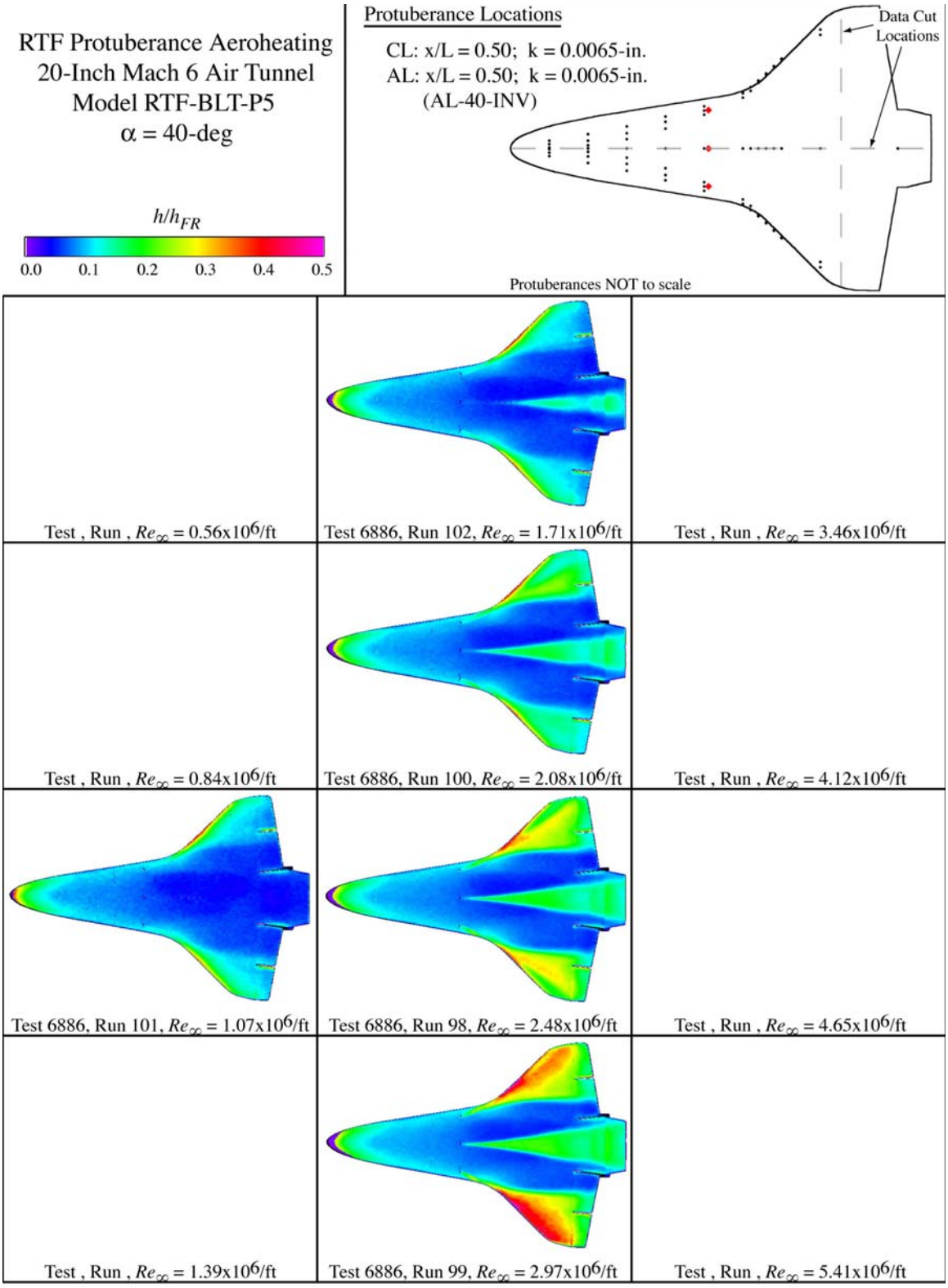

Figure A.52: RTF-BLT-P5 global aeroheating in the 20-Inch Mach 6 Air Tunnel at α = 40-deg, x/L = 0.50, k_{CL} = 0.0065-in., $k_{AL\text{-}40\text{-}INV}$ = 0.0065-in.

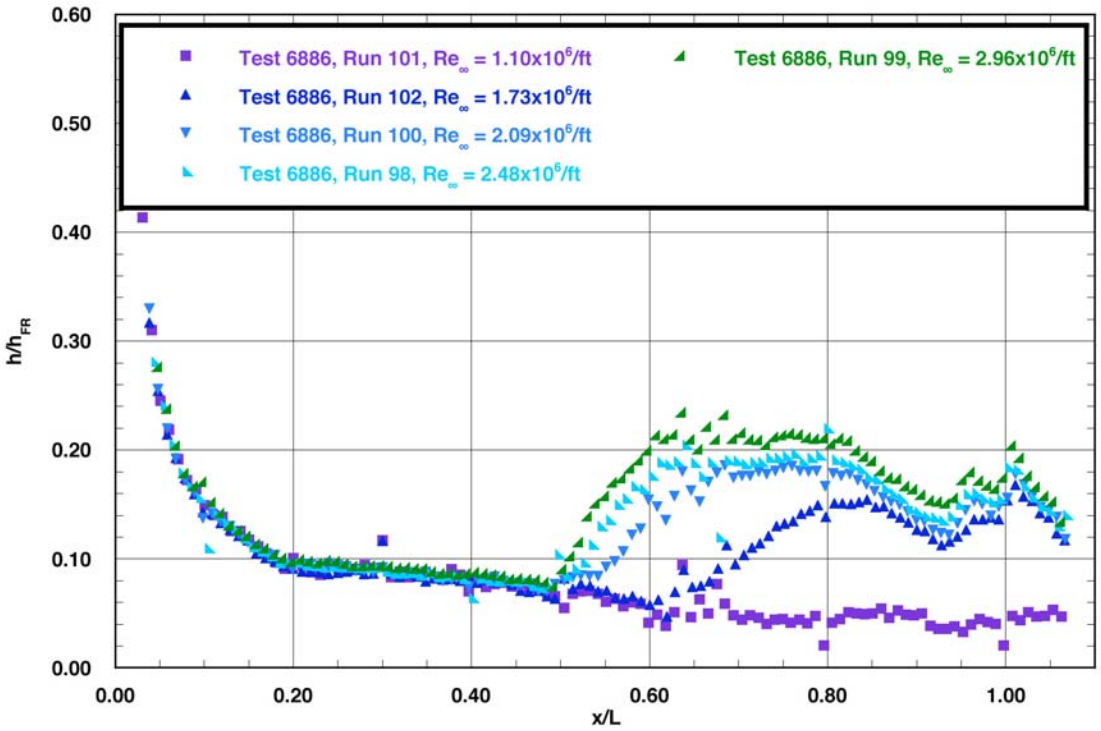

Figure A.53: RTF-BLT-P5 centerline data in the 20-Inch Mach 6 Air Tunnel at α = 40-deg, x/L = 0.50, k_{CL} = 0.0065-in., $k_{AL\text{-}40\text{-}INV}$ = 0.0065-in.

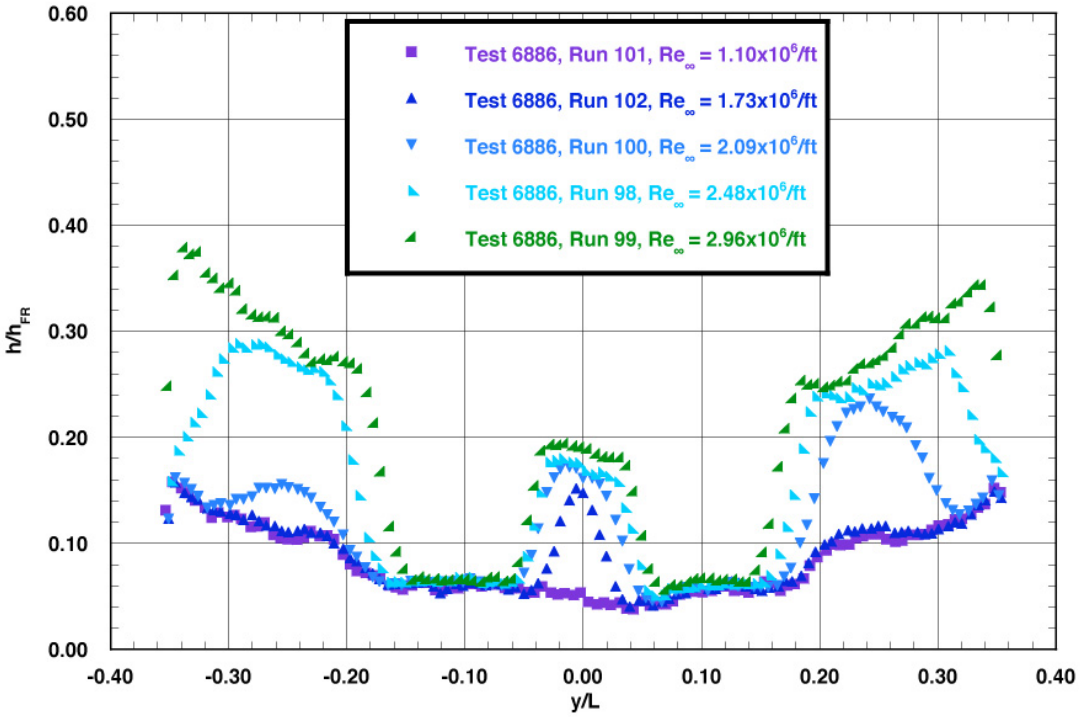

Figure A.54: RTF-BLT-P5 spanwise data (x/L = 0.85) in the 20-Inch Mach 6 Air Tunnel at α = 40-deg, x/L = 0.50, k_{CL} = 0.0065-in., $k_{AL\text{-}40\text{-}INV}$ = 0.0065-in.

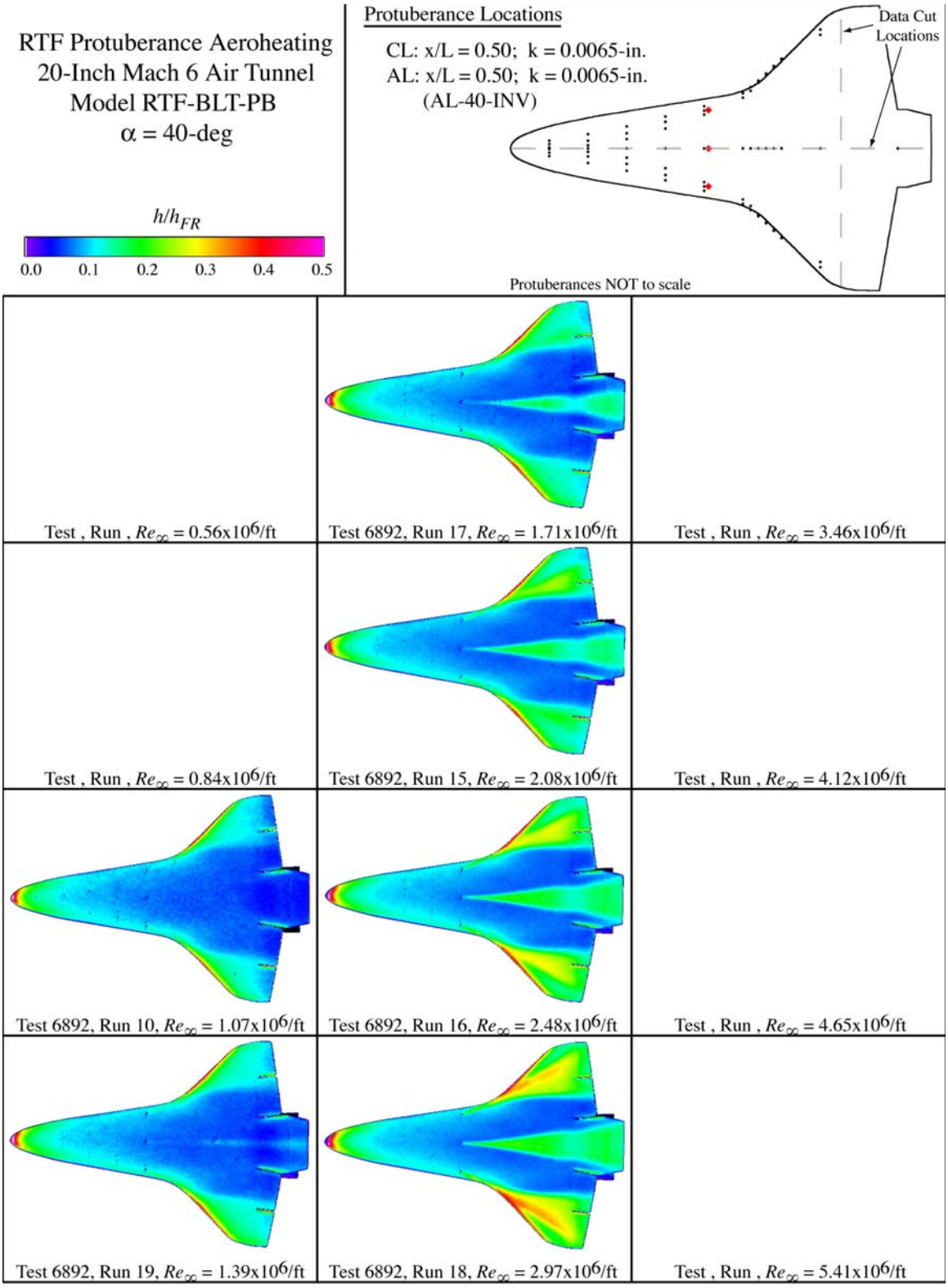

Figure A.55: RTF-BLT-PB global aeroheating in the 20-Inch Mach 6 Air Tunnel at α = 40-deg, x/L = 0.50, k_{CL} = 0.0065-in., $k_{AL\text{-}40\text{-}INV}$ = 0.0065-in.

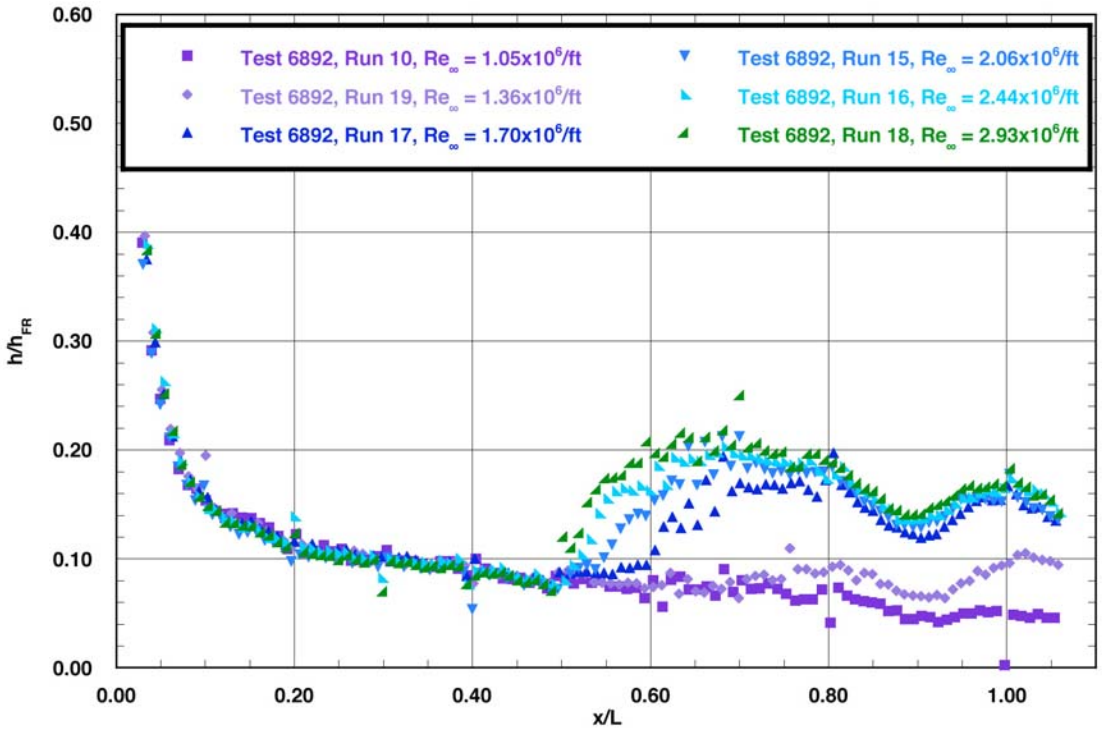

Figure A.56: RTF-BLT-PB centerline data in the 20-Inch Mach 6 Air Tunnel at α = 40-deg, x/L = 0.50, k_{CL} = 0.0065-in., $k_{AL\text{-}40\text{-}INV}$ = 0.0065-in.

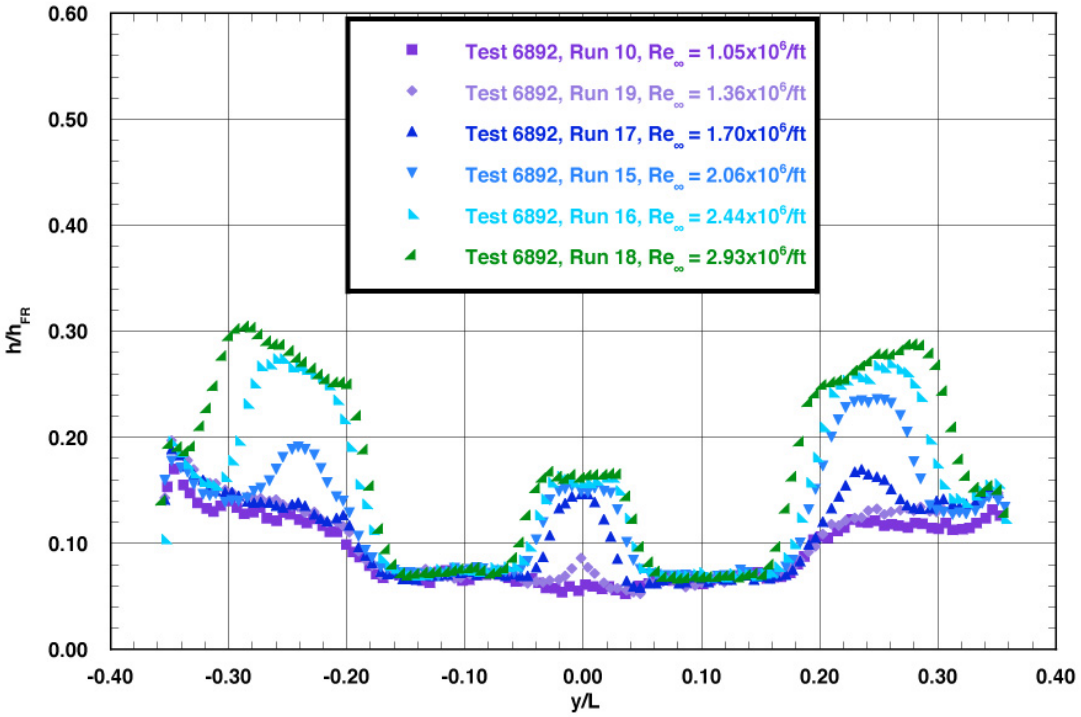

Figure A.57: RTF-BLT-PB spanwise data (x/L = 0.85) in the 20-Inch Mach 6 Air Tunnel at α = 40-deg, x/L = 0.50, k_{CL} = 0.0065-in., $k_{AL\text{-}40\text{-}INV}$ = 0.0065-in.

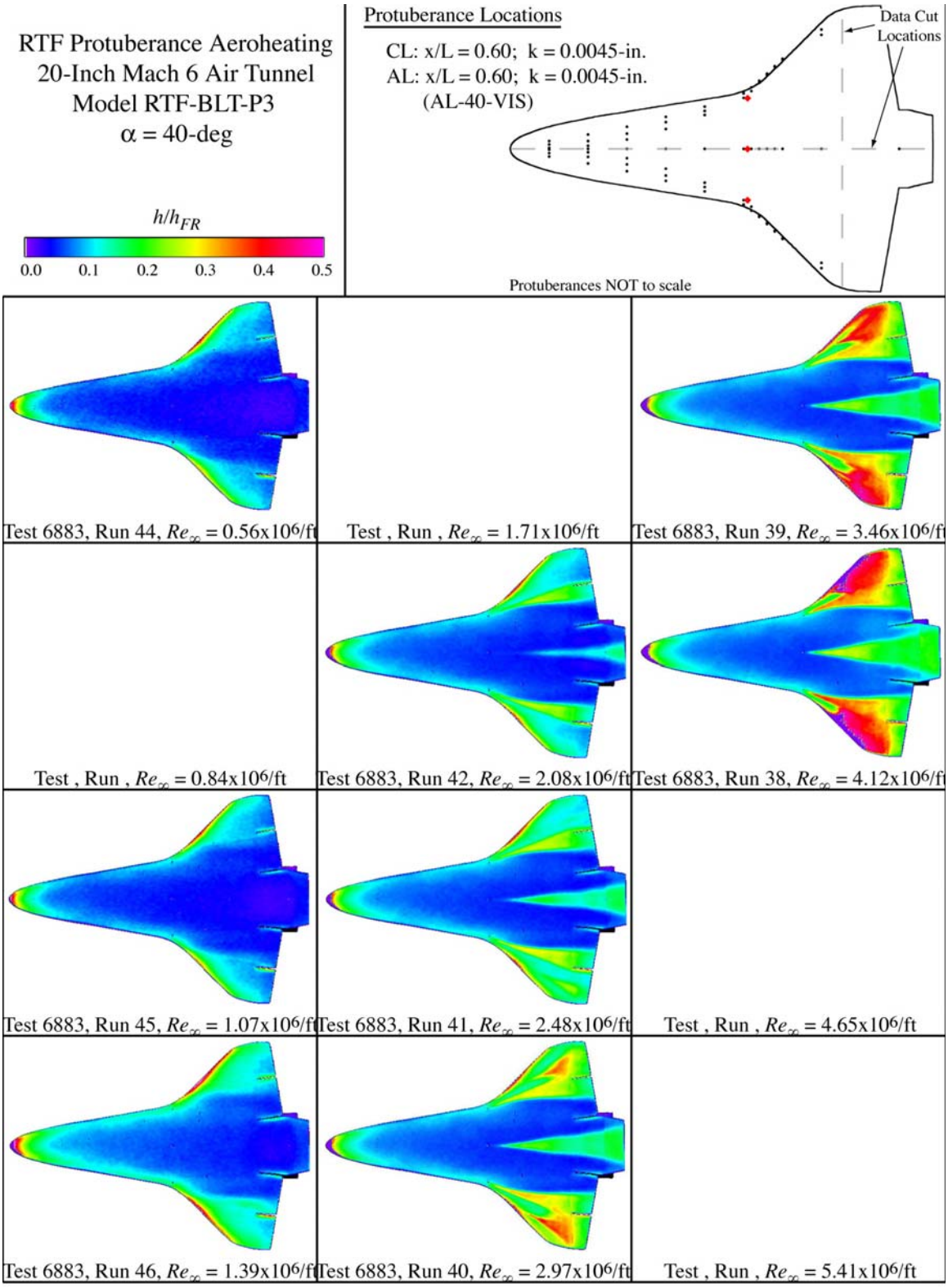

Figure A.58: RTF-BLT-P3 global aeroheating in the 20-Inch Mach 6 Air Tunnel at α = 40-deg, x/L = 0.60, k_{CL} = 0.0045-in., $k_{AL\text{-}40\text{-}VIS}$ = 0.0045-in.

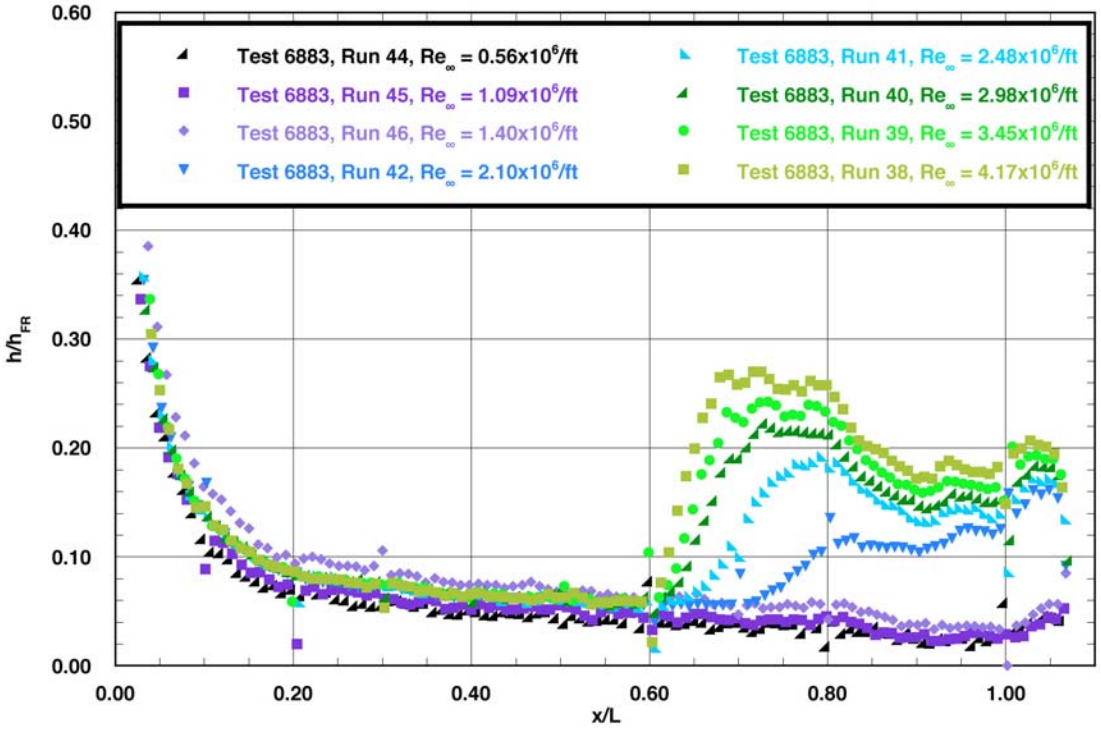

Figure A.59: RTF-BLT-P3 centerline data in the 20-Inch Mach 6 Air Tunnel at α = 40-deg, x/L = 0.60, k_{CL} = 0.0045-in., $k_{AL\text{-}40\text{-}VIS}$ = 0.0045-in.

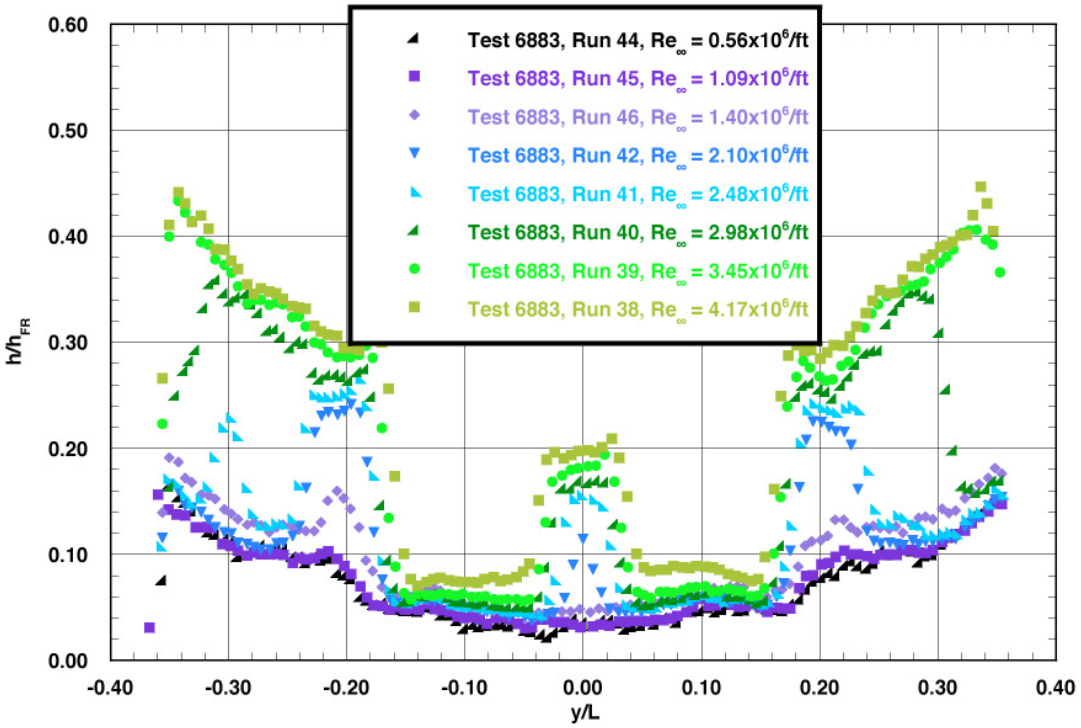

Figure A.60: RTF-BLT-P3 spanwise data (x/L = 0.85) in the 20-Inch Mach 6 Air Tunnel at α = 40-deg, x/L = 0.60, k_{CL} = 0.0045-in., $k_{AL\text{-}40\text{-}VIS}$ = 0.0045-in.

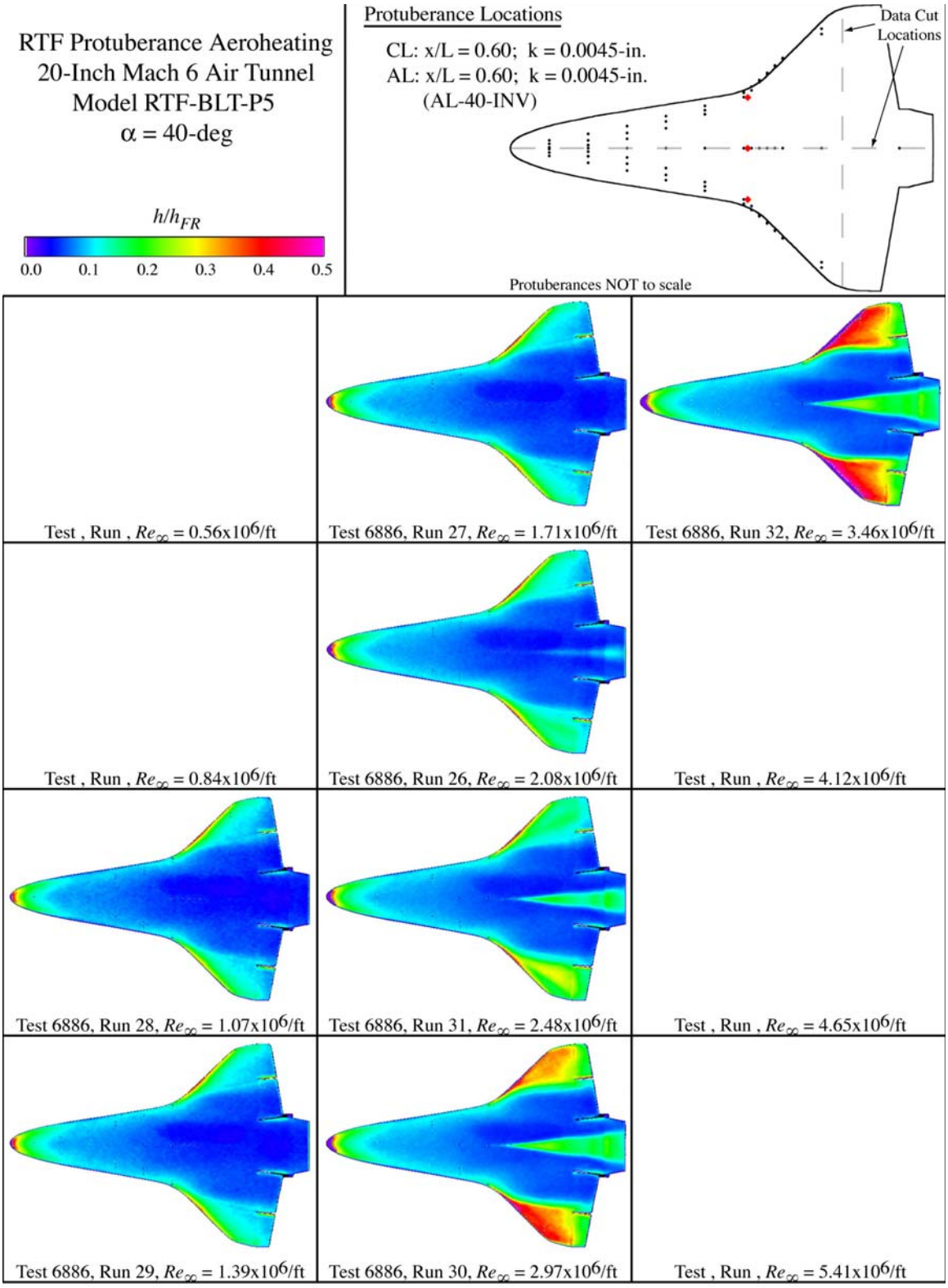

Figure A.61: RTF-BLT-P5 global aeroheating in the 20-Inch Mach 6 Air Tunnel at α = 40-deg, x/L = 0.60, k_{CL} = 0.0045-in., $k_{AL\text{-}40\text{-}INV}$ = 0.0045-in.

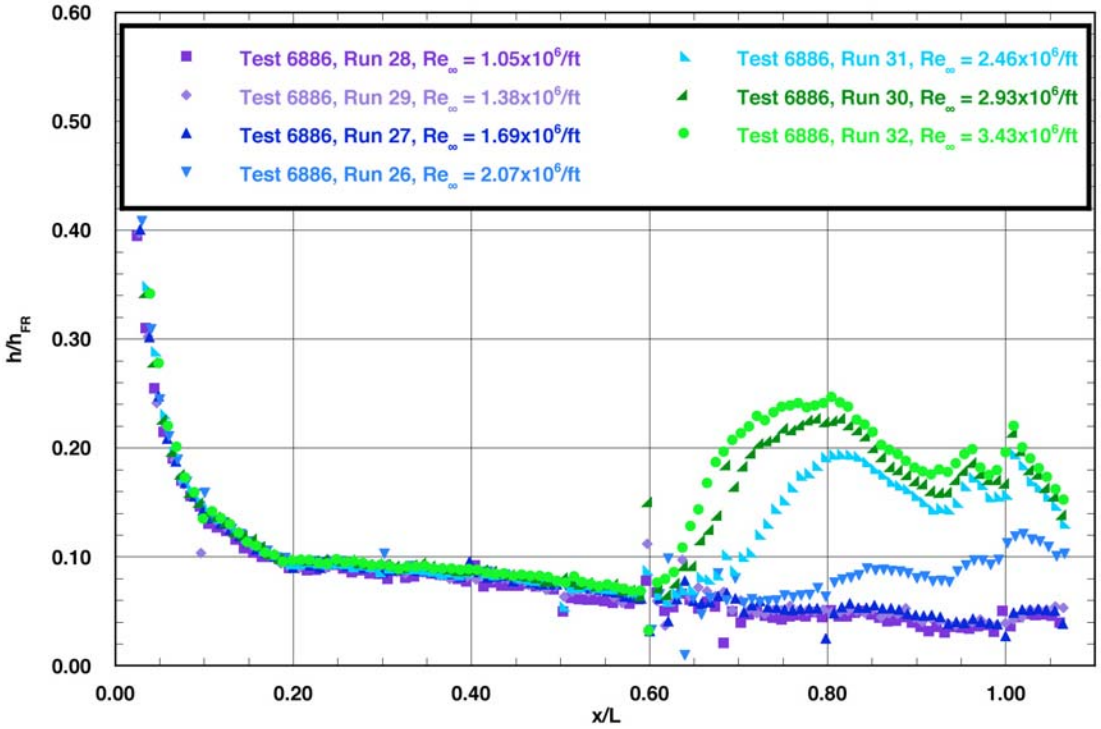

Figure A.62: RTF-BLT-P5 centerline data in the 20-Inch Mach 6 Air Tunnel at α = 40-deg, x/L = 0.60, k_{CL} = 0.0045-in., $k_{AL\text{-}40\text{-}INV}$ = 0.0045-in.

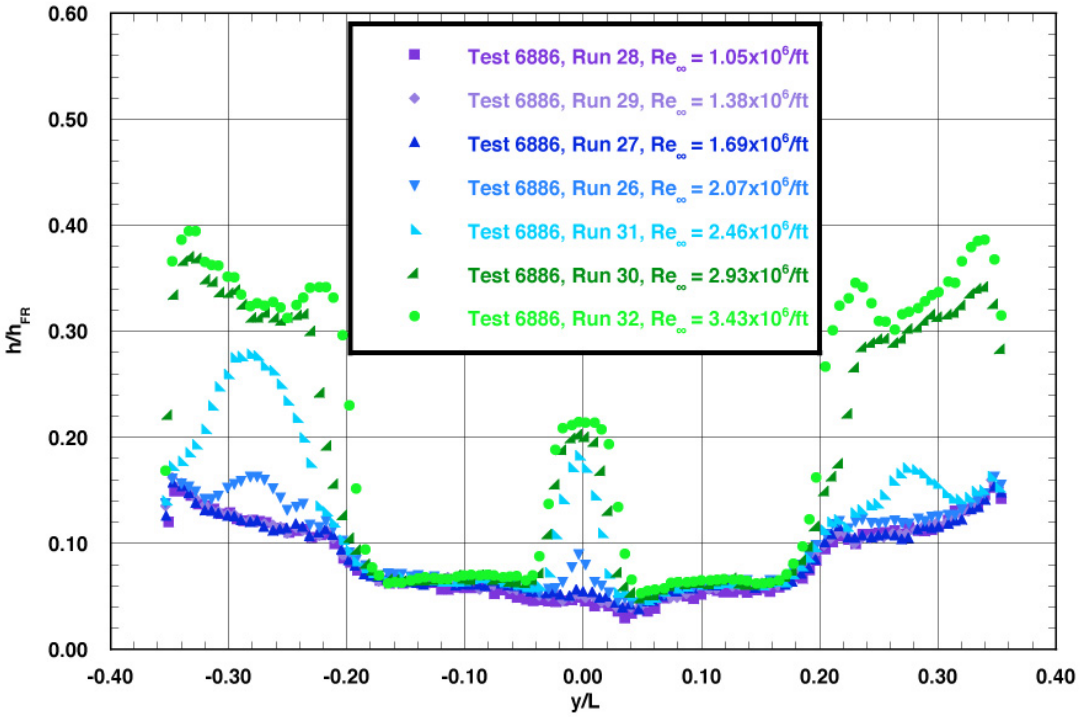

Figure A.63: RTF-BLT-P5 spanwise data (x/L = 0.85) in the 20-Inch Mach 6 Air Tunnel at α = 40-deg, x/L = 0.60, k_{CL} = 0.0045-in., $k_{AL\text{-}40\text{-}INV}$ = 0.0045-in.

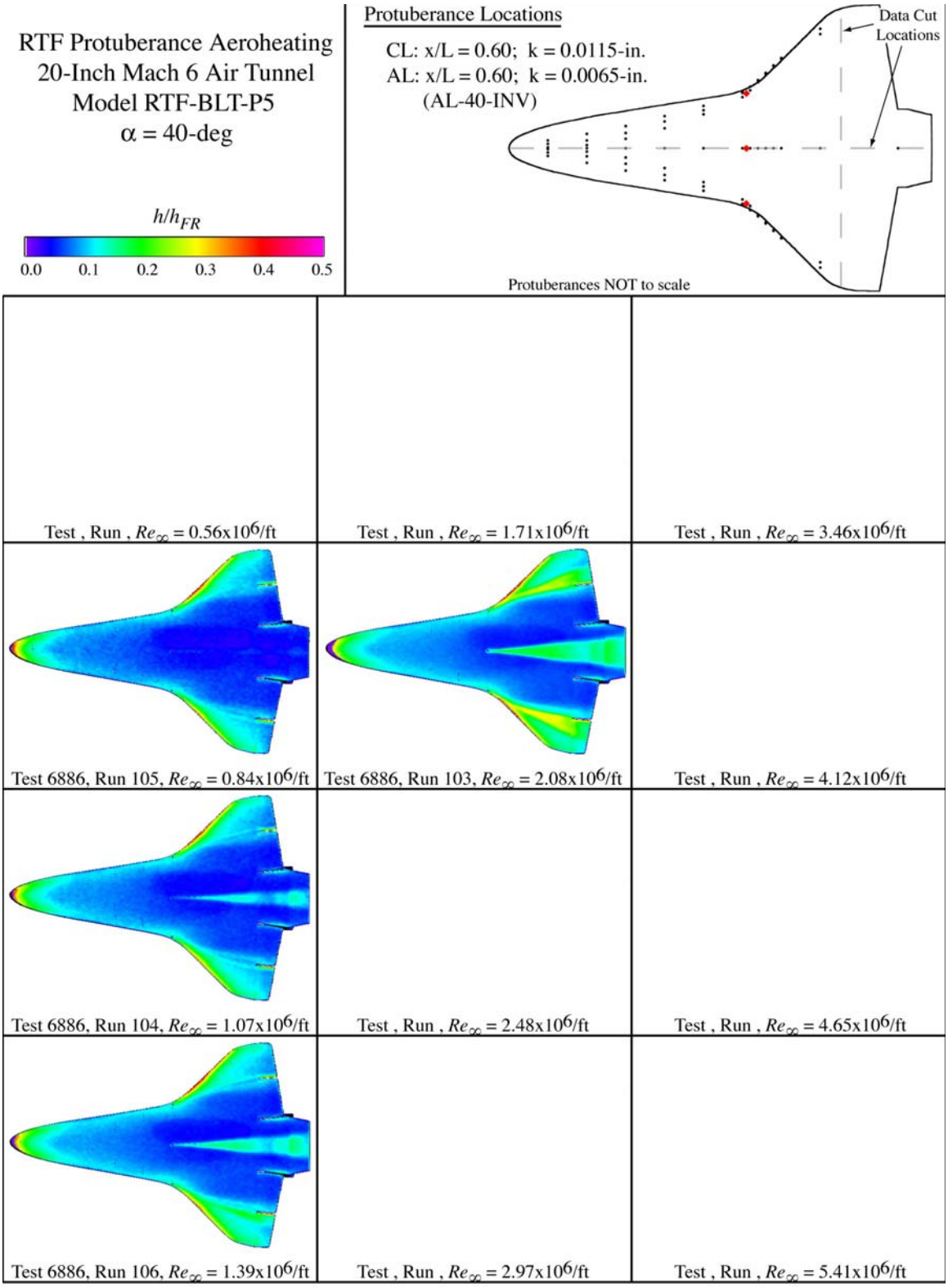

Figure A.64: RTF-BLT-P5 global aeroheating in the 20-Inch Mach 6 Air Tunnel at α = 40-deg, x/L = 0.60, k_{CL} = 0.0115-in., $k_{AL\text{-}40\text{-}INV}$ = 0.0065-in.

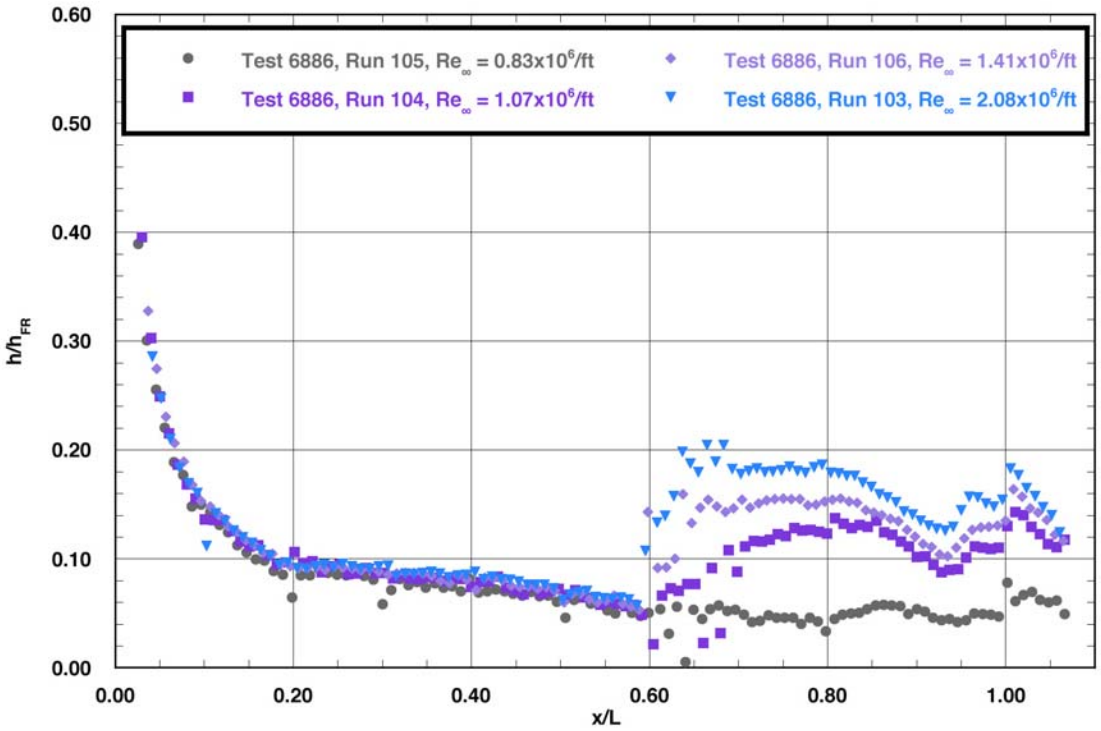

Figure A.65: RTF-BLT-P5 centerline data in the 20-Inch Mach 6 Air Tunnel at α = 40-deg, x/L = 0.60, k_{CL} = 0.0115-in., $k_{AL\text{-}40\text{-}INV}$ = 0.0065-in.

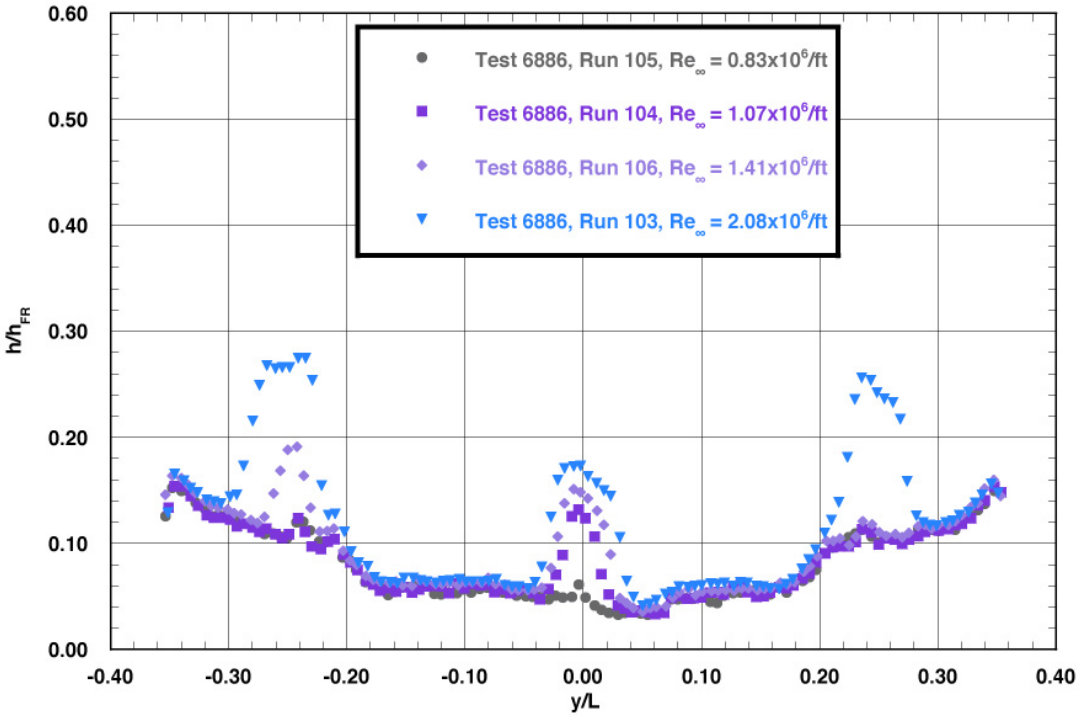

Figure A.66: RTF-BLT-P5 spanwise data (x/L = 0.85) in the 20-Inch Mach 6 Air Tunnel at α = 40-deg, x/L = 0.60, k_{CL} = 0.0115-in., $k_{AL\text{-}40\text{-}INV}$ = 0.0065-in.

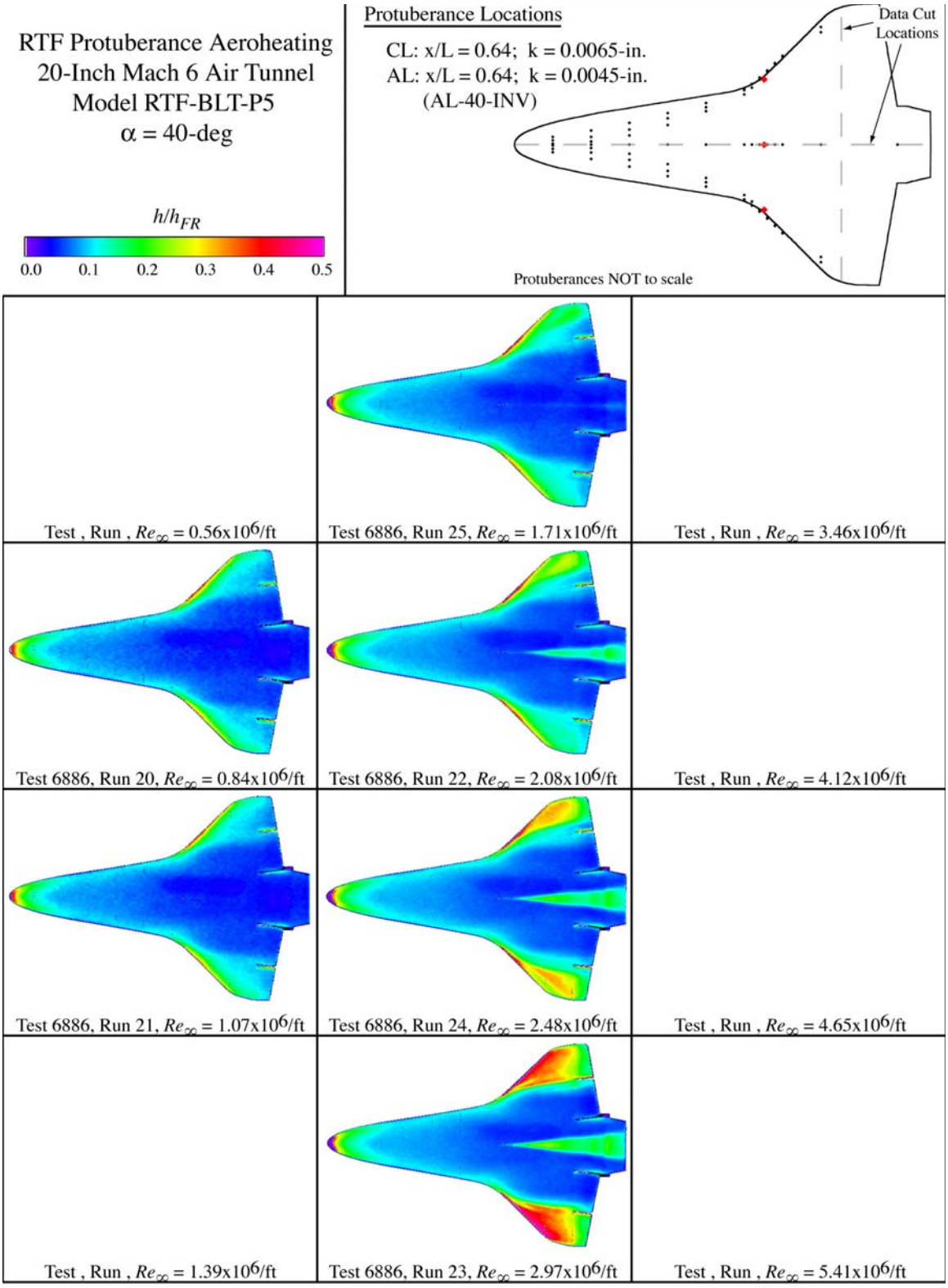

Figure A.67: RTF-BLT-P5 global aeroheating in the 20-Inch Mach 6 Air Tunnel at α = 40-deg, x/L = 0.64, k_{CL} = 0.0065-in., $k_{AL\text{-}40\text{-}INV}$ = 0.0045-in.

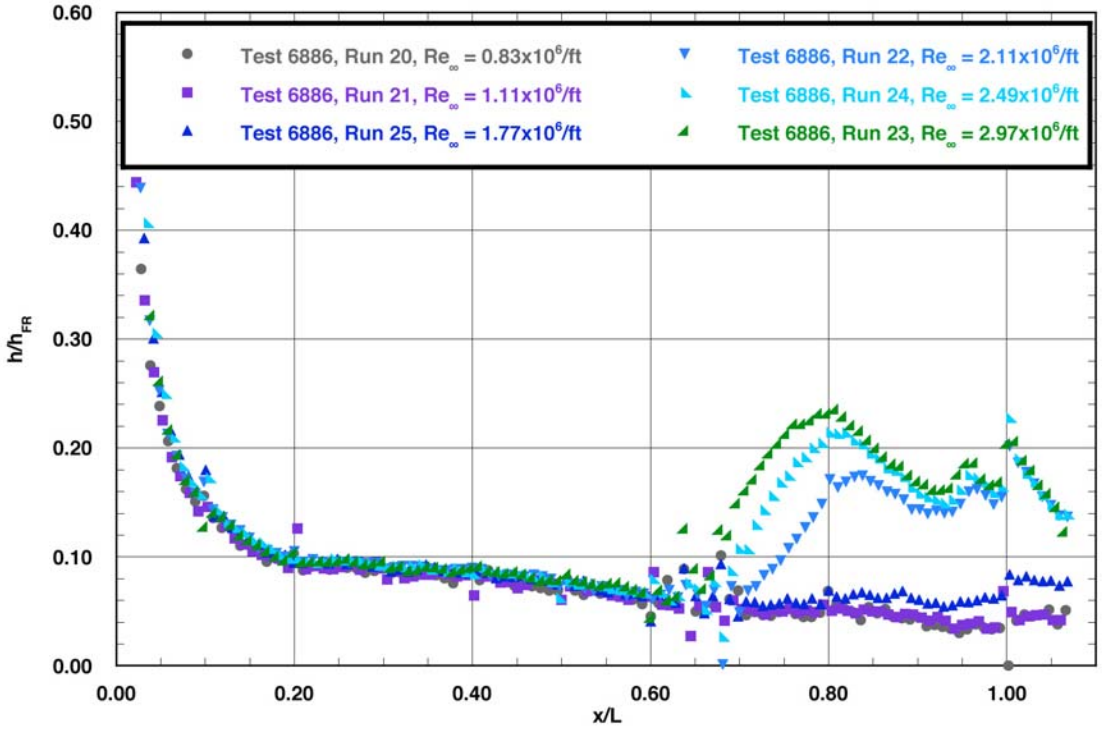

Figure A.68: RTF-BLT-P5 centerline data in the 20-Inch Mach 6 Air Tunnel at α = 40-deg, x/L = 0.64, k_{CL} = 0.0065-in., $k_{AL\text{-}40\text{-}INV}$ = 0.0045-in.

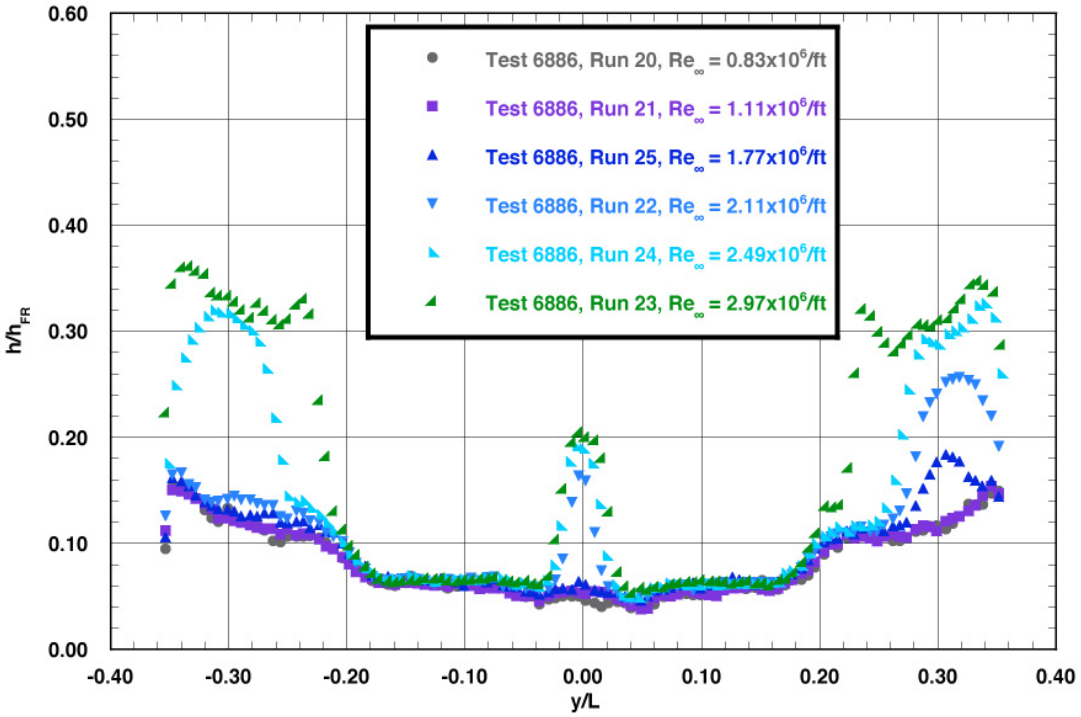

Figure A.69: RTF-BLT-P5 spanwise data (x/L = 0.85) in the 20-Inch Mach 6 Air Tunnel at α = 40-deg, x/L = 0.64, k_{CL} = 0.0065-in., $k_{AL\text{-}40\text{-}INV}$ = 0.0045-in.

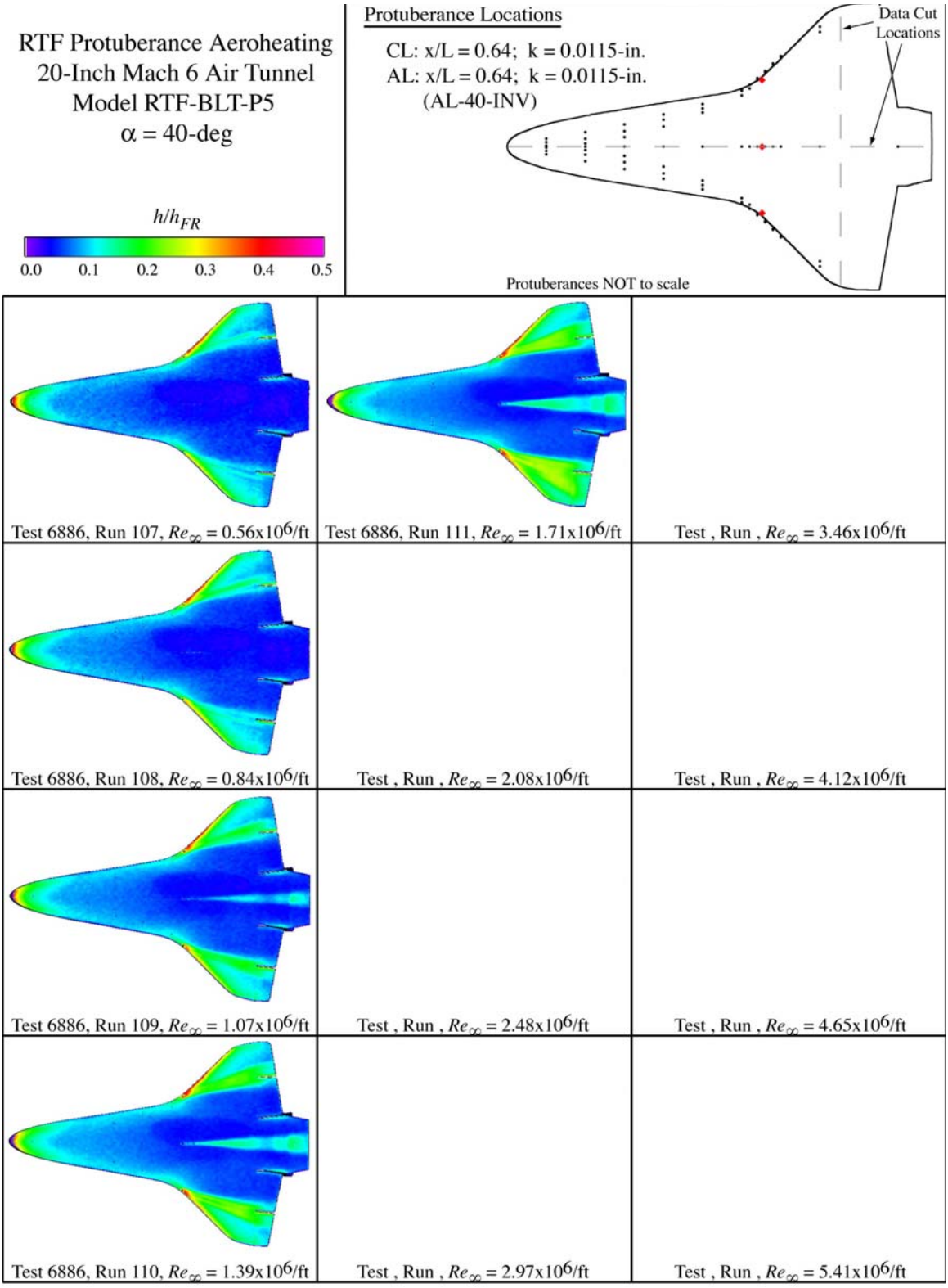

Figure A.70: RTF-BLT-P5 global aeroheating in the 20-Inch Mach 6 Air Tunnel at α = 40-deg, x/L = 0.64, k_{CL} = 0.0115-in., $k_{AL\text{-}40\text{-}INV}$ = 0.0115-in.

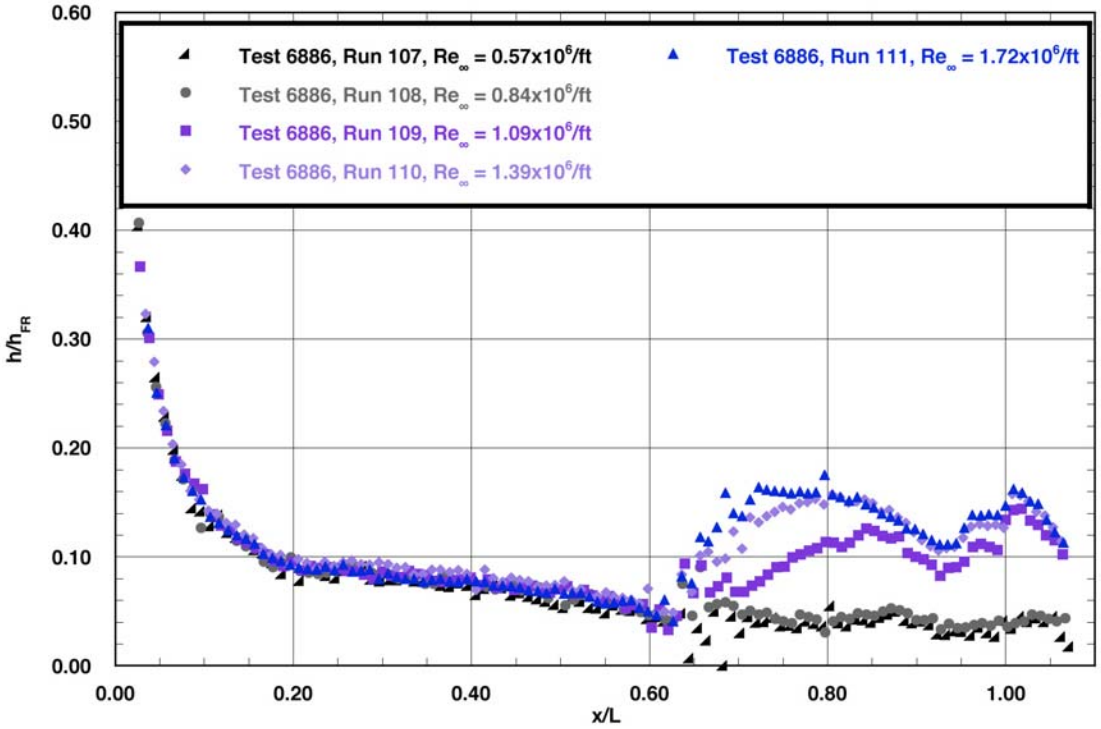

Figure A.71: RTF-BLT-P5 centerline data in the 20-Inch Mach 6 Air Tunnel at α = 40-deg, x/L = 0.64, k_{CL} = 0.0115-in., $k_{AL\text{-}40\text{-}INV}$ = 0.0115-in.

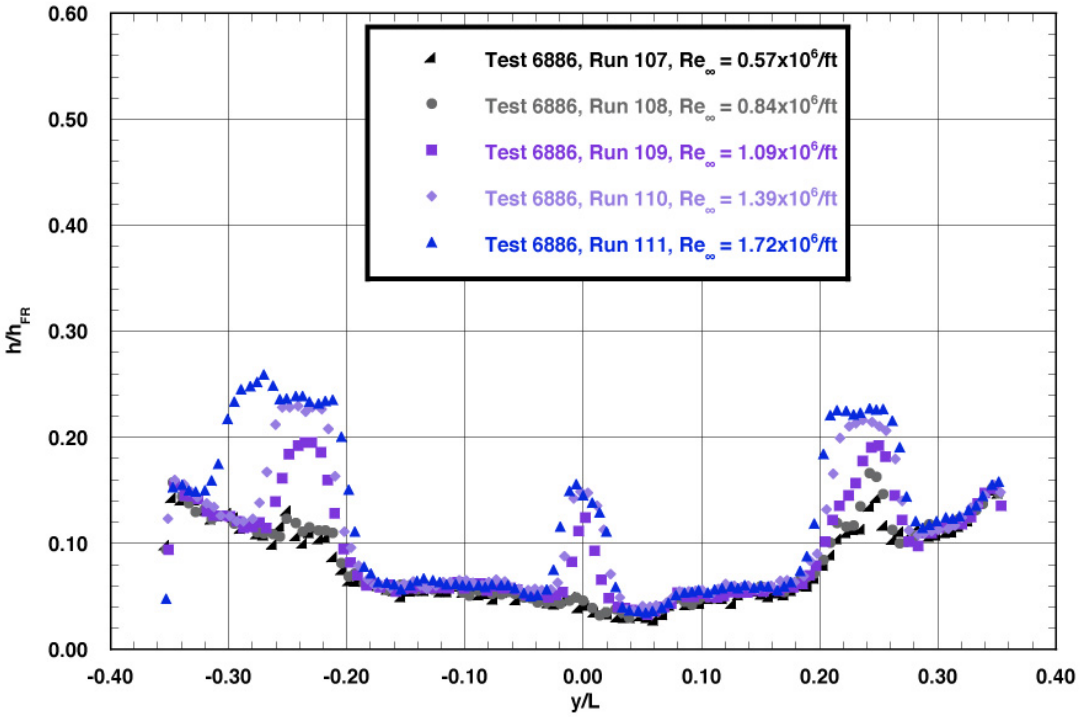

Figure A.72: RTF-BLT-P5 spanwise data (x/L = 0.85) in the 20-Inch Mach 6 Air Tunnel at α = 40-deg, x/L = 0.64, k_{CL} = 0.0115-in., $k_{AL\text{-}40\text{-}INV}$ = 0.0115-in.

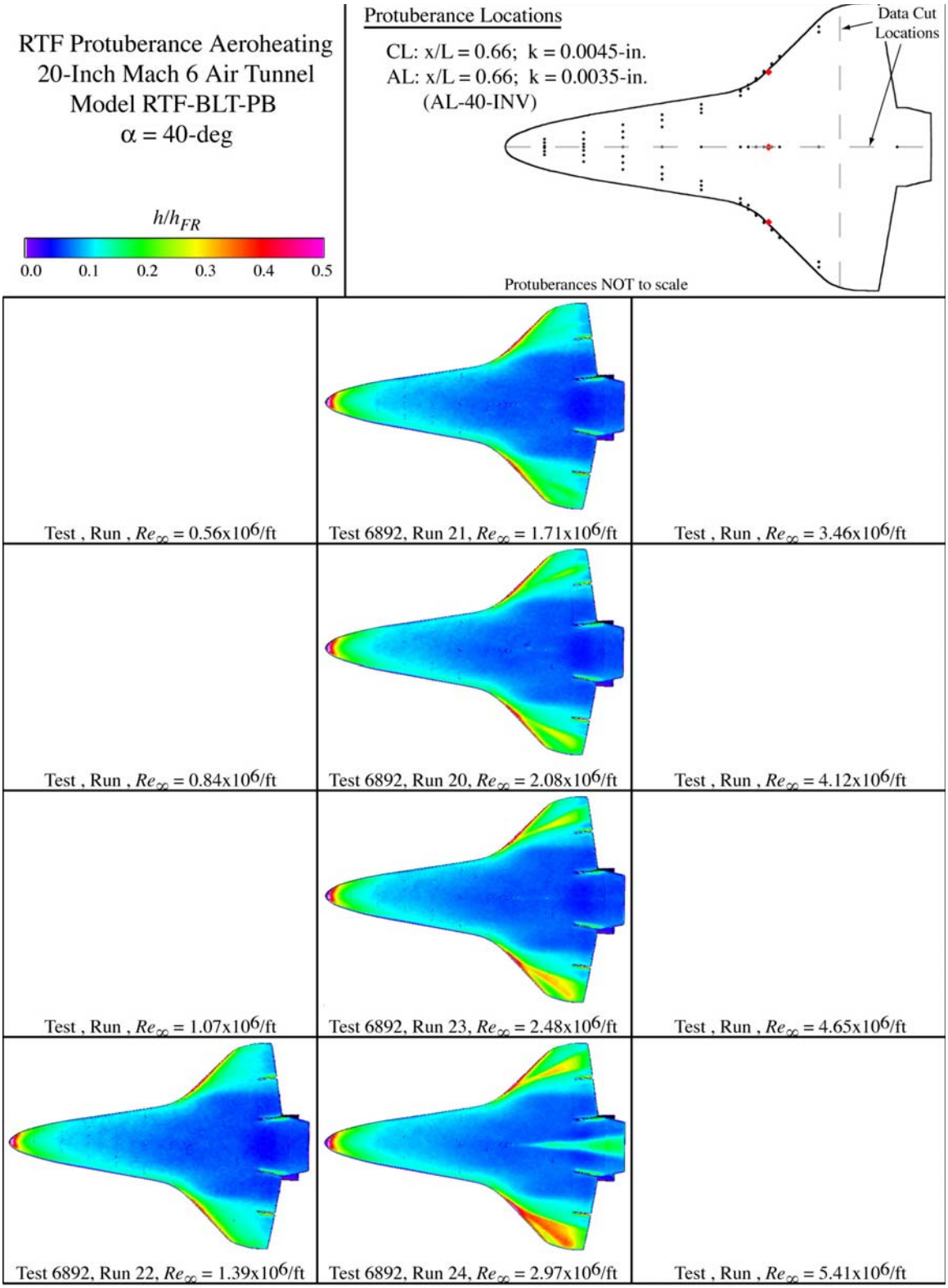

Figure A.73: RTF-BLT-PB global aeroheating in the 20-Inch Mach 6 Air Tunnel at α = 40-deg, x/L = 0.66, k_{CL} = 0.0045-in., $k_{AL\text{-}40\text{-}INV}$ = 0.0035-in.

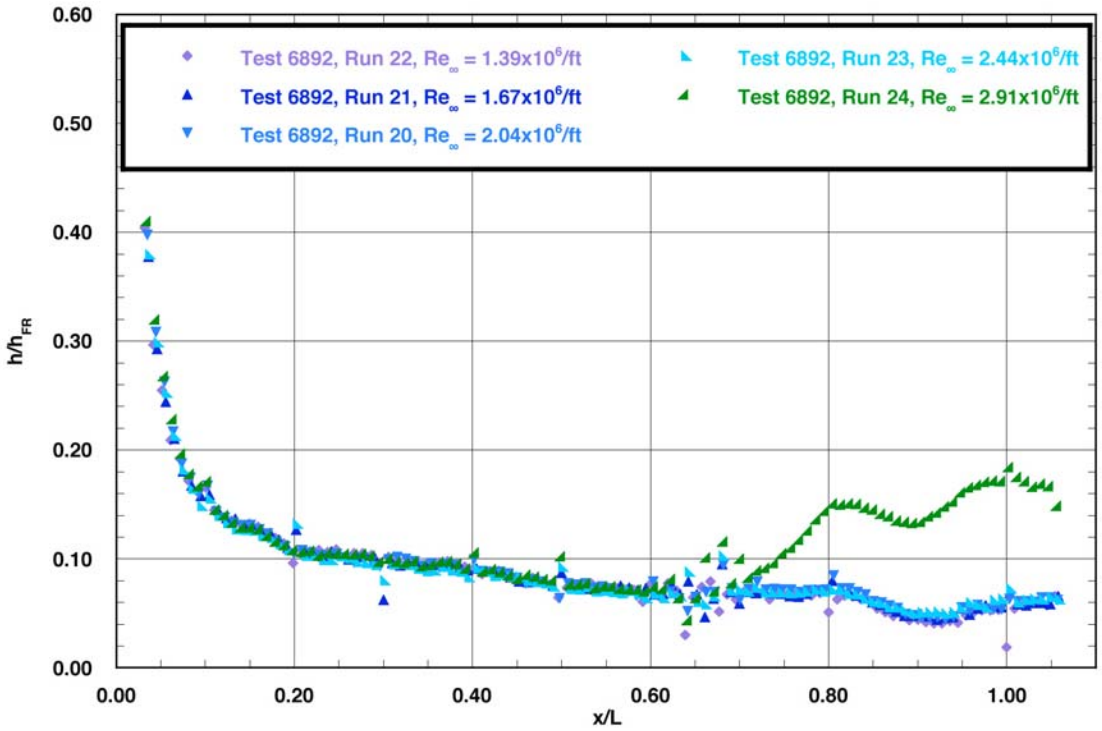

Figure A.74: RTF-BLT-PB centerline data in the 20-Inch Mach 6 Air Tunnel at α = 40-deg, x/L = 0.66, k_{CL} = 0.0045-in., $k_{AL\text{-}40\text{-}INV}$ = 0.0035-in.

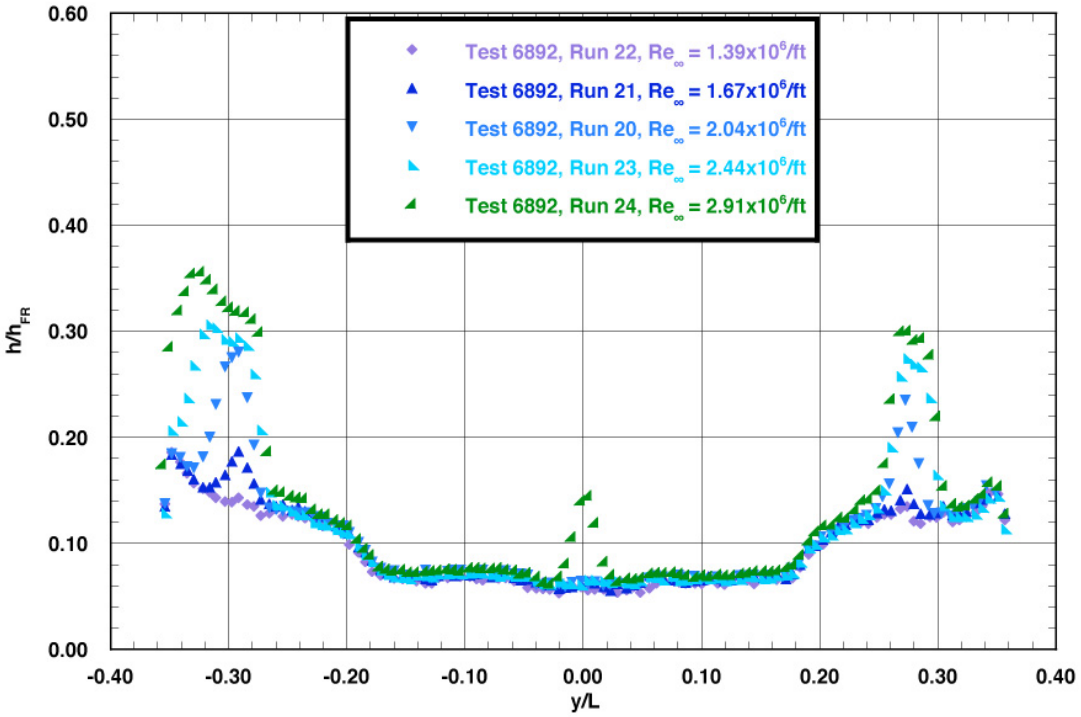

Figure A.75: RTF-BLT-PB spanwise data (x/L = 0.85) in the 20-Inch Mach 6 Air Tunnel at α = 40-deg, x/L = 0.66, k_{CL} = 0.0045-in., $k_{AL\text{-}40\text{-}INV}$ = 0.0035-in.

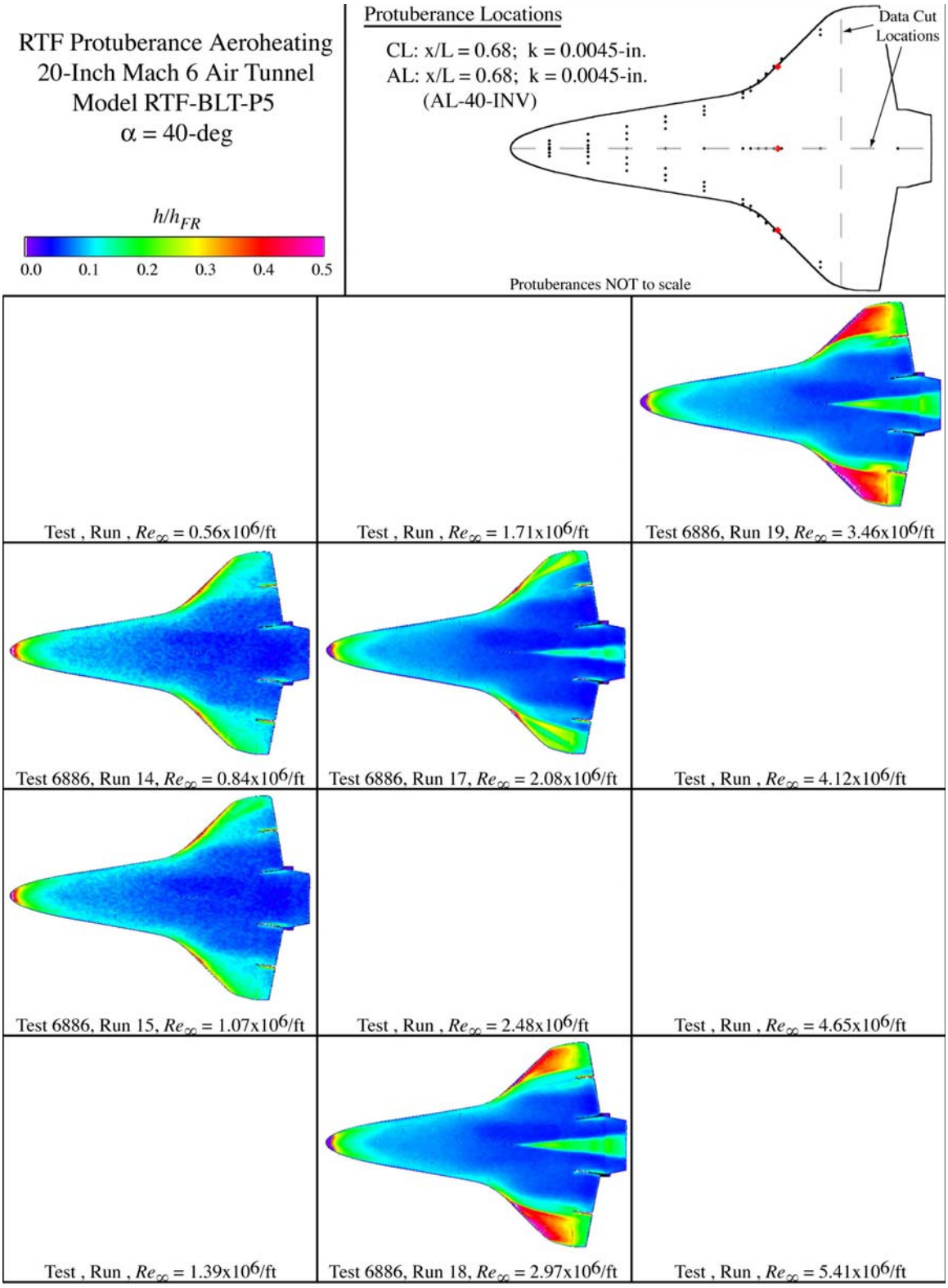

Figure A.76: RTF-BLT-P5 global aeroheating in the 20-Inch Mach 6 Air Tunnel at α = 40-deg, x/L = 0.68, k_{CL} = 0.0045-in., $k_{AL\text{-}40\text{-}INV}$ = 0.0045-in.

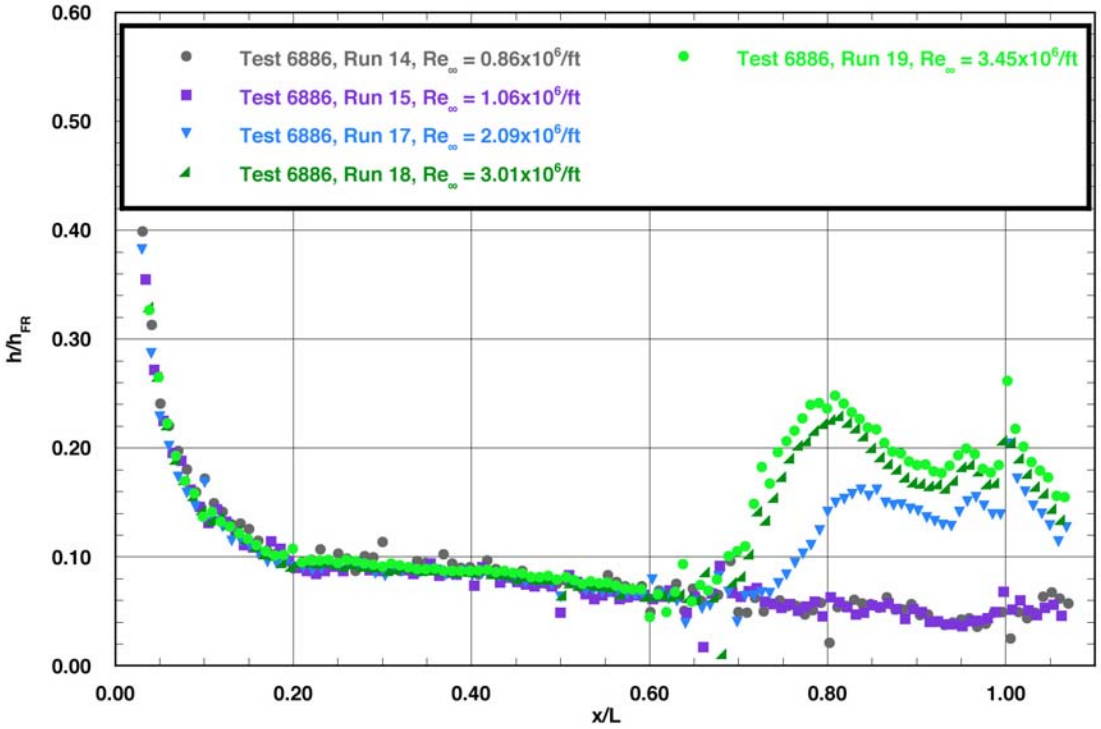

Figure A.77: RTF-BLT-P5 centerline data in the 20-Inch Mach 6 Air Tunnel at α = 40-deg, x/L = 0.68, k_{CL} = 0.0045-in., $k_{AL\text{-}40\text{-}INV}$ = 0.0045-in.

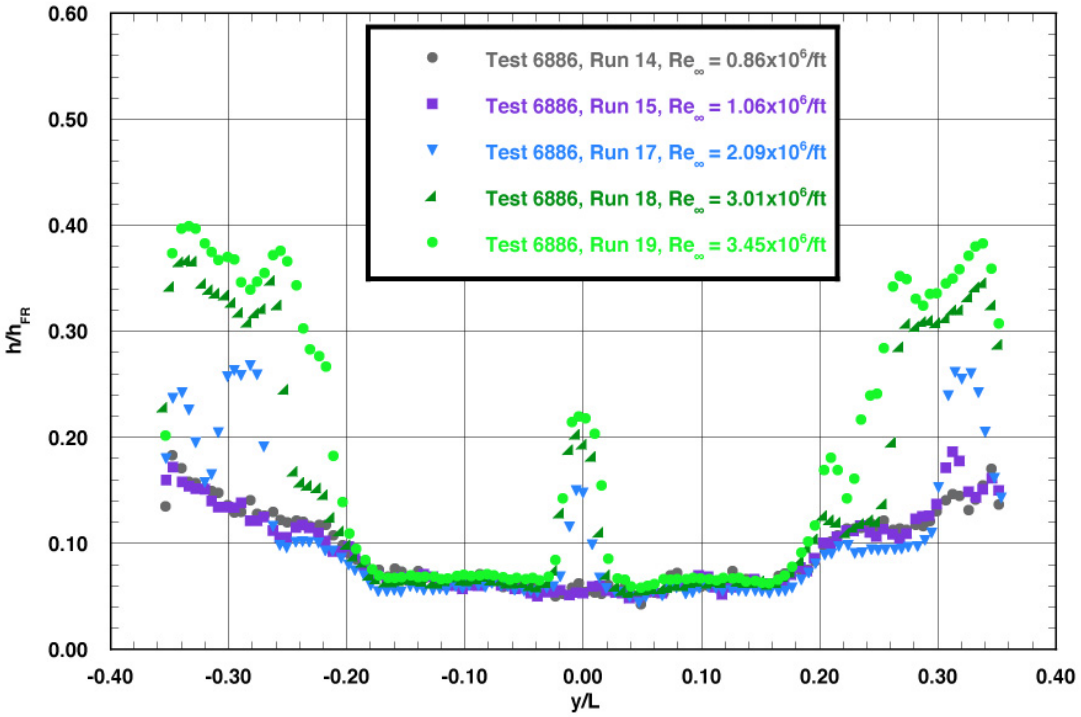

Figure A.78: RTF-BLT-P5 spanwise data (x/L = 0.85) in the 20-Inch Mach 6 Air Tunnel at α = 40-deg, x/L = 0.68, k_{CL} = 0.0045-in., $k_{AL\text{-}40\text{-}INV}$ = 0.0045-in.

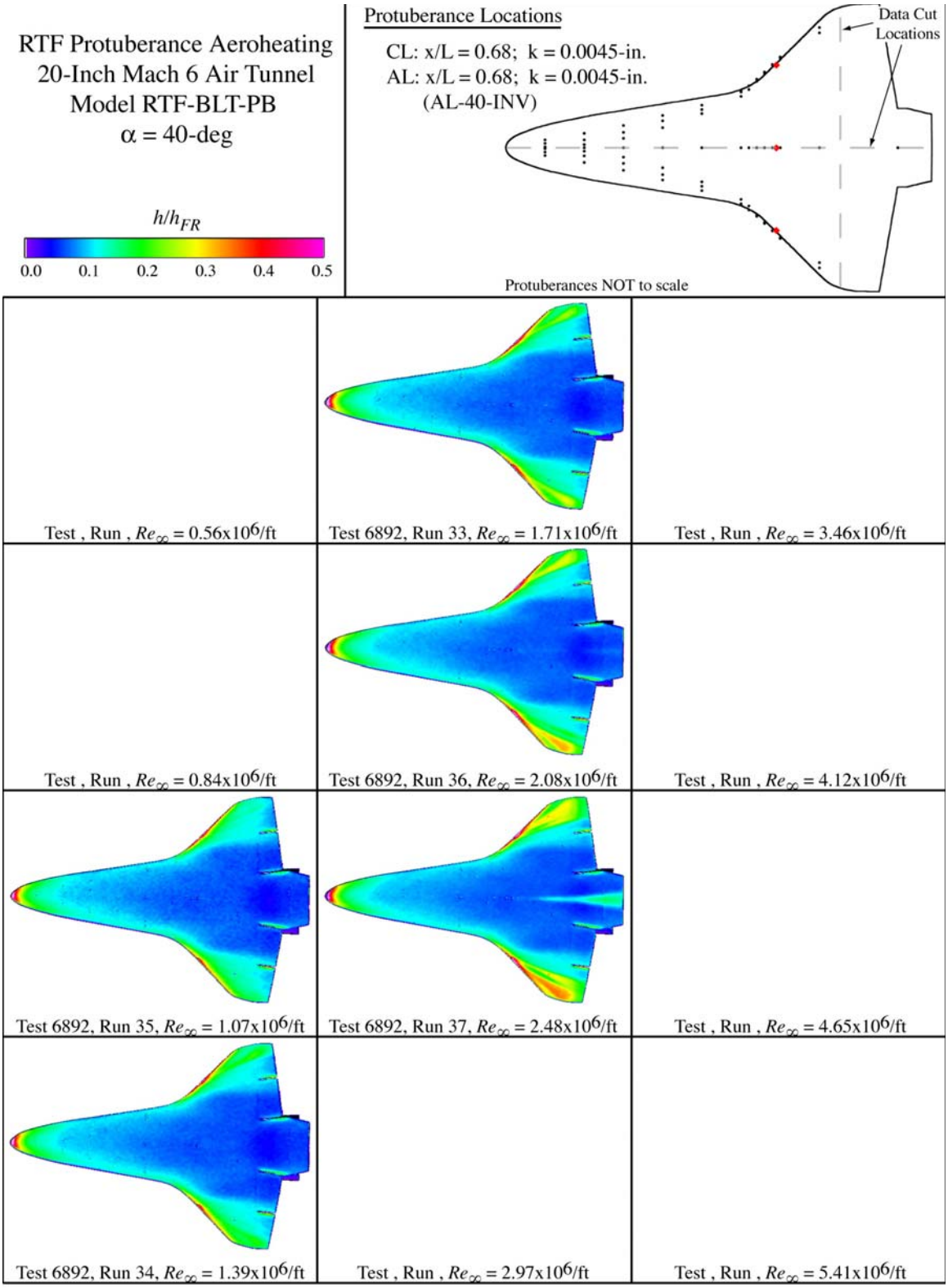

Figure A.79: RTF-BLT-PB global aeroheating in the 20-Inch Mach 6 Air Tunnel at α = 40-deg, x/L = 0.68, k_{CL} = 0.0045-in., $k_{AL\text{-}40\text{-}INV}$ = 0.0045-in.

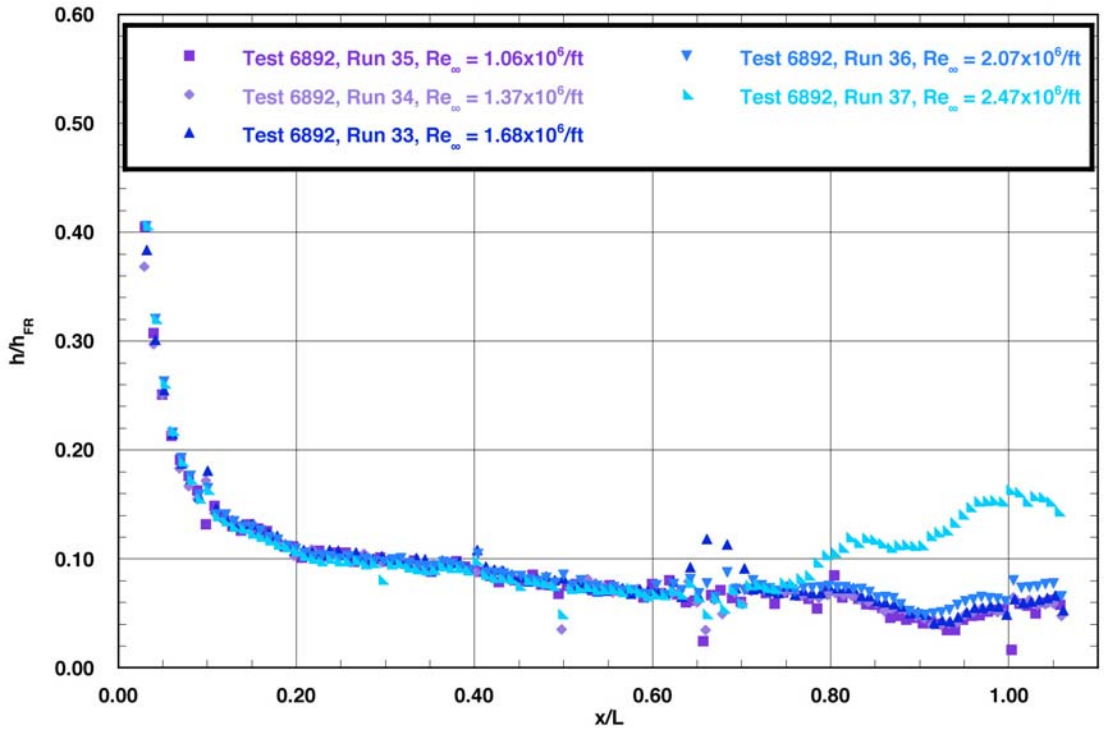

Figure A.80: RTF-BLT-PB centerline data in the 20-Inch Mach 6 Air Tunnel at α = 40-deg, x/L = 0.68, k_{CL} = 0.0045-in., $k_{AL\text{-}40\text{-}INV}$ = 0.0045-in.

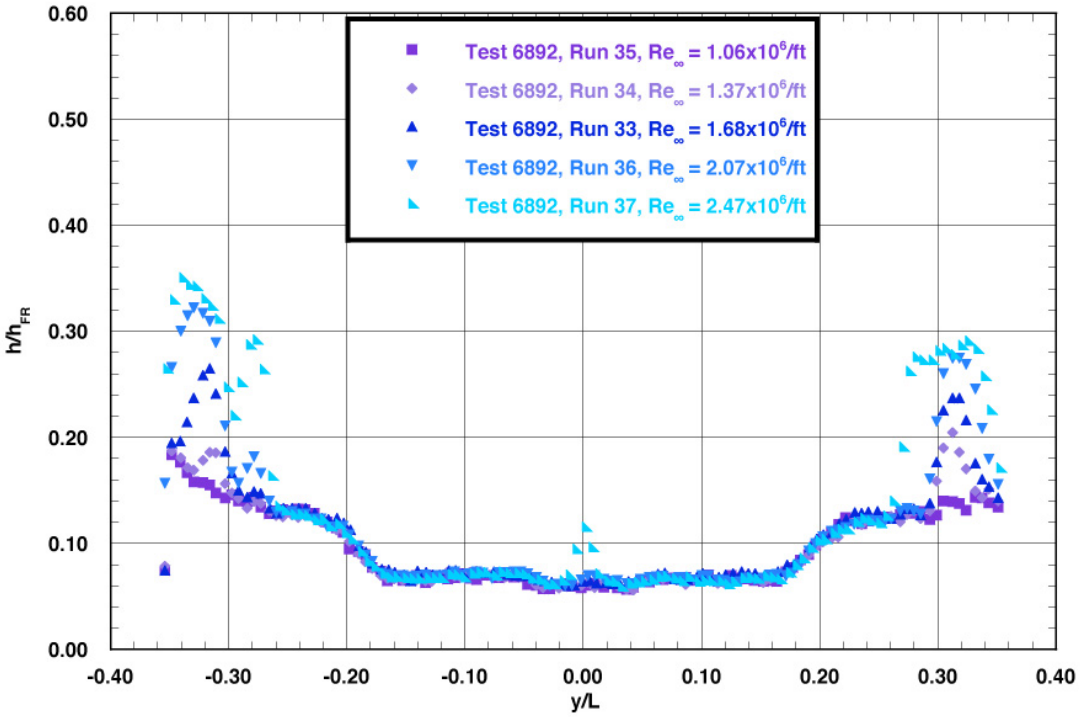

Figure A.81: RTF-BLT-PB spanwise data (x/L = 0.85) in the 20-Inch Mach 6 Air Tunnel at α = 40-deg, x/L = 0.68, k_{CL} = 0.0045-in., $k_{AL\text{-}40\text{-}INV}$ = 0.0045-in.

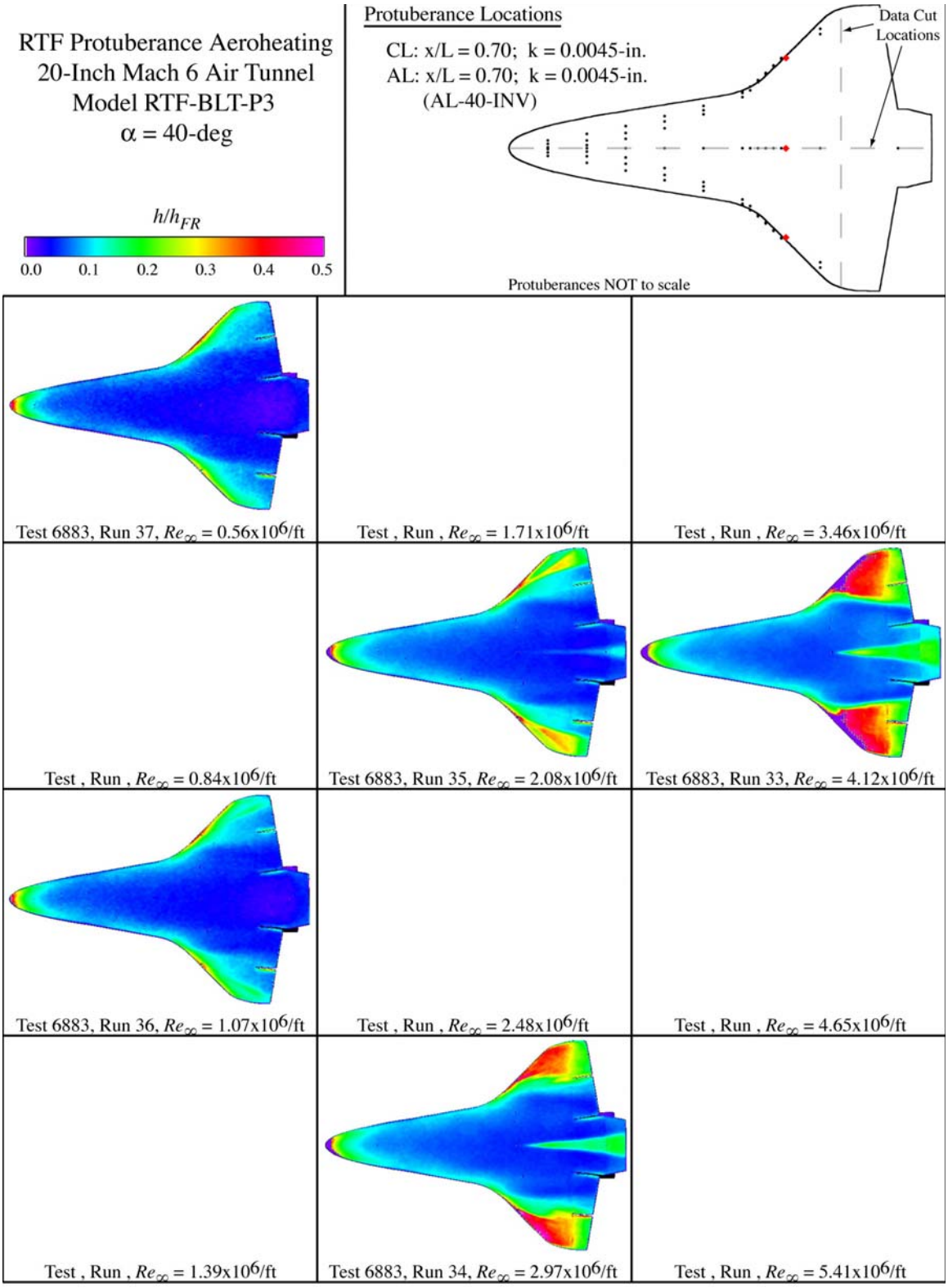

Figure A.82: RTF-BLT-P3 global aeroheating in the 20-Inch Mach 6 Air Tunnel at α = 40-deg, x/L = 0.70, k_{CL} = 0.0045-in., $k_{AL\text{-}40\text{-}INV}$ = 0.0045-in.

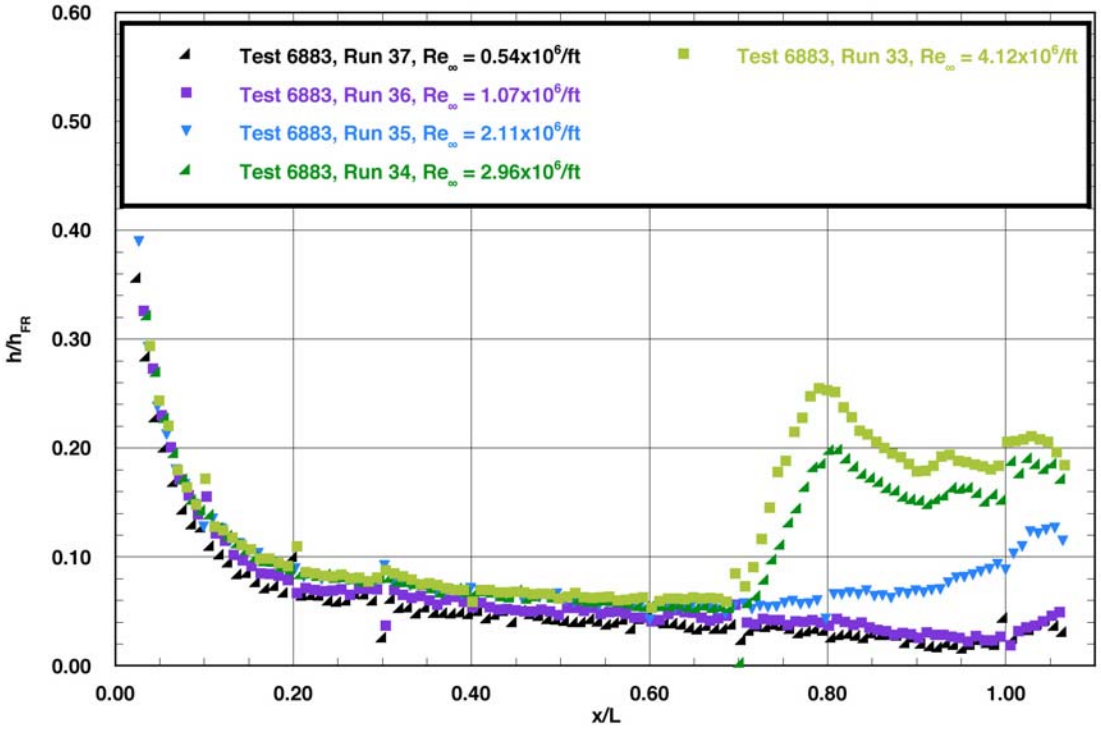

Figure A.83: RTF-BLT-P3 centerline data in the 20-Inch Mach 6 Air Tunnel at α = 40-deg, x/L = 0.70, k_{CL} = 0.0045-in., $k_{AL\text{-}40\text{-}INV}$ = 0.0045-in.

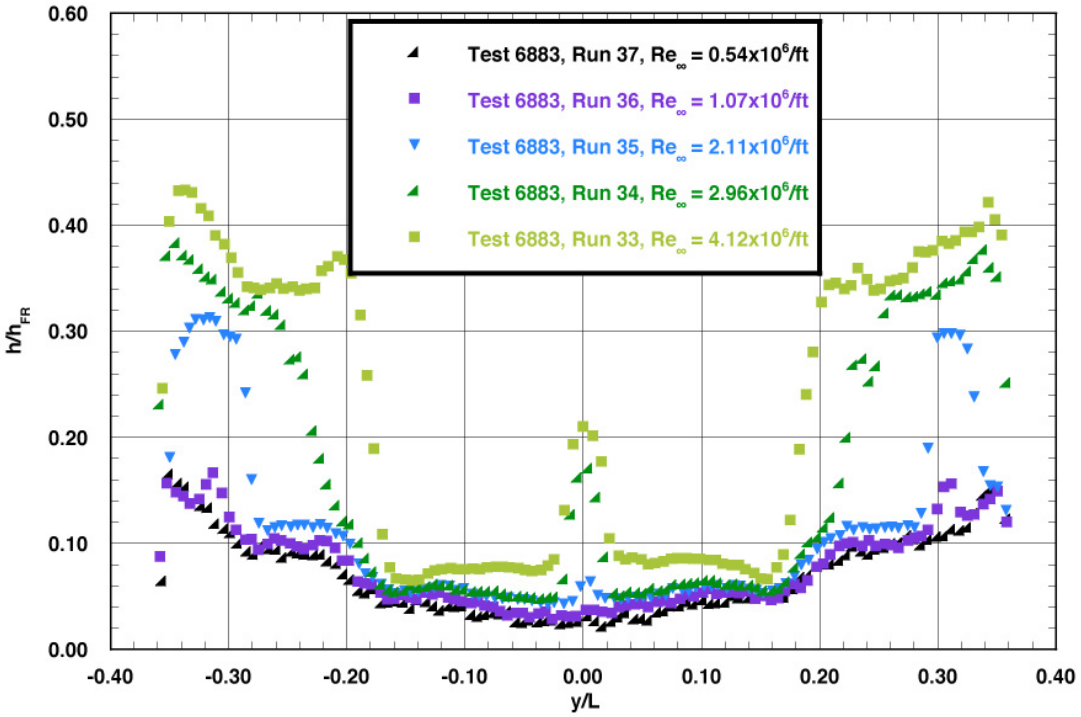

Figure A.84: RTF-BLT-P3 spanwise data (x/L = 0.85) in the 20-Inch Mach 6 Air Tunnel at α = 40-deg, x/L = 0.70, k_{CL} = 0.0045-in., $k_{AL\text{-}40\text{-}INV}$ = 0.0045-in.

Appendix B: 31-Inch Mach 10 Air Tunnel Aeroheating

Table B.1: Cross Reference of Figure Numbers Versus Parametrics for Phosphor Images from the 31-Inch Mach 10 Air Tunnel.

α (deg.)	Model	$(x/L)_{CL}$	k_{CL} (in.)	AL	$(x/L)_{AL}$ (in.)	k_{AL}	Figure
30	RTF-BLT-P7	-	-	-	-	-	B.1
30	RTF-BLT-P7	0.20	0.0115	30-INV	0.20	0.0115	B.4
30	RTF-BLT-P7	0.30	0.0115	30-INV	0.30	0.0115	B.7
30	RTF-BLT-P7	0.40	0.0115	30-INV	0.40	0.0115	B.10
30	RTF-BLT-P7	0.50	0.0115	30-INV	0.50	0.0115	B.13
40	RTF-BLT-P7	-	-	-	-	-	B.16
40	RTF-BLT-P7	0.20	0.0115	40-INV	0.20	0.0115	B.19
40	RTF-BLT-P8	0.20	0.0115	40-INV	0.20	0.0115	B.22
40	RTF-BLT-P7	0.30	0.0115	40-INV	0.30	0.0115	B.25
40	RTF-BLT-P8	0.40	0.0065	40-INV	0.40	0.0065	B.28
40	RTF-BLT-P7	0.40	0.0115	40-INV	0.40	0.0115	B.31
40	RTF-BLT-P7	0.50	0.0115	40-INV	0.50	0.0115	B.34
40	RTF-BLT-P8	0.60	0.0065	40-INV	0.60	0.0065	B.37
40	RTF-BLT-P7	0.60	0.0115	40-INV	0.60	0.0115	B.40
40	RTF-BLT-P7	0.70	0.0115	40-INV	0.70	0.0115	B.43

Note: Corresponding data cuts are located immediately after figures.

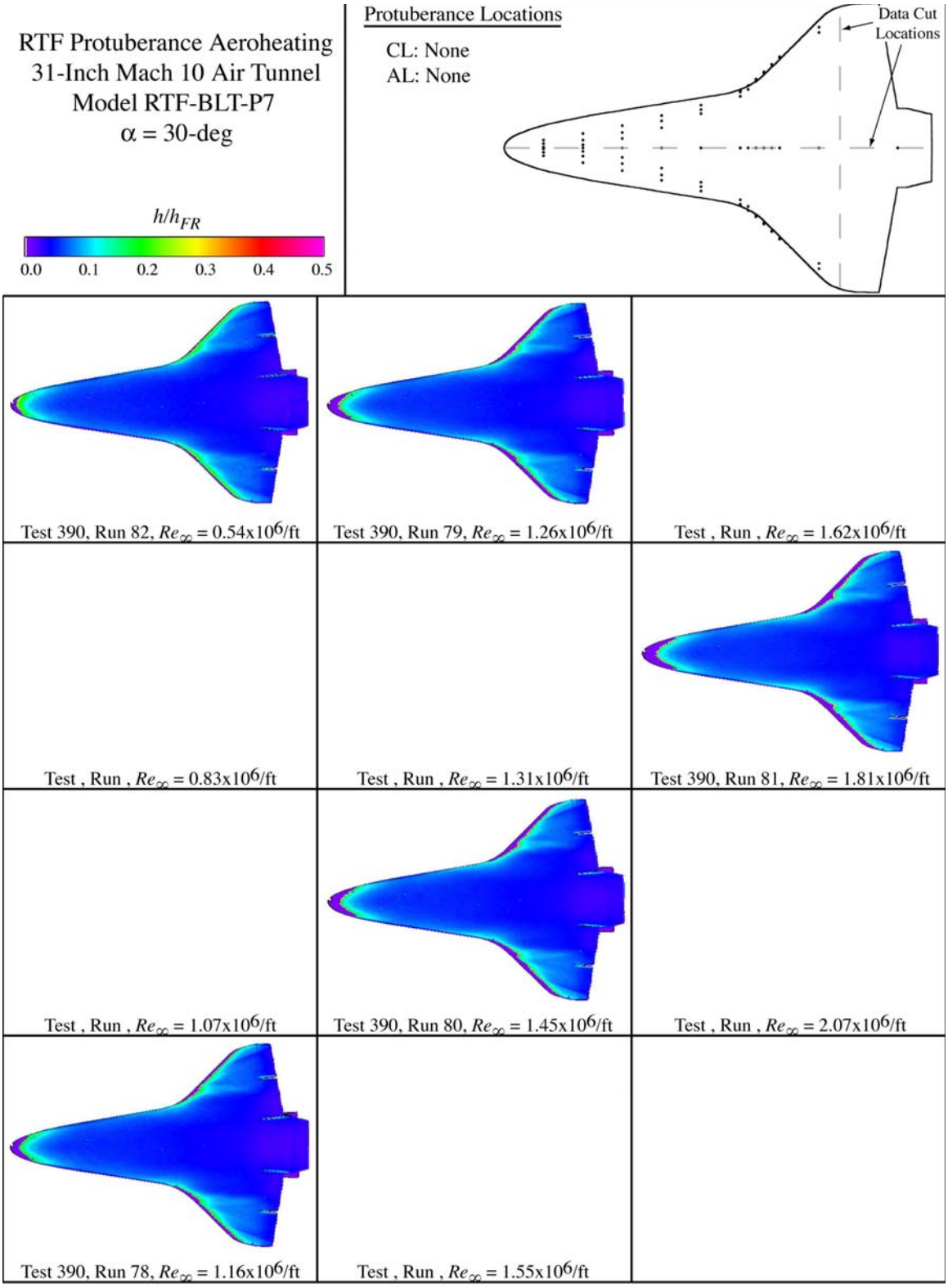

Figure B.1: RTF-BLT-P7 global aeroheating in the 31-Inch Mach 10 Air Tunnel at α = 30-deg, baseline.

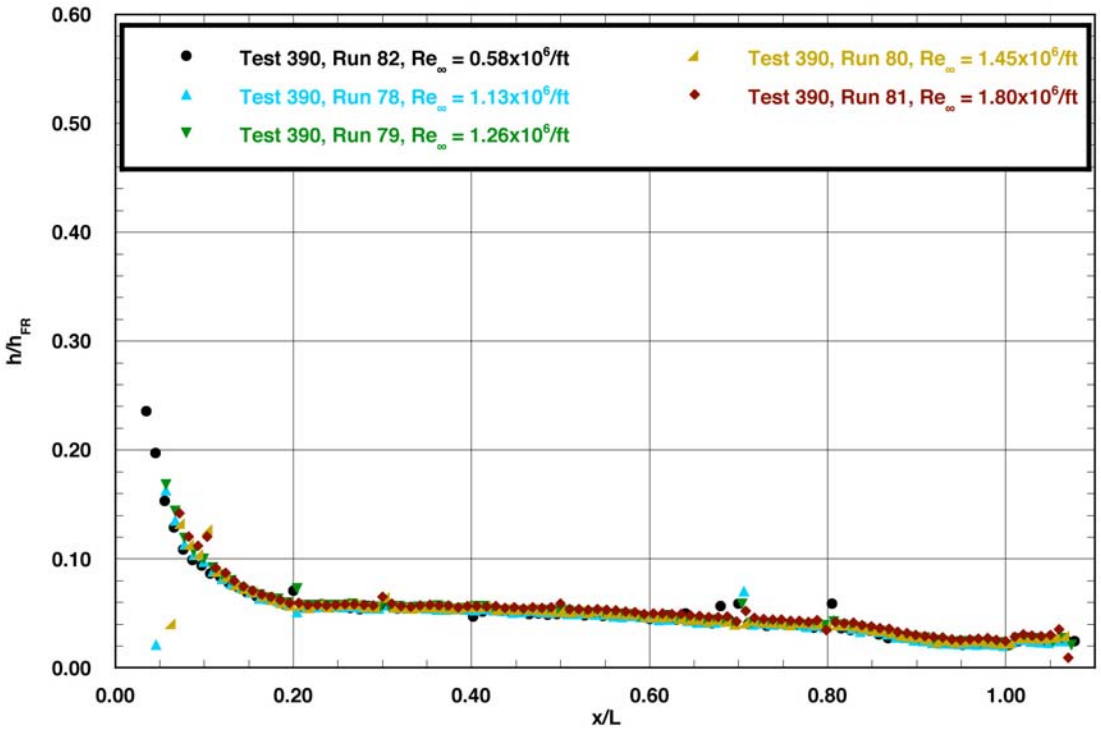

Figure B.2: RTF-BLT-P7 centerline data in the 31-Inch Mach 10 Air Tunnel at α = 30-deg, baseline.

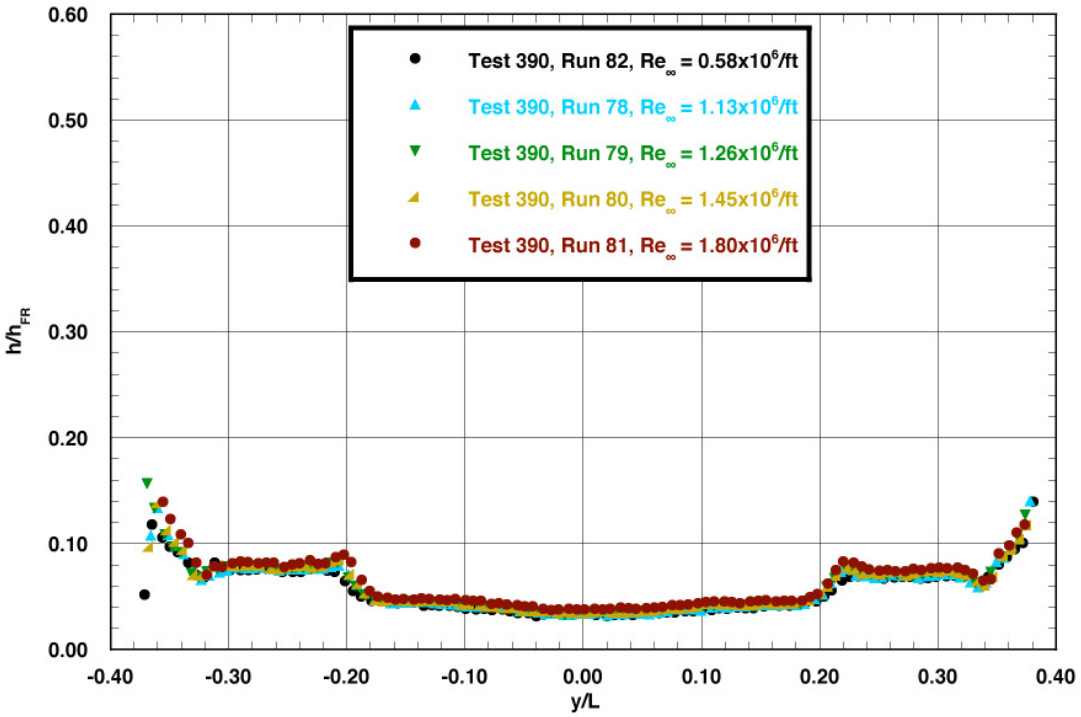

Figure B.3: RTF-BLT-P7 spanwise data (*x/L* = 0.85) in the 31-Inch Mach 10 Air Tunnel at α = 30-deg, baseline.

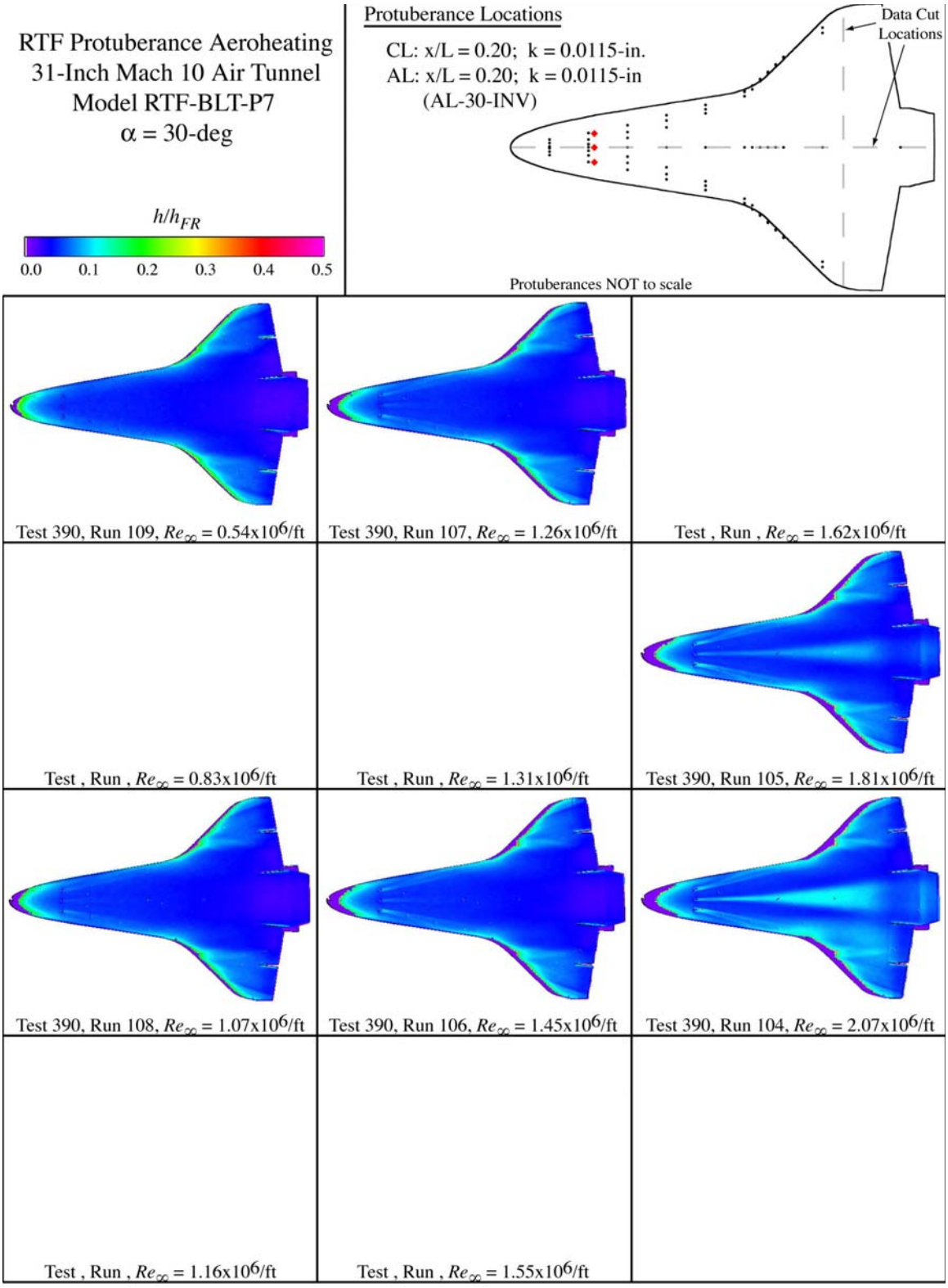

Figure B.4: RTF-BLT-P7 global aeroheating in the 31-Inch Mach 10 Air Tunnel at α = 30-deg, x/L = 0.20, k_{CL} = 0.0115-in., $k_{AL\text{-}30\text{-}INV}$ = 0.0115-in.

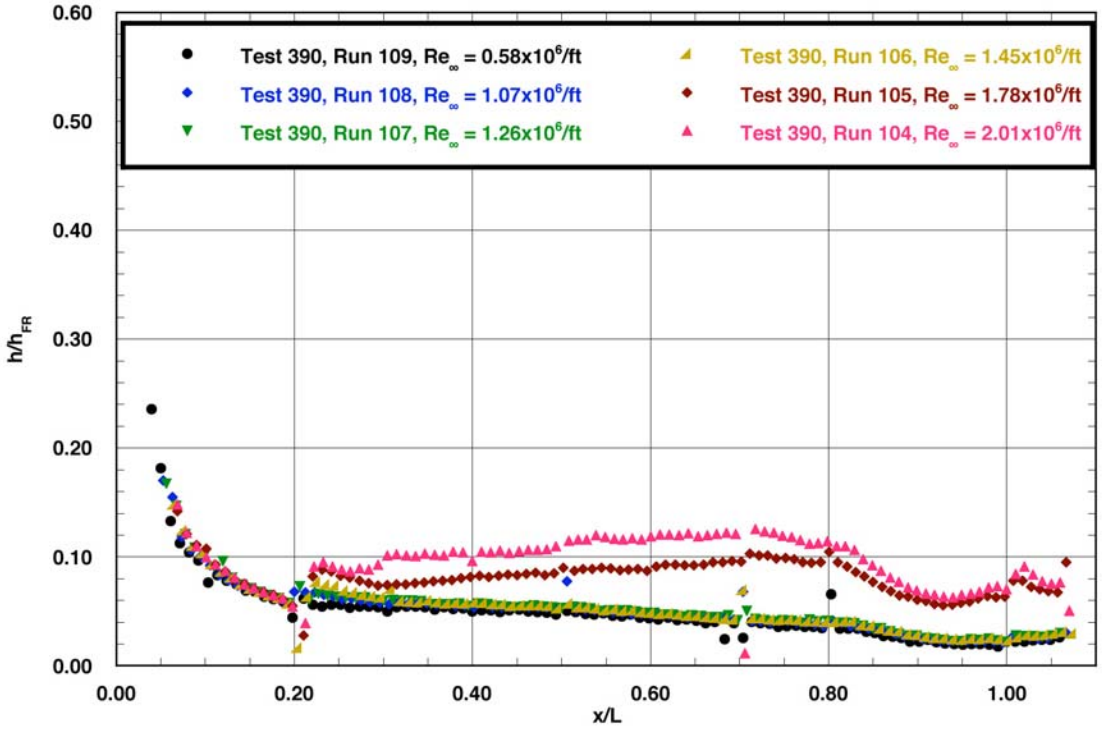

Figure B.5: RTF-BLT-P7 centerline data in the 31-Inch Mach 10 Air Tunnel at α = 30-deg, x/L = 0.20, k_{CL} = 0.0115-in., $k_{AL\text{-}30\text{-}INV}$ = 0.0115-in.

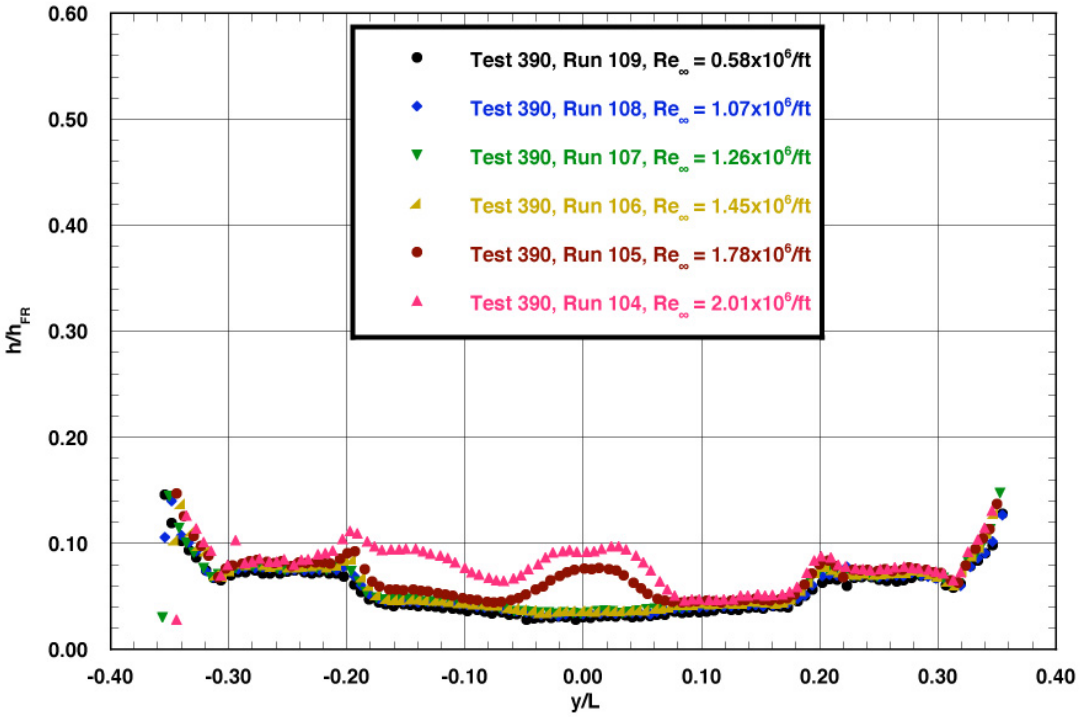

Figure B.6: RTF-BLT-P7 spanwise data (x/L = 0.85) in the 31-Inch Mach 10 Air Tunnel at α = 30-deg, x/L = 0.20, k_{CL} = 0.0115-in., $k_{AL\text{-}30\text{-}INV}$ = 0.0115-in.

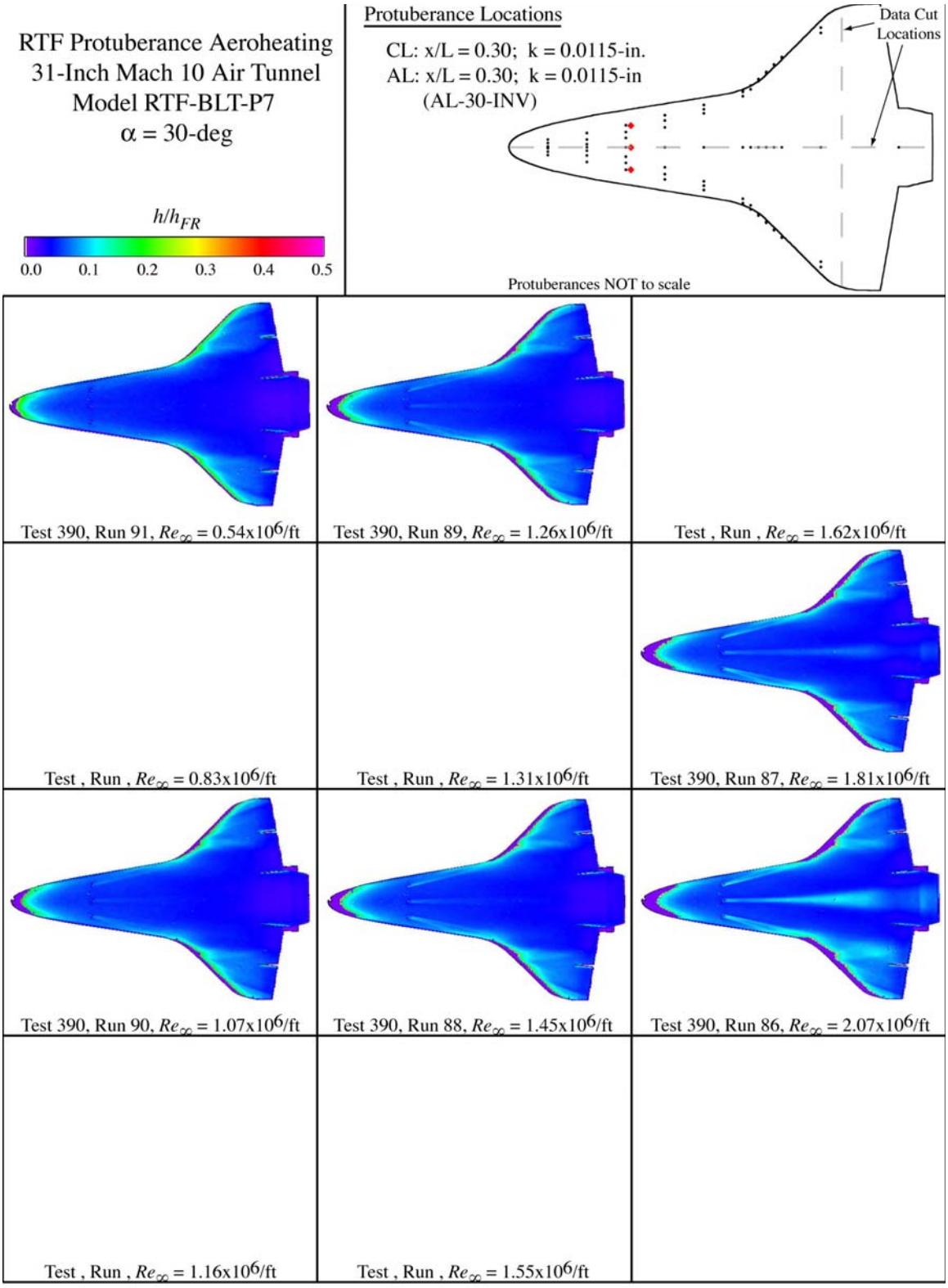

Figure B.7: RTF-BLT-P7 global aeroheating in the 31-Inch Mach 10 Air Tunnel at α = 30-deg, x/L = 0.30, k_{CL} = 0.0115-in., $k_{AL\text{-}30\text{-}INV}$ = 0.0115-in.

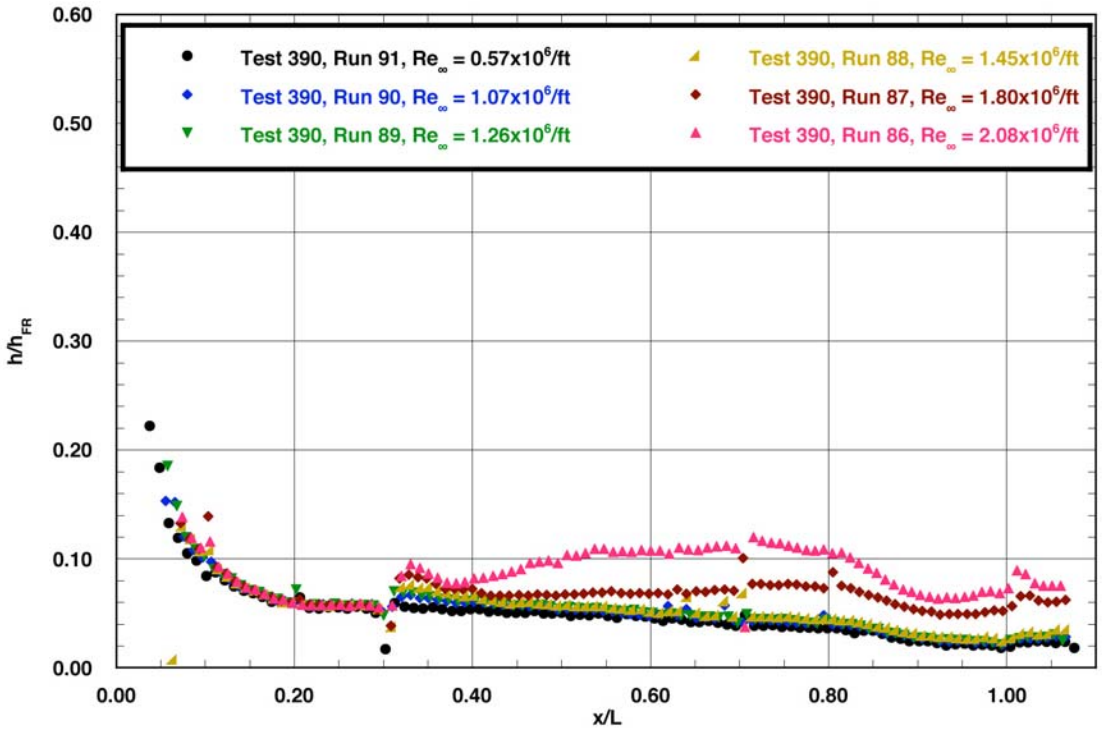

Figure B.8: RTF-BLT-P7 centerline data in the 31-Inch Mach 10 Air Tunnel at α = 30-deg, x/L = 0.30, k_{CL} = 0.0115-in., $k_{AL\text{-}30\text{-}INV}$ = 0.0115-in.

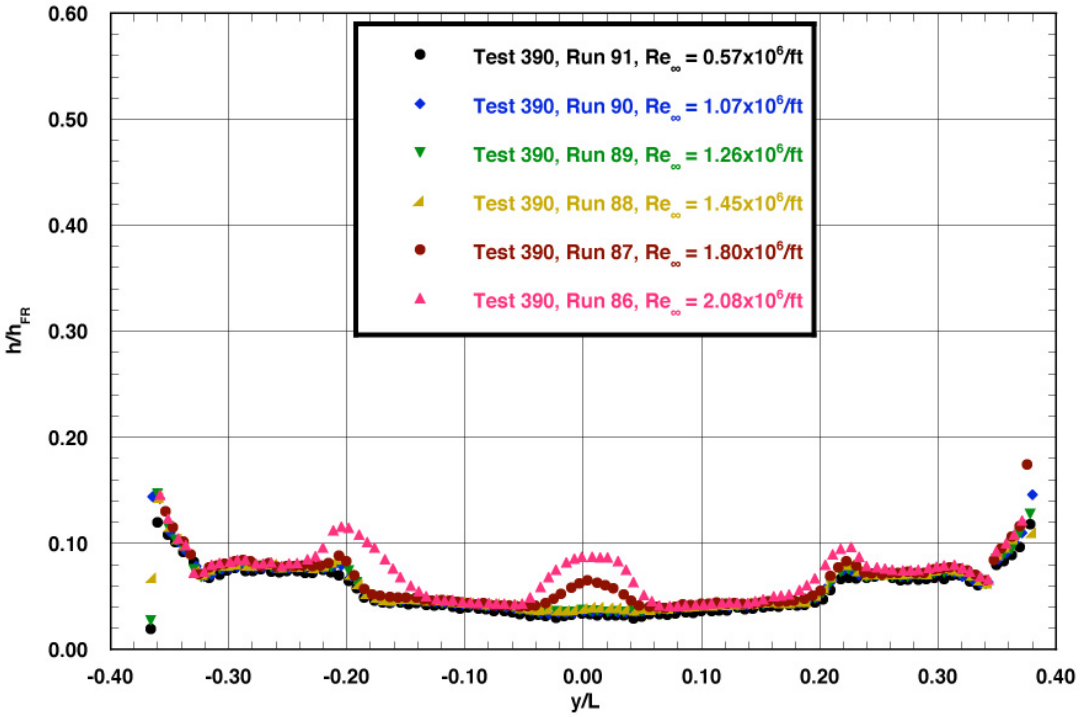

Figure B.9: RTF-BLT-P7 spanwise data (x/L = 0.85) in the 31-Inch Mach 10 Air Tunnel at α = 30-deg, x/L = 0.30, k_{CL} = 0.0115-in., $k_{AL\text{-}30\text{-}INV}$ = 0.0115-in.

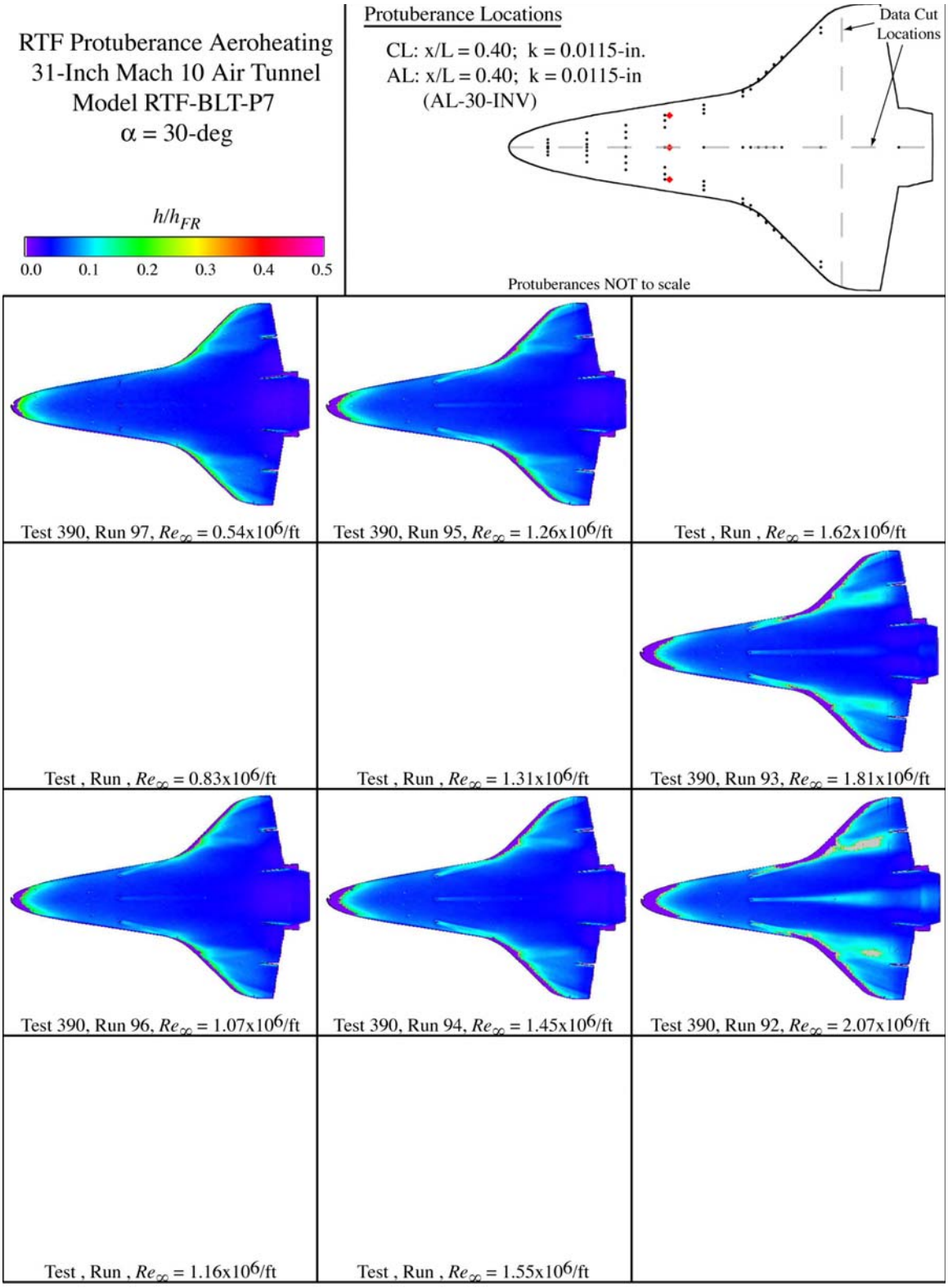

Figure B.10: RTF-BLT-P7 global aeroheating in the 31-Inch Mach 10 Air Tunnel at α = 30-deg, x/L = 0.40, k_{CL} = 0.0115-in., $k_{AL\text{-}30\text{-}INV}$ = 0.0115-in.

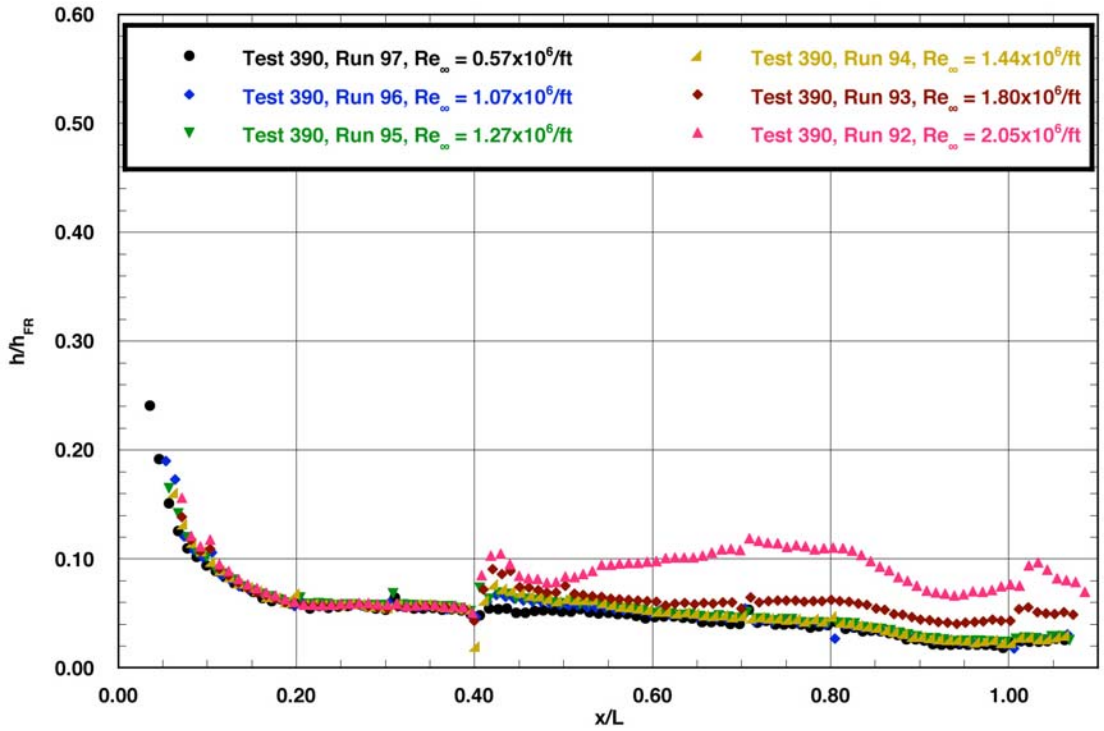

Figure B.11: RTF-BLT-P7 centerline data in the 31-Inch Mach 10 Air Tunnel at α = 30-deg, x/L = 0.40, k_{CL} = 0.0115-in., $k_{AL\text{-}30\text{-}INV}$ = 0.0115-in.

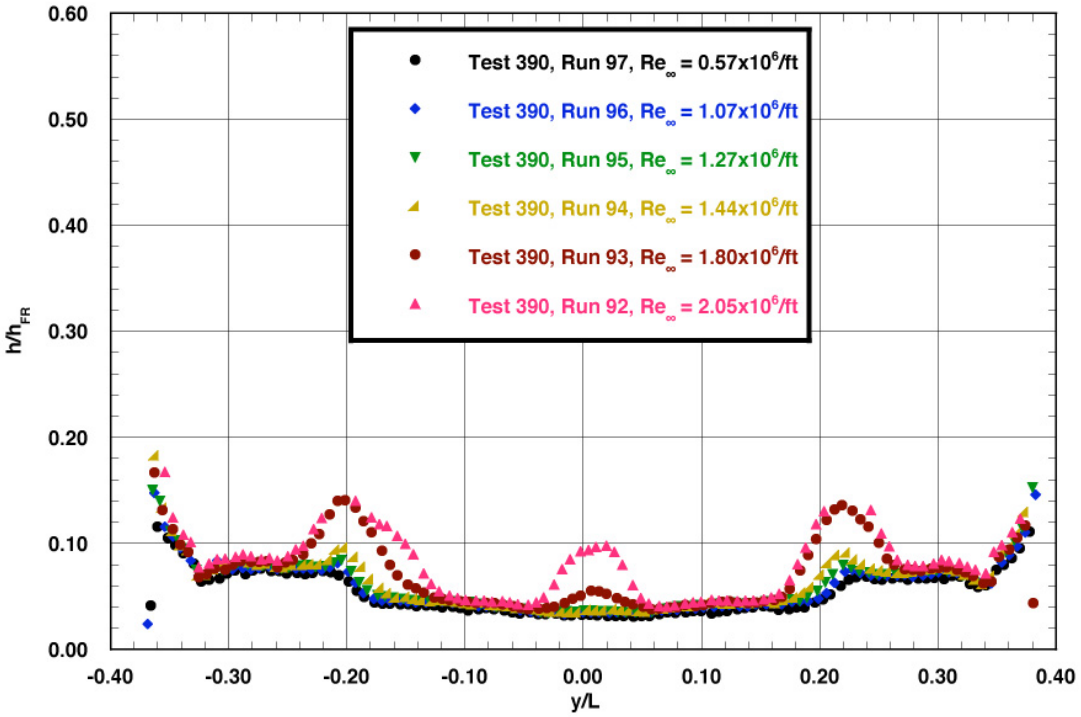

Figure B.12: RTF-BLT-P7 spanwise data (x/L = 0.85) in the 31-Inch Mach 10 Air Tunnel at α = 30-deg, x/L = 0.40, k_{CL} = 0.0115-in., $k_{AL\text{-}30\text{-}INV}$ = 0.0115-in.

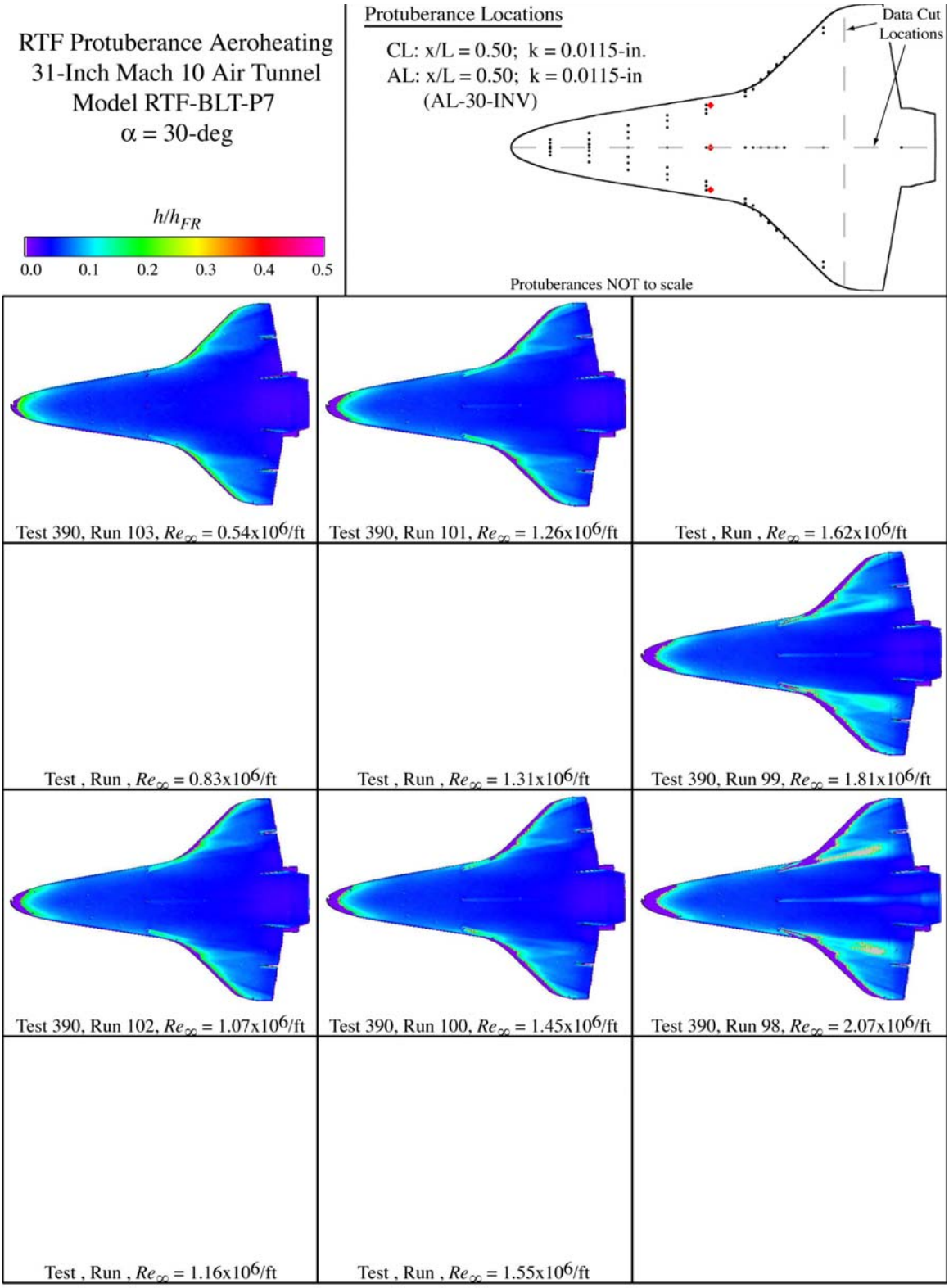

Figure B.13: RTF-BLT-P7 global aeroheating in the 31-Inch Mach 10 Air Tunnel at α = 30-deg, x/L = 0.50, k_{CL} = 0.0115-in., $k_{AL\text{-}30\text{-}INV}$ = 0.0115-in.

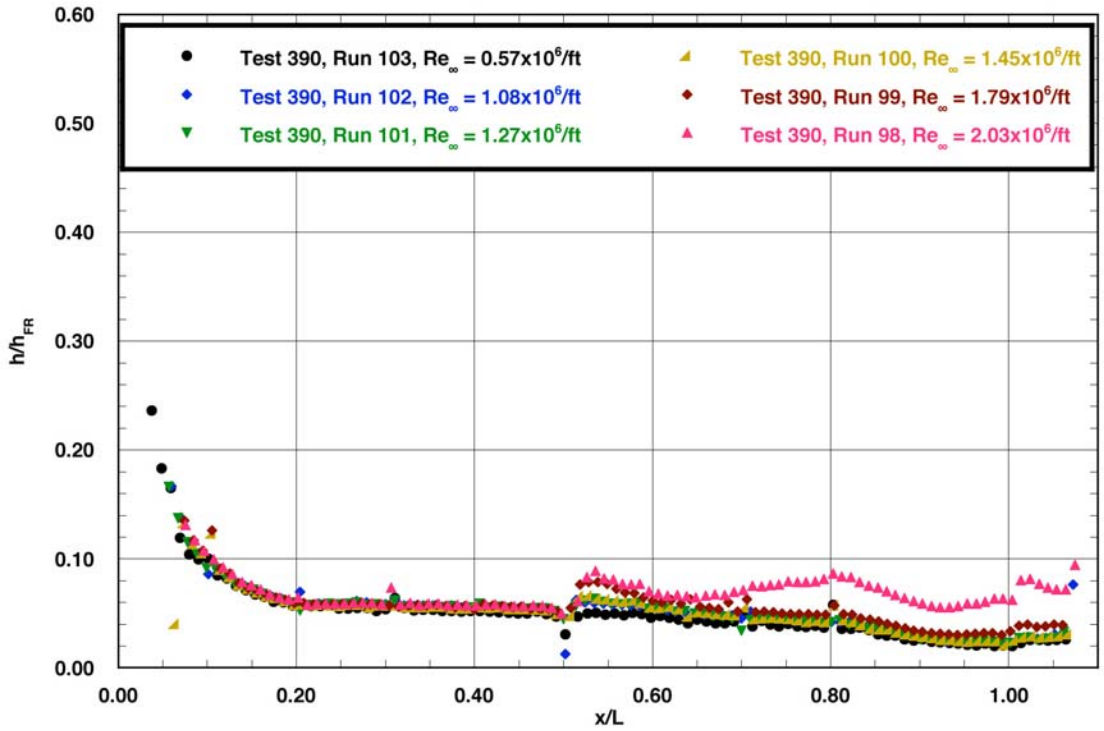

Figure B.14: RTF-BLT-P7 centerline data in the 31-Inch Mach 10 Air Tunnel at α = 30-deg, x/L = 0.50, k_{CL} = 0.0115-in., $k_{AL\text{-}30\text{-}INV}$ = 0.0115-in.

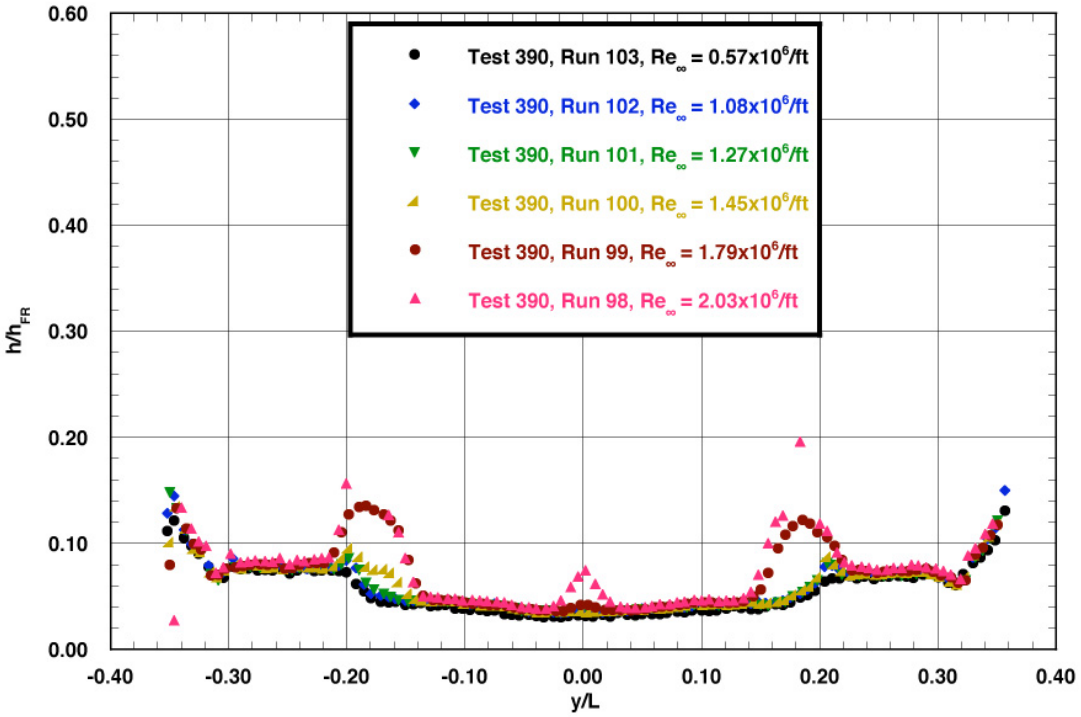

Figure B.15: RTF-BLT-P7 spanwise data (x/L = 0.85) in the 31-Inch Mach 10 Air Tunnel at α = 30-deg, x/L = 0.50, k_{CL} = 0.0115-in., $k_{AL\text{-}30\text{-}INV}$ = 0.0115-in.

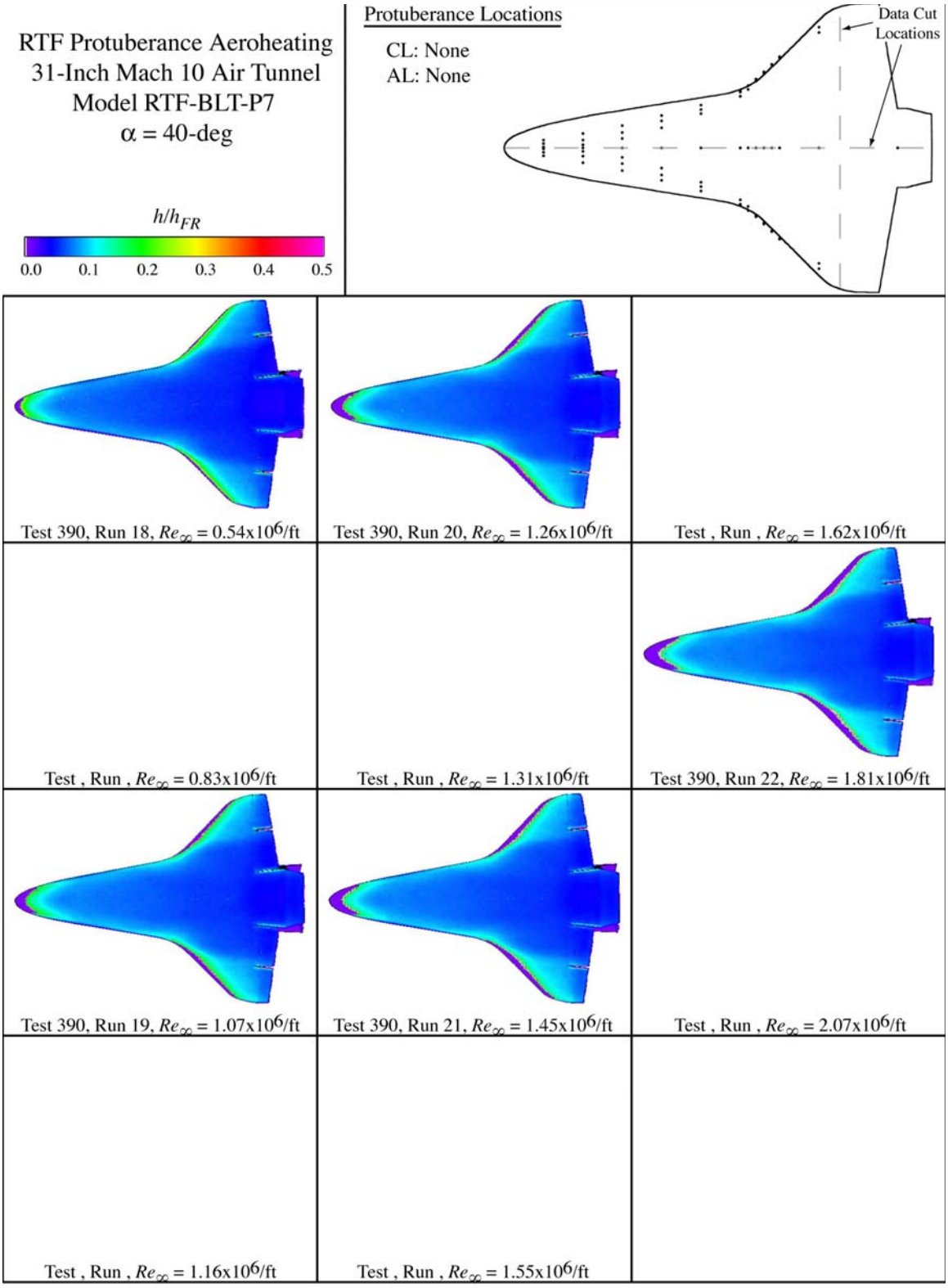

Figure B.16: RTF-BLT-P7 global aeroheating in the 31-Inch Mach 10 Air Tunnel at α = 40-deg, baseline.

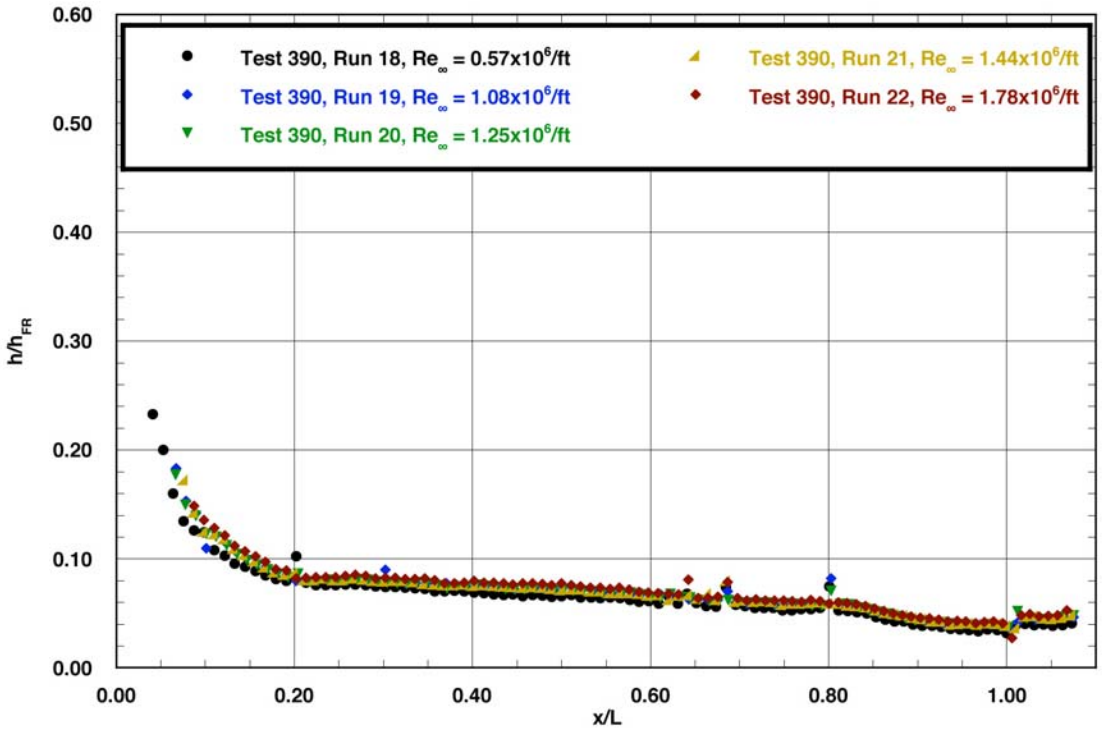

Figure B.17: RTF-BLT-P7 centerline data in the 31-Inch Mach 10 Air Tunnel at α = 40-deg, baseline.

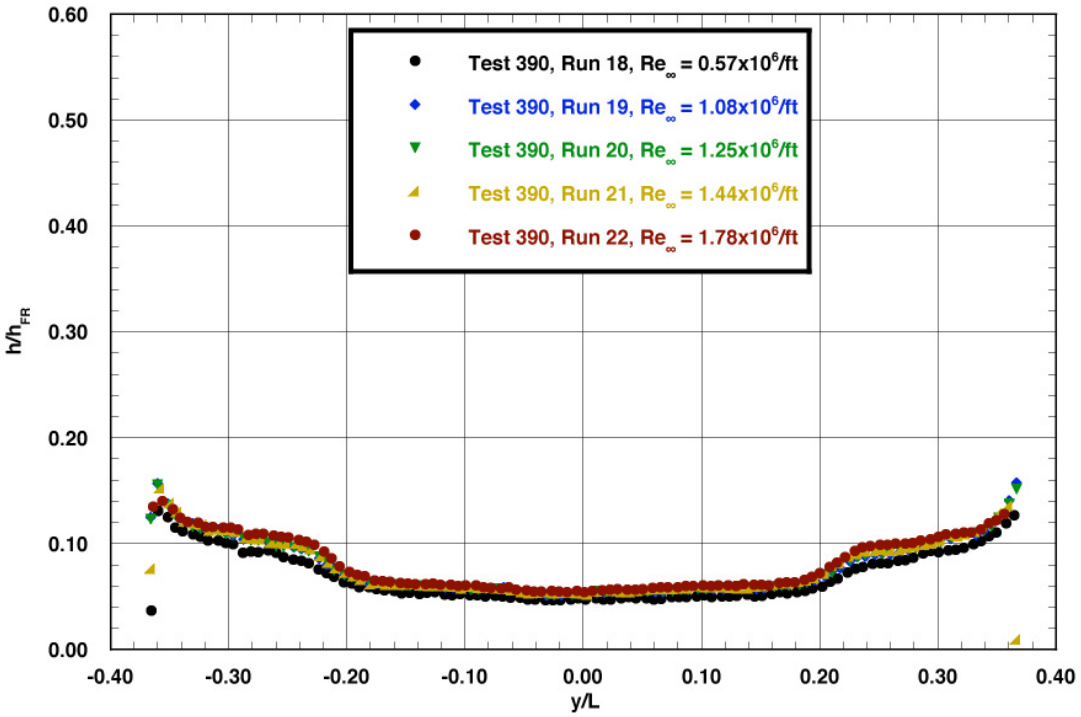

Figure B.18: RTF-BLT-P7 spanwise data (*x/L* = 0.85) in the 31-Inch Mach 10 Air Tunnel at α = 40-deg, baseline.

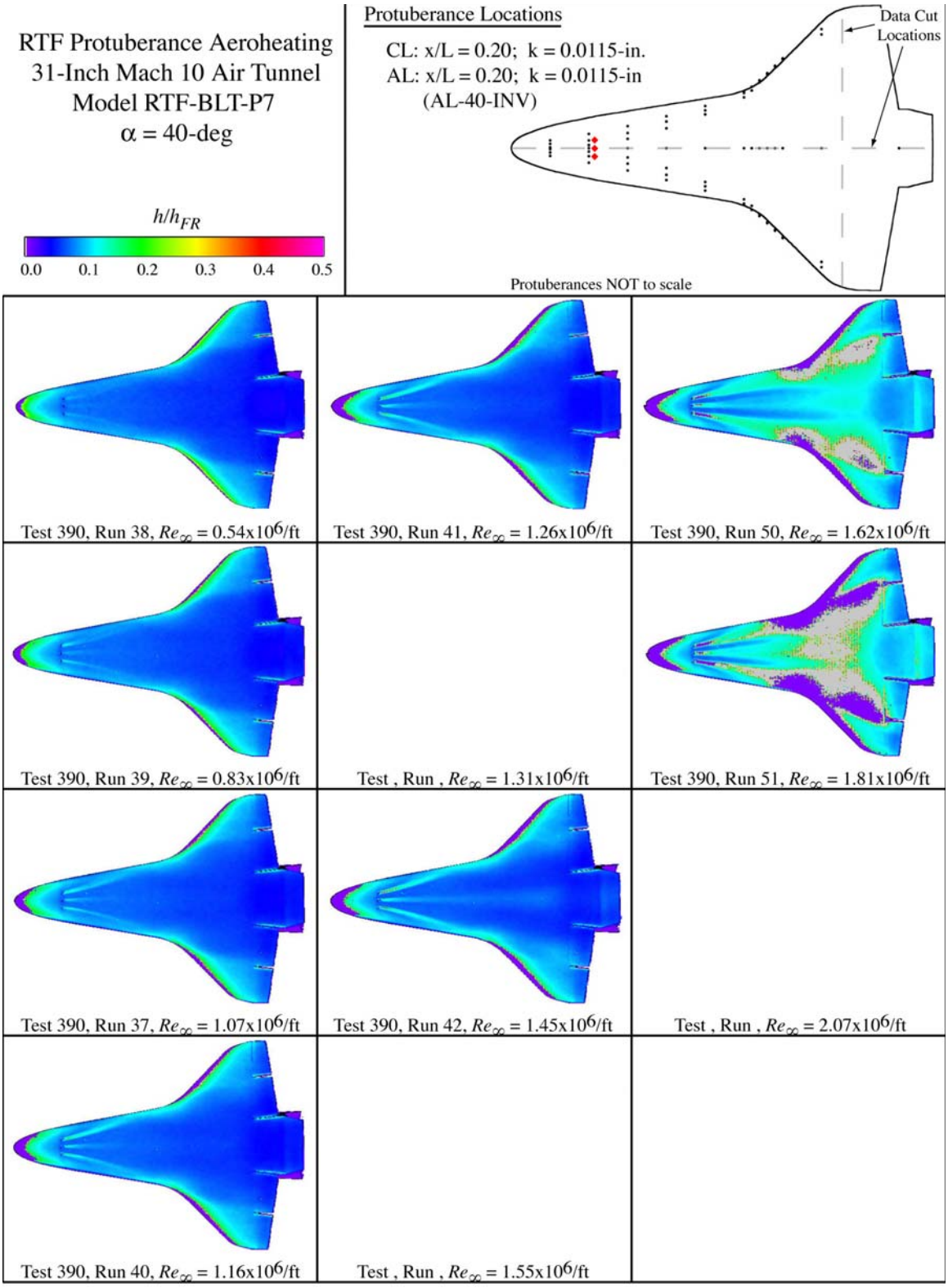

Figure B.19: RTF-BLT-P7 global aeroheating in the 31-Inch Mach 10 Air Tunnel at α = 40-deg, x/L = 0.20, k_{CL} = 0.0115-in., $k_{AL\text{-}40\text{-}INV}$ = 0.0115-in.

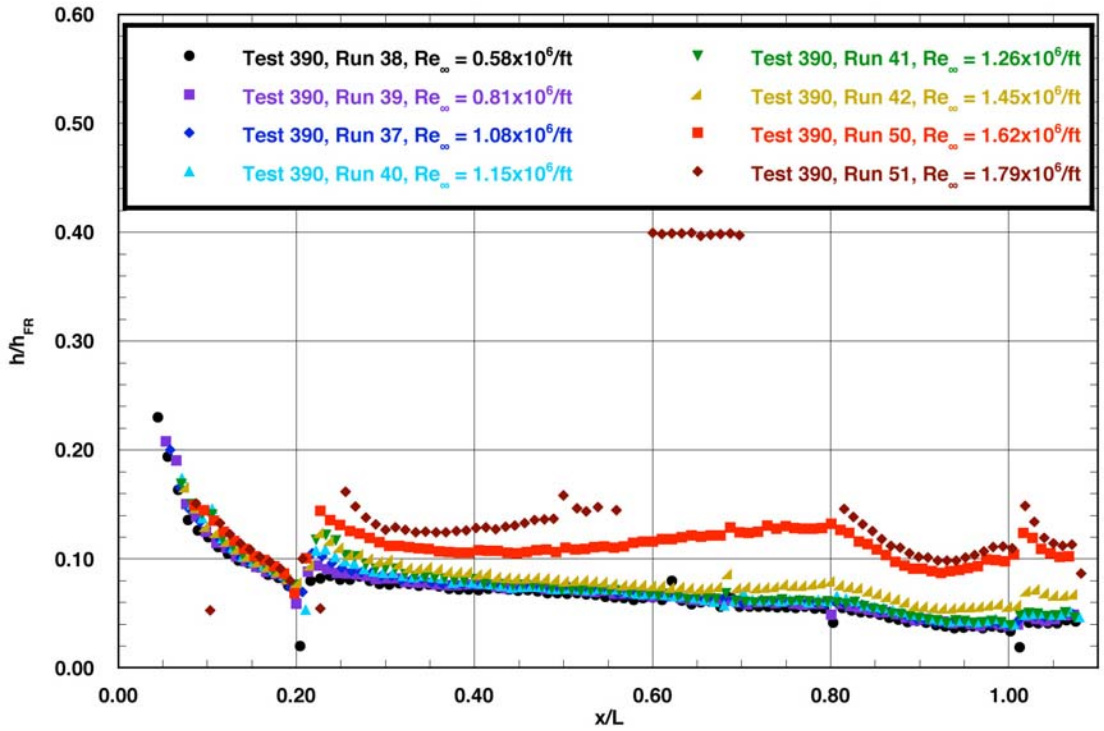

Figure B.20: RTF-BLT-P7 centerline data in the 31-Inch Mach 10 Air Tunnel at α = 40-deg, x/L = 0.20, k_{CL} = 0.0115-in., $k_{AL\text{-}40\text{-}INV}$ = 0.0115-in.

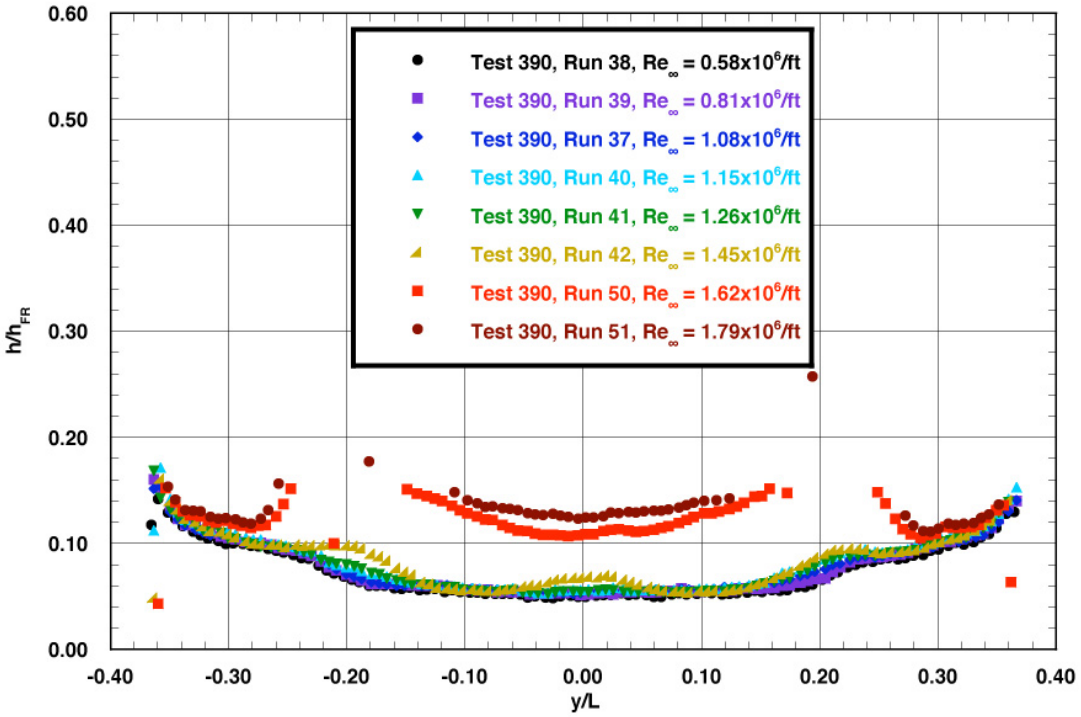

Figure B.21: RTF-BLT-P7 spanwise data (x/L = 0.85) in the 31-Inch Mach 10 Air Tunnel at α = 40-deg, x/L = 0.20, k_{CL} = 0.0115-in., $k_{AL\text{-}40\text{-}INV}$ = 0.0115-in.

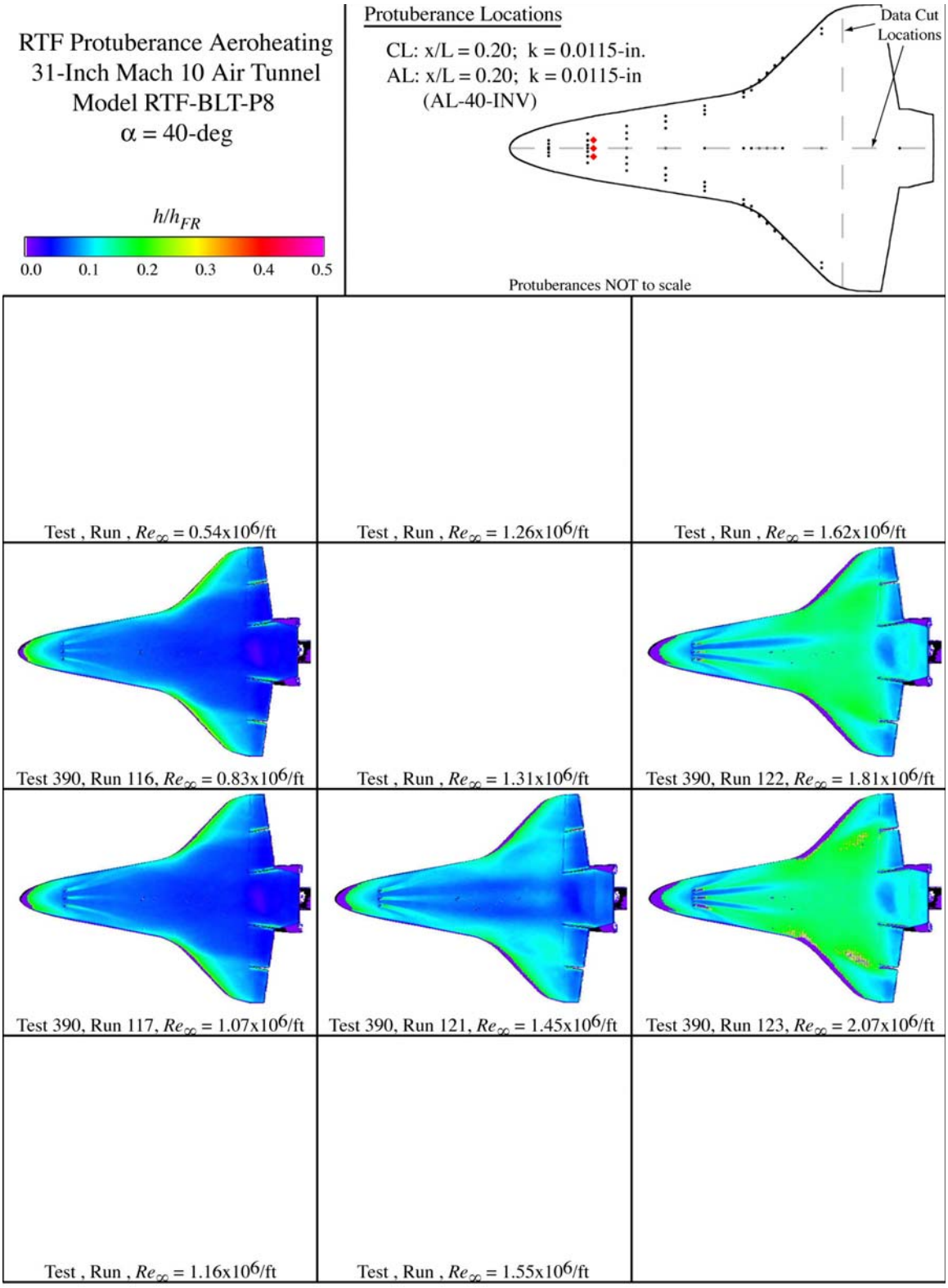

Figure B.22: RTF-BLT-P8 global aeroheating in the 31-Inch Mach 10 Air Tunnel at α = 40-deg, x/L = 0.20, k_{CL} = 0.0115-in., $k_{AL\text{-}40\text{-}INV}$ = 0.0115-in.

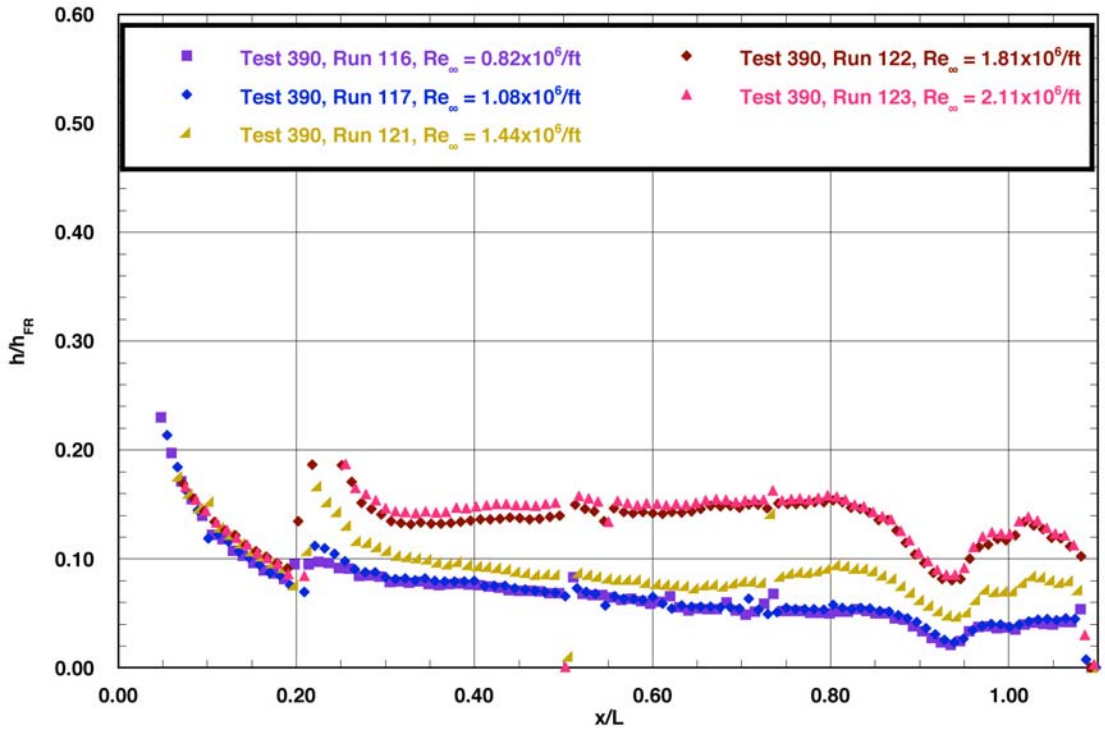

Figure B.23: RTF-BLT-P8 centerline data in the 31-Inch Mach 10 Air Tunnel at α = 40-deg, x/L = 0.20, k_{CL} = 0.0115-in., $k_{AL\text{-}40\text{-}INV}$ = 0.0115-in.

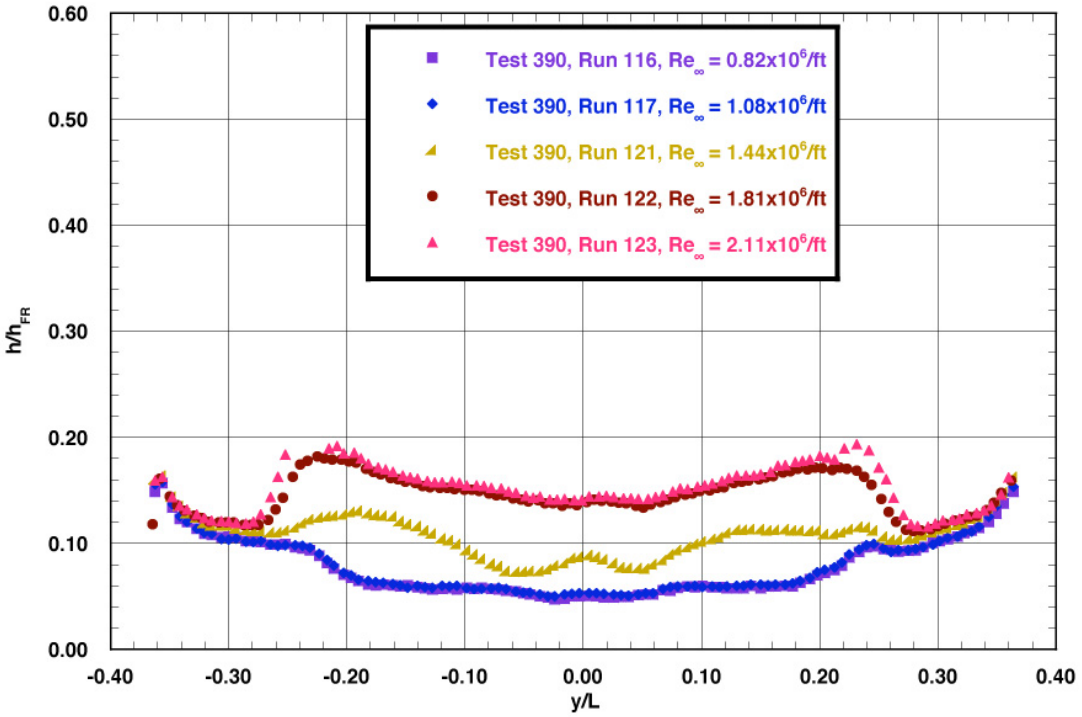

Figure B.24: RTF-BLT-P8 spanwise data (x/L = 0.85) in the 31-Inch Mach 10 Air Tunnel at α = 40-deg, x/L = 0.20, k_{CL} = 0.0115-in., $k_{AL\text{-}40\text{-}INV}$ = 0.0115-in.

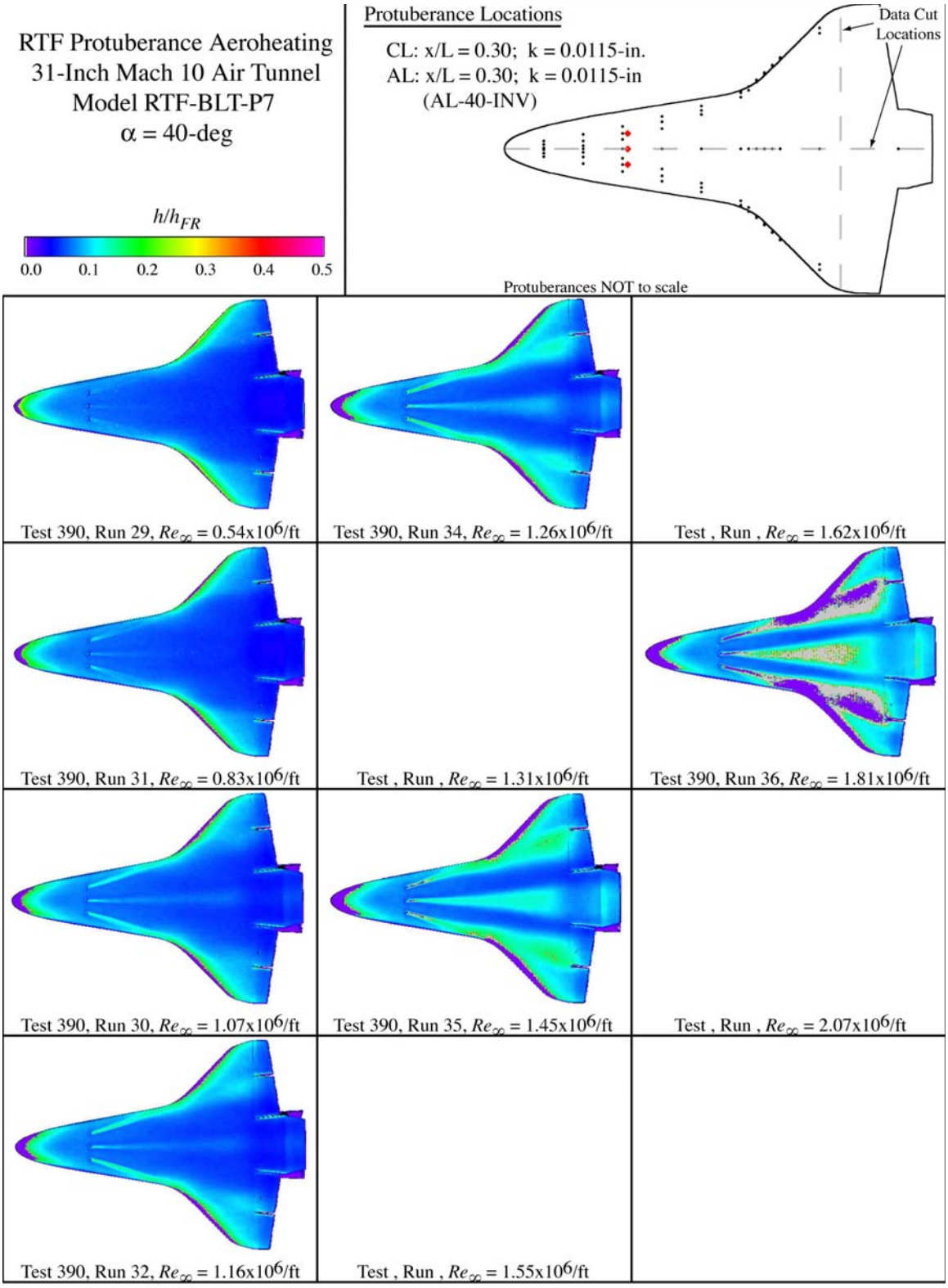

Figure B.25: RTF-BLT-P7 global aeroheating in the 31-Inch Mach 10 Air Tunnel at α = 40-deg, x/L = 0.30, k_{CL} = 0.0115-in., $k_{AL\text{-}40\text{-}INV}$ = 0.0115-in.

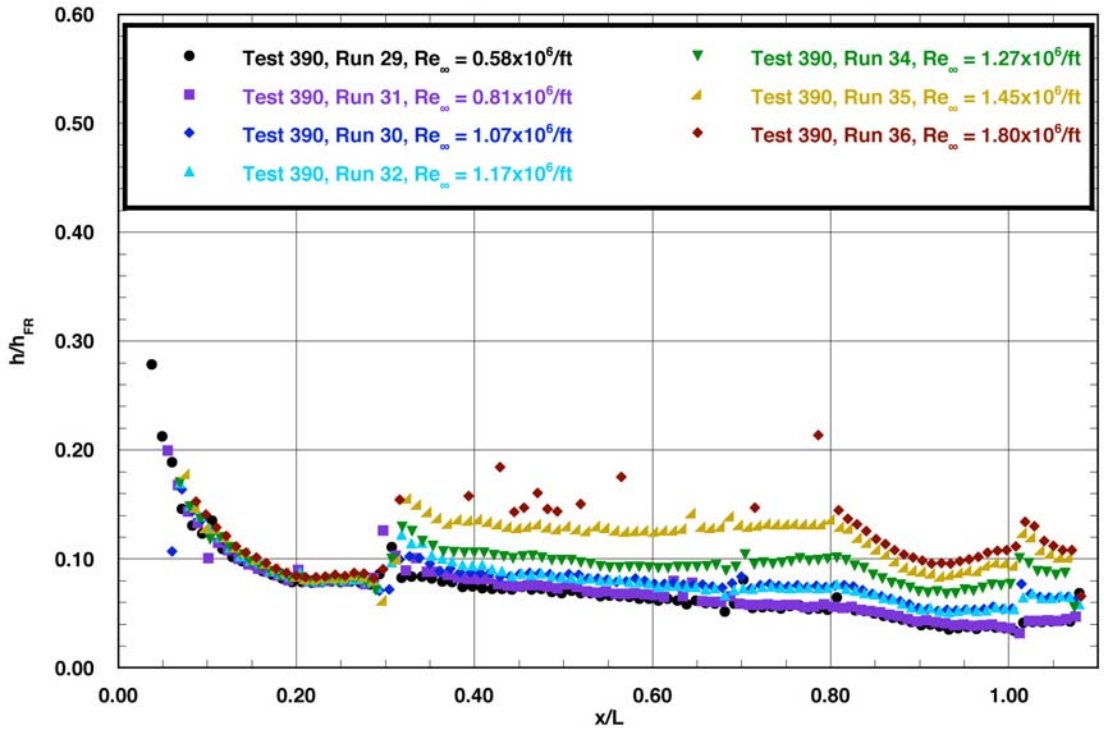

Figure B.26: RTF-BLT-P7 centerline data in the 31-Inch Mach 10 Air Tunnel at α = 40-deg, x/L = 0.30, k_{CL} = 0.0115-in., $k_{AL\text{-}40\text{-}INV}$ = 0.0115-in.

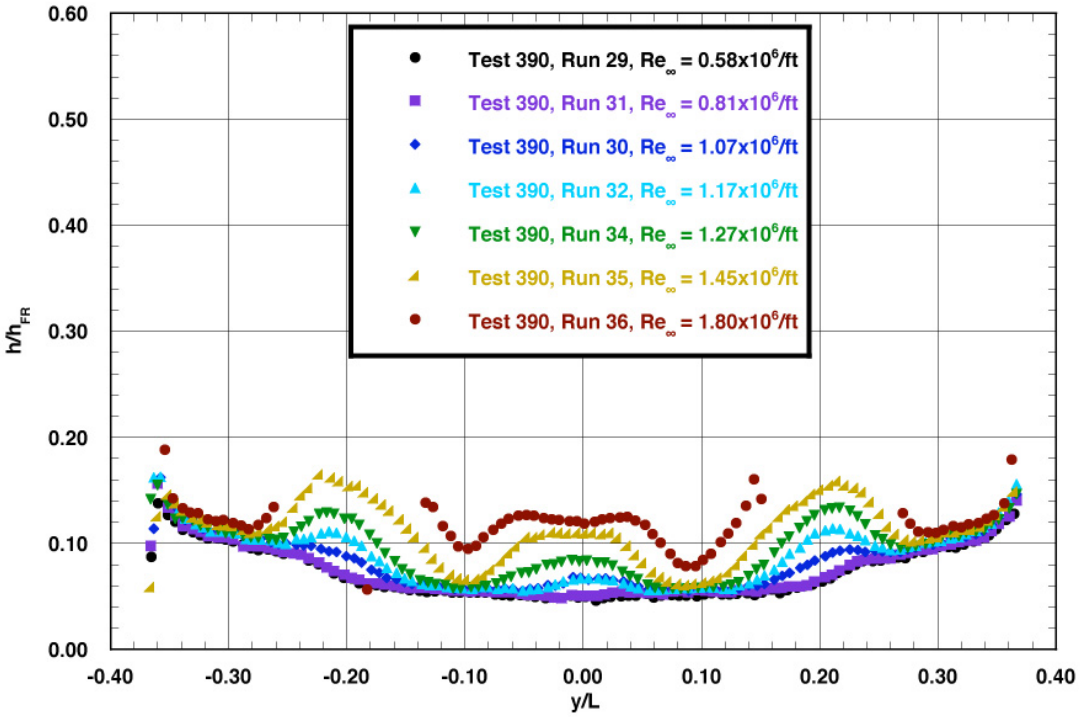

Figure B.27: RTF-BLT-P7 spanwise data (x/L = 0.85) in the 31-Inch Mach 10 Air Tunnel at α = 40-deg, x/L = 0.30, k_{CL} = 0.0115-in., $k_{AL\text{-}40\text{-}INV}$ = 0.0115-in.

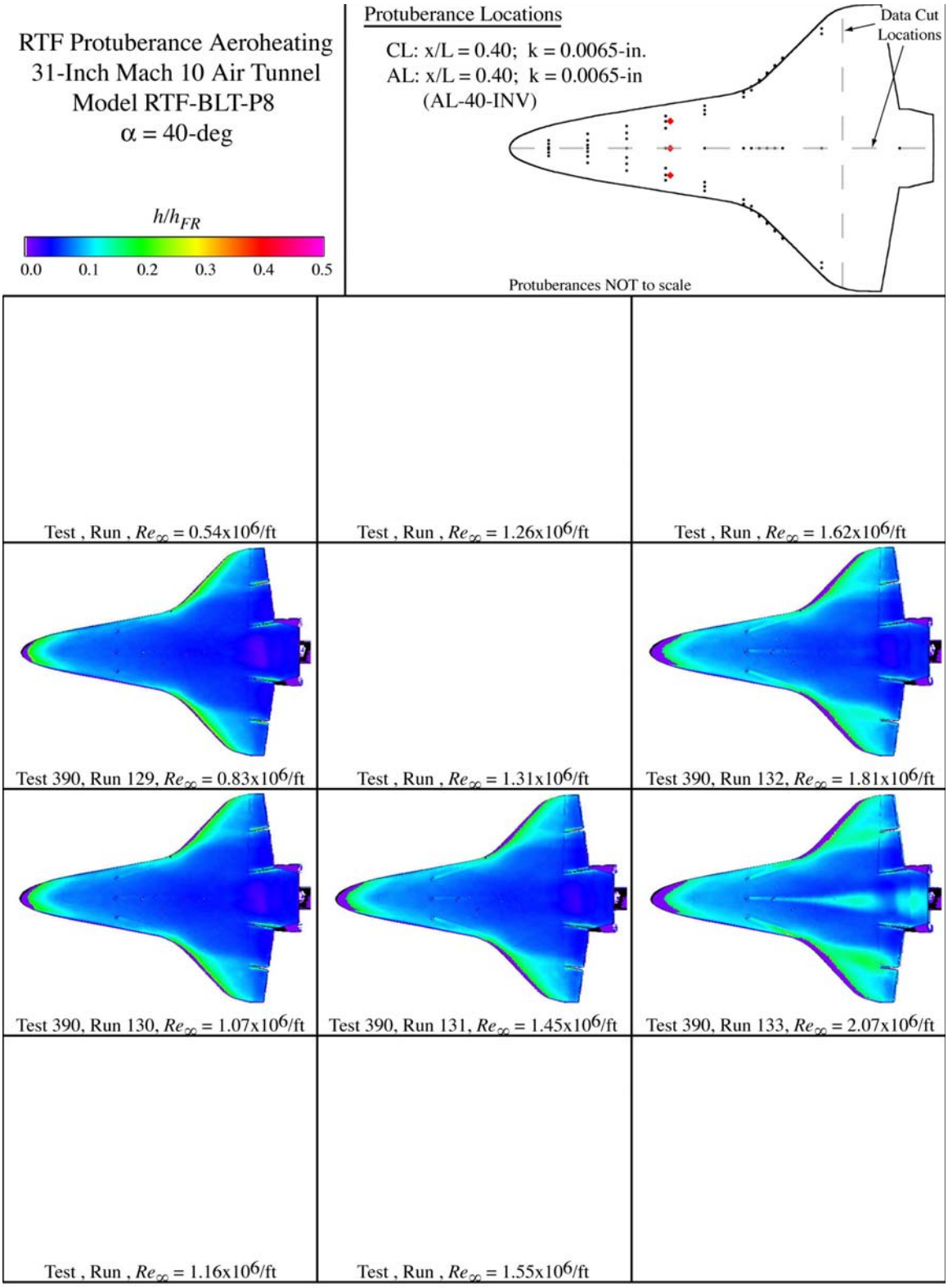

Figure B.28: RTF-BLT-P8 global aeroheating in the 31-Inch Mach 10 Air Tunnel at α = 40-deg, x/L = 0.40, k_{CL} = 0.0065-in., $k_{AL\text{-}40\text{-}INV}$ = 0.0065-in.

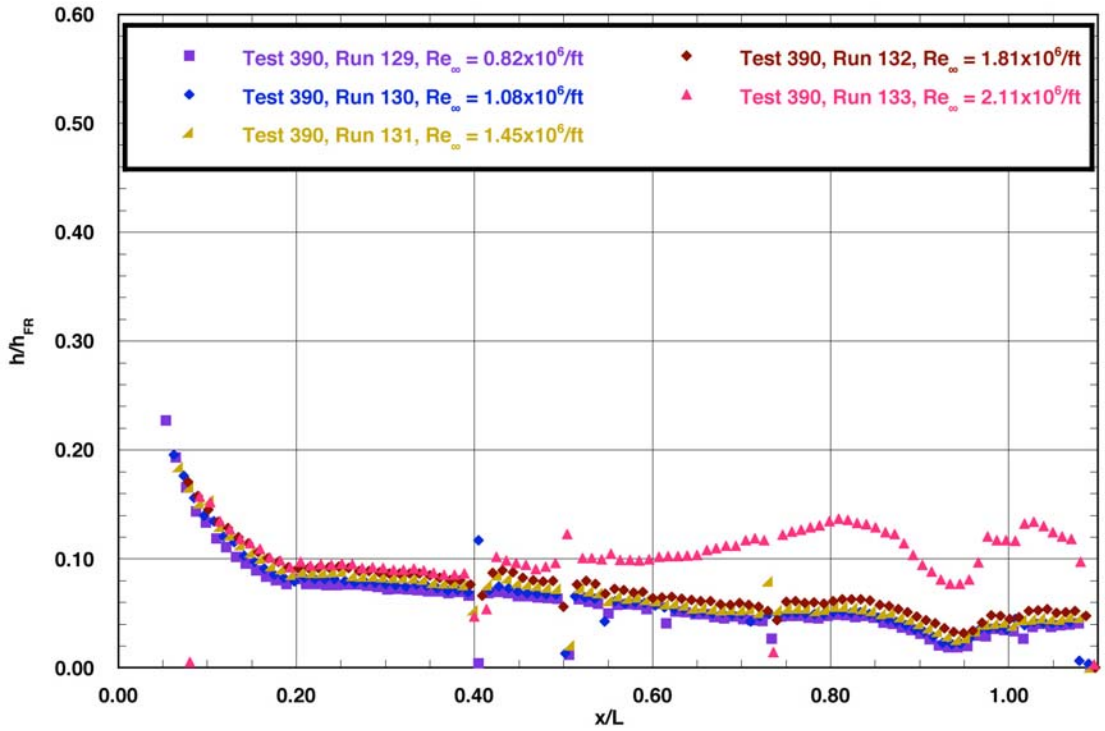

Figure B.29: RTF-BLT-P8 centerline data in the 31-Inch Mach 10 Air Tunnel at α = 40-deg, x/L = 0.40, k_{CL} = 0.0065-in., $k_{AL\text{-}40\text{-}INV}$ = 0.0065-in.

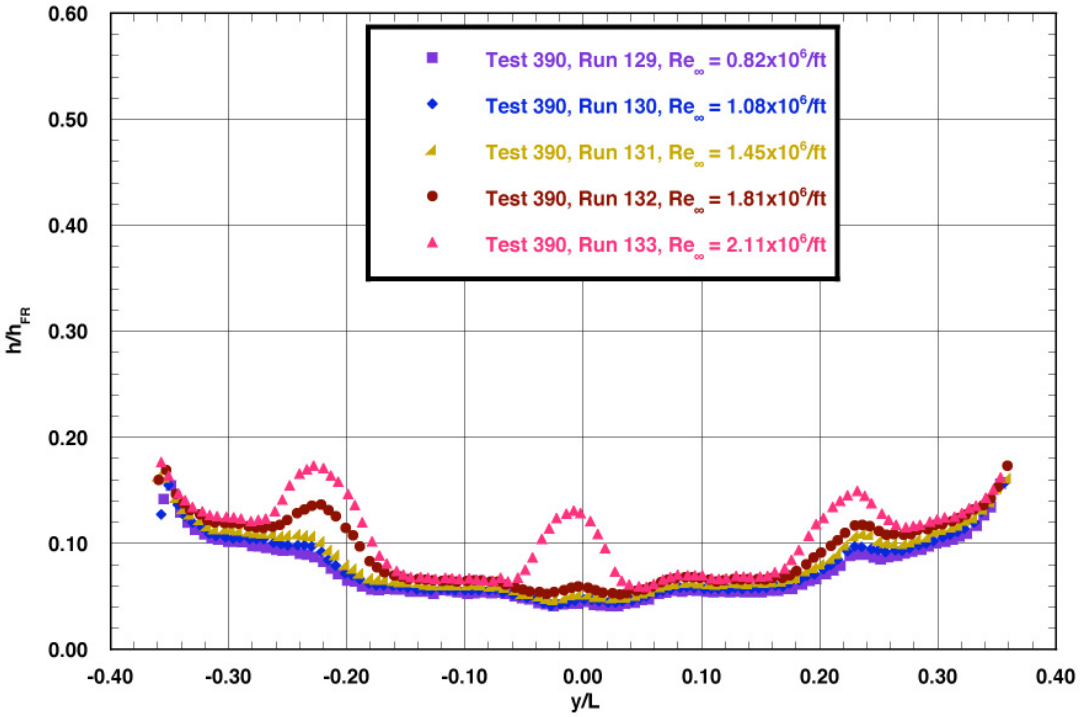

Figure B.30: RTF-BLT-P8 spanwise data (x/L = 0.85) in the 31-Inch Mach 10 Air Tunnel at α = 40-deg, x/L = 0.40, k_{CL} = 0.0065-in., $k_{AL\text{-}40\text{-}INV}$ = 0.0065-in.

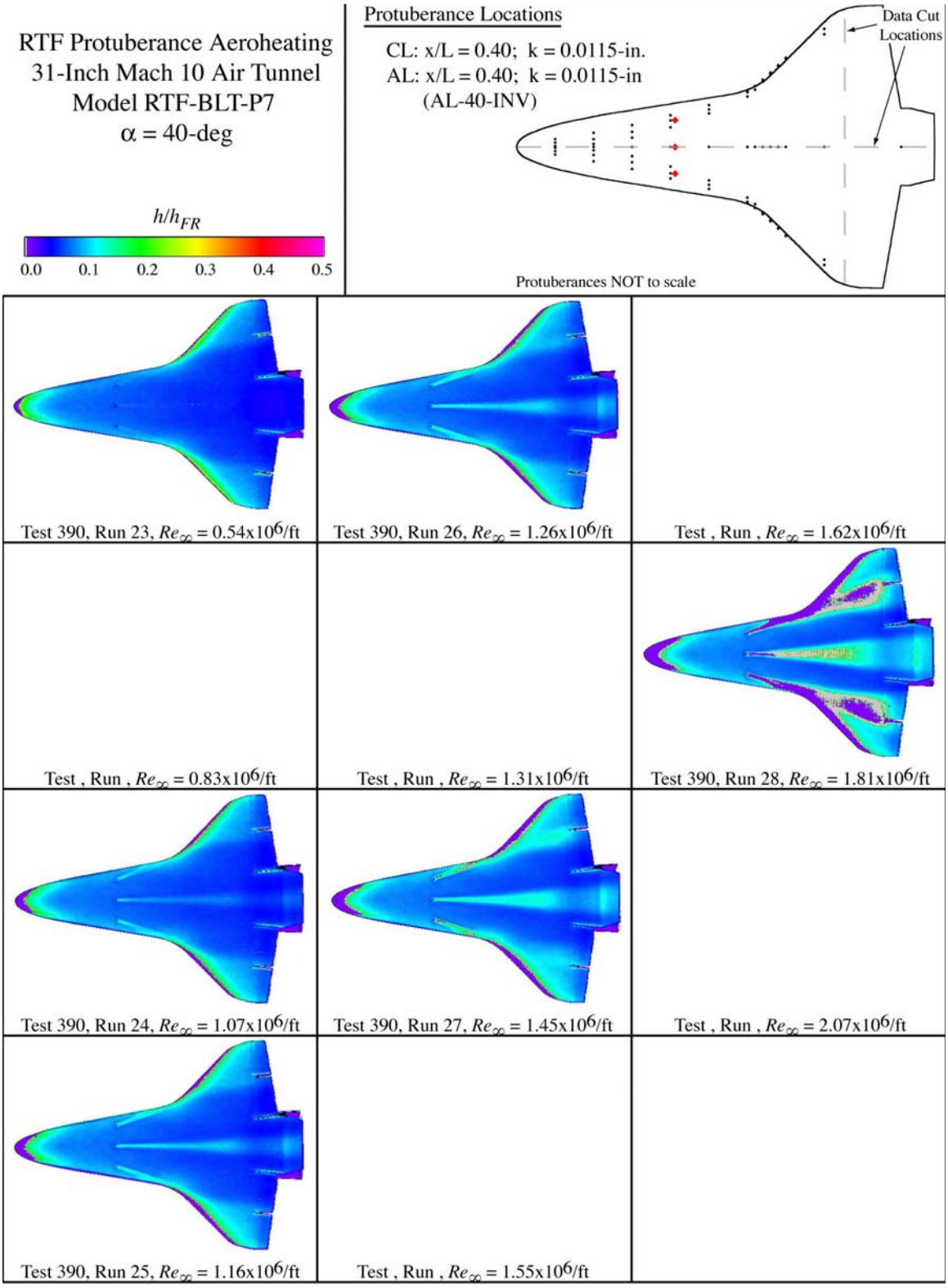

Figure B.31: RTF-BLT-P7 global aeroheating in the 31-Inch Mach 10 Air Tunnel at α = 40-deg, x/L = 0.40, k_{CL} = 0.0115-in., $k_{AL\text{-}40\text{-}INV}$ = 0.0115-in.

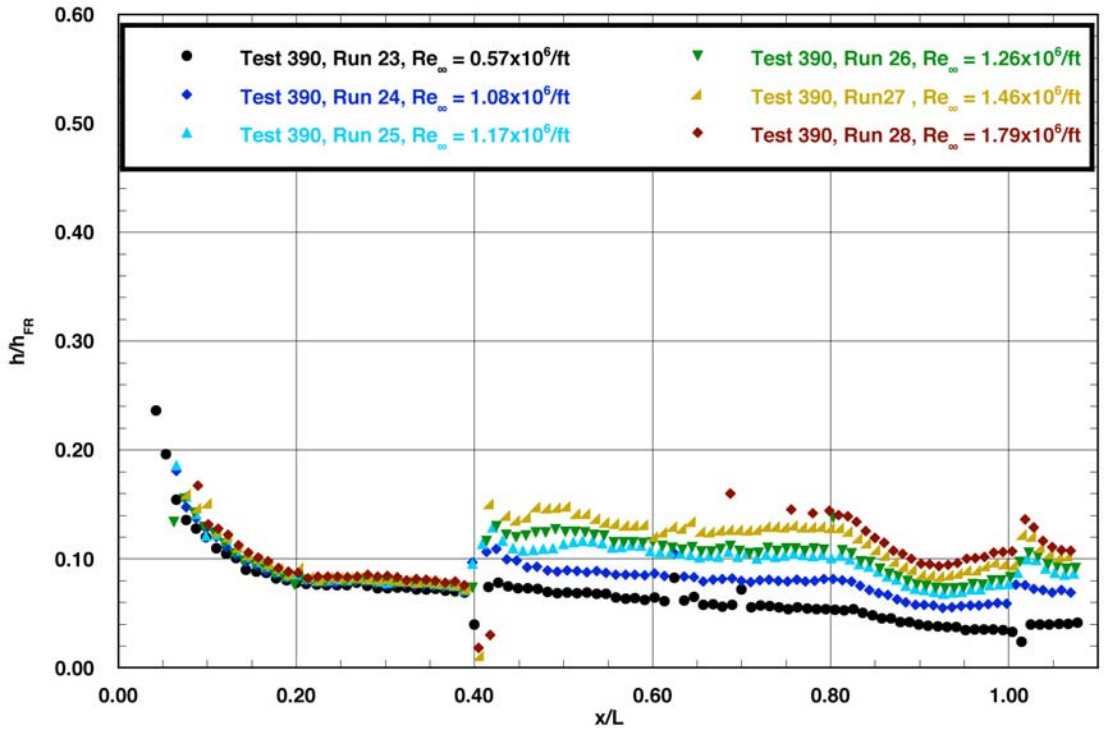

Figure B.32: RTF-BLT-P7 centerline data in the 31-Inch Mach 10 Air Tunnel at α = 40-deg, x/L = 0.40, k_{CL} = 0.0115-in., $k_{AL\text{-}40\text{-}INV}$ = 0.0115-in.

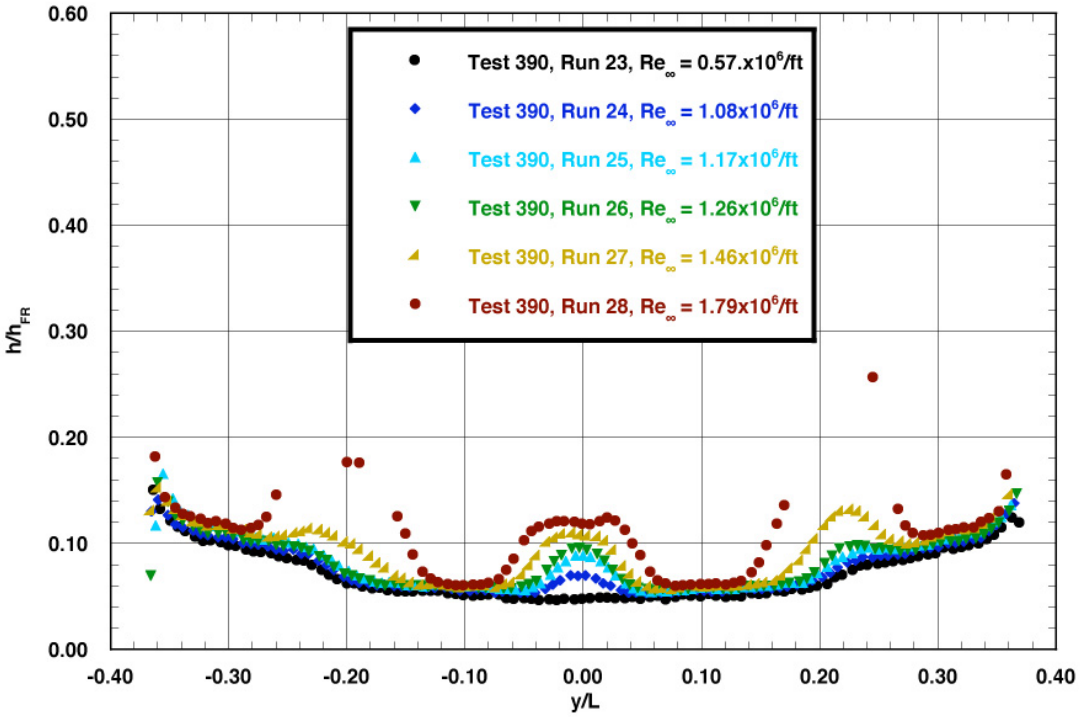

Figure B.33: RTF-BLT-P7 spanwise data (x/L = 0.85) in the 31-Inch Mach 10 Air Tunnel at α = 40-deg, x/L = 0.40, k_{CL} = 0.0115-in., $k_{AL\text{-}40\text{-}INV}$ = 0.0115-in.

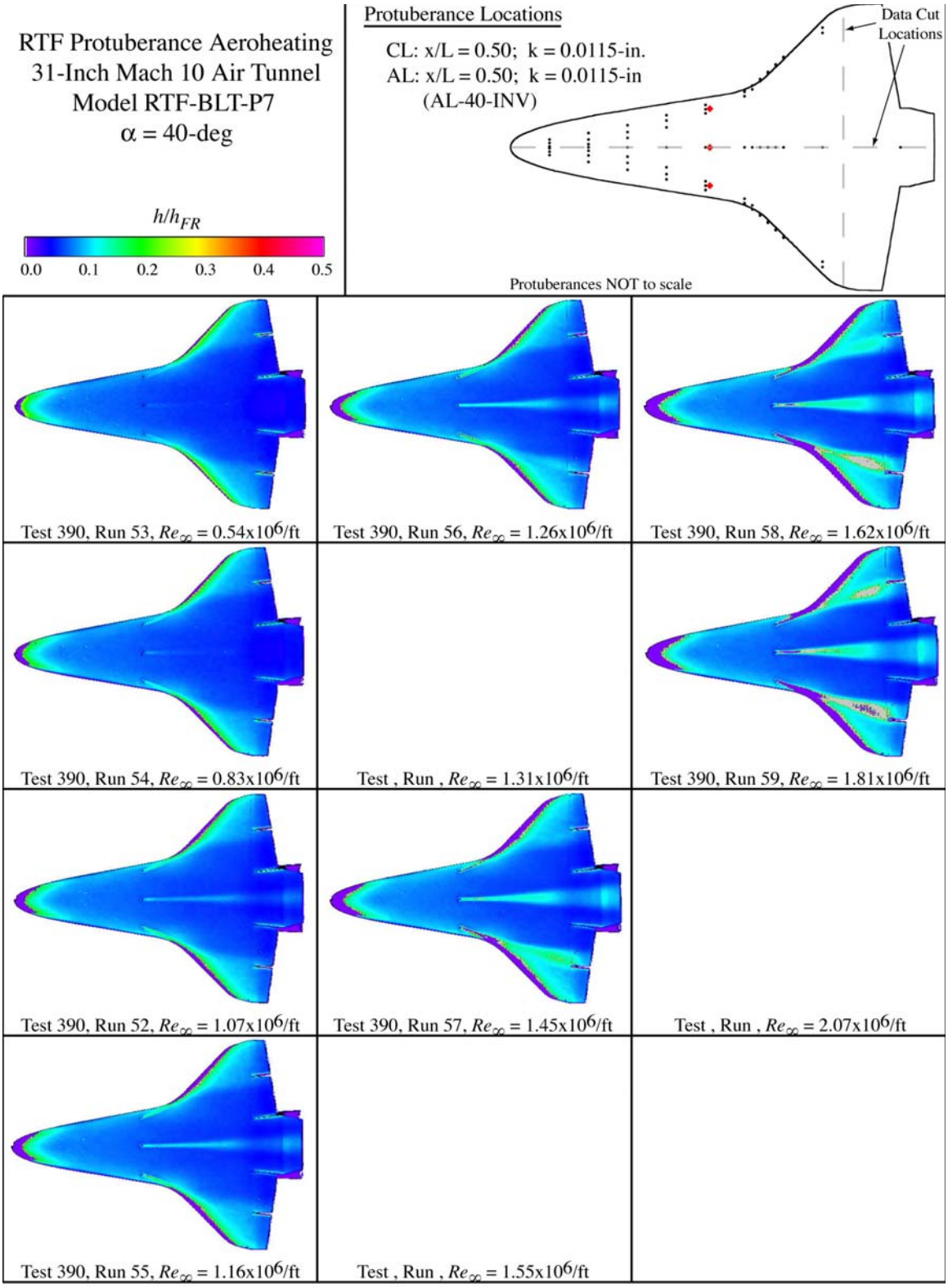

Figure B.34: RTF-BLT-P7 global aeroheating in the 31-Inch Mach 10 Air Tunnel at α = 40-deg, x/L = 0.50, k_{CL} = 0.0115-in., $k_{AL\text{-}40\text{-}INV}$ = 0.0115-in.

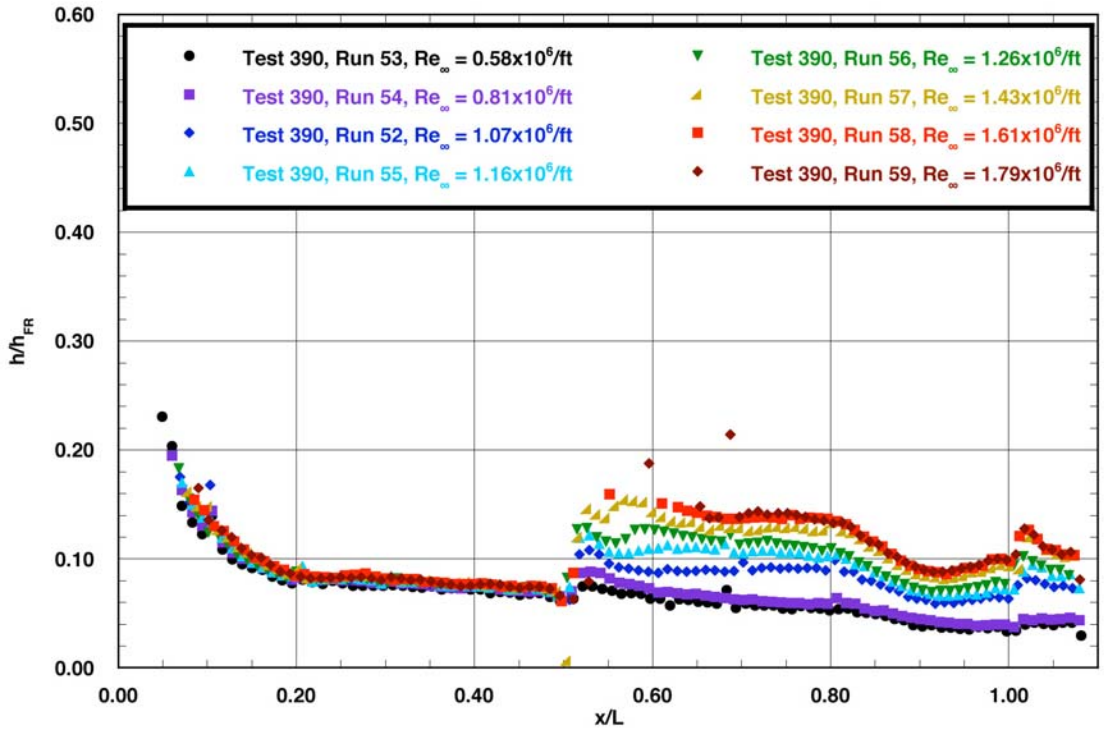

Figure B.35: RTF-BLT-P7 centerline data in the 31-Inch Mach 10 Air Tunnel at α = 40-deg, x/L = 0.50, k_{CL} = 0.0115-in., $k_{AL\text{-}40\text{-}INV}$ = 0.0115-in.

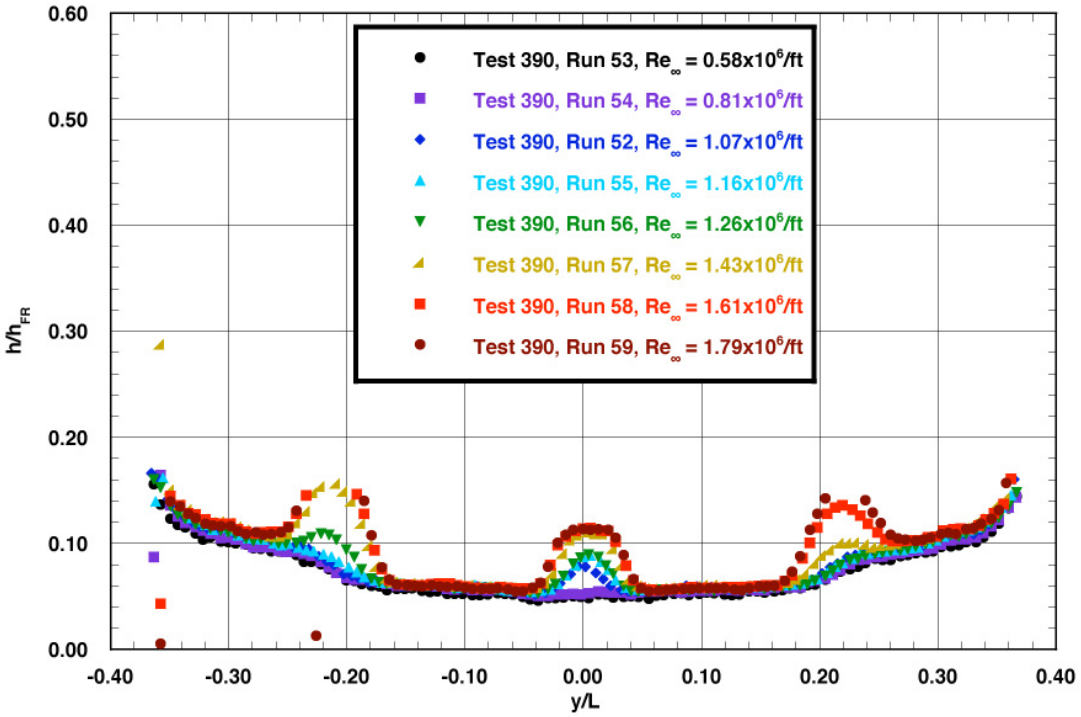

Figure B.36: RTF-BLT-P7 spanwise data (x/L = 0.85) in the 31-Inch Mach 10 Air Tunnel at α = 40-deg, x/L = 0.50, k_{CL} = 0.0115-in., $k_{AL\text{-}40\text{-}INV}$ = 0.0115-in.

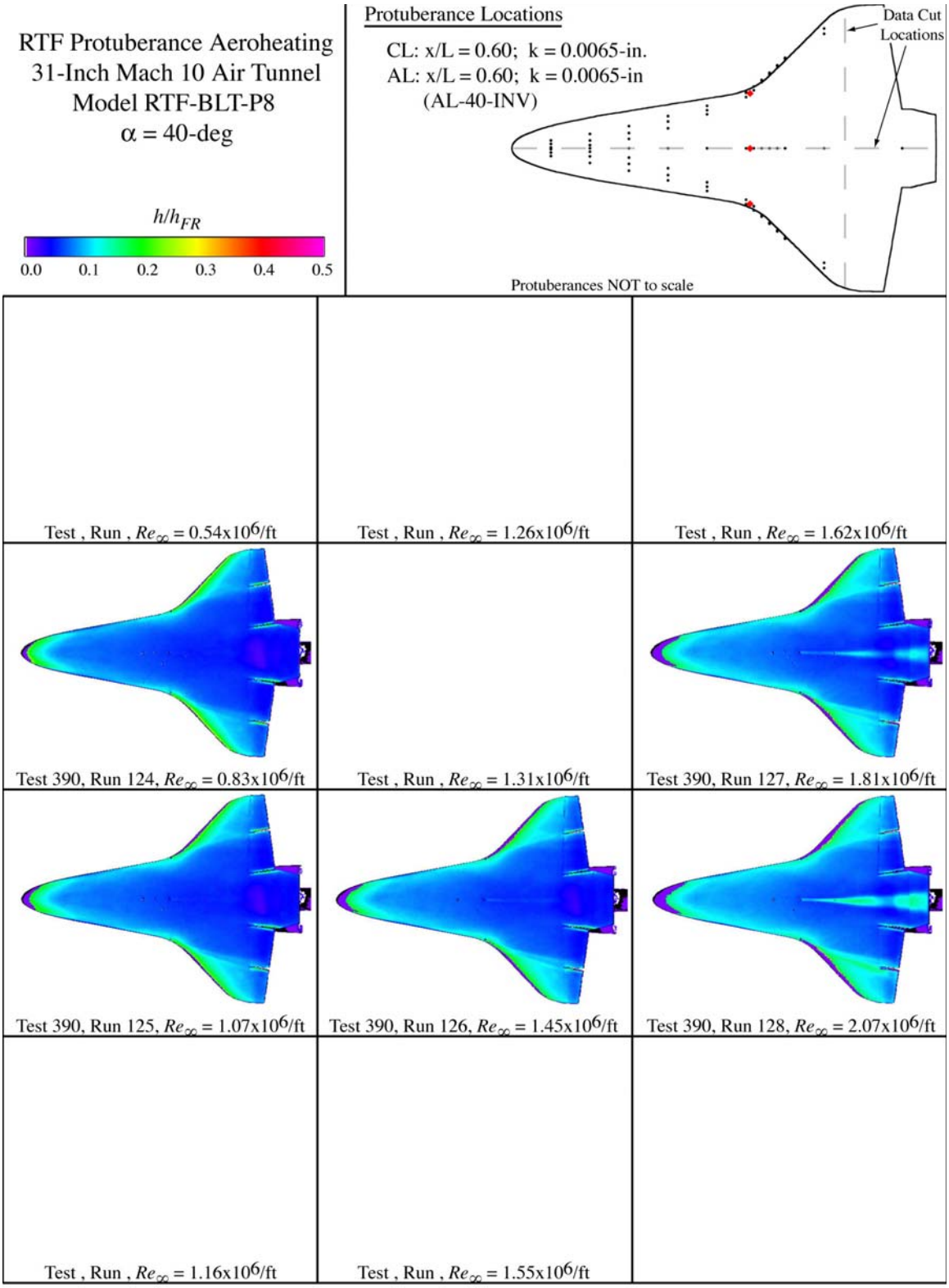

Figure B.37: RTF-BLT-P8 global aeroheating in the 31-Inch Mach 10 Air Tunnel at α = 40-deg, x/L = 0.60, k_{CL} = 0.0065-in., $k_{AL\text{-}40\text{-}INV}$ = 0.0065-in.

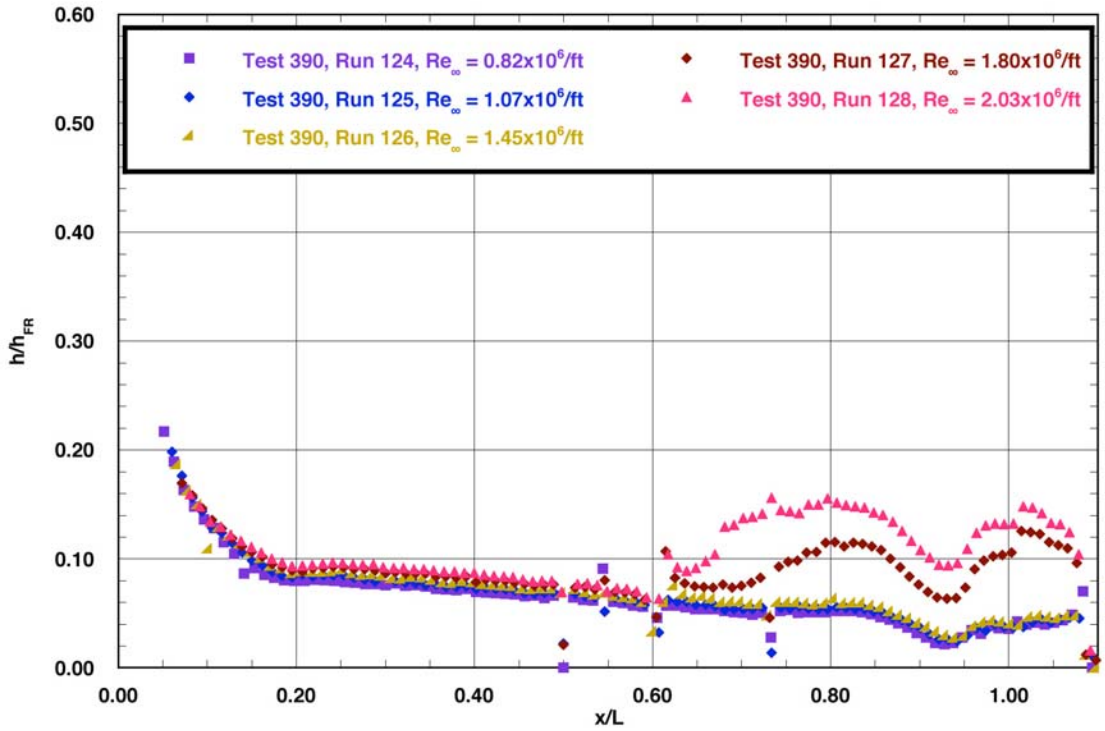

Figure B.38: RTF-BLT-P8 centerline data in the 31-Inch Mach 10 Air Tunnel at α = 40-deg, x/L = 0.60, k_{CL} = 0.0065-in., $k_{AL\text{-}40\text{-}INV}$ = 0.0065-in.

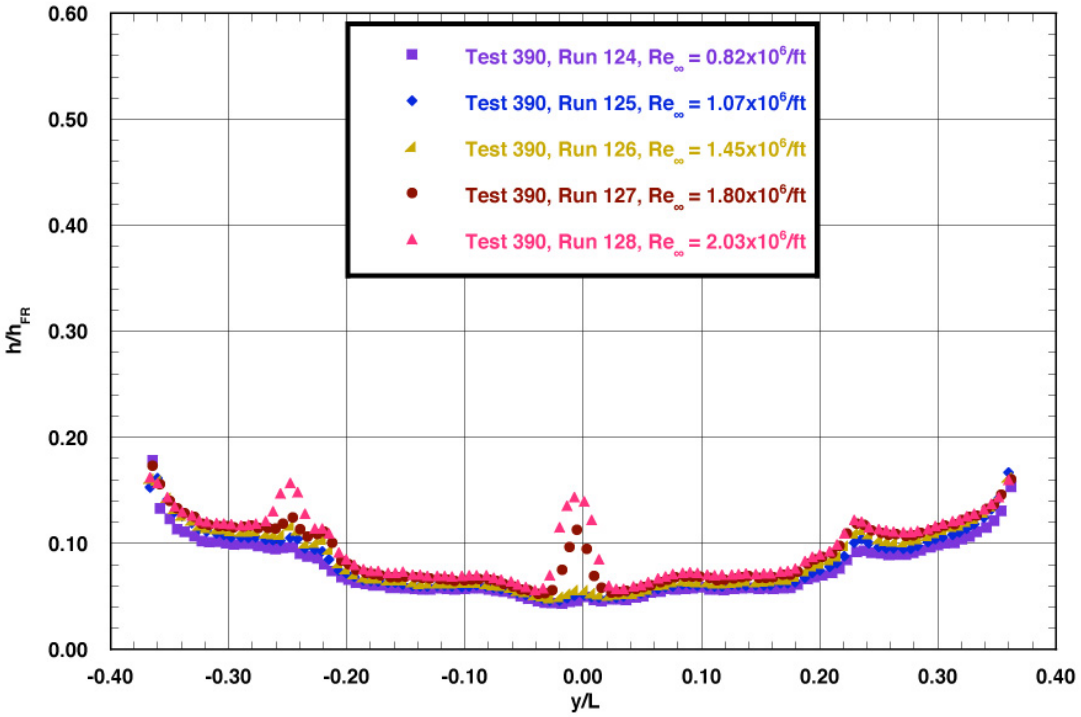

Figure B.39: RTF-BLT-P8 spanwise data (x/L = 0.85) in the 31-Inch Mach 10 Air Tunnel at α = 40-deg, x/L = 0.60, k_{CL} = 0.0065-in., $k_{AL\text{-}40\text{-}INV}$ = 0.0065-in.

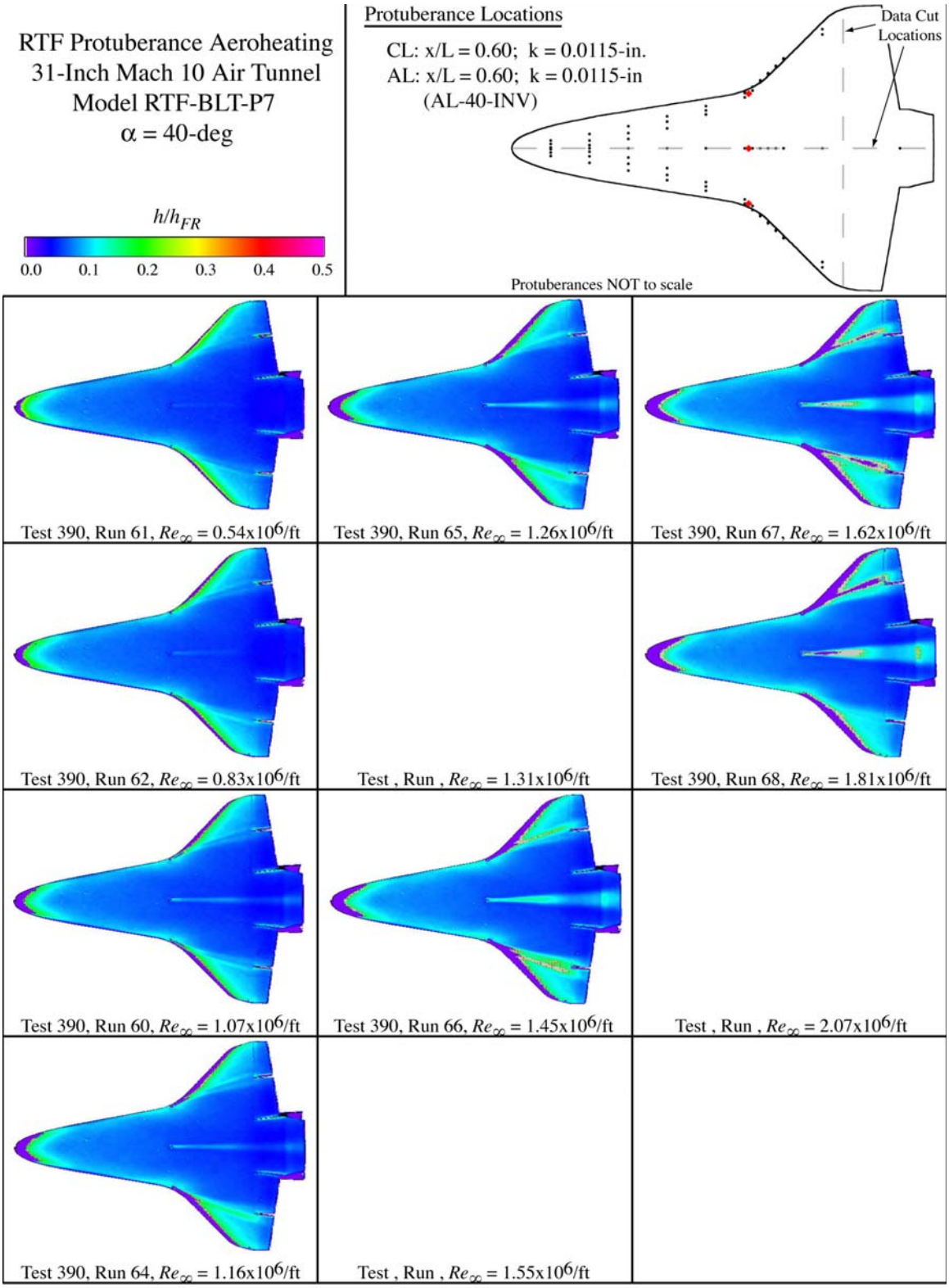

Figure B.40: RTF-BLT-P7 global aeroheating in the 31-Inch Mach 10 Air Tunnel at α = 40-deg, x/L = 0.60, k_{CL} = 0.0115-in., $k_{AL\text{-}40\text{-}INV}$ = 0.0115-in.

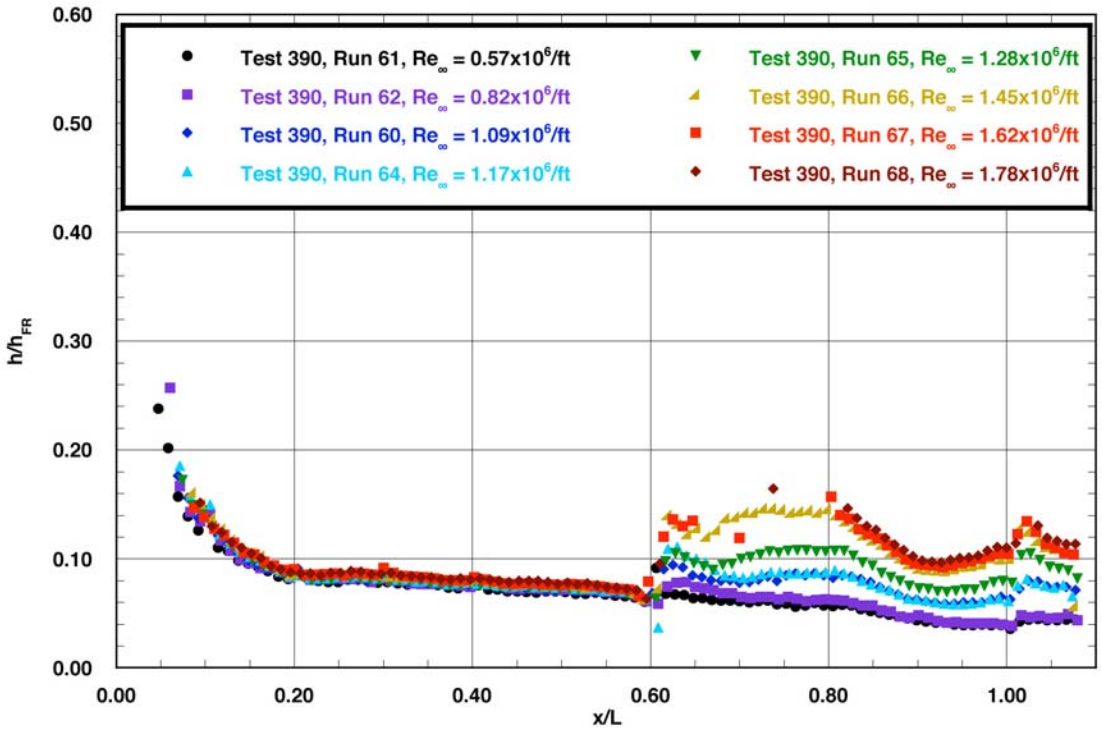

Figure B.41: RTF-BLT-P7 centerline data in the 31-Inch Mach 10 Air Tunnel at α = 40-deg, x/L = 0.60, k_{CL} = 0.0115-in., $k_{AL\text{-}40\text{-}INV}$ = 0.0115-in.

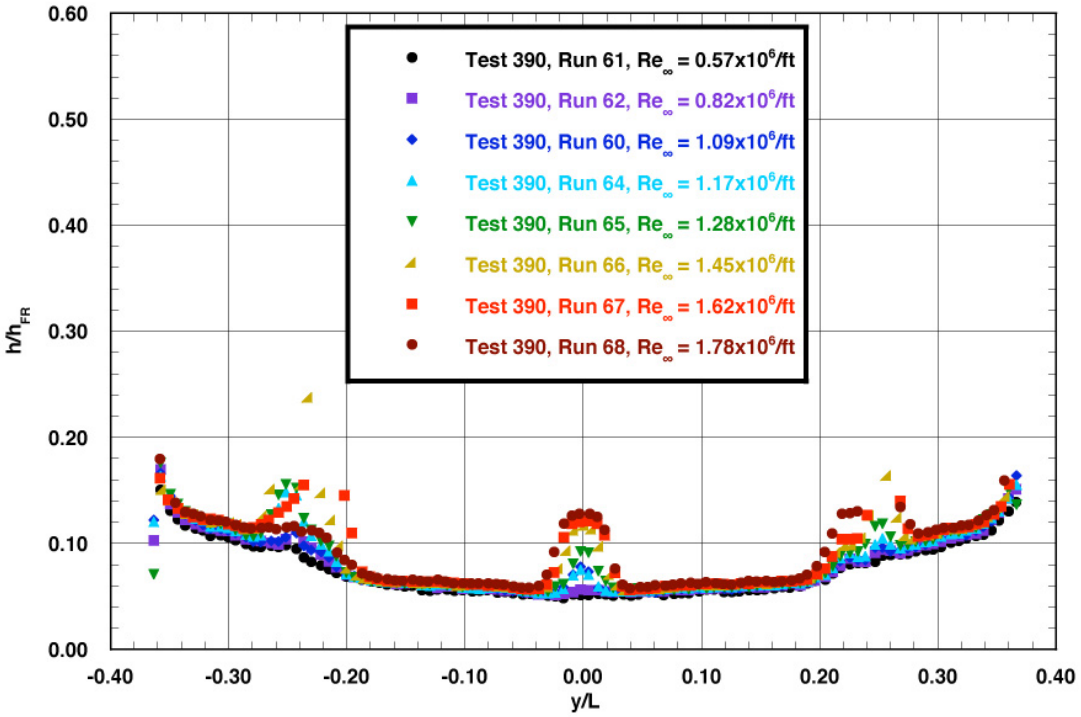

Figure B.42: RTF-BLT-P7 spanwise data (x/L = 0.85) in the 31-Inch Mach 10 Air Tunnel at α = 40-deg, x/L = 0.60, k_{CL} = 0.0115-in., $k_{AL\text{-}40\text{-}INV}$ = 0.0115-in.

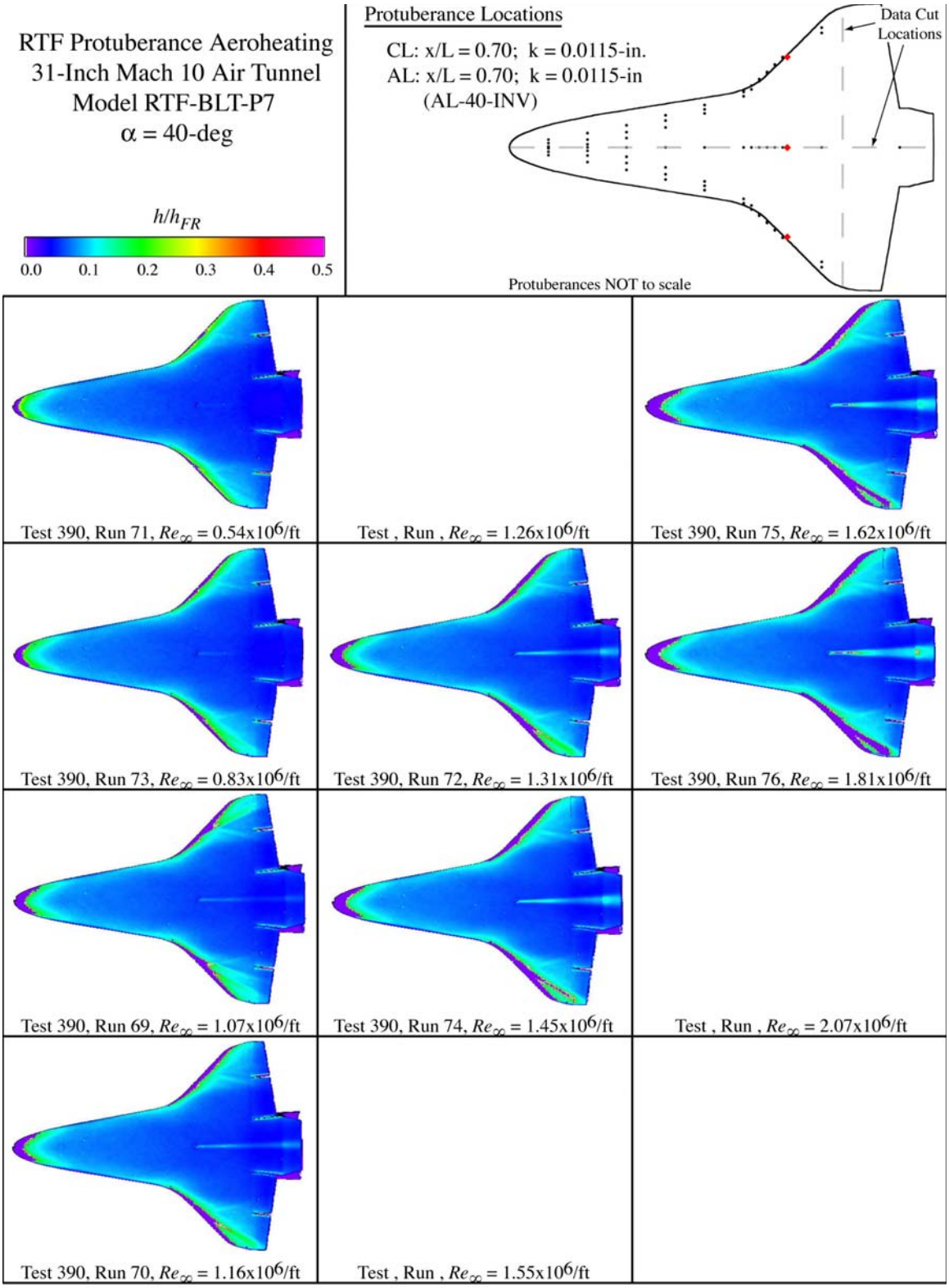

Figure B.43: RTF-BLT-P7 global aeroheating in the 31-Inch Mach 10 Air Tunnel at α = 40-deg, x/L = 0.70, k_{CL} = 0.0115-in., $k_{AL\text{-}40\text{-}INV}$ = 0.0115-in.

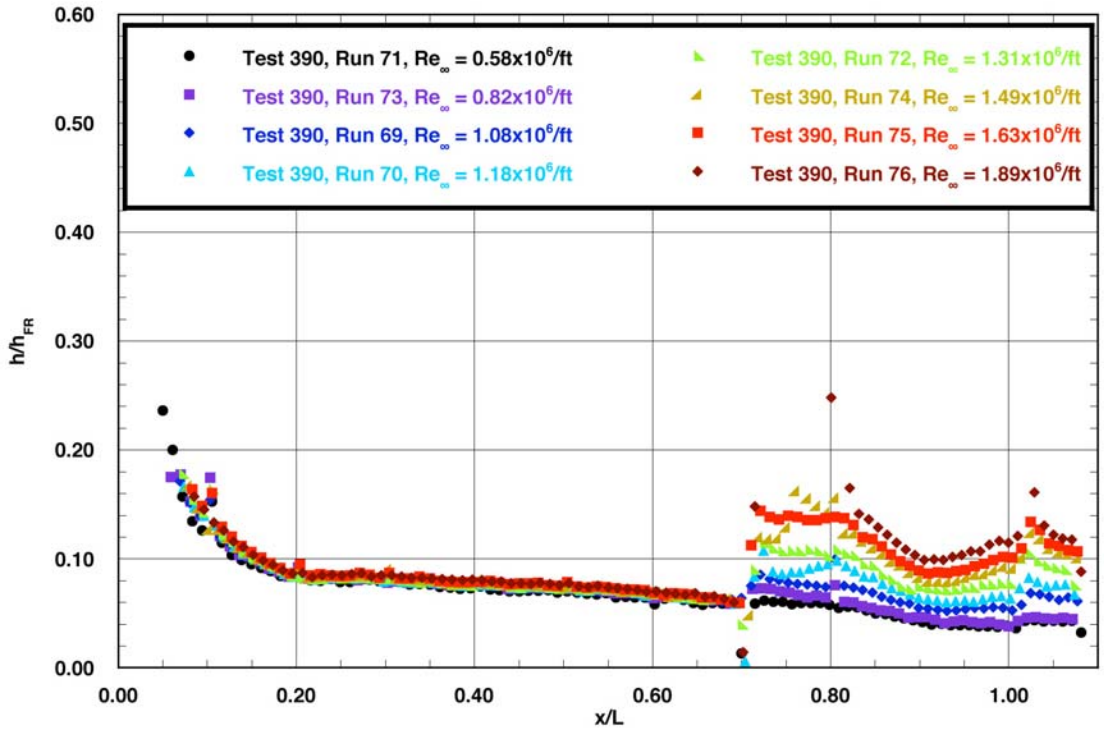

Figure B.44: RTF-BLT-P7 centerline data in the 31-Inch Mach 10 Air Tunnel at α = 40-deg, x/L = 0.70, k_{CL} = 0.0115-in., $k_{AL\text{-}40\text{-}INV}$ = 0.0115-in.

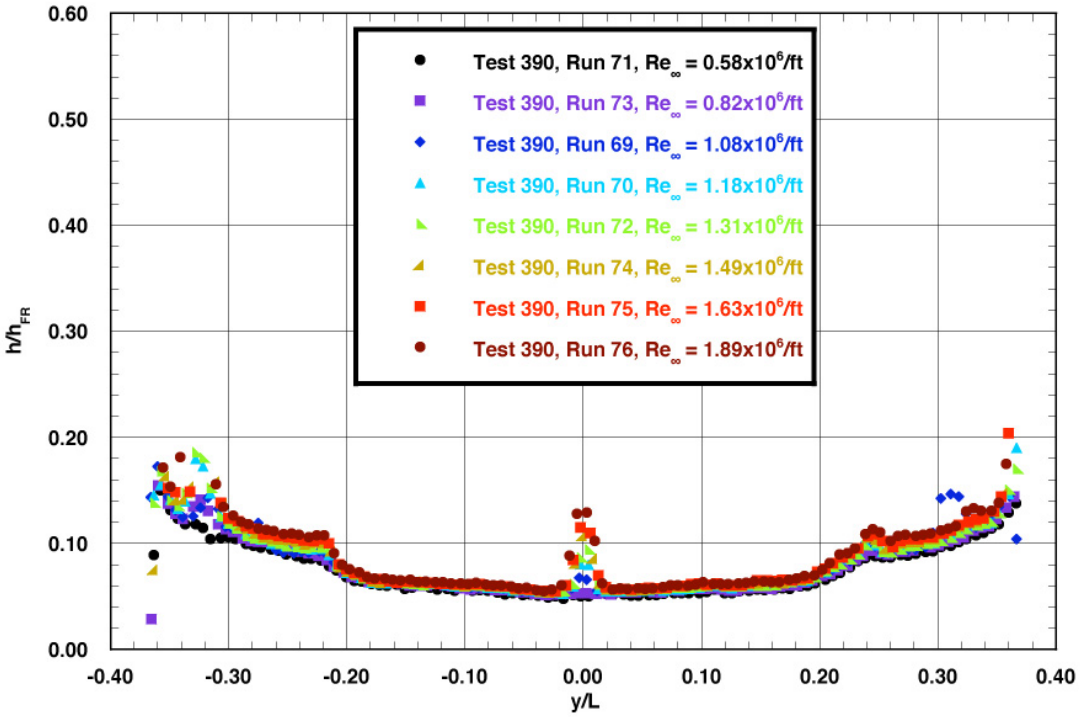

Figure B.45: RTF-BLT-P7 spanwise data (x/L = 0.85) in the 31-Inch Mach 10 Air Tunnel at α = 40-deg, x/L = 0.70, k_{CL} = 0.0115-in., $k_{AL\text{-}40\text{-}INV}$ = 0.0115-in.

Appendix C: 20-Inch CF_4 Tunnel Aeroheating

Table C.1: Cross Reference of Figure Numbers Versus Parametrics for Phosphor Images from the 20-Inch CF_4 Tunnel.

α (deg.)	Model	$(x/L)_{CL}$	k_{CL} (in.)	AL	$(x/L)_{AL}$ (in.)	k_{AL}	Figure
30	RTF-BLT-PC	0.20	0.0065	30-INV	0.20	0.0065	C.1
30	RTF-BLT-PC	0.20	0.0115	30-INV	0.20	0.0115	C.4
30	RTF-BLT-PC	0.50	0.0115	30-INV	0.66	0.0065	C.7
30	RTF-BLT-PC	0.66	0.0115	30-INV	0.66	0.0115	C.10
40	RTF-BLT-PC	-	-	-	-	-	C.13
40	RTF-BLT-PC	0.20	0.0065	40-INV+	0.20	0.0065	C.16
40	RTF-BLT-PB	0.40	0.0065	30-INV	0.40	0.0065	C.19
40	RTF-BLT-PB	0.40	0.0065	40-INV	0.40	0.0065	C.22
40	RTF-BLT-PC	0.40	0.0065	40-INV+	0.40	0.0065	C.25
40	RTF-BLT-PC	0.40	0.0115	40-INV+	0.40	0.0115	C.28
40	RTF-BLT-PC	0.60	0.0045	40-INV	0.60	0.0045	C.31
40	RTF-BLT-PC	0.60	0.0065	40-INV	0.60	0.0065	C.34
40	RTF-BLT-PC	0.60	0.0115	40-INV	0.60	0.0115	C.37
40	RTF-BLT-PC	0.60	0.0065	40-INV+	0.60	0.0065	C.40
40	RTF-BLT-PB	0.62	0.0115	40-INV	0.62	0.0115	C.43
40	RTF-BLT-PC	0.64	0.0065	40-INV	0.64	0.0065	C.46
40	RTF-BLT-PC	0.64	0.0115	40-INV	0.64	0.0115	C.49
40	RTF-BLT-PC	0.68	0.0065	40-INV	0.68	0.0065	C.52

Note: Corresponding data cuts are located immediately after figures.

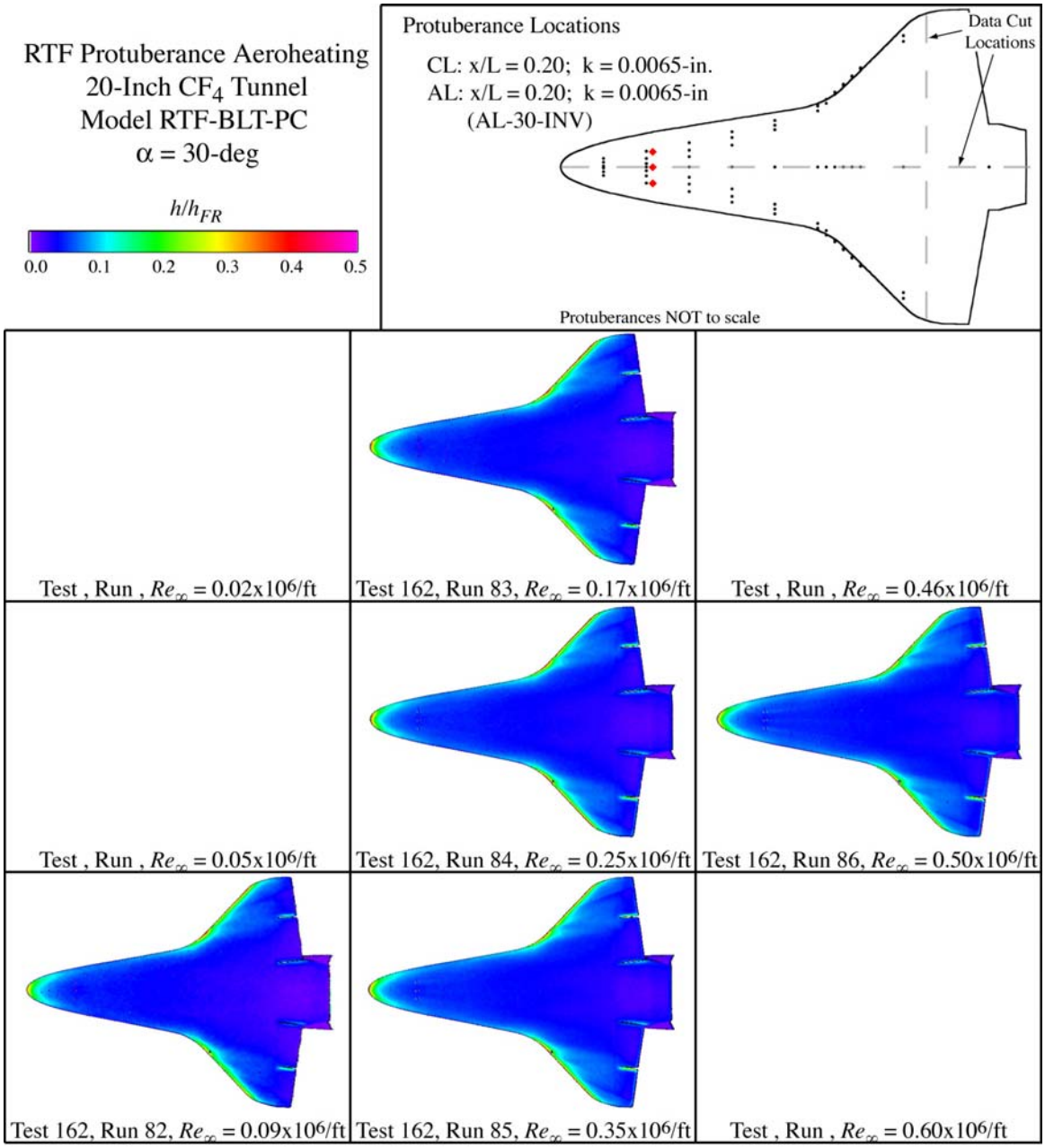

Figure C.1: RTF-BLT-PC global aeroheating in the 20-Inch CF_4 Tunnel at α = 30-deg, x/L = 0.20, k_{CL} = 0.0065-in., $k_{AL\text{-}30\text{-}INV}$ = 0.0065-in.

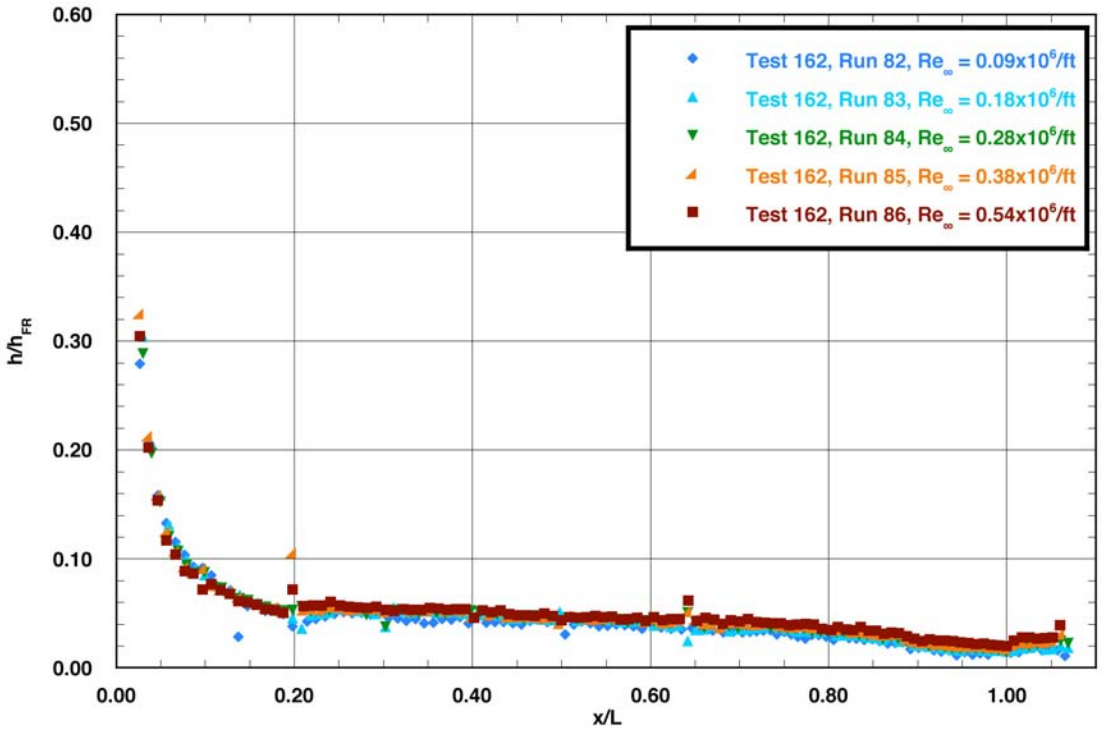

Figure C.2: RTF-BLT-PC centerline data in the 20-Inch CF_4 Tunnel at α = 30-deg, x/L = 0.20, k_{CL} = 0.0065-in., $k_{AL\text{-}30\text{-}INV}$ = 0.0065-in.

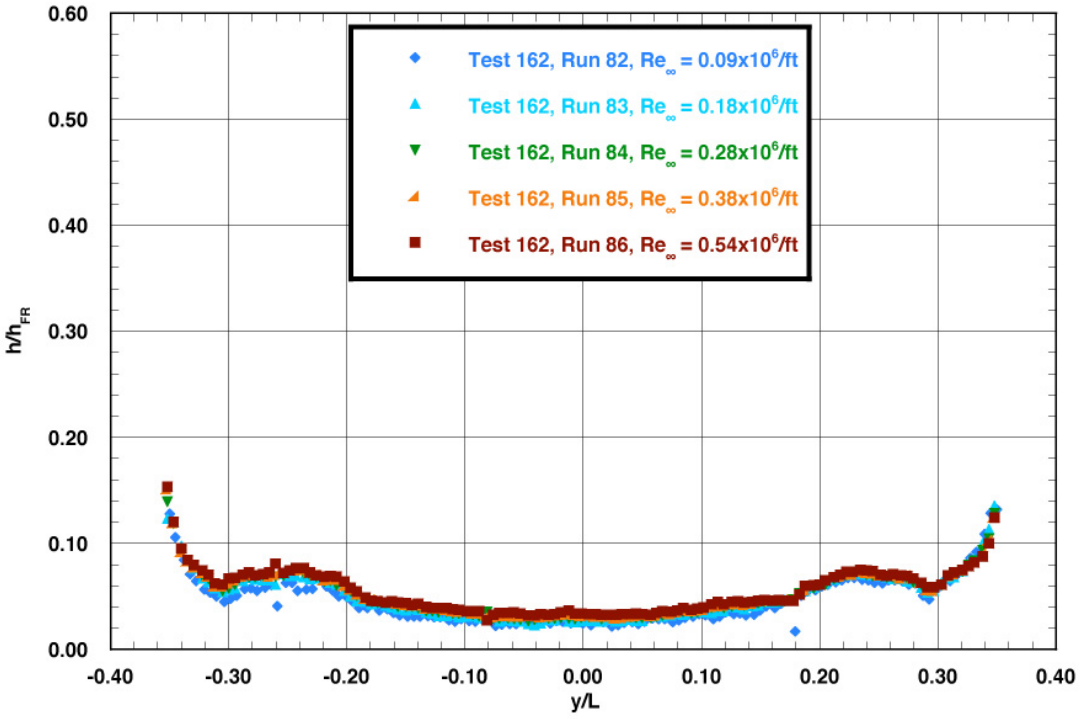

Figure C.3: RTF-BLT-PC spanwise data (x/L = 0.85) in the 20-Inch CF_4 Tunnel at α = 30-deg, x/L = 0.20, k_{CL} = 0.0065-in., $k_{AL\text{-}30\text{-}INV}$ = 0.0065-in.

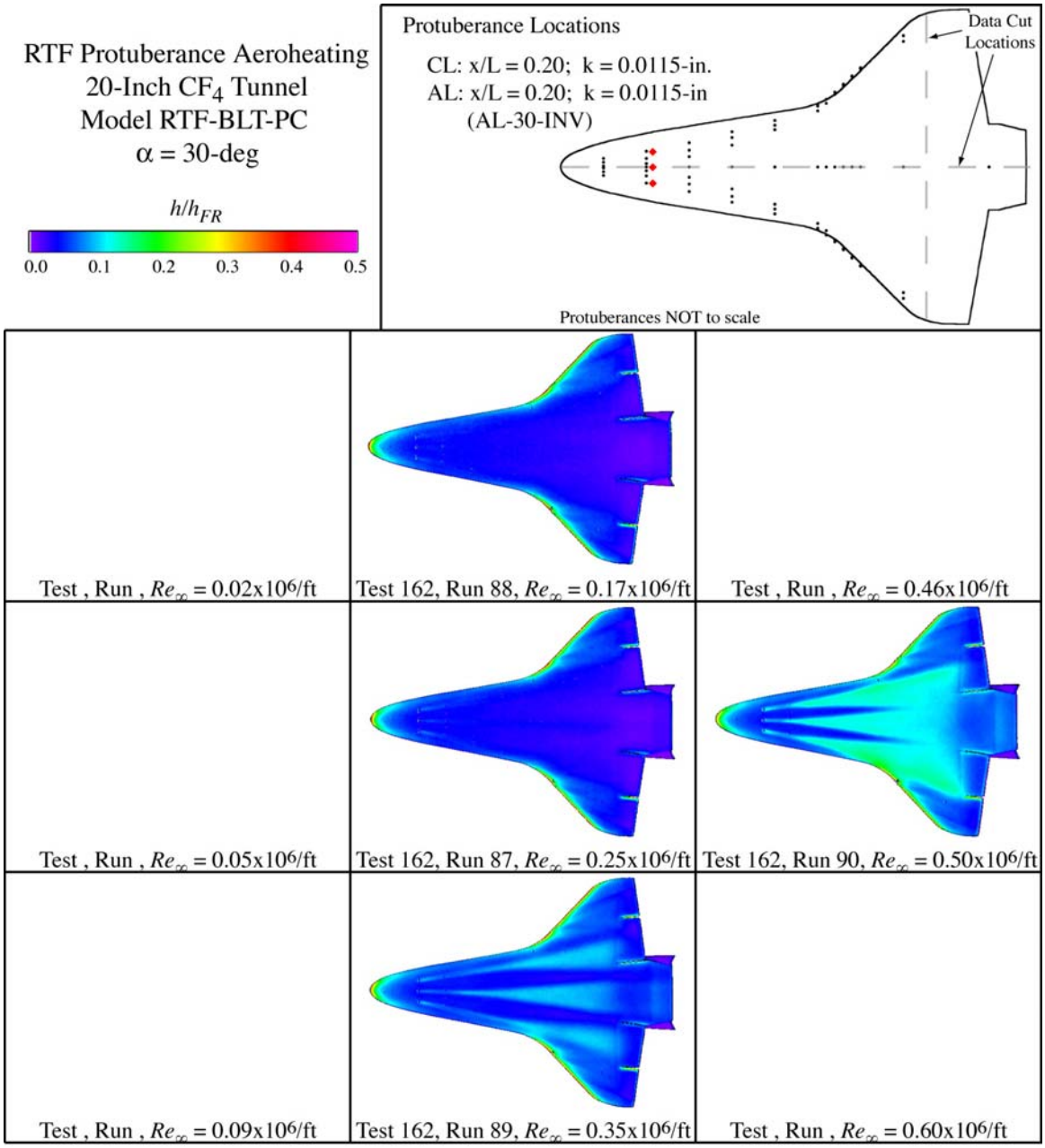

Figure C.4: RTF-BLT-PC global aeroheating in the 20-Inch CF_4 Tunnel at α = 30-deg, x/L = 0.20, k_{CL} = 0.0115-in., $k_{AL\text{-}30\text{-}INV}$ = 0.0115-in.

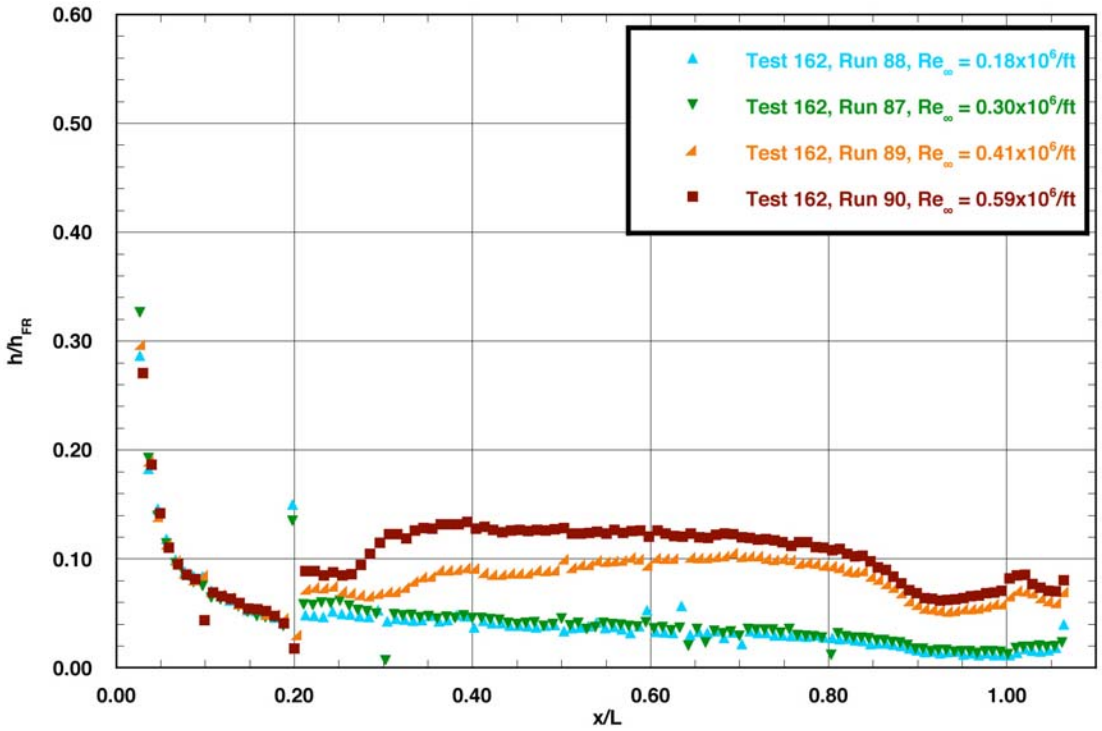

Figure C.5: RTF-BLT-PC centerline data in the 20-Inch CF_4 Tunnel at α = 30-deg, x/L = 0.20, k_{CL} = 0.0115-in., $k_{AL\text{-}30\text{-}INV}$ = 0.0115-in.

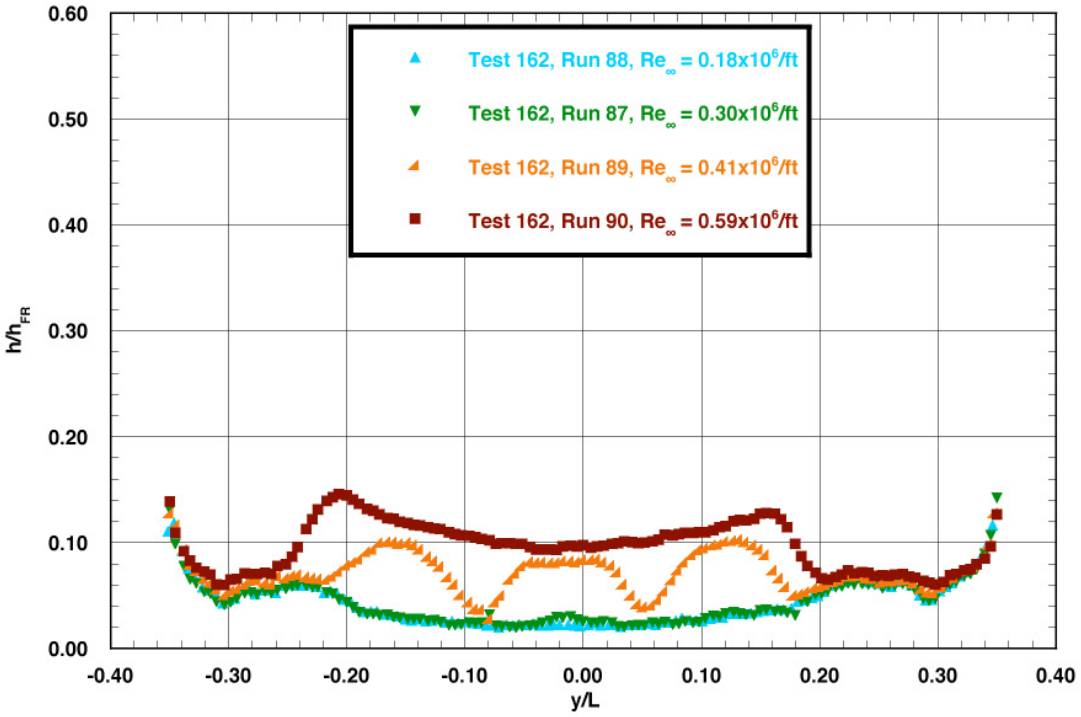

Figure C.6: RTF-BLT-PC spanwise data (x/L = 0.85) in the 20-Inch CF_4 Tunnel at α = 30-deg, x/L = 0.20, k_{CL} = 0.0115-in., $k_{AL\text{-}30\text{-}INV}$ = 0.0115-in.

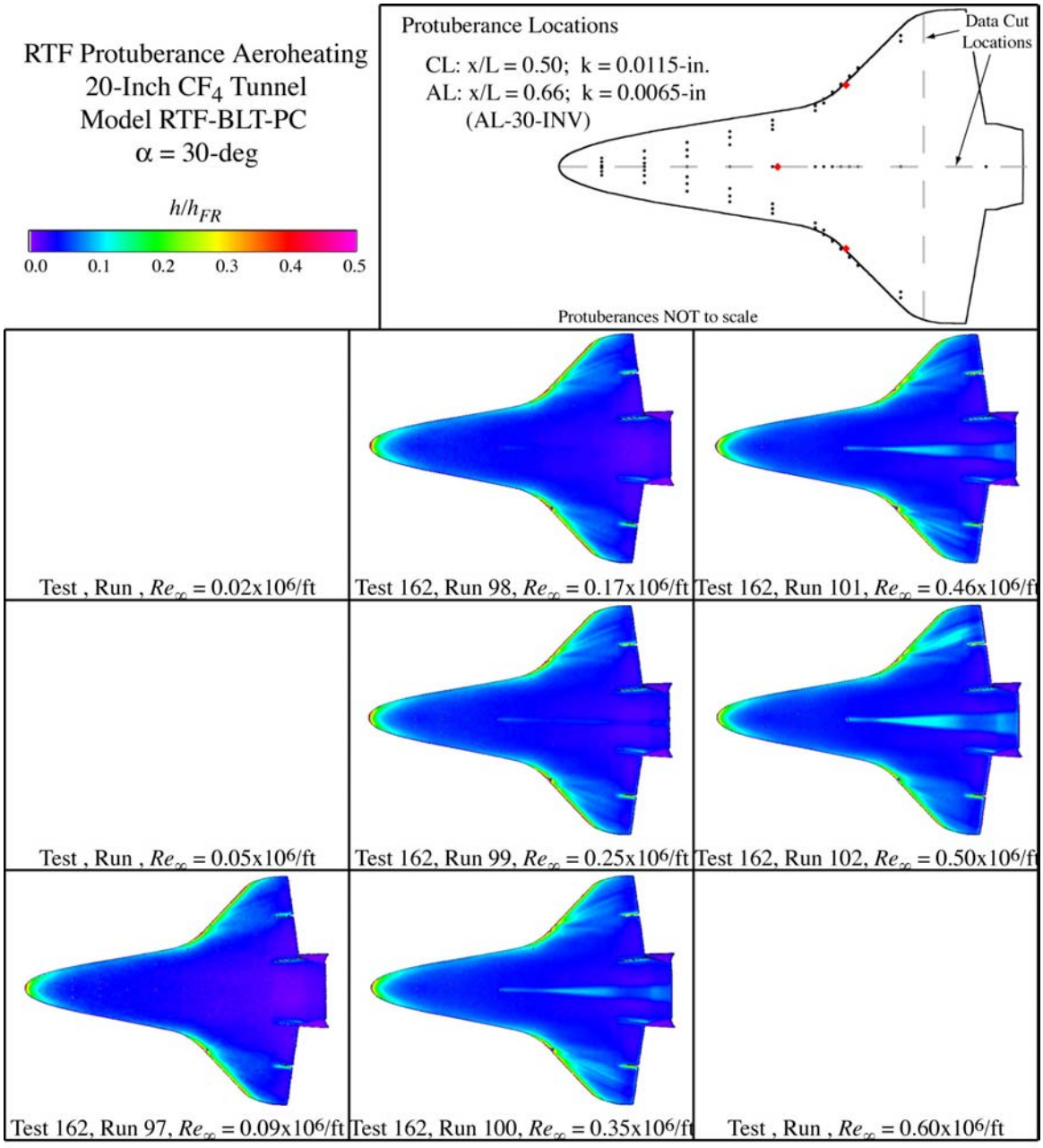

Figure C.7: RTF-BLT-PC global aeroheating in the 20-Inch CF_4 Tunnel at α = 30-deg, $(x/L)_{CL}$ = 0.50, k_{CL} = 0.0115-in., $(x/L)_{AL\text{-}30\text{-}INV}$ = 0.66, $k_{AL\text{-}30\text{-}INV}$ = 0.0065-in.

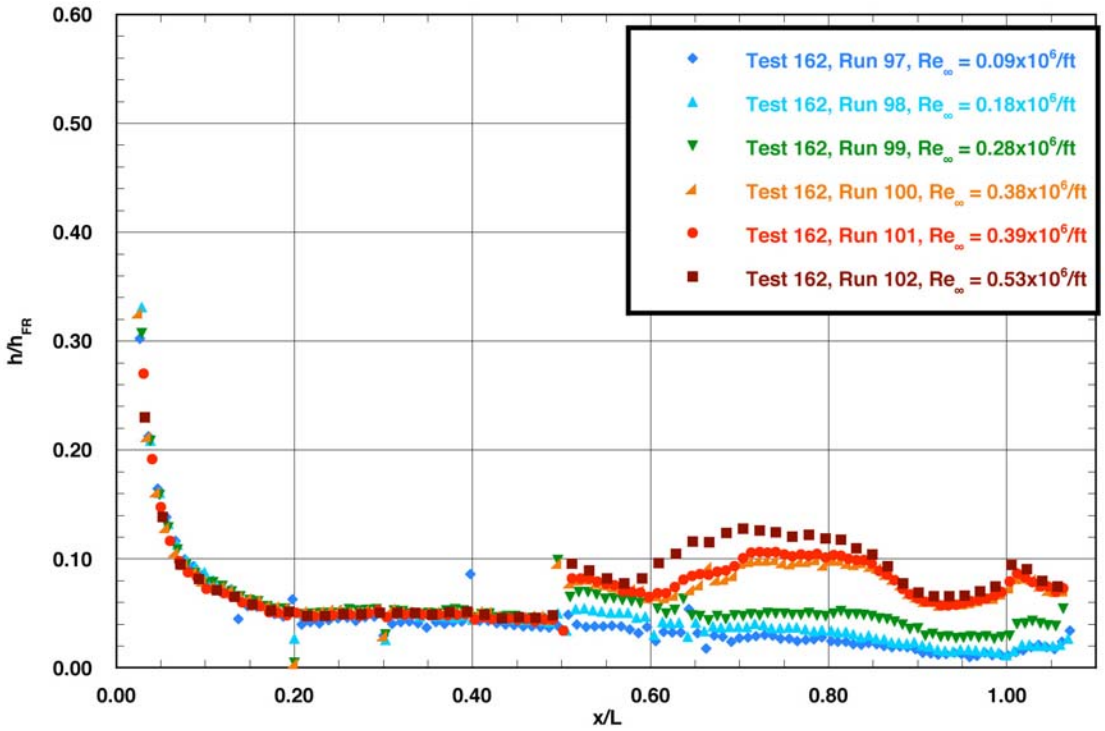

Figure C.8: RTF-BLT-PC centerline data in the 20-Inch CF_4 Tunnel at α = 30-deg, $(x/L)_{CL}$ = 0.50, k_{CL} = 0.0115-in., $(x/L)_{AL\text{-}30\text{-}INV}$ = 0.66, $k_{AL\text{-}30\text{-}INV}$ = 0.0065-in.

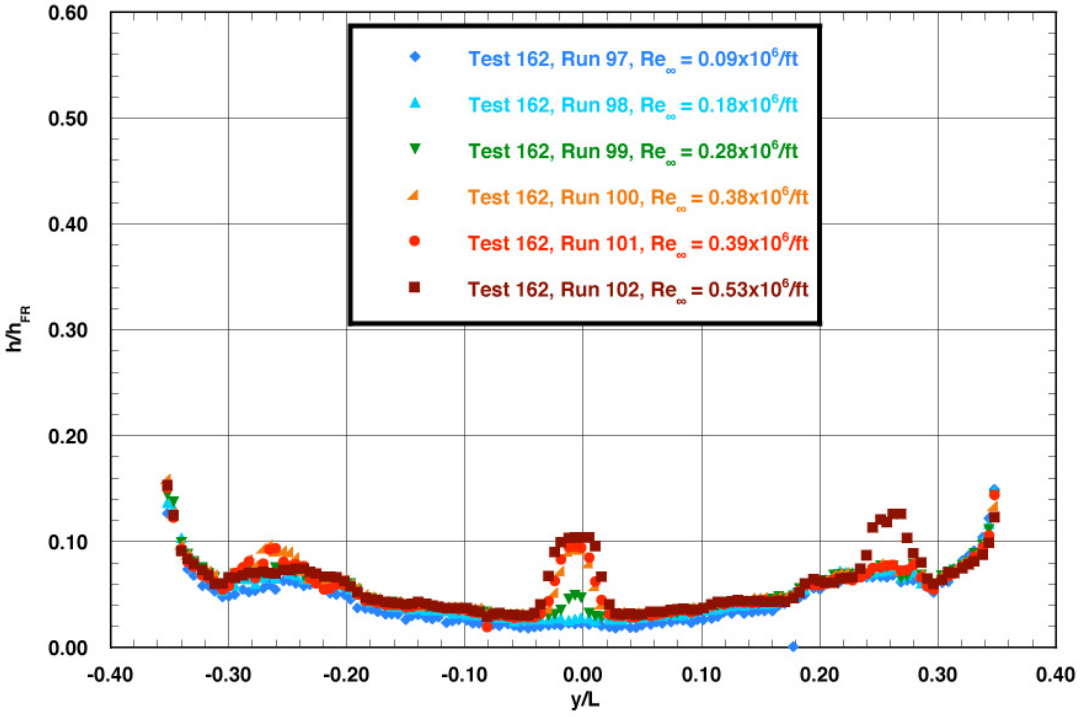

Figure C.9: RTF-BLT-PC spanwise data (x/L = 0.85) in the 20-Inch CF_4 Tunnel at α = 30-deg, $(x/L)_{CL}$ = 0.50, k_{CL} = 0.0115-in., $(x/L)_{AL\text{-}30\text{-}INV}$ = 0.66, $k_{AL\text{-}30\text{-}INV}$ = 0.0065-in.

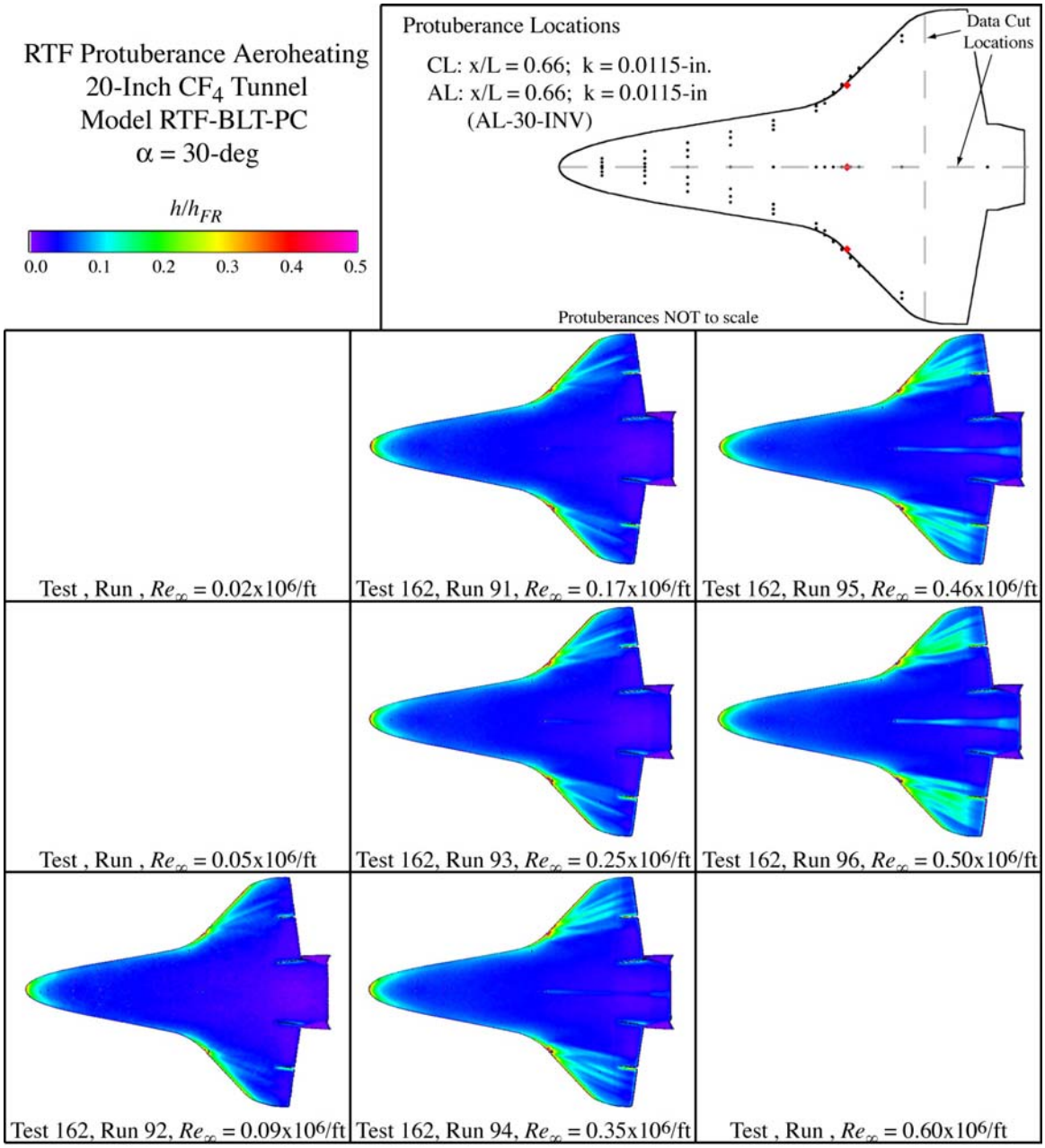

Figure C.10: RTF-BLT-PC global aeroheating in the 20-Inch CF_4 Tunnel at α = 30-deg, x/L = 0.66, k_{CL} = 0.0115-in., $k_{AL\text{-}30\text{-}INV}$ = 0.0115-in.

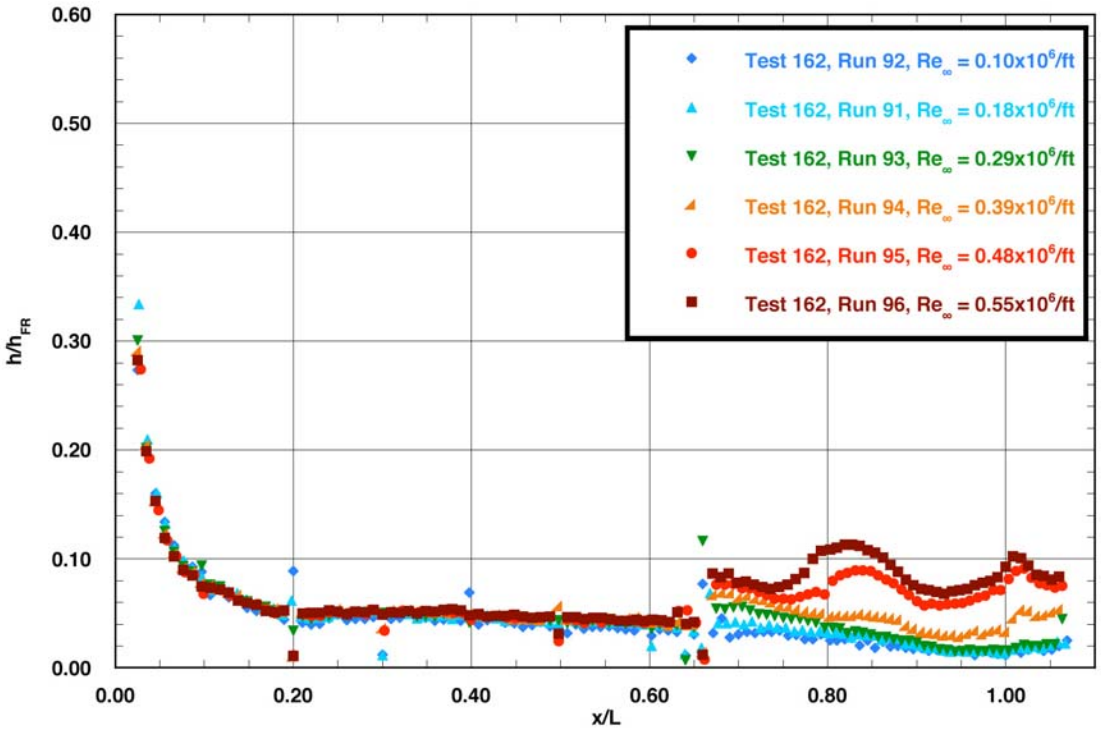

Figure C.11: RTF-BLT-PC centerline data in the 20-Inch CF_4 Tunnel at α = 30-deg, x/L = 0.66, k_{CL} = 0.0115-in., $k_{AL\text{-}30\text{-}INV}$ = 0.0115-in.

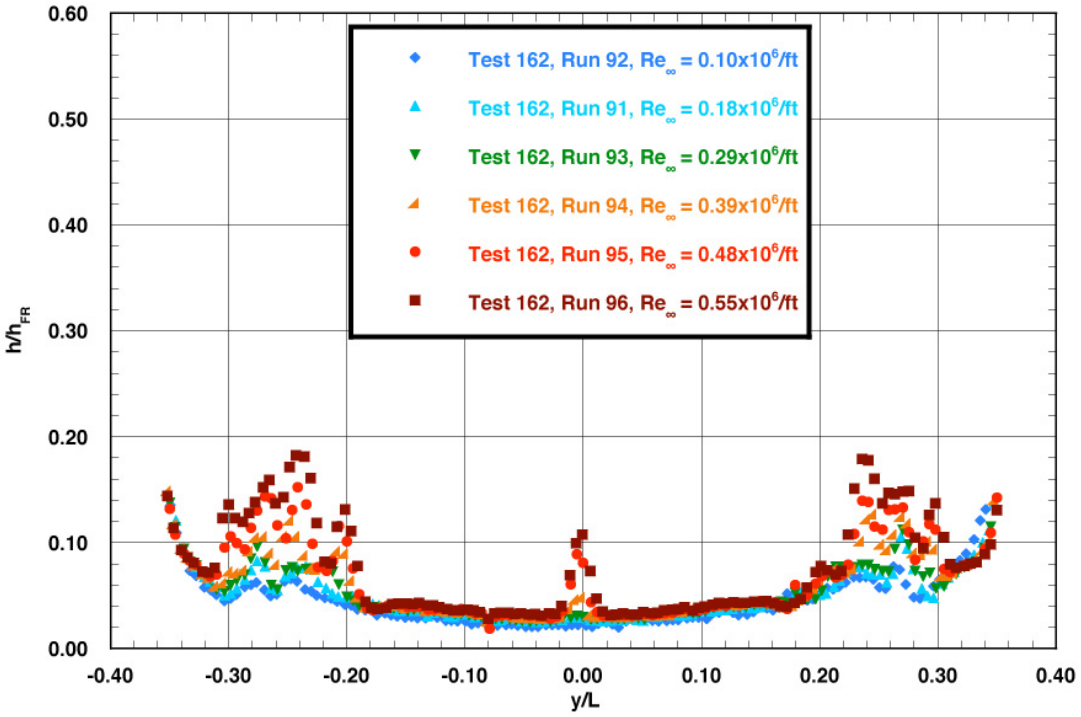

Figure C.12: RTF-BLT-PC spanwise data (x/L = 0.85) in the 20-Inch CF_4 Tunnel at α = 30-deg, x/L = 0.66, k_{CL} = 0.0115-in., $k_{AL\text{-}30\text{-}INV}$ = 0.0115-in.

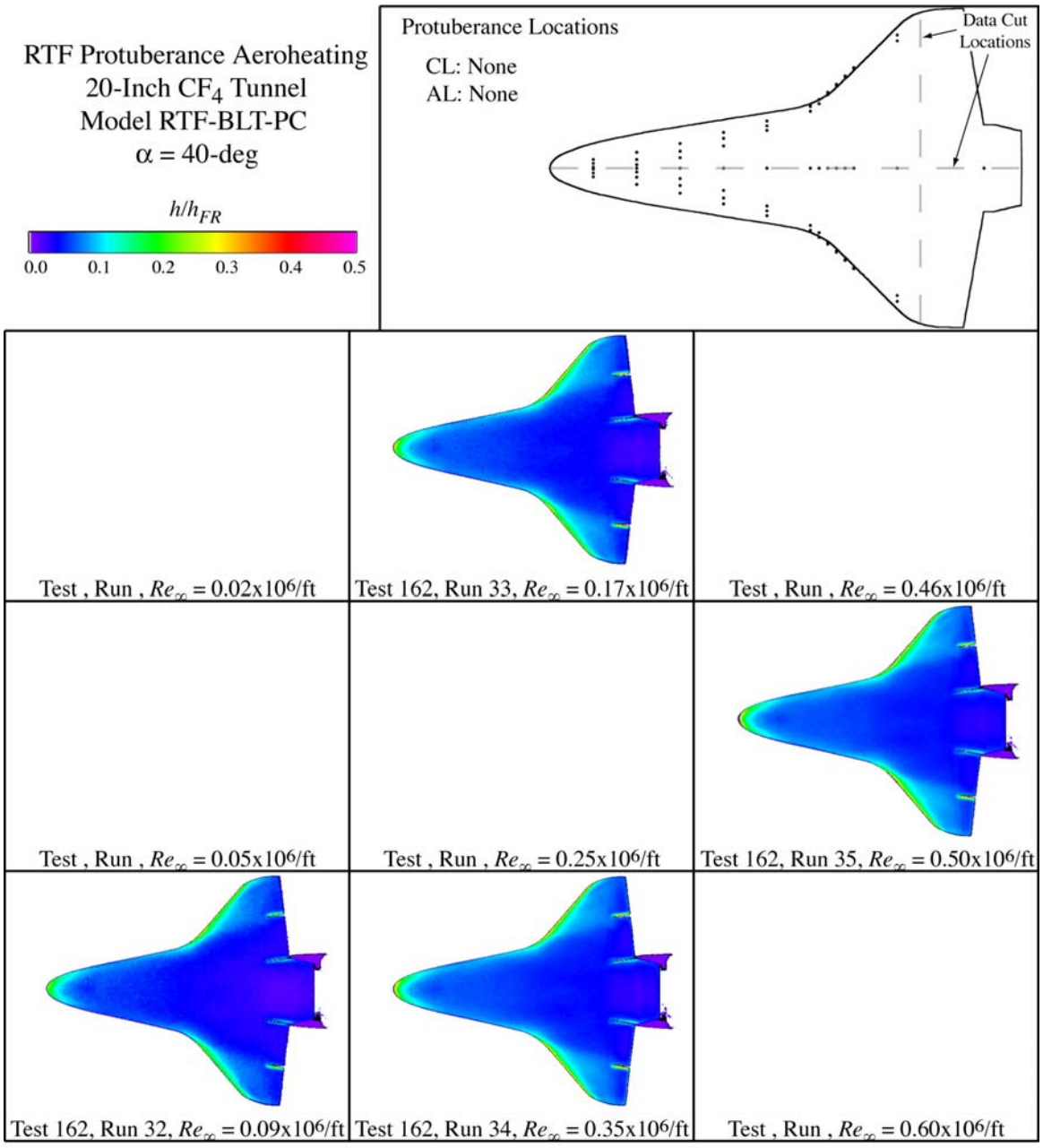

Figure C.13: RTF-BLT-PC global aeroheating in the 20-Inch CF_4 Tunnel at α = 40-deg, baseline.

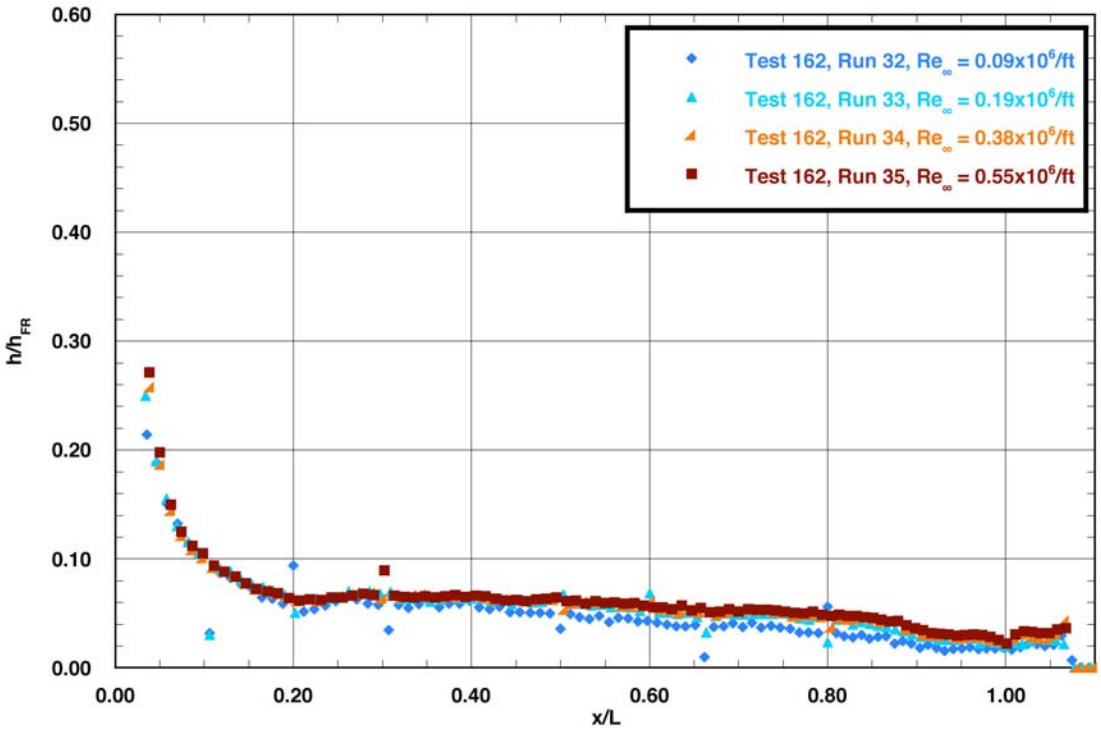

Figure C.14: RTF-BLT-PC centerline data in the 20-Inch CF_4 Tunnel at α = 40-deg, baseline.

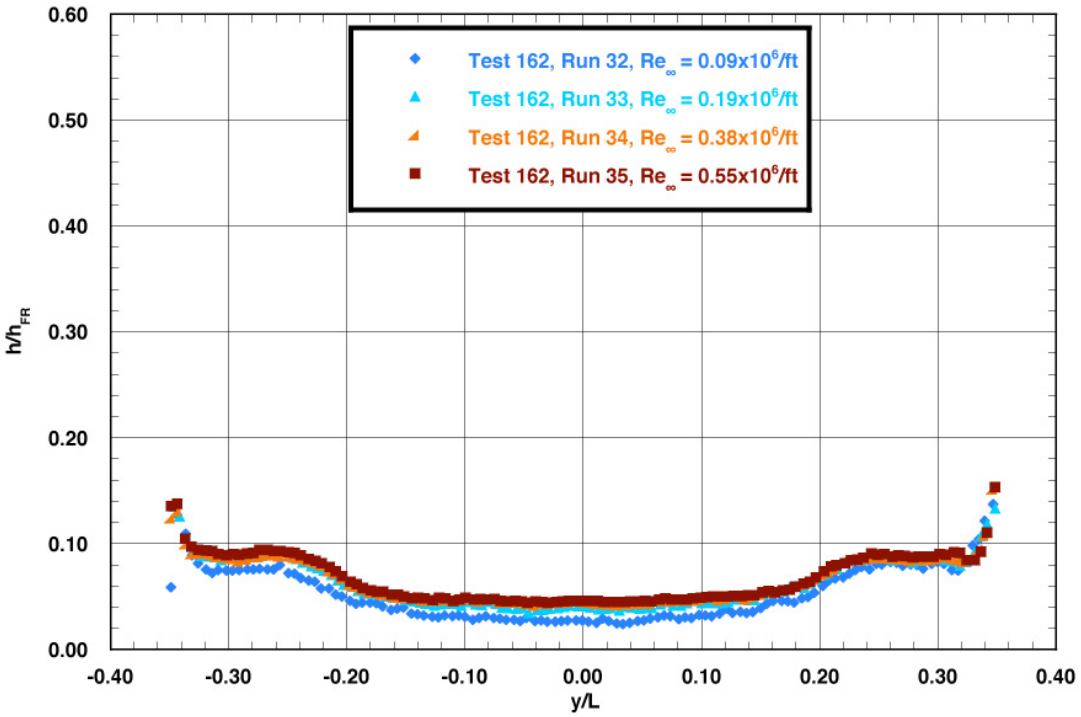

Figure C.15: RTF-BLT-PC spanwise data (*x/L* = 0.85) in the 20-Inch CF_4 Tunnel at α = 40-deg, baseline.

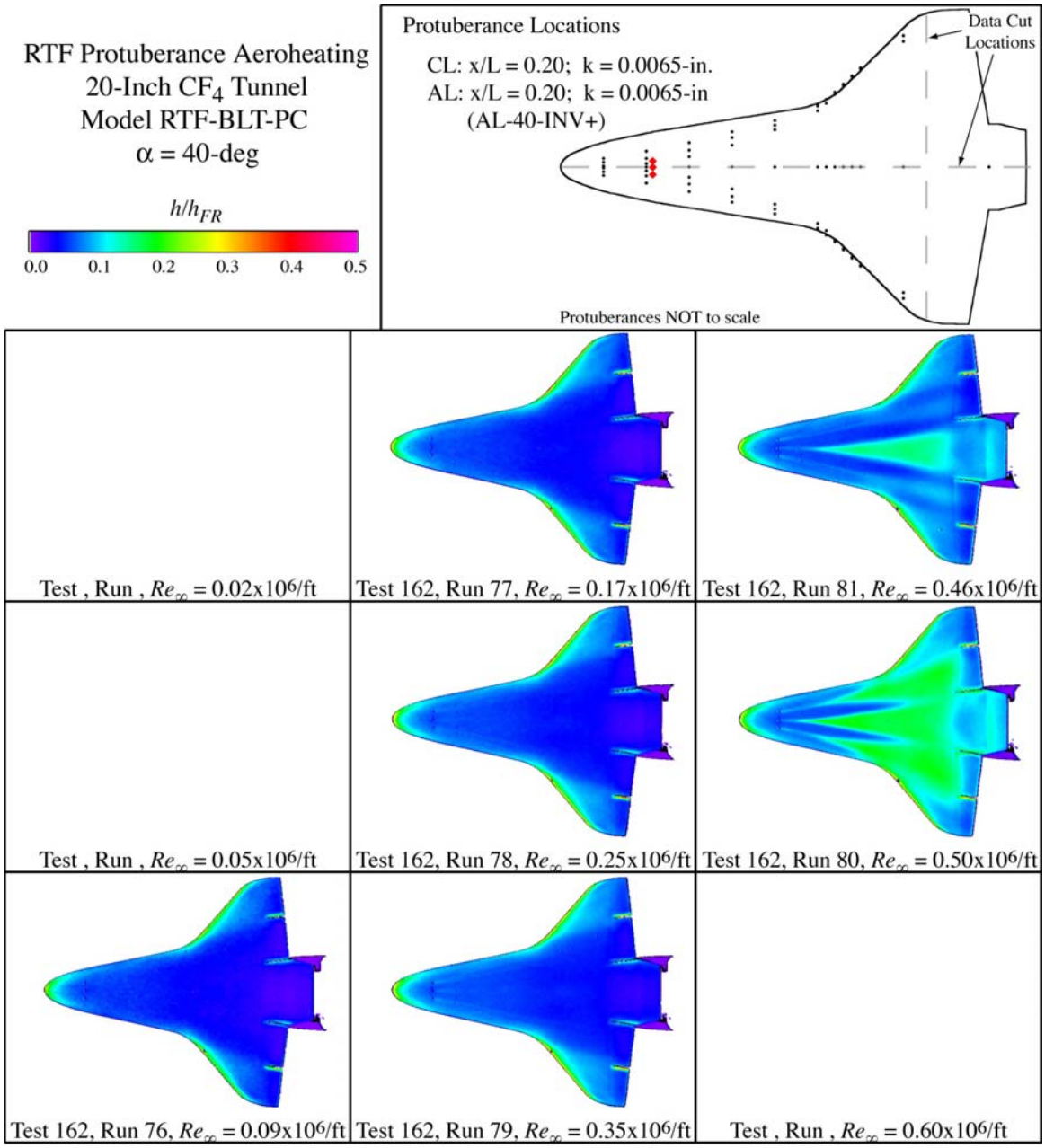

Figure C.16: RTF-BLT-PC global aeroheating in the 20-Inch CF_4 Tunnel at α = 40-deg, x/L = 0.20, k_{CL} = 0.0065-in., $k_{AL\text{-}40\text{-}INV+}$ = 0.0065-in.

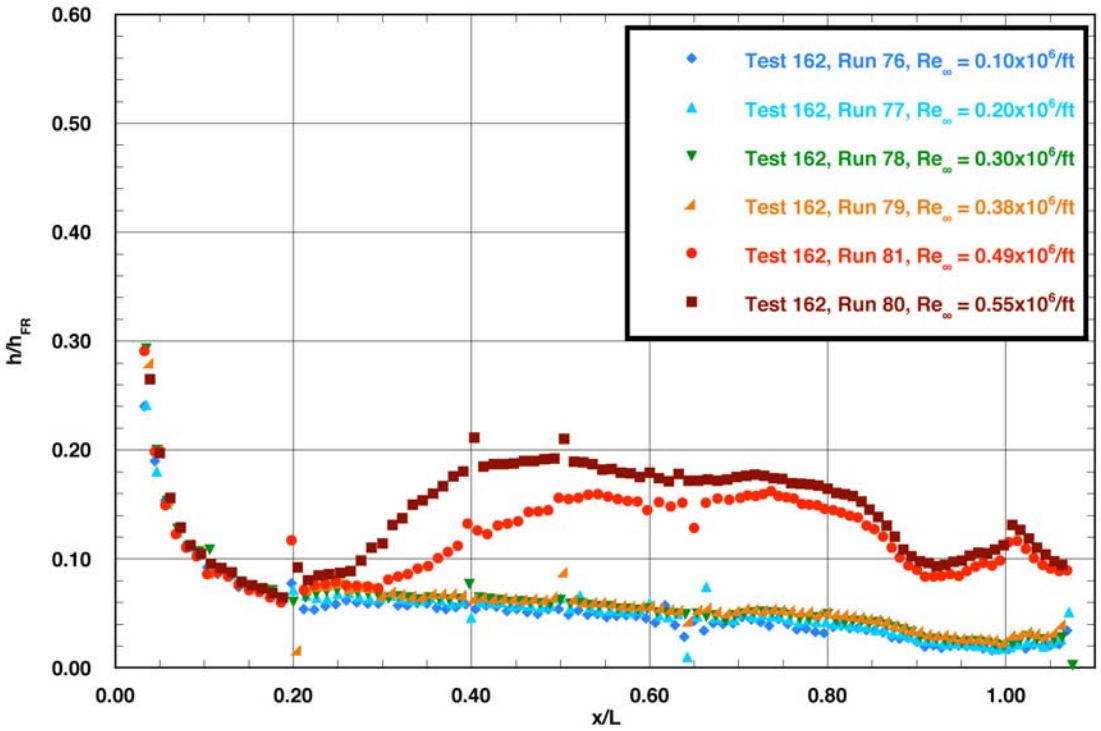

Figure C.17: RTF-BLT-PC centerline data in the 20-Inch CF_4 Tunnel at α = 40-deg, x/L = 0.20, k_{CL} = 0.0065-in., $k_{AL\text{-}40\text{-}INV+}$ = 0.0065-in.

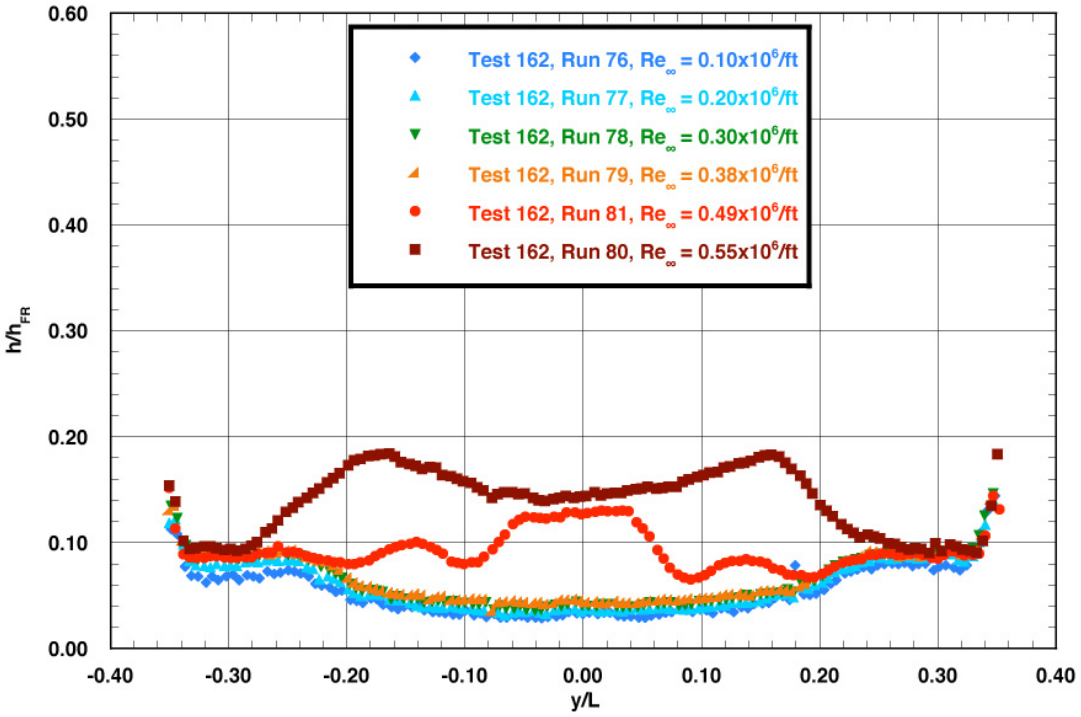

Figure C.18: RTF-BLT-PC spanwise data (x/L = 0.85) in the 20-Inch CF_4 Tunnel at α = 40-deg, x/L = 0.20, k_{CL} = 0.0065-in., $k_{AL\text{-}40\text{-}INV+}$ = 0.0065-in.

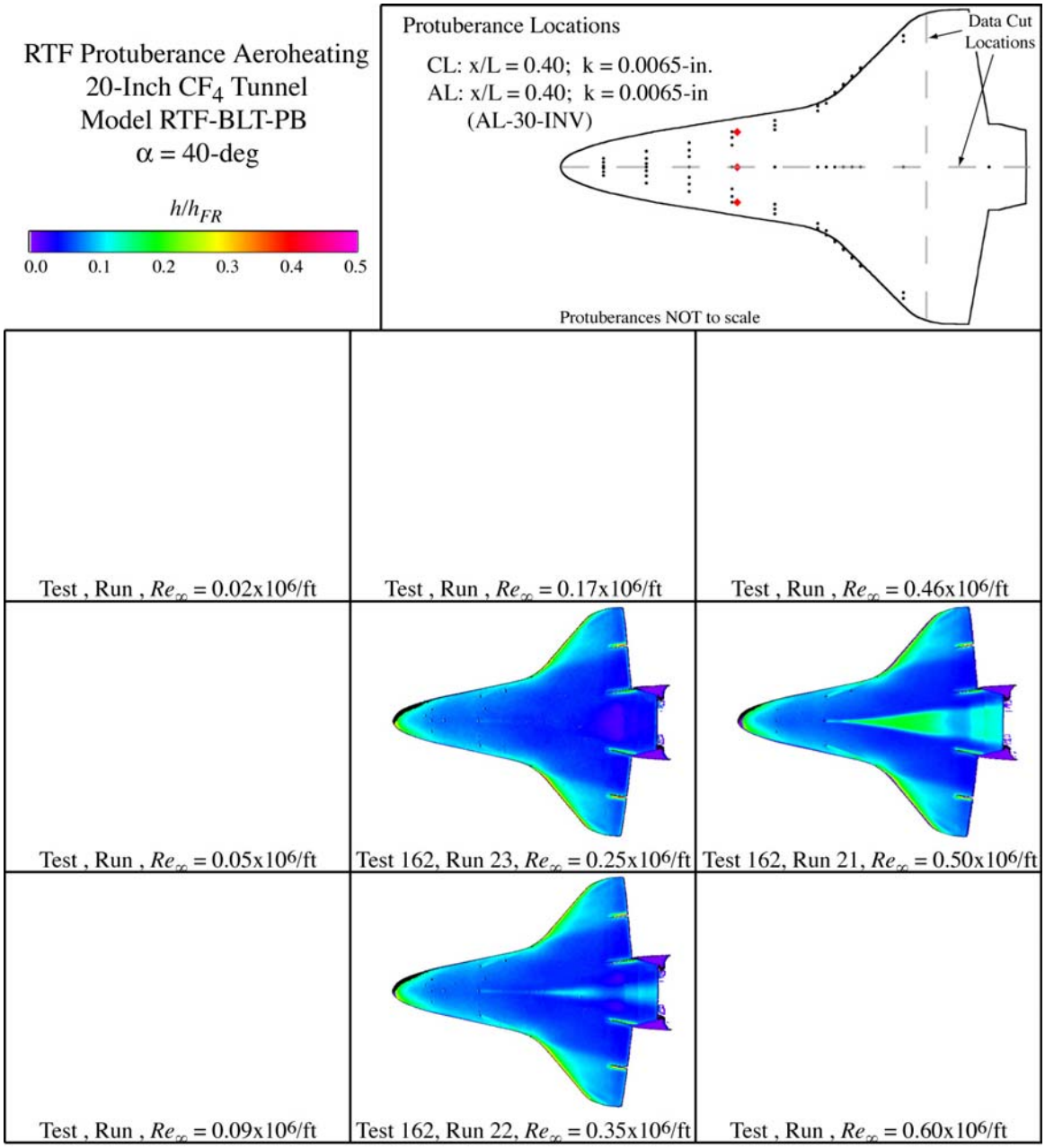

Figure C.19: RTF-BLT-PB global aeroheating in the 20-Inch CF_4 Tunnel at α = 40-deg, x/L = 0.40, k_{CL} = 0.0065-in., $k_{AL\text{-}30\text{-}INV}$ = 0.0065-in.

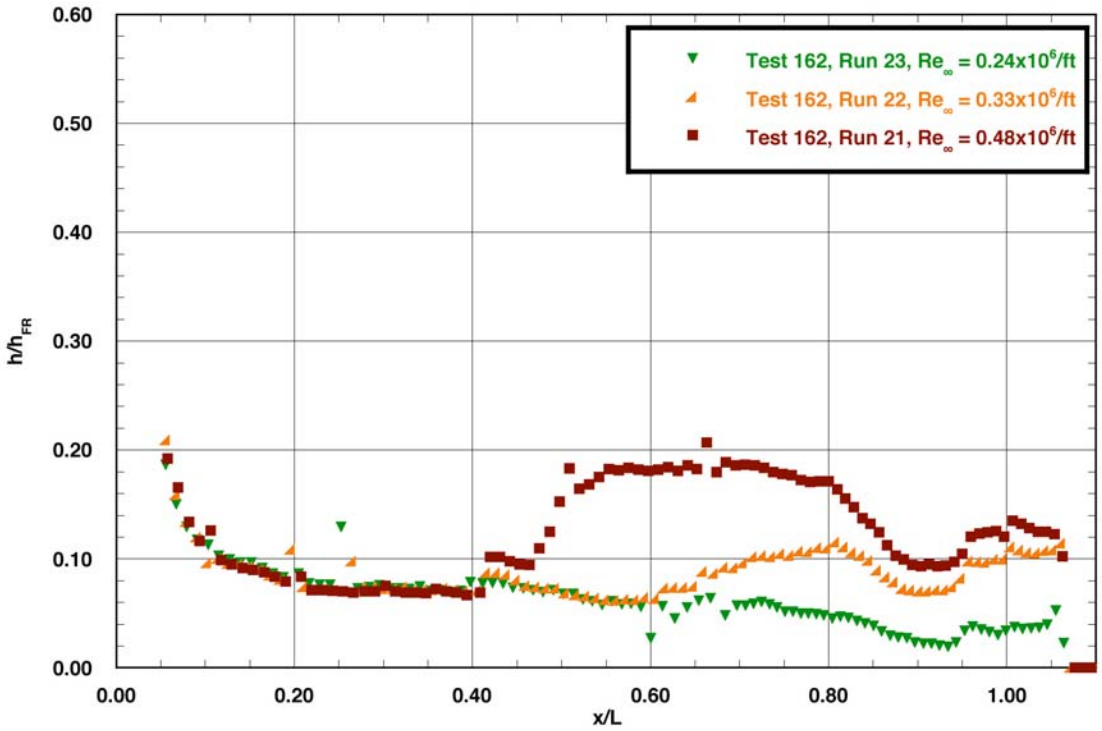

Figure C.20: RTF-BLT-PB centerline data in the 20-Inch CF_4 Tunnel at α = 40-deg, x/L = 0.40, k_{CL} = 0.0065-in., $k_{AL\text{-}30\text{-}INV}$ = 0.0065-in.

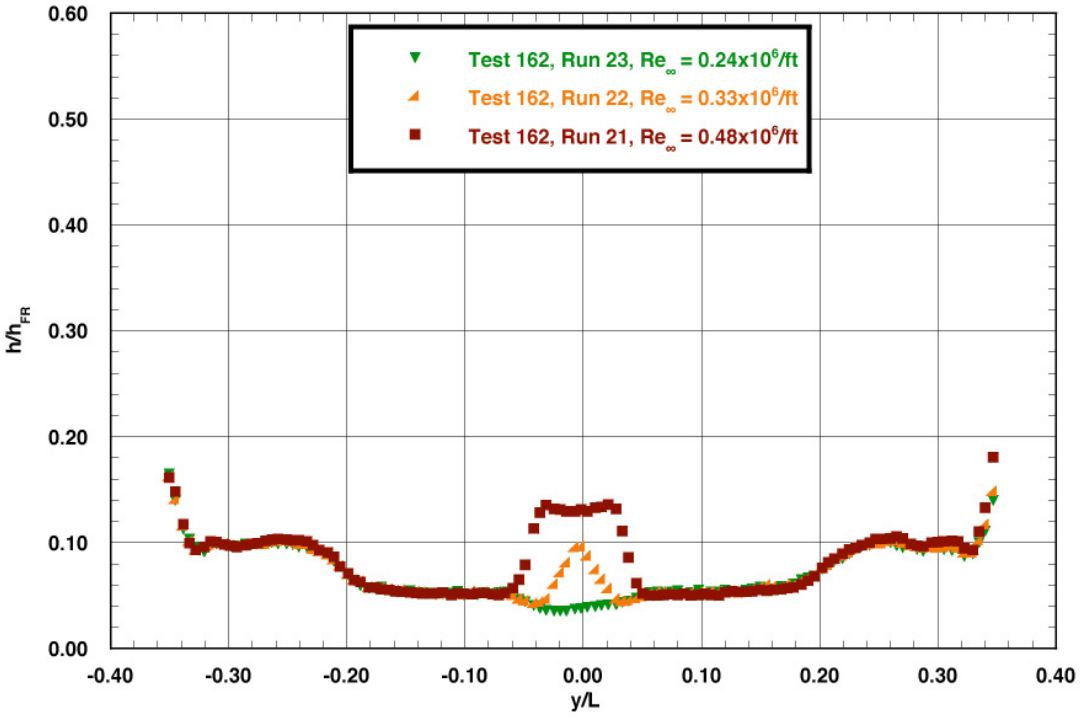

Figure C.21: RTF-BLT-PB spanwise data (x/L = 0.85) in the 20-Inch CF_4 Tunnel at α = 40-deg, x/L = 0.40, k_{CL} = 0.0065-in., $k_{AL\text{-}30\text{-}INV}$ = 0.0065-in.

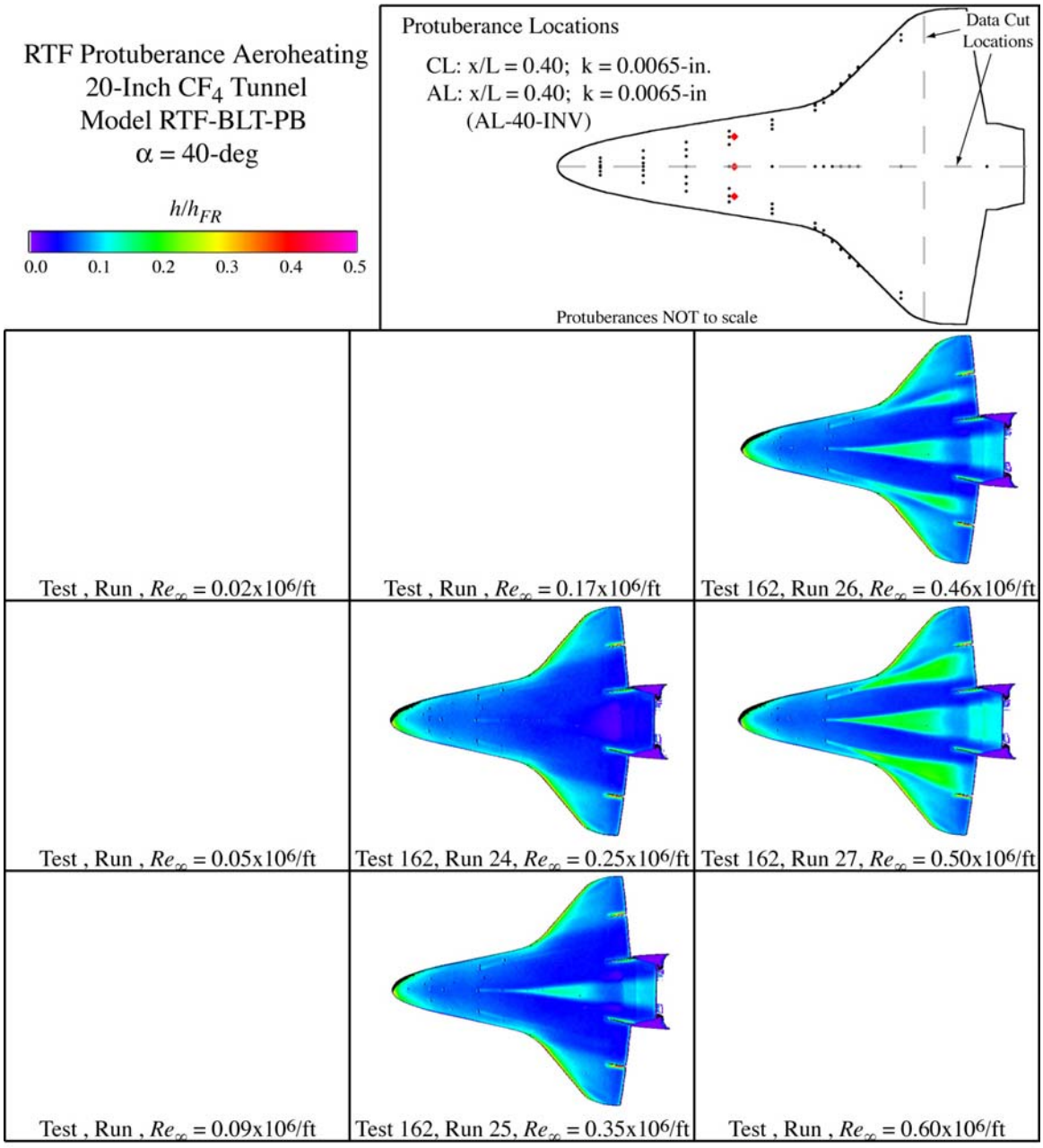

Figure C.22: RTF-BLT-PB global aeroheating in the 20-Inch CF_4 Tunnel at α = 40-deg, x/L = 0.40, k_{CL} = 0.0065-in., $k_{AL\text{-}40\text{-}INV}$ = 0.0065-in.

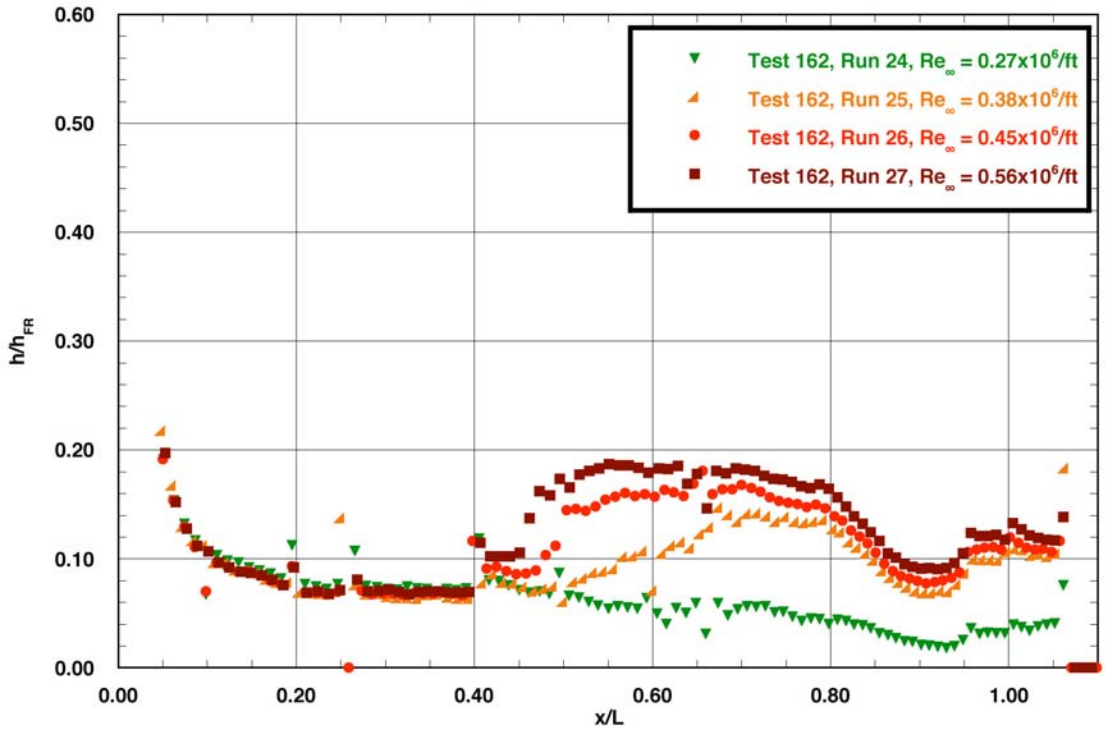

Figure C.23: RTF-BLT-PB centerline data in the 20-Inch CF_4 Tunnel at α = 40-deg, x/L = 0.40, k_{CL} = 0.0065-in., $k_{AL\text{-}40\text{-}INV}$ = 0.0065-in.

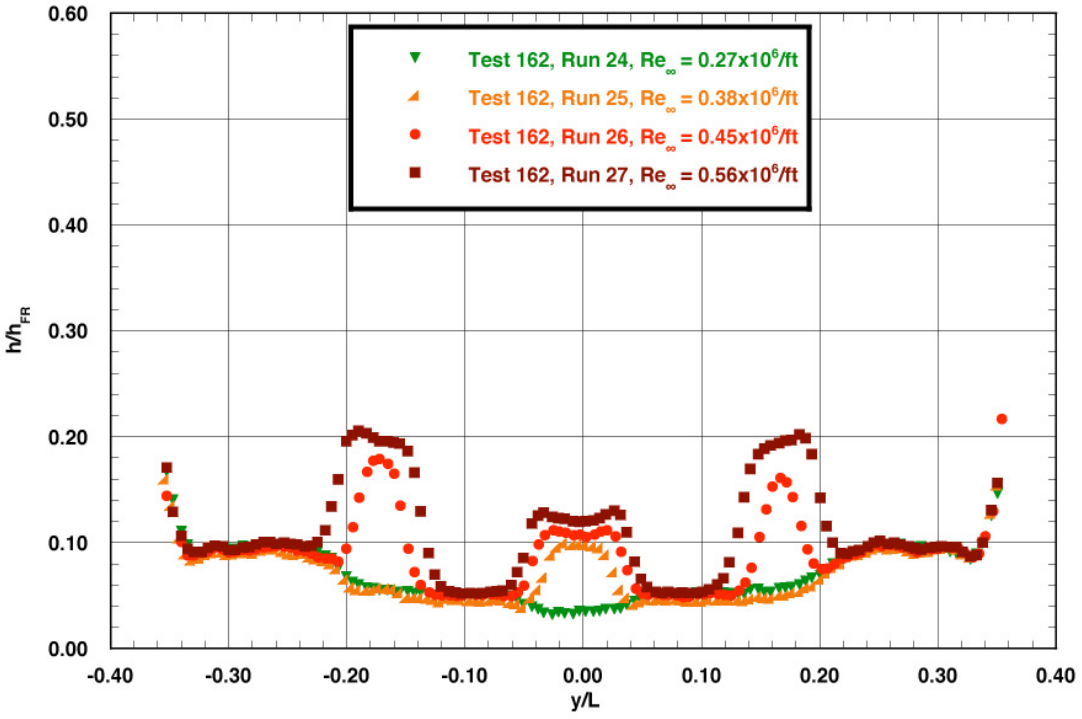

Figure C.24: RTF-BLT-PB spanwise data (x/L = 0.85) in the 20-Inch CF_4 Tunnel at α = 40-deg, x/L = 0.40, k_{CL} = 0.0065-in., $k_{AL\text{-}40\text{-}INV}$ = 0.0065-in.

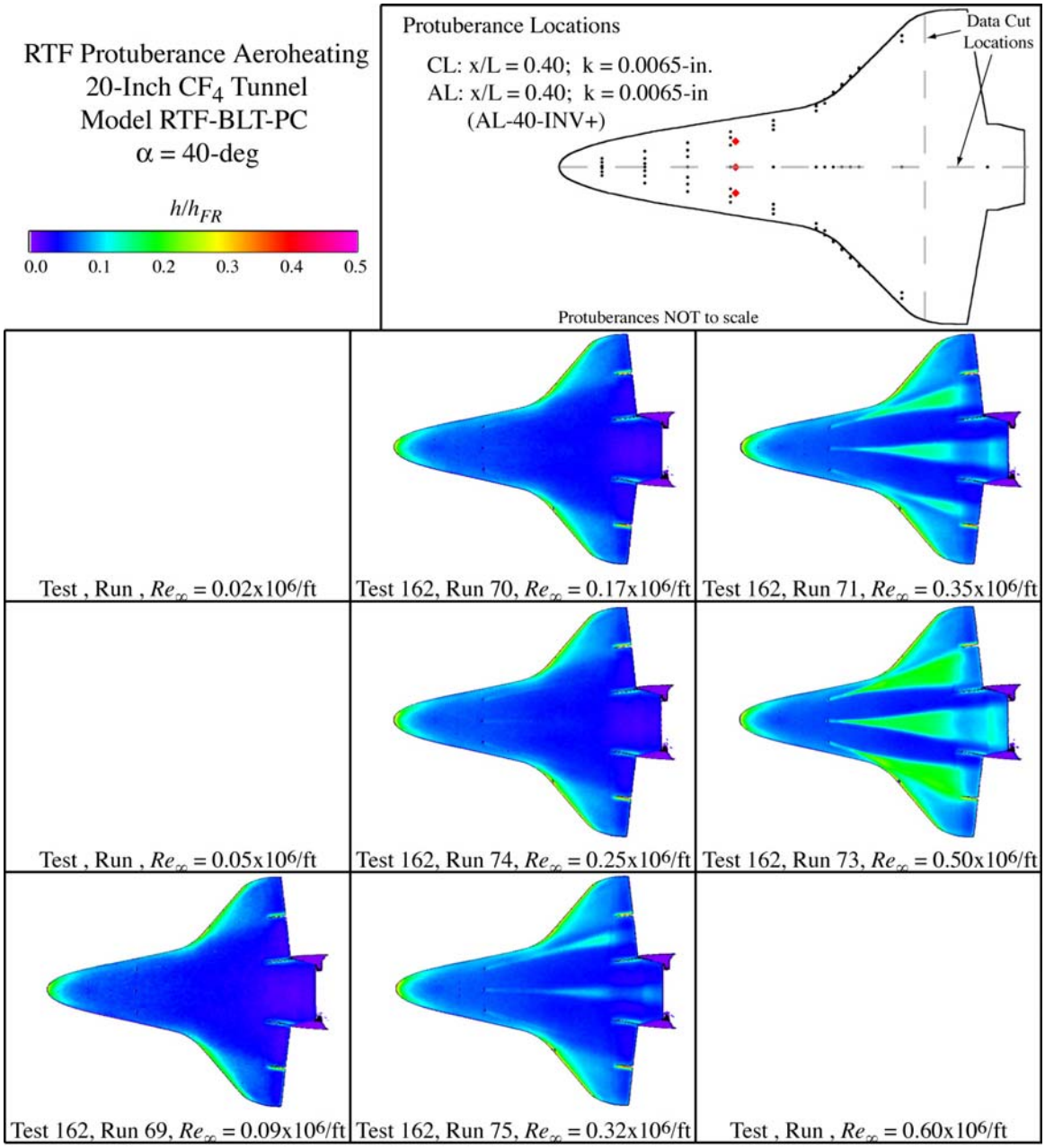

Figure C.25: RTF-BLT-PC global aeroheating in the 20-Inch CF_4 Tunnel at α = 40-deg, x/L = 0.40, k_{CL} = 0.0065-in., $k_{AL\text{-}40\text{-}INV+}$ = 0.0065-in.

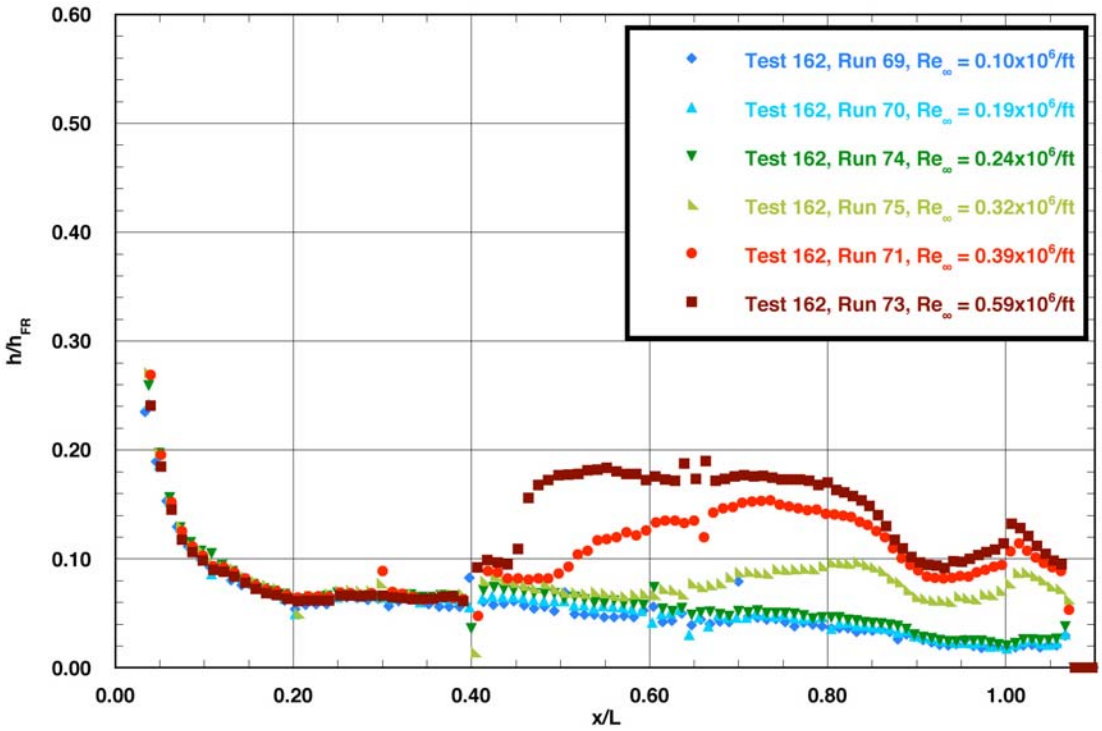

Figure C.26: RTF-BLT-PC centerline data in the 20-Inch CF_4 Tunnel at α = 40-deg, x/L = 0.40, k_{CL} = 0.0065-in., $k_{AL\text{-}40\text{-}INV+}$ = 0.0065-in.

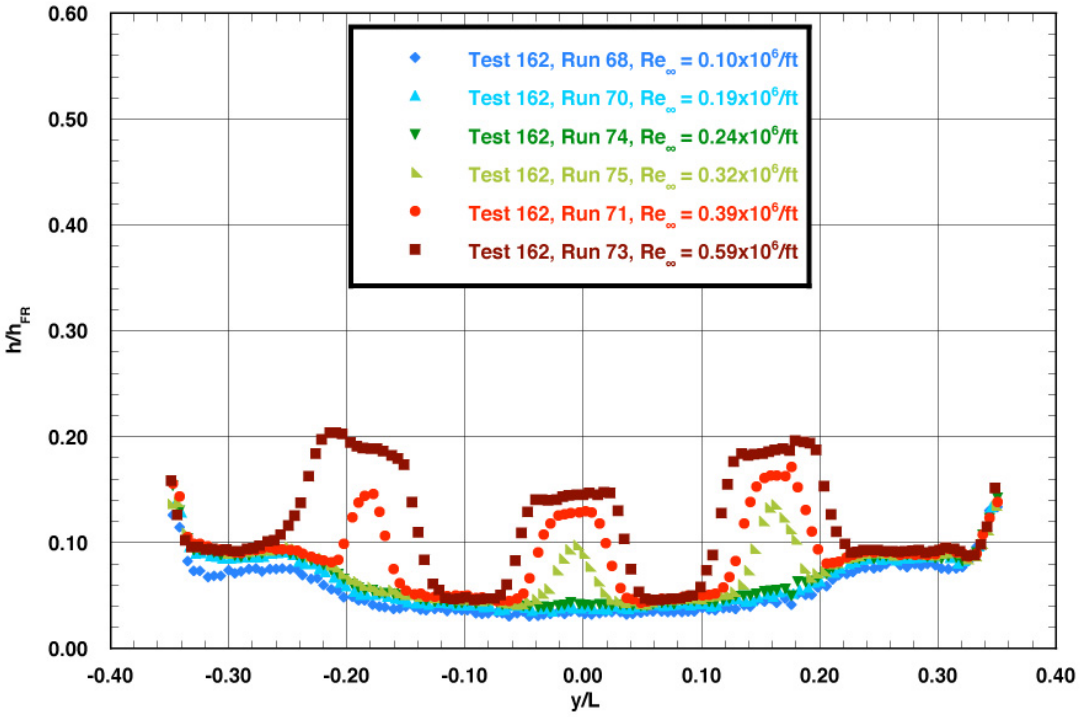

Figure C.27: RTF-BLT-PC spanwise data (x/L = 0.85) in the 20-Inch CF_4 Tunnel at α = 40-deg, x/L = 0.40, k_{CL} = 0.0065-in., $k_{AL\text{-}40\text{-}INV+}$ = 0.0065-in.

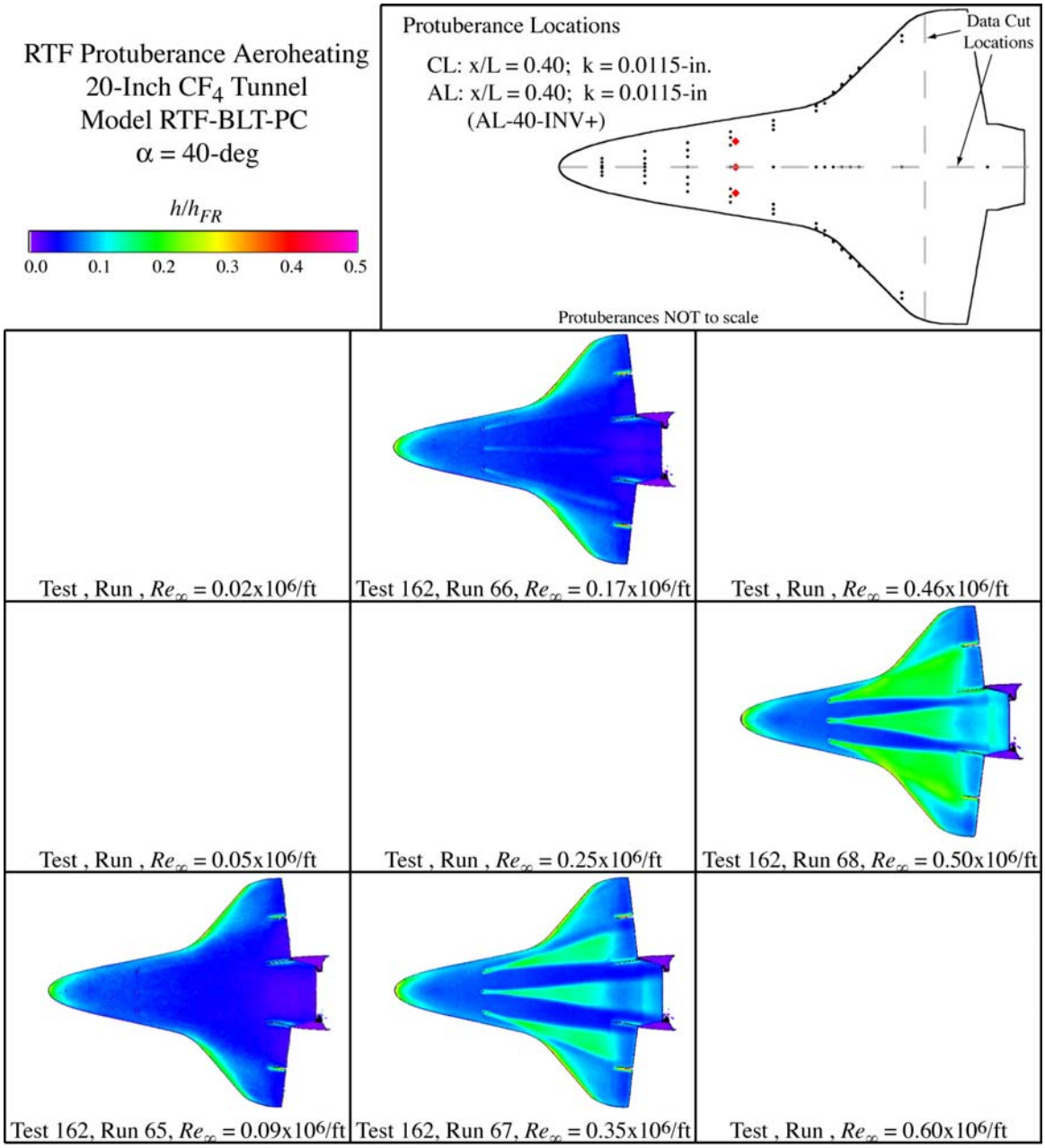

Figure C.28: RTF-BLT-PC global aeroheating in the 20-Inch CF_4 Tunnel at α = 40-deg, x/L = 0.40, k_{CL} = 0.0115-in., $k_{AL\text{-}40\text{-}INV+}$ = 0.0115-in.

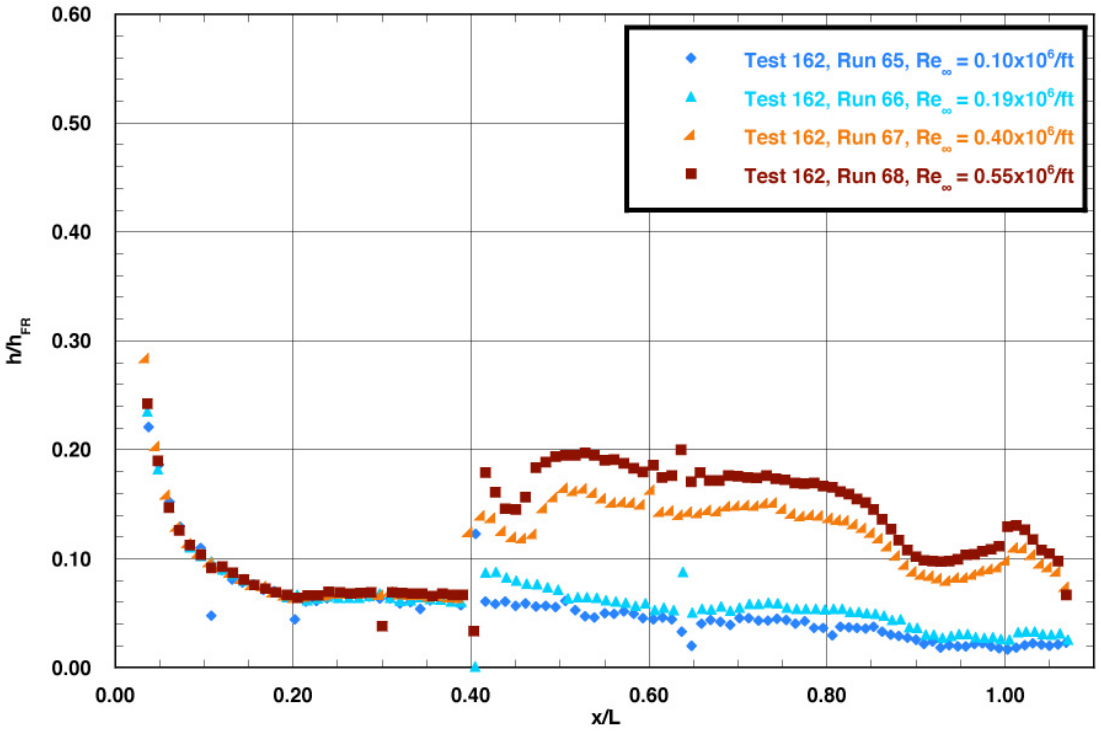

Figure C.29: RTF-BLT-PC centerline data in the 20-Inch CF_4 Tunnel at α = 40-deg, x/L = 0.40, k_{CL} = 0.0115-in., $k_{AL\text{-}40\text{-}INV+}$ = 0.0115-in.

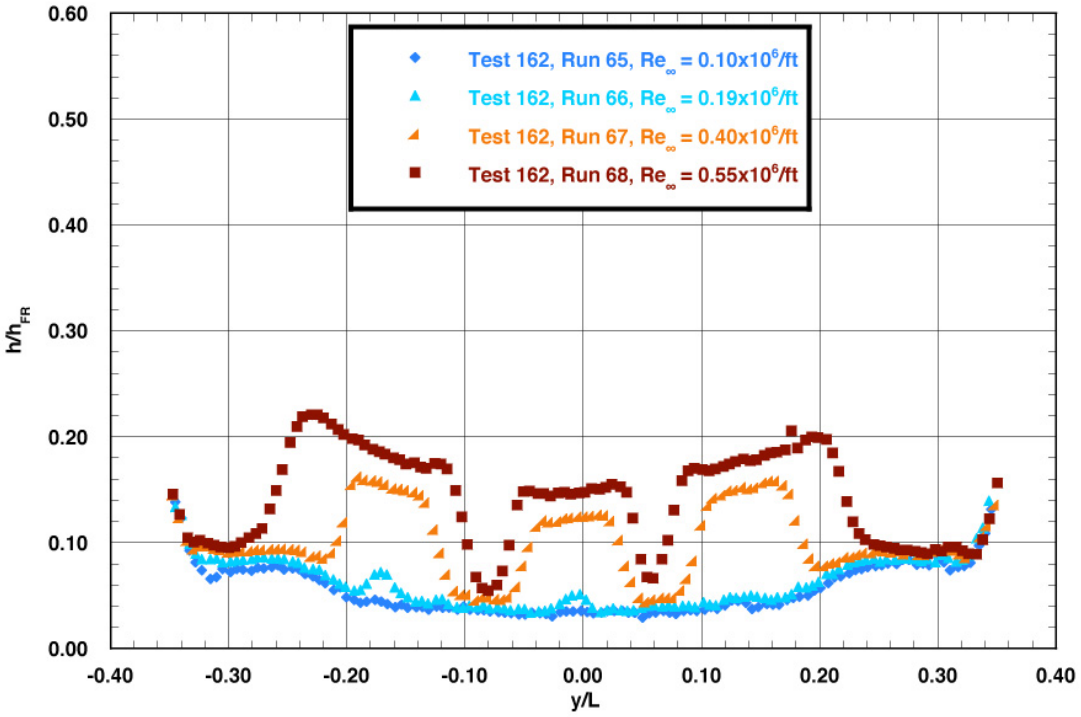

Figure C.30: RTF-BLT-PC spanwise data (x/L = 0.85) in the 20-Inch CF_4 Tunnel at α = 40-deg, x/L = 0.40, k_{CL} = 0.0115-in., $k_{AL\text{-}40\text{-}INV+}$ = 0.0115-in.

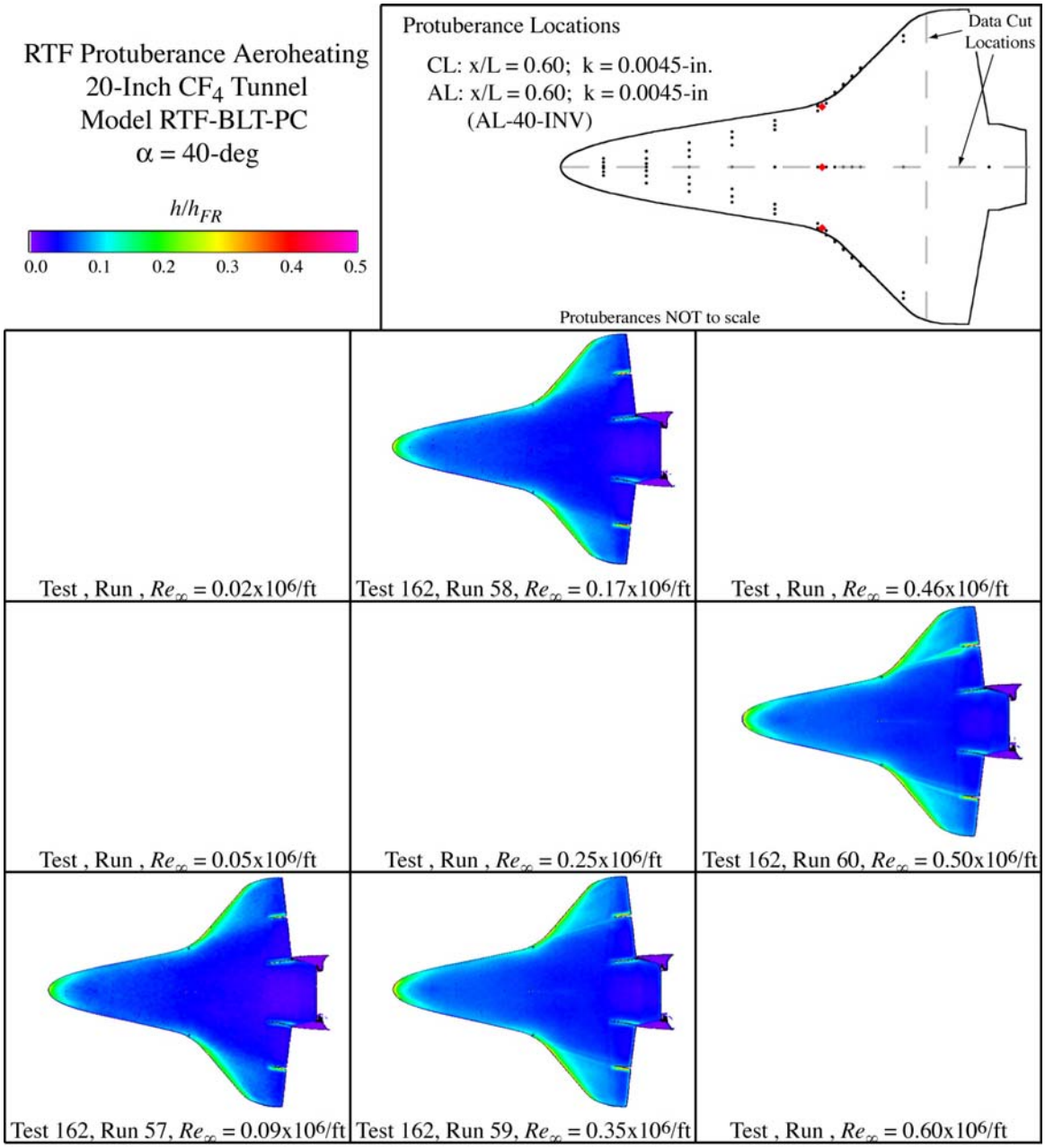

Figure C.31: RTF-BLT-PC global aeroheating in the 20-Inch CF_4 Tunnel at α = 40-deg, x/L = 0.60, k_{CL} = 0.0045-in., $k_{AL\text{-}40\text{-}INV}$ = 0.0045-in.

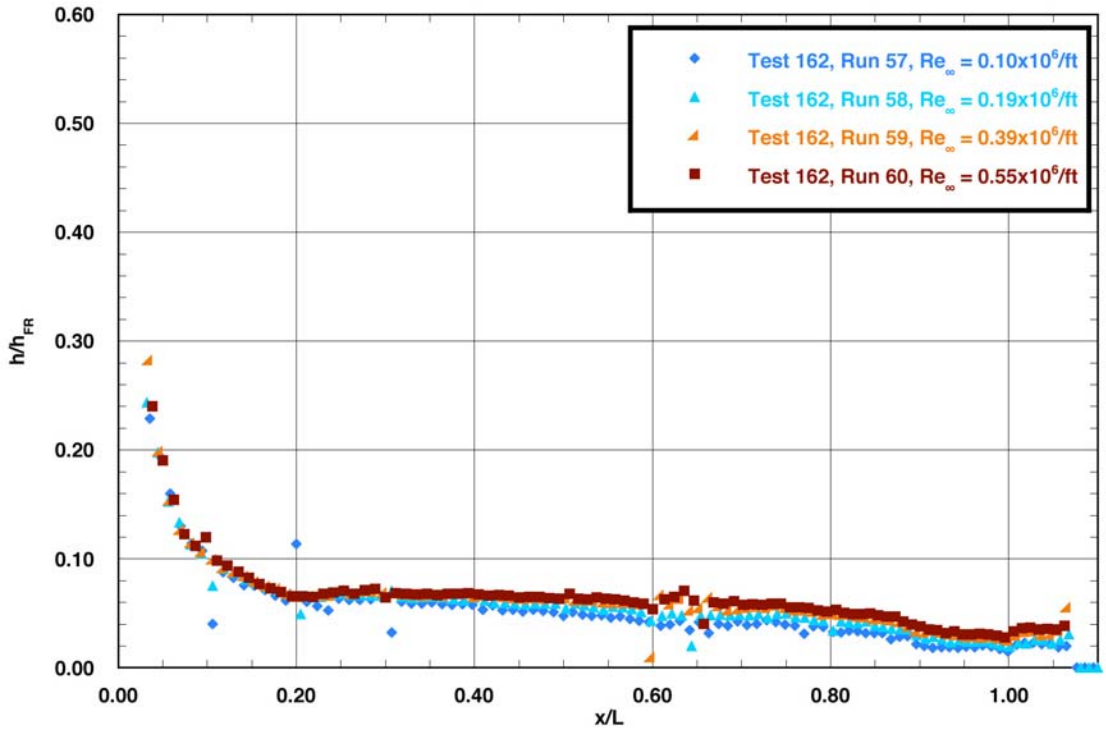

Figure C.32: RTF-BLT-PC centerline data in the 20-Inch CF_4 Tunnel at α = 40-deg, x/L = 0.60, k_{CL} = 0.0045-in., $k_{AL\text{-}40\text{-}INV}$ = 0.0045-in.

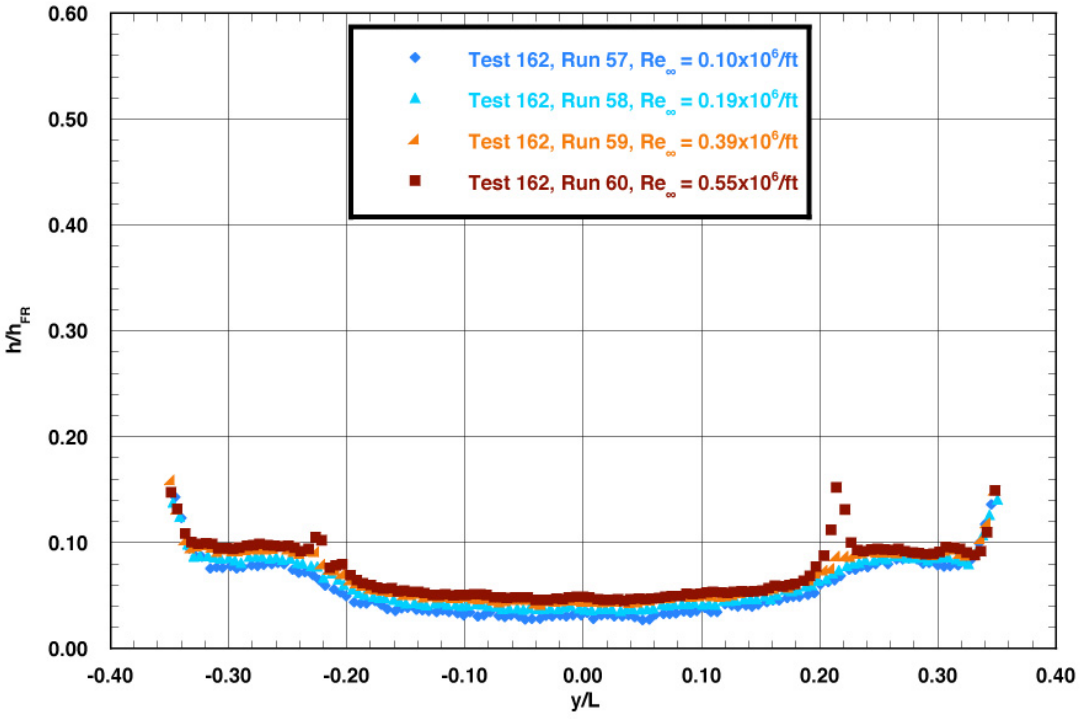

Figure C.33: RTF-BLT-PC spanwise data (x/L = 0.85) in the 20-Inch CF_4 Tunnel at α = 40-deg, x/L = 0.60, k_{CL} = 0.0045-in., $k_{AL\text{-}40\text{-}INV}$ = 0.0045-in

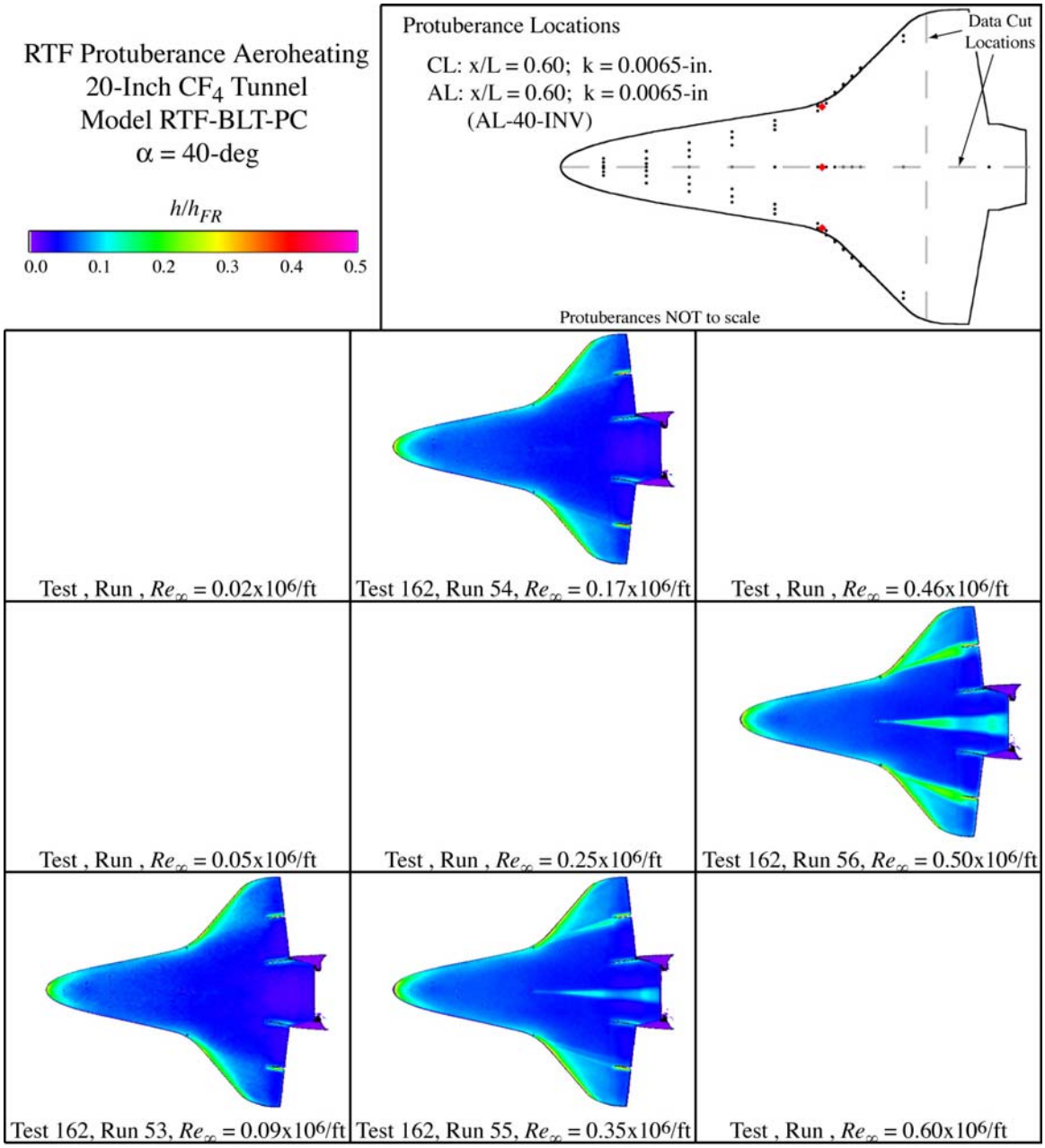

Figure C.34: RTF-BLT-PC global aeroheating in the 20-Inch CF_4 Tunnel at α = 40-deg, x/L = 0.60, k_{CL} = 0.0065-in., $k_{AL\text{-}40\text{-}INV}$ = 0.0065-in.

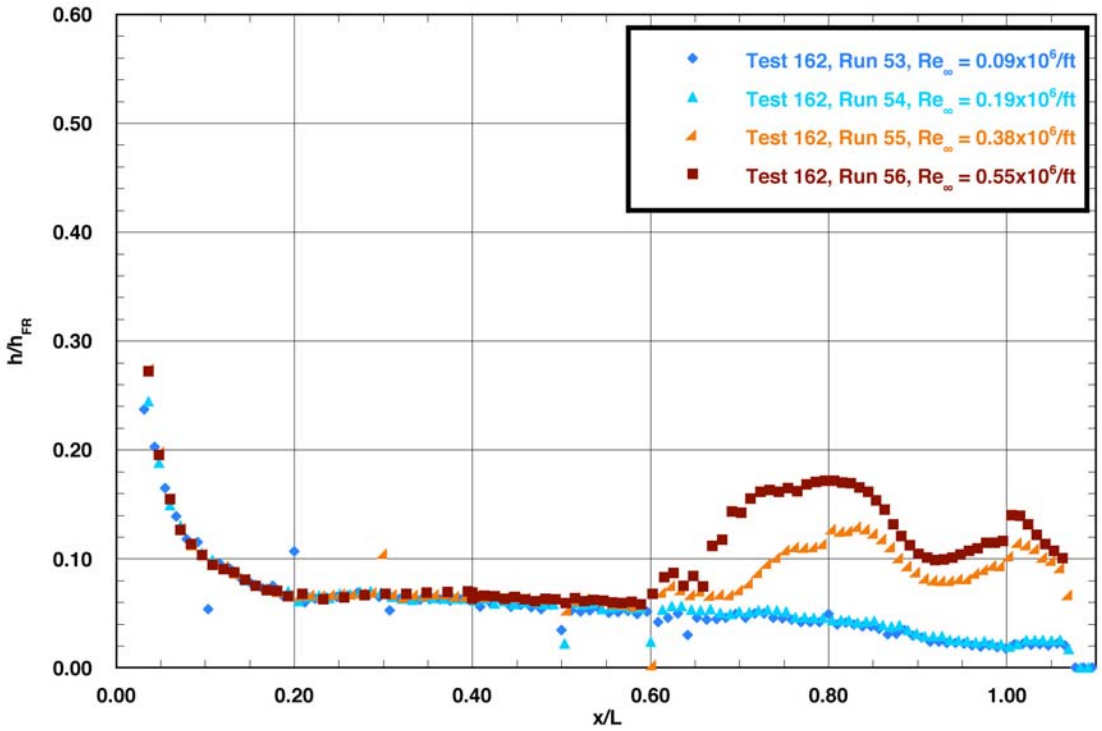

Figure C.35: RTF-BLT-PC centerline data in the 20-Inch CF_4 Tunnel at α = 40-deg, x/L = 0.60, k_{CL} = 0.0065-in., $k_{AL\text{-}40\text{-}INV}$ = 0.0065-in.

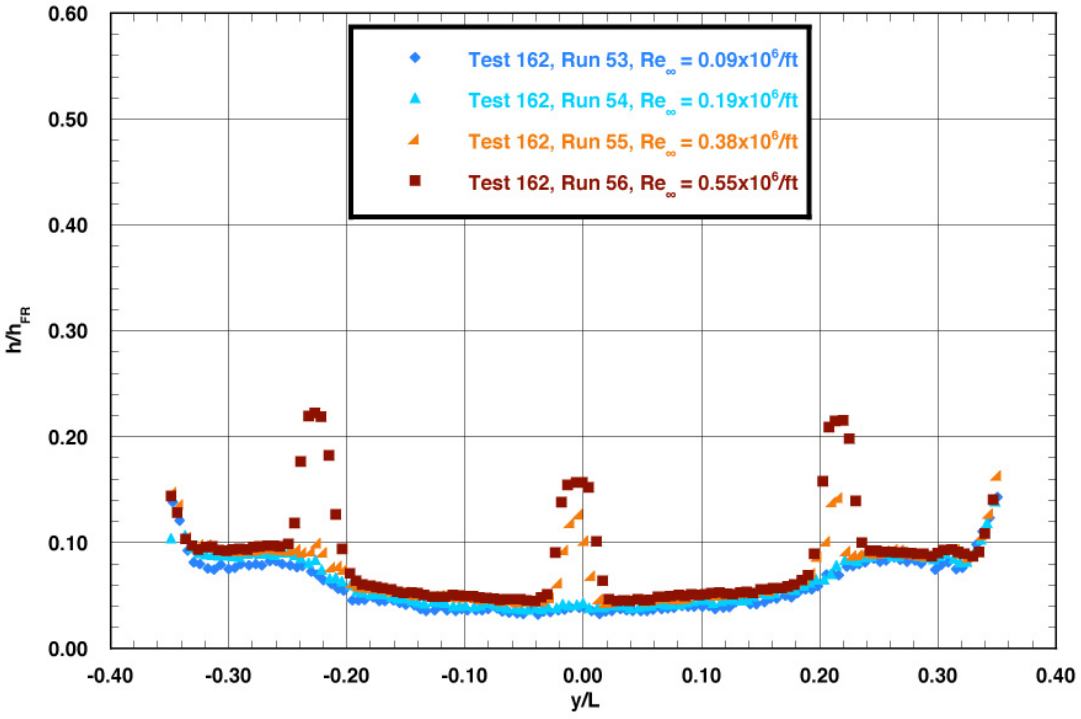

Figure C.36: RTF-BLT-PC spanwise data (x/L = 0.85) in the 20-Inch CF_4 Tunnel at α = 40-deg, x/L = 0.60, k_{CL} = 0.0065-in., $k_{AL\text{-}40\text{-}INV}$ = 0.0065-in.

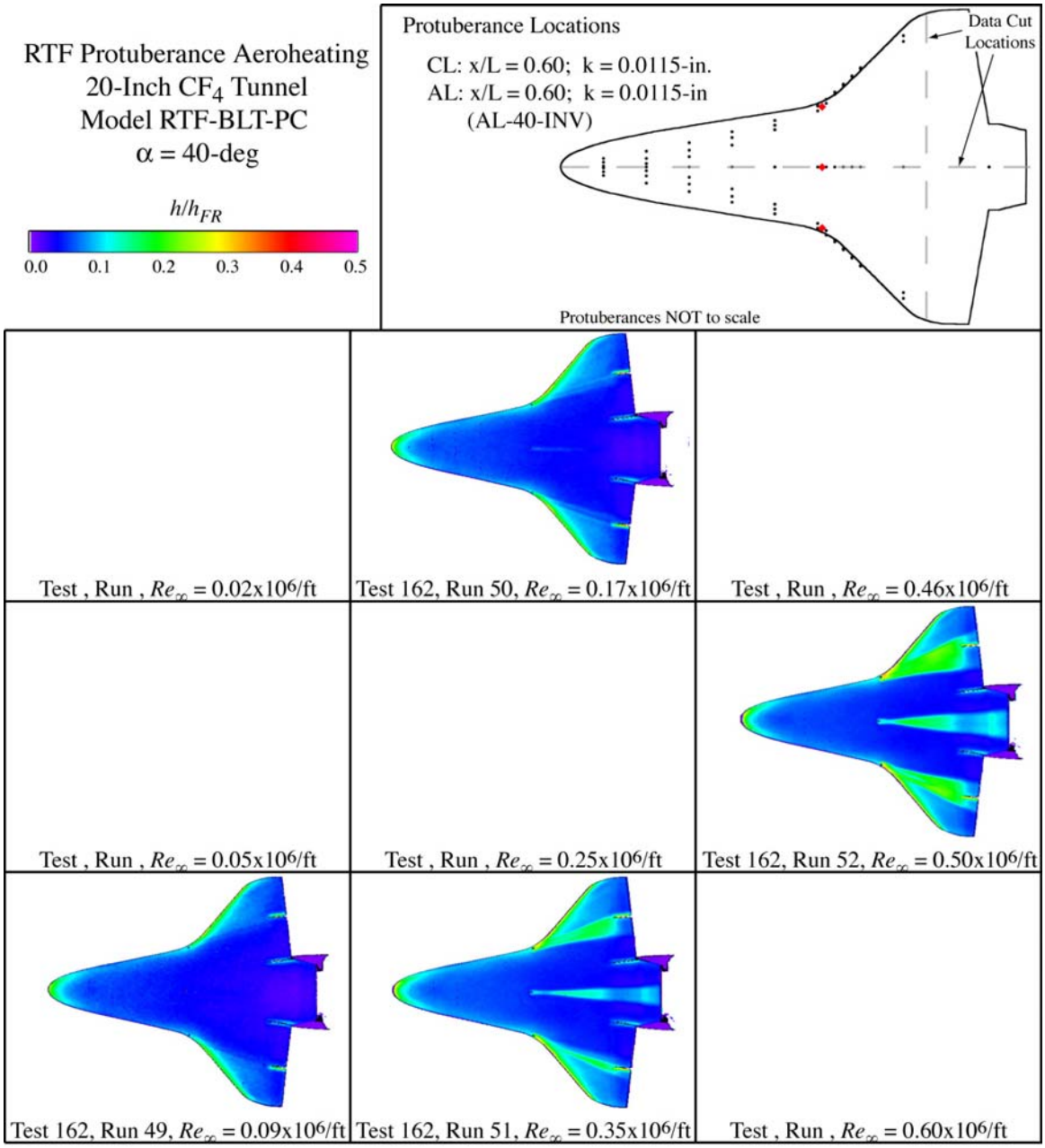

Figure C.37: RTF-BLT-PC global aeroheating in the 20-Inch CF_4 Tunnel at α = 40-deg, x/L = 0.60, k_{CL} = 0.0115-in., $k_{AL\text{-}40\text{-}INV}$ = 0.0115-in.

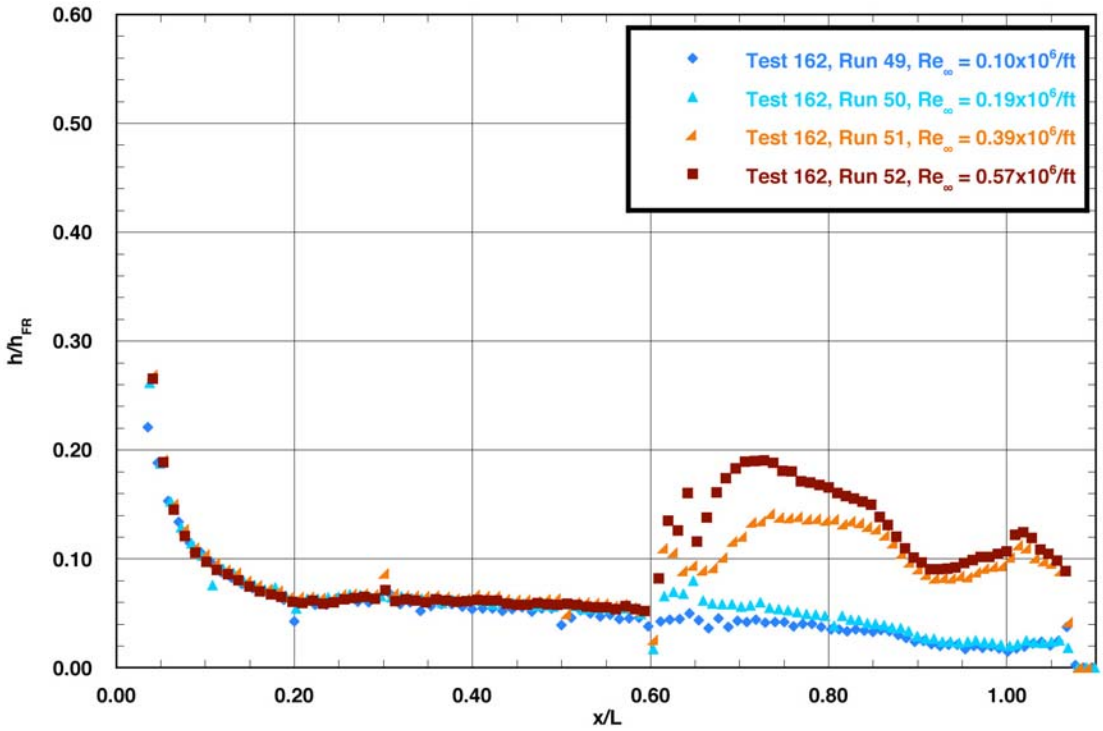

Figure C.38: RTF-BLT-PC centerline data in the 20-Inch CF_4 Tunnel at α = 40-deg, x/L = 0.60, k_{CL} = 0.0115-in., $k_{AL\text{-}40\text{-}INV}$ = 0.0115-in.

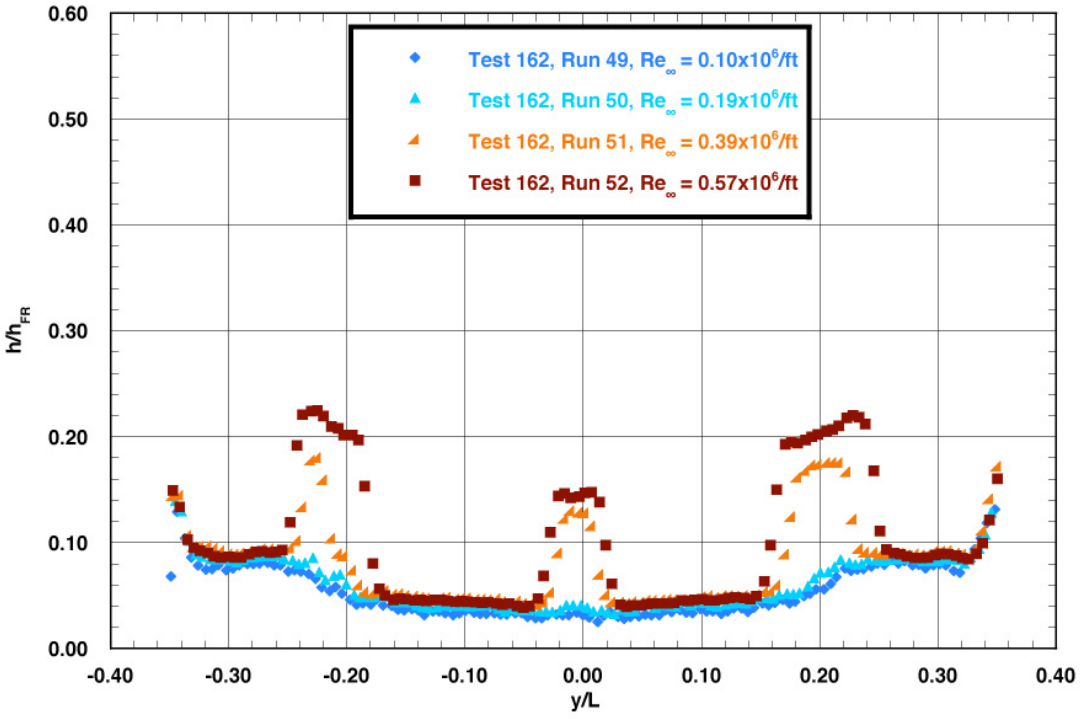

Figure C.39: RTF-BLT-PC spanwise data (x/L = 0.85) in the 20-Inch CF_4 Tunnel at α = 40-deg, x/L = 0.60, k_{CL} = 0.0115-in., $k_{AL\text{-}40\text{-}INV}$ = 0.0115-in.

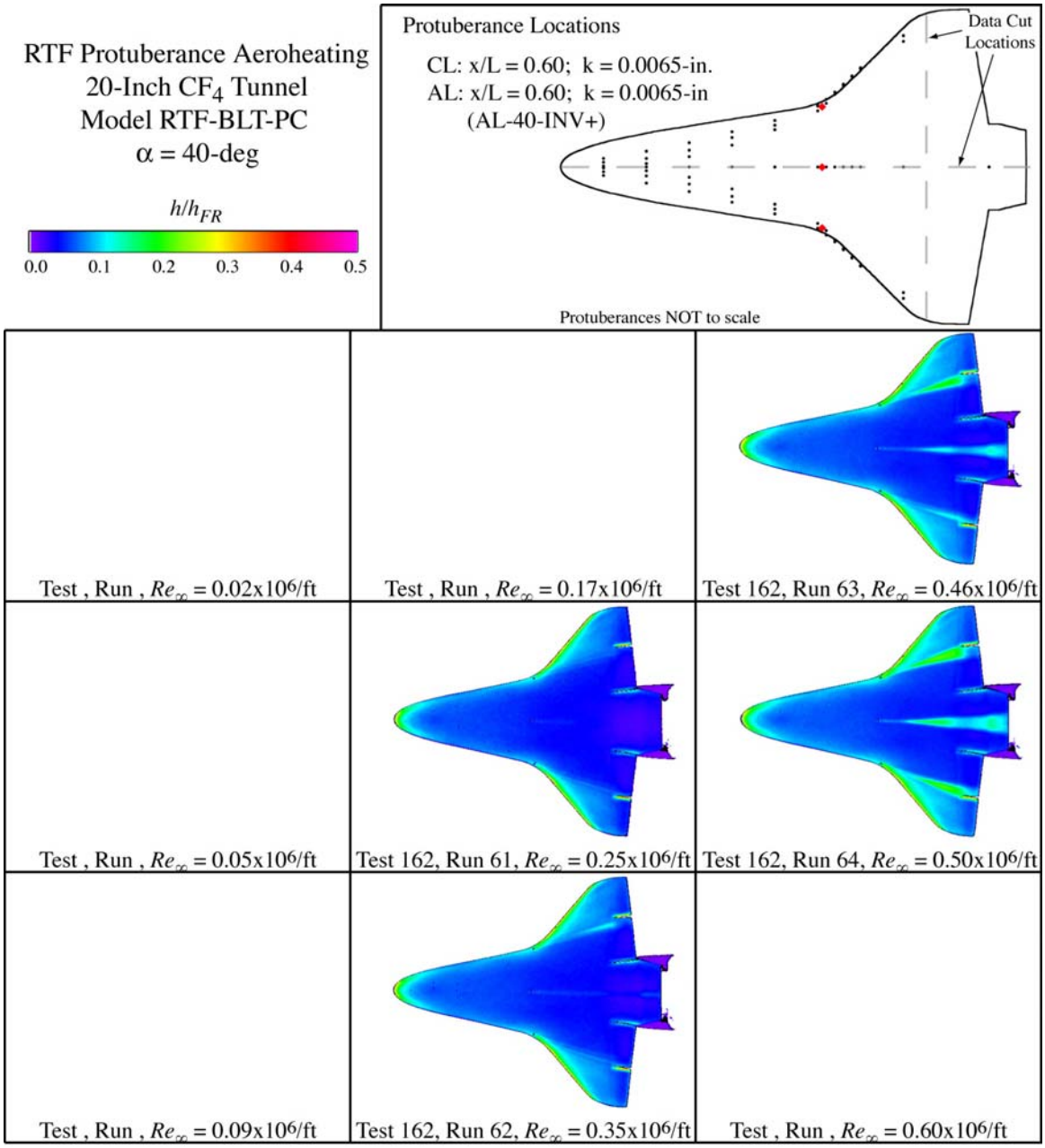

Figure C.40: RTF-BLT-PC global aeroheating in the 20-Inch CF_4 Tunnel at α = 40-deg, x/L = 0.60, k_{CL} = 0.0065-in., $k_{AL\text{-}40\text{-}INV+}$ = 0.0065-in.

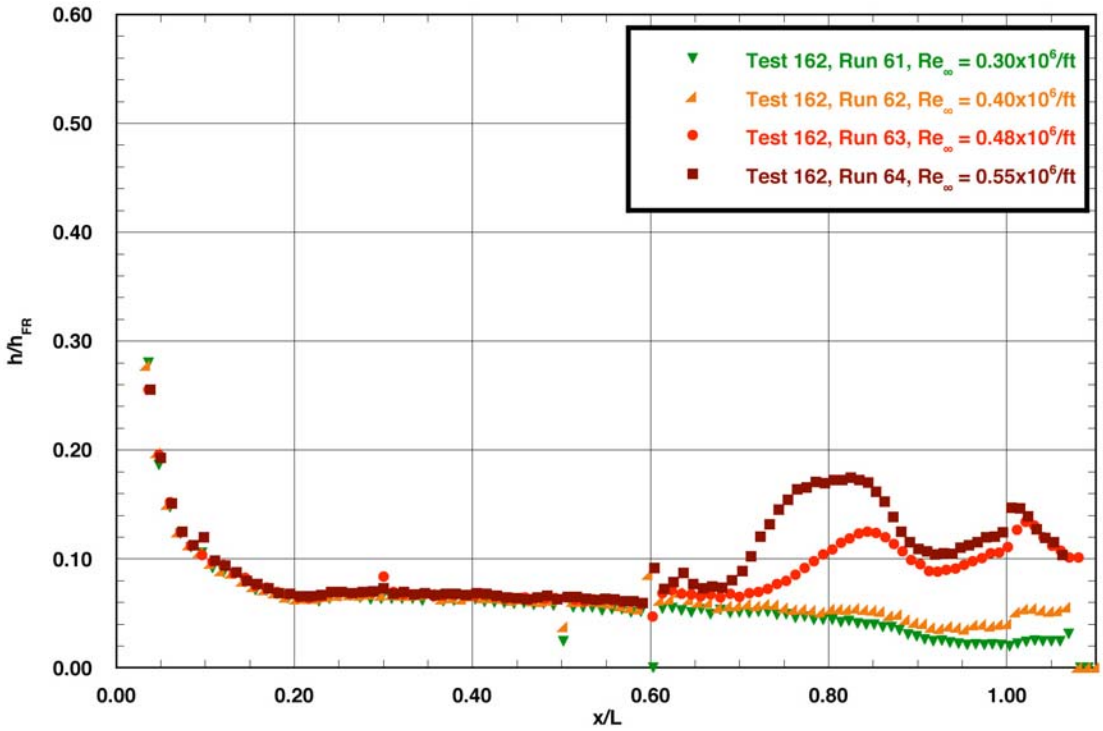

Figure C.41: RTF-BLT-PC centerline data in the 20-Inch CF_4 Tunnel at α = 40-deg, x/L = 0.60, k_{CL} = 0.0065-in., $k_{AL\text{-}40\text{-}INV+}$ = 0.0065-in.

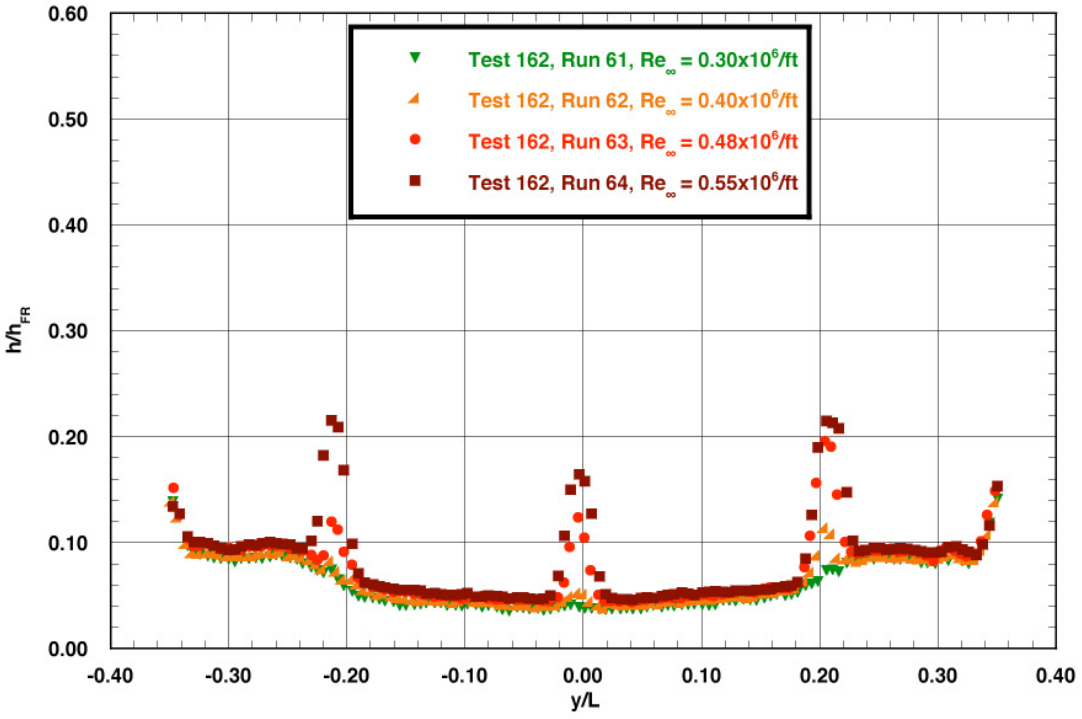

Figure C.42: RTF-BLT-PC spanwise data (x/L = 0.85) in the 20-Inch CF_4 Tunnel at α = 40-deg, x/L = 0.60, k_{CL} = 0.0065-in., $k_{AL\text{-}40\text{-}INV+}$ = 0.0065-in.

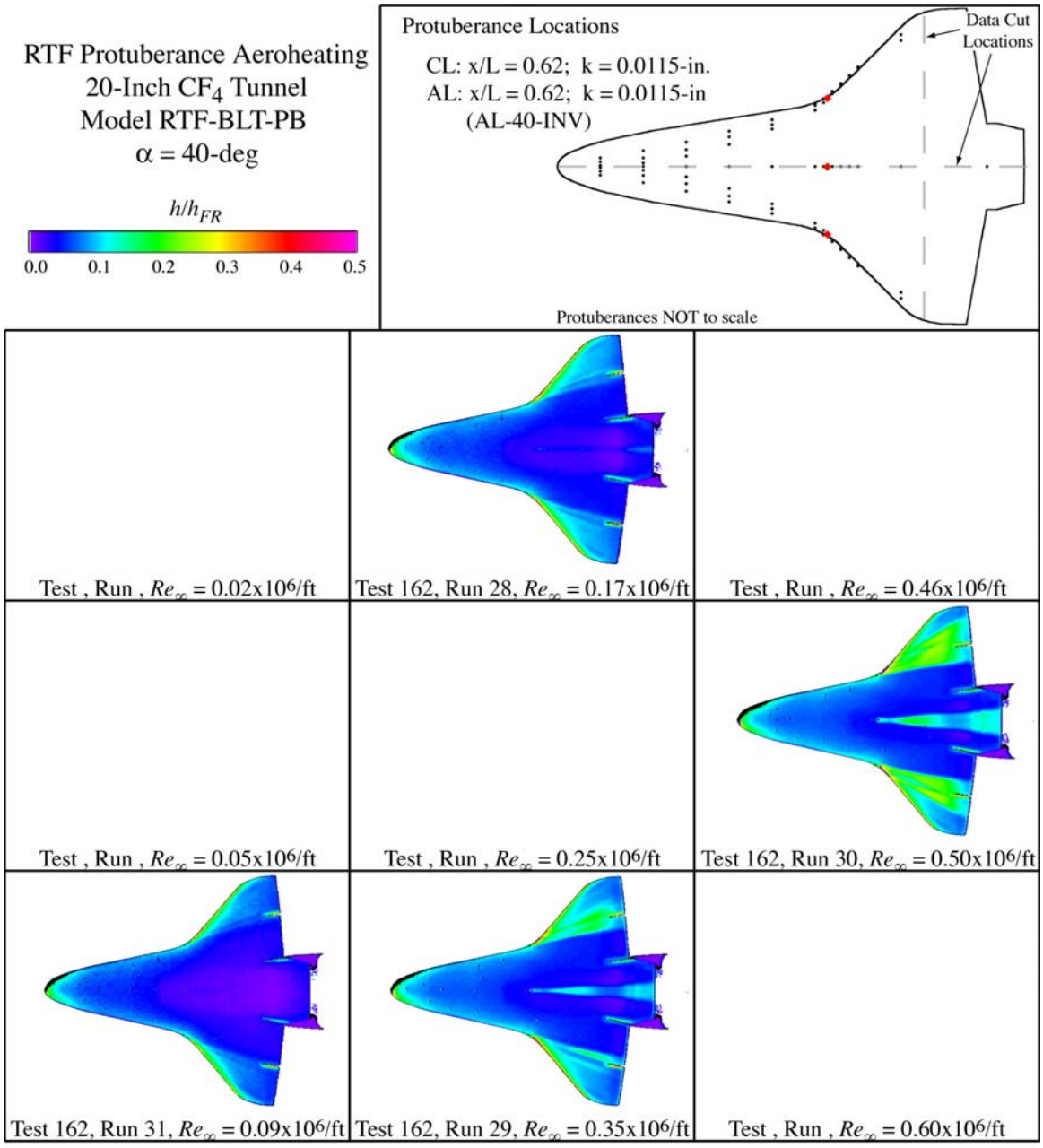

Figure C.43: RTF-BLT-PB global aeroheating in the 20-Inch CF_4 Tunnel at α = 40-deg, x/L = 0.62, k_{CL} = 0.0115-in., $k_{AL\text{-}40\text{-}INV}$ = 0.0115-in.

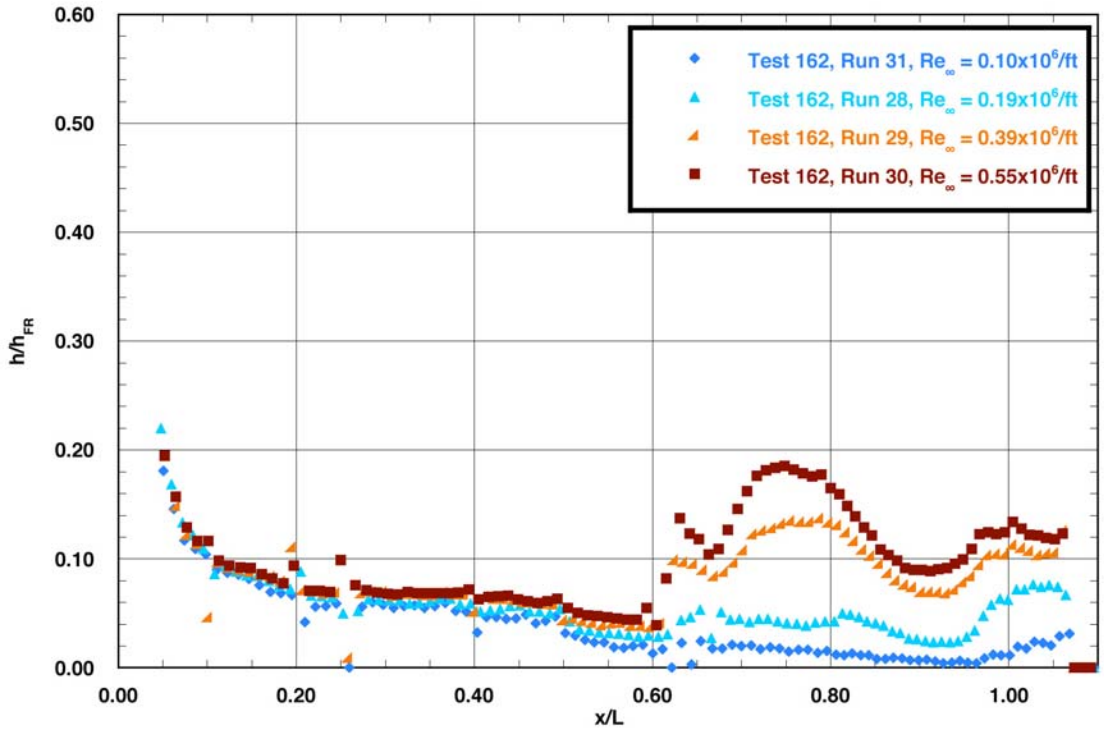

Figure C.44: RTF-BLT-PB centerline data in the 20-Inch CF_4 Tunnel at α = 40-deg, x/L = 0.62, k_{CL} = 0.0115-in., $k_{AL\text{-}40\text{-}INV}$ = 0.0115-in.

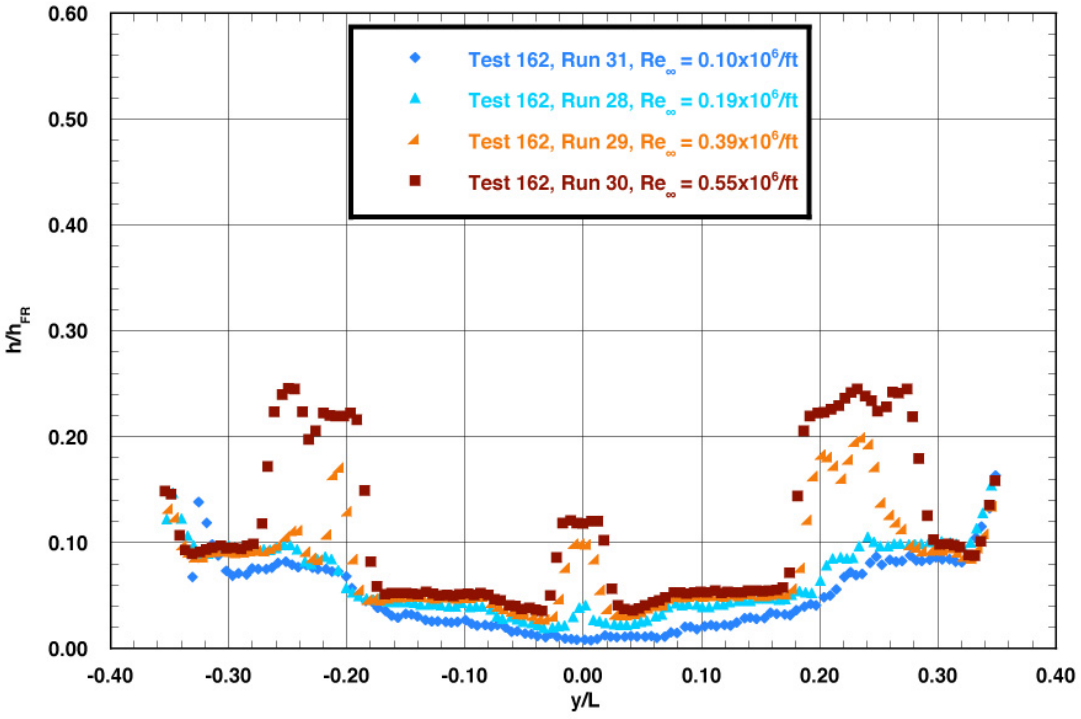

Figure C.45: RTF-BLT-PB spanwise data (x/L = 0.85) in the 20-Inch CF_4 Tunnel at α = 40-deg, x/L = 0.62, k_{CL} = 0.0115-in., $k_{AL\text{-}40\text{-}INV}$ = 0.0115-in.

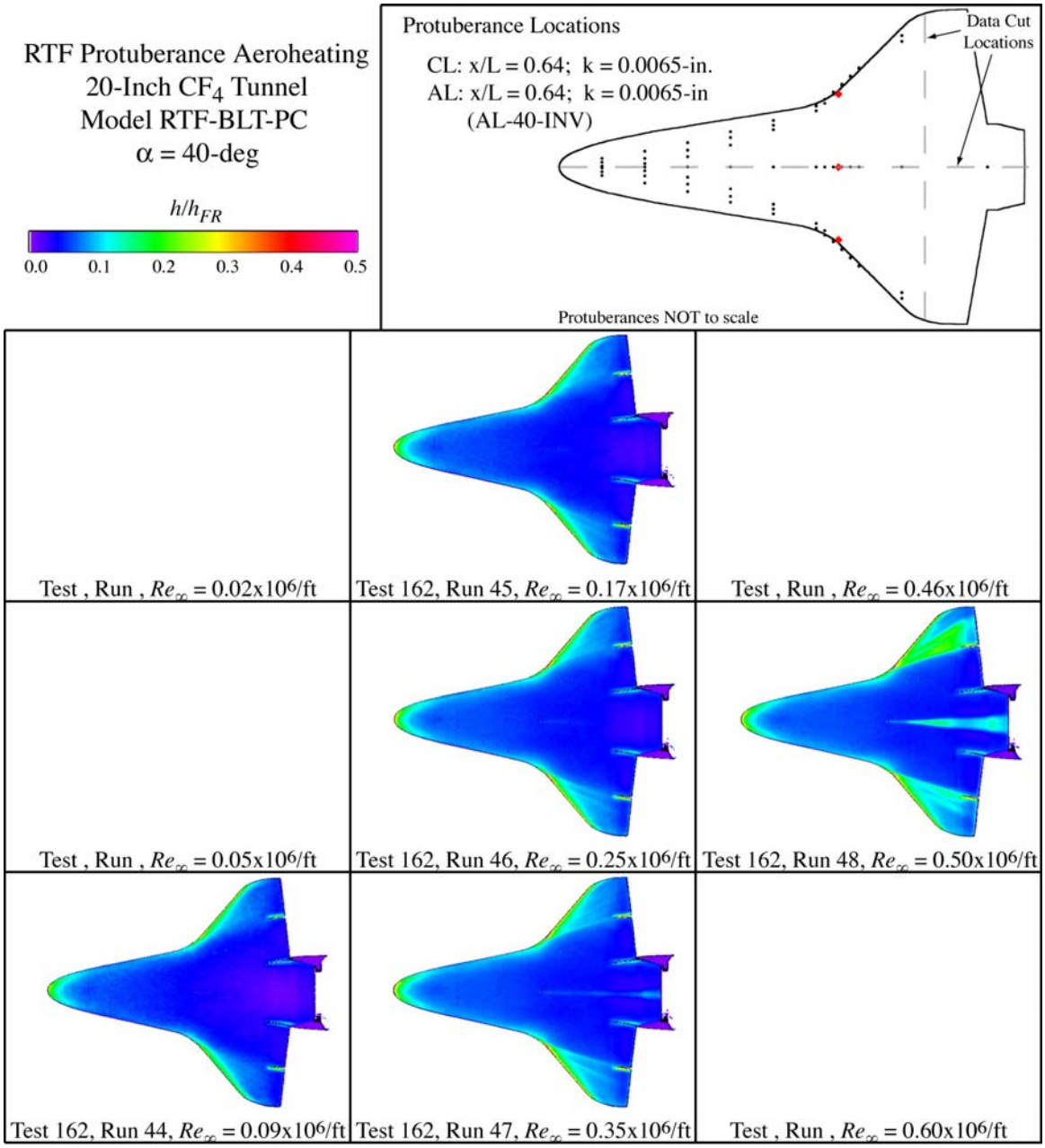

Figure C.46: RTF-BLT-PC global aeroheating in the 20-Inch CF_4 Tunnel at α = 40-deg, x/L = 0.64, k_{CL} = 0.0065-in., $k_{AL\text{-}40\text{-}INV}$ = 0.0065-in.

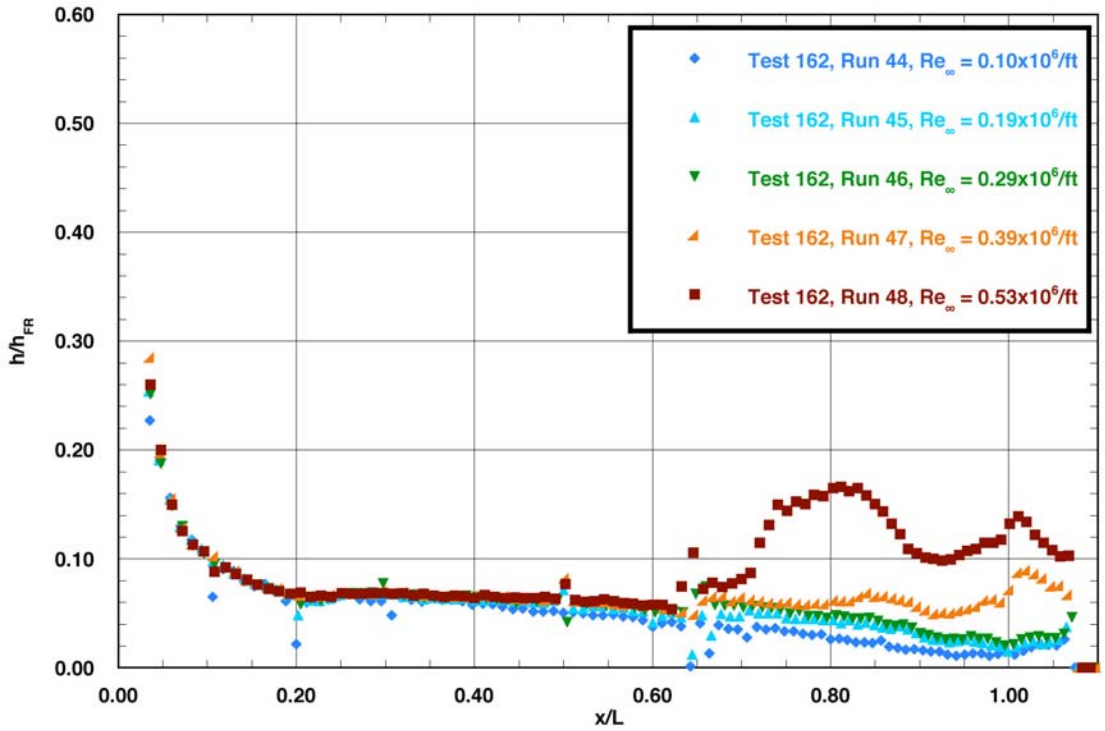

Figure C.47: RTF-BLT-PC centerline data in the 20-Inch CF_4 Tunnel at α = 40-deg, x/L = 0.64, k_{CL} = 0.0065-in., $k_{AL\text{-}40\text{-}INV}$ = 0.0065-in.

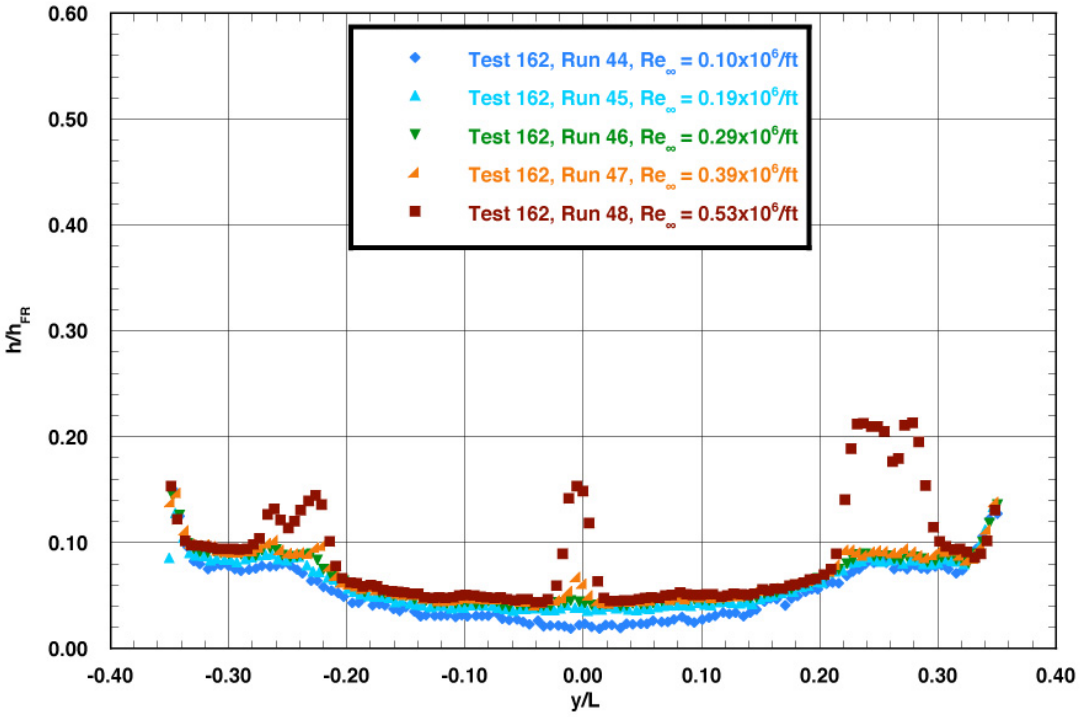

Figure C.48: RTF-BLT-PC spanwise data (x/L = 0.85) in the 20-Inch CF_4 Tunnel at α = 40-deg, x/L = 0.64, k_{CL} = 0.0065-in., $k_{AL\text{-}40\text{-}INV}$ = 0.0065-in.

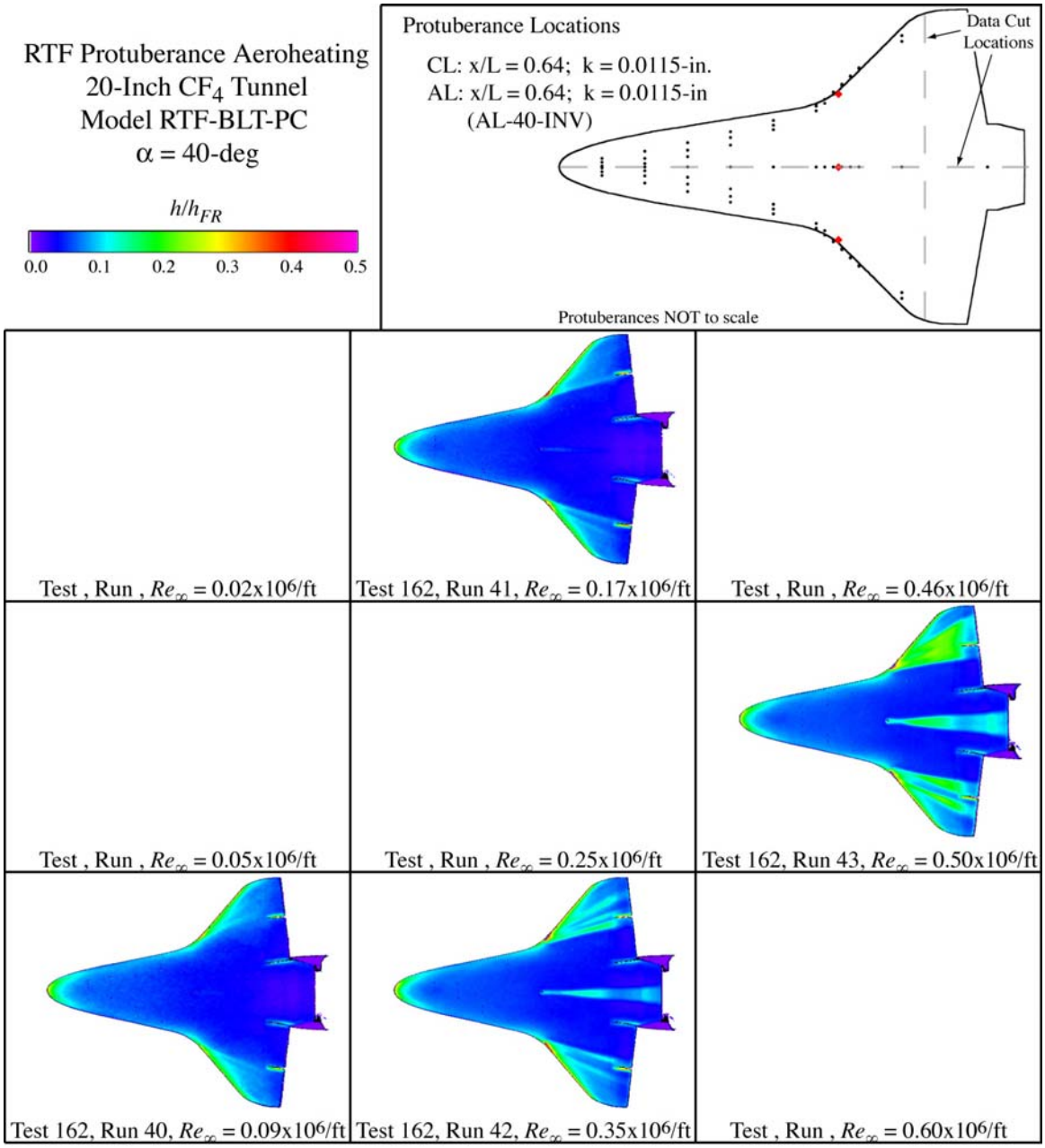

Figure C.49: RTF-BLT-PC global aeroheating in the 20-Inch CF_4 Tunnel at α = 40-deg, x/L = 0.64, k_{CL} = 0.0115-in., $k_{AL\text{-}40\text{-}INV}$ = 0.0115-in.

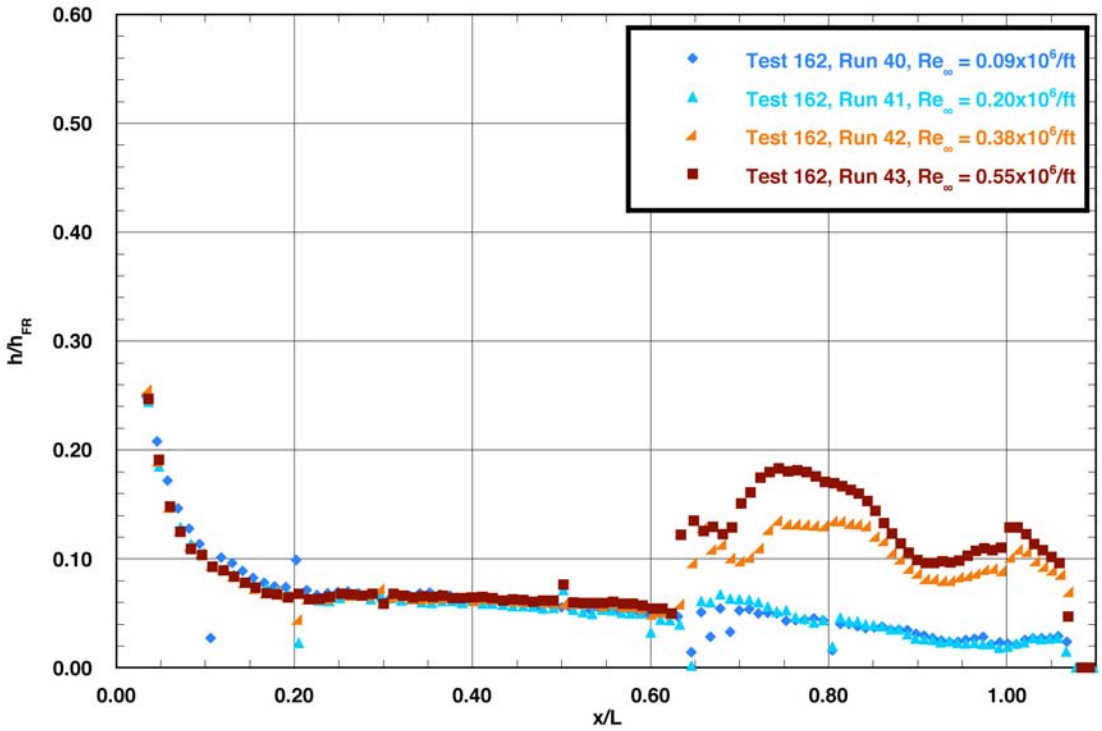

Figure C.50: RTF-BLT-PC centerline data in the 20-Inch CF_4 Tunnel at α = 40-deg, x/L = 0.64, k_{CL} = 0.0115-in., $k_{AL\text{-}40\text{-}INV}$ = 0.0115-in.

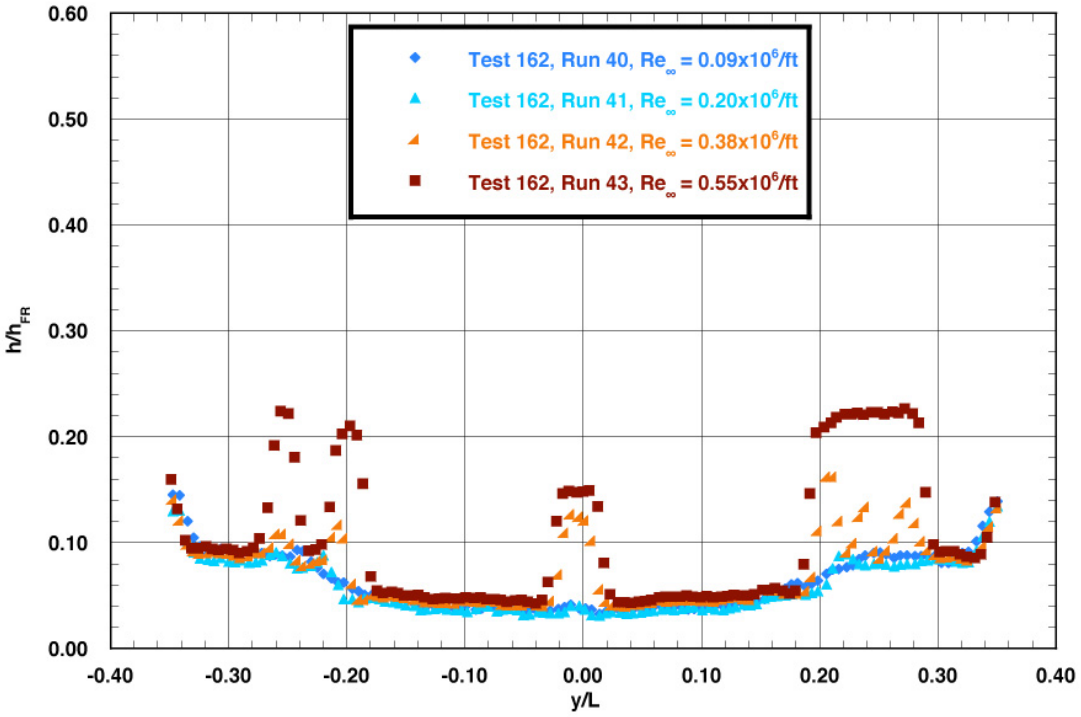

Figure C.51: RTF-BLT-PC spanwise data (x/L = 0.85) in the 20-Inch CF_4 Tunnel at α = 40-deg, x/L = 0.64, k_{CL} = 0.0115-in., $k_{AL\text{-}40\text{-}INV}$ = 0.0115-in.

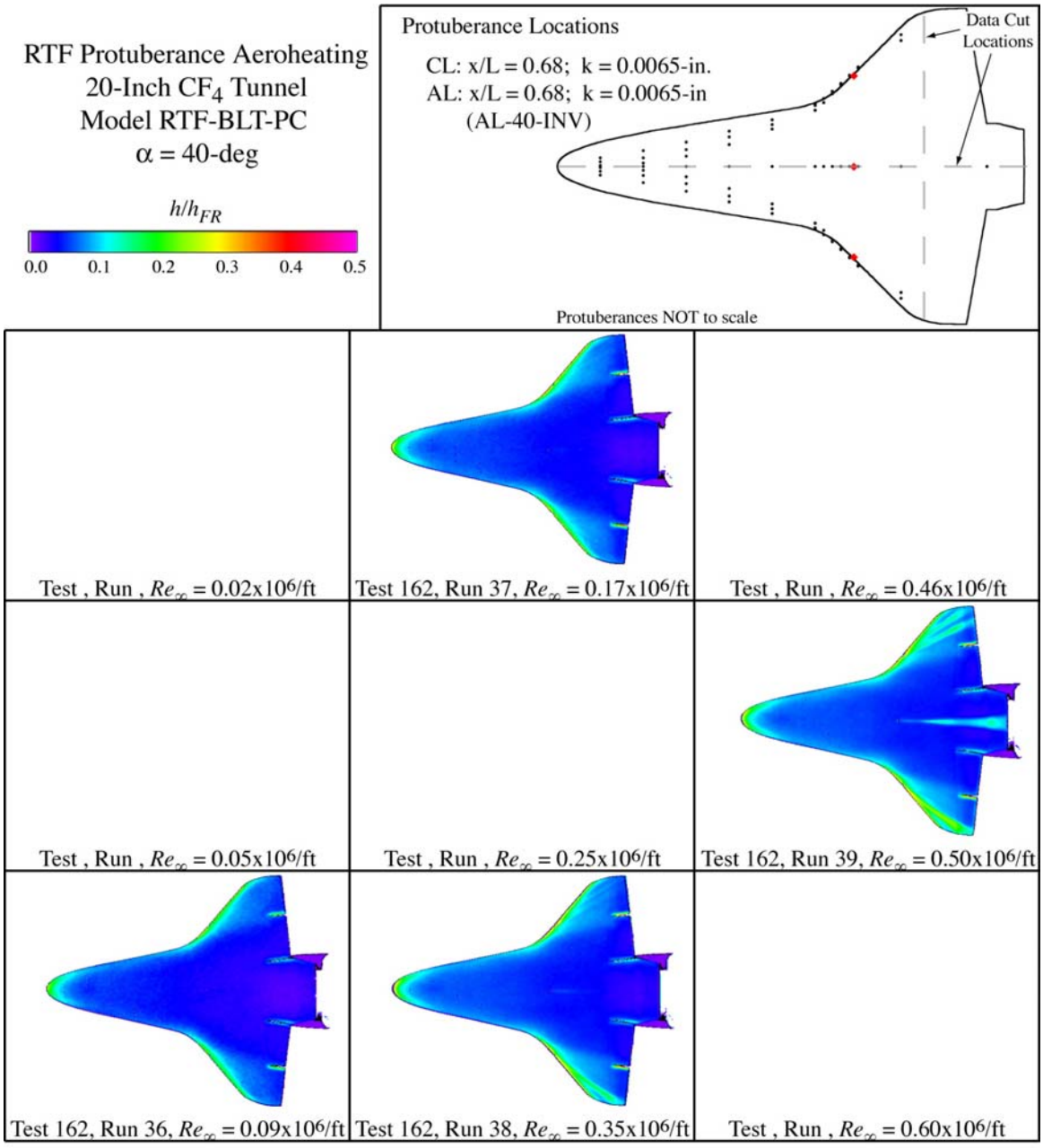

Figure C.52: RTF-BLT-PC global aeroheating in the 20-Inch CF_4 Tunnel at α = 40-deg, x/L = 0.68, k_{CL} = 0.0065-in., $k_{AL\text{-}40\text{-}INV}$ = 0.0065-in.

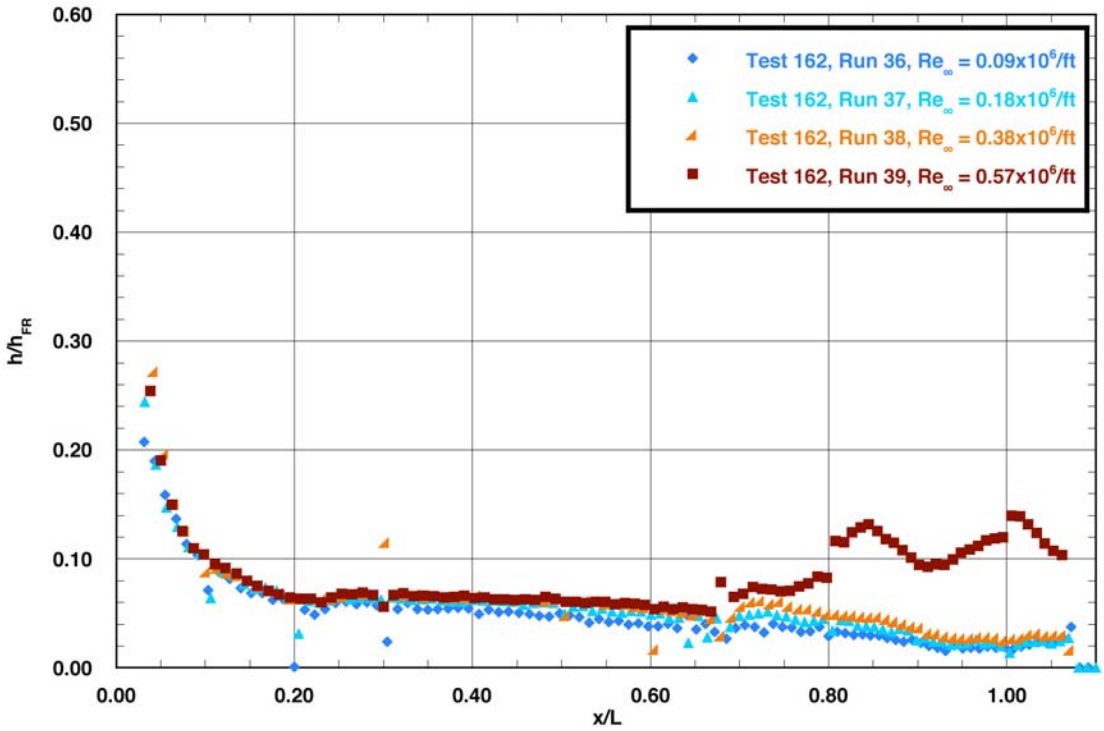

Figure C.53: RTF-BLT-PC centerline data in the 20-Inch CF_4 Tunnel at α = 40-deg, x/L = 0.68, k_{CL} = 0.0065-in., $k_{AL\text{-}40\text{-}INV}$ = 0.0065-in.

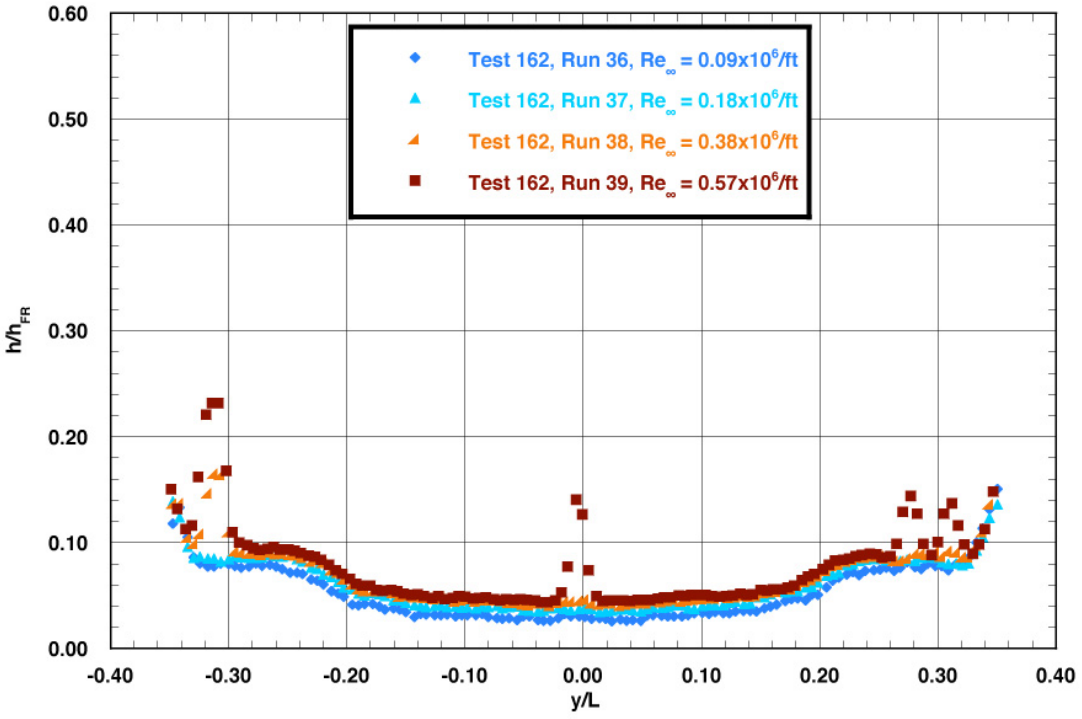

Figure C.54: RTF-BLT-PC spanwise data (x/L = 0.85) in the 20-Inch CF_4 Tunnel at α = 40-deg, x/L = 0.68, k_{CL} = 0.0065-in., $k_{AL\text{-}40\text{-}INV}$ = 0.0065-in.

REPORT DOCUMENTATION PAGE

Form Approved
OMB No. 0704-0188

1. REPORT DATE *(DD-MM-YYYY)*	2. REPORT TYPE	3. DATES COVERED *(From - To)*
01- 06 - 2006	Technical Memorandum	

4. TITLE AND SUBTITLE

Shuttle Return To Flight Experimental Results: Protuberance Effects on Boundary Layer Transition

5a. CONTRACT NUMBER

5b. GRANT NUMBER

5c. PROGRAM ELEMENT NUMBER

6. AUTHOR(S)

Liechty, Derek S.; Berry, Scott A.; and Horvath, Thomas J.

5d. PROJECT NUMBER

5e. TASK NUMBER

5f. WORK UNIT NUMBER

732759.07.05

7. PERFORMING ORGANIZATION NAME(S) AND ADDRESS(ES)

NASA Langley Research Center
Hampton, VA 23681-2199

8. PERFORMING ORGANIZATION REPORT NUMBER

L-19259

9. SPONSORING/MONITORING AGENCY NAME(S) AND ADDRESS(ES)

National Aeronautics and Space Administration
Washington, DC 20546-0001

10. SPONSOR/MONITOR'S ACRONYM(S)

NASA

11. SPONSOR/MONITOR'S REPORT NUMBER(S)

NASA/TM-2006-214306

12. DISTRIBUTION/AVAILABILITY STATEMENT

Unclassified - Unlimited
Subject Category 34
Availability: NASA CASI (301) 621-0390

13. SUPPLEMENTARY NOTES

An electronic version can be found at http://ntrs.nasa.gov

14. ABSTRACT

The effect of isolated roughness elements on the windward boundary layer of the Shuttle Orbiter has been experimentally examined in the Langley Aerothermodynamic Laboratory in support of an agency-wide effort to prepare the Shuttle Orbiter for return to flight. This experimental effort was initiated to provide a roughness effects database for developing transition criteria to support on-orbit decisions to repair damage to the thermal protection system. Boundary layer transition results were obtained using trips of varying heights and locations along the centerline and attachment lines of 0.0075-scale models. Global heat transfer images using phosphor thermography of the Orbiter windward surface and the corresponding heating distributions were used to infer the state of the boundary layer (laminar, transitional, or turbulent). The database contained within this report will be used to formulate protuberance-induced transition correlations using predicted boundary layer edge parameters.

15. SUBJECT TERMS

Space Shuttle Orbiter; Thermal protection system; Boundary layer transition; Protuberance effects

16. SECURITY CLASSIFICATION OF:			17. LIMITATION OF ABSTRACT	18. NUMBER OF PAGES	19a. NAME OF RESPONSIBLE PERSON
a. REPORT	b. ABSTRACT	c. THIS PAGE			STI Help Desk (email: help@sti.nasa.gov)
					19b. TELEPHONE NUMBER *(Include area code)*
U	U	U	UU	162	(301) 621-0390